Performance considerations in high-speed TDFA-band silicon photonic micro-ring resonator modulators

Performance considerations in high-speed TDFA-band silicon photonic micro-ring resonator modulators

By David Hagan,

A Thesis Submitted to the School of Graduate Studies in the Partial Fulfillment of the Requirements for the Degree Ph.D.

McMaster University © Copyright by David Hagan December 19, 2019

McMaster University

Ph.D. (2019)

Hamilton, Ontario (Department of Engineering Physics)

TITLE: Performance considerations in high-speed TDFA-band silicon photonic micro-ring resonator modulators

AUTHOR: David Hagan (McMaster University)

SUPERVISOR: Dr. Andrew P. Knights

NUMBER OF PAGES: xxv, 229

Abstract

The ever-increasing bandwidth requirements to support telecommunications infrastructure necessitates large-scale fabrication of low-cost and scalable silicon photonic integrated circuits. Wavelength-division multiplexing (WDM) schemes are fundamentally limited in the number of channels supported in long-haul transmission by the erbium doped fiber amplifier (EDFA). To address this, researchers have turned focus toward the thulium doped fiber amplifier (TDFA), which provides 3× more bandwidth. This thesis describes the development of high-speed silicon-on-insulator (SOI) micro-ring resonator (MRR) modulators optimized for wavelengths in the TDFA band. Chapter 2 presents a theoretical performance comparison between MRR modulators designed for optimized use at EDFA and TDFA wavelengths. Chapter 3 presents an experimental study of optical loss mechanisms at extended wavelengths which suggests reduced waveguide scattering and enhanced divacancy defect absorption as well as larger bending and substrate leakage losses when compared with shorter wavelengths. An electronic variable optical attenuator is characterized in Chapter 4 to experimentally verify the predicted 1.7× TDFA-band free-carrier effect enhancement over EDFA-band wavelengths. The first steady-state operation of an MMR modulator near a central wavelength of 1.97 μm is also demonstrated under the enhanced free-carrier effect. Chapter 5 demonstrates the first high-speed reverse bias operation of an MRR modulator with a measured bandwidth of 12.5 GHz, and an on-chip optical link consisting of a modulator followed by a defect-mediated detector with open eye-diagrams up to data rates of 12.5 Gbps. Chapter 6 introduces an electrically-driven post-fabrication defect-assisted resonance trimming technique via local annealing for use in MRR devices. Chapter 7 presents a Monte Carlo simulation of resonance alignment in multi-MRR systems subjected to spatially-correlated wafer variation created through the Virtual Wafer Model process to predict thermal power consumption and power reduction through resonance trimming.

Acknowledgements

First and foremost, I would like to thank my supervisor and mentor Dr. Andrew Knights, who offered me every possible opportunity to excel in my academic career and made me the professional I am today. Thank you for entertaining all of my deranged ideas, keeping me motivated, and being a friend. My time here wasn't just *"alright!"*, it was *"great stuff!"*.

I would also like to extend thanks to my committee members: Dr. Daniel Cassidy, who inspired my decision toward pursuing optics through a simple pinhole lens. Dr. Harold Haugen, who has always been a source of wisdom and guidance since my time as an undergraduate. Dr. Jonathan Bradley, who inspired confidence in me. I would like to also thank Zhilin Peng, Doris Stevanovic, Peter Jonasson, and Marilyn Marlow for their support throughout my graduate studies.

I would like to thank Lukas Chrostowski for providing excellent workshop training and design tools through the SiEPIC CREATE program, Dan Deptuck and Jessica Zhang for their support through CMC Microsystems, Jack Hendrix at Western University, and Dr. John Cartledge and Peng Wang at Queen's University for their assistance and guidance.

A huge thanks to my group members Jason (*'J-roc'*) Ackert, Edgar (*'Dr. H-bomb'*) Huante-Ceron, Dixon (*'D$'*) Paez-Capacho, Ross (*'the boss'*) Anthony, (*'Chairman'*) Zhao Wang, Jeremy (*'Jear-bear'*) Miller, and my 2 μm compadre, Khadijeh Kiani.

Many thanks to the rest of the 'Knights' and 'Bradley' lab groups along with our summer students Zachary, Liam, Ben, and Jackson. A special thanks to my co-workers during my time at Ranovus Inc. including Dylan Logan, Kyle Murray, Edgar Huante-Ceron, Prova Gomes, Ana Villafranca, Chris Brooks, and Jeff Wheeldon.

To my band members who never took "I'm too busy studying" as an answer, thank

you for allowing me the catharsis I needed and for keeping my love of music burning. To my friends in the Math department, Ramsha, Pip, and Tyler, thank you for giving me a home away from home away from home. To my housemates, Miles, Taylor, Evan, Dustin, Alex, Melissa, Paul, Ross, Shane, Martin, and Adrian, every moment I can remember, I cherish. Every moment I can't, I treasure. To my close friends back home, thank you for being the universal constant in my life and keeping me tied to the outside world. To Courtney Anderson, the kindest soul who touched so many lives, including my own, thank you for helping me believe in myself.

To the baristas at My Dog Joe / Paisley House, Democracy, Ark + Anchor, Brown Dog, Mighty Good Coffee, and Phin Coffee Bar, I owe every ounce of late-night work to you.

To Toby Z. Rutherford Klunk, you have helped me in countless ways through the final hurdles of my graduate career, helped me hold onto my sanity while writing this thesis, and continue to inspire me to be a better person. Thank you for every walk we've taken, every song we've sung together, and for always making me laugh. To Toby's owner Jen, similar comments apply.

Lastly, I would like to thank my parents and my sister. I would not have made it to this point without their love and support.

Contents

Abstract iii

Acknowledgements iv

List of Acronyms xxi

Declaration of Authorship xxiv

1 Introduction 1

1.1 Optical telecommunication . . . 1

1.1.1 Silicon photonics . . . 4

1.1.2 TDFA-band silicon photonics . . . 7

1.1.3 Manufacturing variation . . . 10

1.1.4 'Fabless' methodology and multi-project wafers . . . 11

1.2 Thesis objectives . . . 13

1.3 Statement of thesis work . . . 13

1.4 Publications . . . 14

1.4.1 Internship statement . . . 15

2 A theoretical performance comparison of EDFA-band and TDFA-band wavelengths in a high-speed micro-ring resonator *p*-*n* junction modulator structure 23

2.1 Introduction . . . 24

2.2 Silicon-on-insulator waveguides 26
2.2.1 Effective index 26
2.2.2 Confinement 29
2.2.3 Group index and dispersion 32
2.3 Free-carrier effect in SOI waveguides 36
2.3.1 The Drude model 36
2.3.2 Empirical models 38
2.3.3 Generation of free-carriers 41
2.4 The *p*-*n* junction modulator 46
2.5 Micro-ring resonator modulator modelling 51
2.5.1 Micro-ring resonator static transfer function 51
2.5.2 Micro-ring resonator modulator static response 58
2.5.3 Micro-ring resonator modulator dynamic response 70
2.6 Conclusion 81

3 Mechanisms for optical loss in SOI waveguides for mid-infrared wavelengths around 2 µm 89

3.1 Introduction 92
3.2 Experimental 93
3.2.1 Design and fabrication 93
3.2.2 Loss measurement 95
3.3 Results and discussion 95
3.3.1 Waveguide propagation loss 95
3.3.2 Bending loss 100
3.3.3 Losses resulting from free-carriers 102
3.3.4 Defect loss 106
3.4 Conclusion and summary 108

4 Experimental quantification of the free-carrier effect in silicon waveguides at extended wavelengths 116

4.1 Introduction 119

4.2 Methods and experimental set-up 120

4.2.1 EVOA 122

4.2.2 MRR 122

4.3 Results and discussion 124

4.4 Conclusion 132

5 High-speed performance of a TDFA-band micro-ring resonator modulator and demonstration of an optical link 137

5.1 Introduction 139

5.2 Design 140

5.2.1 Micro-ring resonator modulator 140

5.2.2 Defect-mediated detector 141

5.3 Methods and experimental setup 142

5.3.1 DC characterization setup 142

5.3.2 RF characterization setup 143

5.4 Results 146

5.4.1 Micro-ring resonator modulator 146

5.4.2 Defect-mediated detector 158

5.4.3 On-chip optical link 161

5.5 Conclusion 163

6 Post-fabrication trimming of silicon ring resonators via integrated annealing 167

6.1 Introduction 169

6.2 Results 171

6.2.1 Heater Efficiency 172
6.2.2 Defect-Induced Resonance Shifts 174
6.2.3 In-Situ Defect Annealing 176
6.2.4 Resonance Trimming 178
6.3 Defect absorption at 1550 and 2000 nm wavelength 179
6.4 Oxide restructuring 181
6.5 Conclusion 182

7 A Monte Carlo simulation of resonance trimming in wavelength-division multiplexing and stacked resonance photonic circuits 187

7.1 Introduction 187
7.2 Method 189
7.2.1 Virtual wafer model 191
7.2.2 Monte Carlo algorithm 192
7.3 Results and discussion 202
7.3.1 Waveguide sensitivity analysis 202
7.3.2 Alignment power consumption 204
7.3.3 Power saving through resonance trimming 213
7.4 Conclusion 216

8 Conclusion 222

8.1 Summary 222
8.2 Suggested future work 227

List of Figures

2.1 Simulated effective indices of TE_0, TM_0 and TE_1 modes in SOI strip waveguides varying width at 1550 nm wavelength. TE_0 indices of ridge waveguide with 90 nm slab included as dashed line. 28

2.2 Simulated effective indices of TE_0, TM_0 and TE_1 modes in SOI strip waveguides varying width at 2000 nm wavelength. TE_0 indices of ridge waveguide with 90 nm slab included as dashed line. 28

2.3 Confinement factor for TE_0 mode in both strip and ridge waveguide geometries for 1550 and 2000 nm wavelengths. 30

2.4 Thermo-optic coefficient for strip and ridge waveguides varying in width for both 1550 and 2000 nm wavelengths. 31

2.5 Mode profiles for 500 and 600 nm wide ridge waveguides for 1550 and 2000 nm wavelengths, respectively. 32

2.6 Fundamental TE_0 mode group indices for 220 nm thick SOI ridge waveguide with 90 nm slab and varying widths. 33

2.7 Material dispersion for bulk silicon and SiO_2, and simulated waveguide dispersion in 220 nm SOI ridge waveguide geometry of varying width. . . 34

2.8 Bulk and waveguide dispersion as a function of width for wavelengths of 1550 and 2000 nm. 35

2.9 Change in refractive index, -Δn, as a function of doping concentration for both 1550 and 2000 nm wavelengths. Green lines denote electron-only concentrations while blue denote hole-only concentrations. 40

2.10 Change in absorption coefficient, $\Delta\alpha$, as a function of doping concentration for both 1550 and 2000 nm wavelengths. Green lines denote electron-only concentrations while blue denote hole-only concentrations. 40

2.11 Equivalent electrical circuit of the p-n junction modulator. 48

2.12 All-pass ring resonator configuration. 52

2.13 Change in effective index relative to n_{eff} at 0.5 V bias for 1550 and 2000 nm wavelengths at waveguide widths of 500 and 600 nm, respectively, with theoretical 100% p-n junction coverage. 59

2.14 α for 1550 and 2000 nm wavelengths at 500 and 600 nm waveguide widths, respectively, as a function of contact-doping separation. Solid and dashed lines represent a 2.5 V peak-to-peak swing. 60

2.15 a) Normalized biased transmission spectra for critically-coupled rings at 1550 (solid lines) and 2000 nm wavelength (dotted lines). b) On-off extinction ratio of transmission spectra for increasing peak-to-peak voltage swings. 61

2.16 *TP* for the transmission spectra shown in Figure 2.15 for 1550 nm (solid lines) and 2000 nm (dotted lines) wavelengths. 63

2.17 a) Normalized transmission of MRR modulator spectra for BPSK applications with operating point at equal transmission levels on red- and blue-side of resonance, respectively. b) Associated π phase-shift at operating point. 64

2.18 a) Required voltage swing for a π phase-shift at discrete contact-doping separations as a function of self-coupling coefficient, r, for the 1550 nm wavelength modulator configuration and b) associated transmission at operating point. 65

2.19 a) Required voltage swing for a π phase-shift at discrete contact-doping separations as a function of self-coupling coefficient, r, for the 2000 nm wavelength modulator configuration and b) associated transmission at operating point. 66
2.20 On-off α-parameter for 1550 nm wavelength modulator configuration a) at fixed values of r calculated across wavelength detunings and b) for fixed detunings across r. 68
2.21 On-off α-parameter for 2000 nm wavelength modulator configuration a) at fixed values of r calculated across wavelength detunings and b) for fixed detunings across r. 69
2.22 Normalized $H_t(\omega_m)$ for a) 1550 nm wavelength modulator with a width of 500 nm, doping separation of 500 nm and $r = 0.977$, and b) 2000 nm wavelength modulator with a width of 600 nm, doping separation of 800 nm and $r = 0.975$. 74
2.23 Extracted 3 dB bandwidth for a) 1550 nm modulator configuration with $r = 0.977$ and b) 2000 nm modulator configuration with $r = 0.975$. 75
2.24 G_{DC} for a) 1550 nm modulator configuration with $r = 0.977$ and b) 2000 nm modulator configuration with $r = 0.975$. 76
2.25 GBW product for a) 1550 nm modulator configuration with $r = 0.977$ and b) 2000 nm modulator configuration with $r = 0.975$. 77
2.26 Blue-side modulation GBW_{max} for 0.5 V bias in a a) 1550 nm wavelength modulator configuration and b) 2000 nm configuration. Markers indicate critical-coupling point. 78
2.27 Red-side modulation GBW_{max} at 0.5 V bias for the a) 1550 nm wavelength modulator configuration and b) 2000 nm wavelength configuration. Markers indicate critical-coupling points. 79
2.28 G_{DC} at highest values of GBW_{max}. 80

2.29 3 dB bandwidths at highest values of GBW_{max}. 80

3.1 (a) Transmitted power for various waveguide lengths in passive strip and rib waveguides for the fundamental TE mode. Data were fit using linear regression to extract waveguide propagation loss. Inset: Mode profiles for fabricated strip (b) and rib (c) waveguides. 96

3.2 (a) Waveguide sidewall scattering loss contours (dB/cm) for 2.02 μm (red) and 1.55 μm (black) wavelengths for the fundamental TE mode in a strip waveguide with dimensions 530×220 nm. (b) Scattering loss as a function of waveguide width for $\sigma = 1$ nm and $L_C = 50$ nm. 98

3.3 Substrate leakage in strip waveguides on SOI simulated using RSoft's FEMSIM™ finite-element software with varying BOX thickness at wavelengths of 1.55 and 2.02 μm for the fundamental TE mode. 99

3.4 Waveguide bending loss plot for various 90° bend radii in strip and rib waveguides for the fundamental TE mode. Waveguide dimensions were used to simulate bending loss (solid lines) using RSoft FullWAVE FDTD software. Loss was calculated analytically (dashed lines) using the Marcuse bending loss model. 100

3.5 Waveguide doping loss plot for two levels of n-type and p-type doping levels (indicated on plot) in fabricated rib waveguides for the fundamental TE mode. Propagation loss was extracted through linear regression. . . . 103

3.6 Propagation loss in n-type (a) and p-type (b) doped rib waveguides for the fundamental TE mode. Measured data are plotted using calculated doping densities against simulations using the aforementioned empirical model. For comparison, simulations are also plotted for a wavelength of 1.55 μm. 105

3.7 Waveguide loss in boron-implanted strip and rib waveguide geometries for the fundamental TE mode. Data were fit using linear regression. The boron ion-implantation energy was 900 keV. 107

3.8 Defect-implanted strip and rib waveguide loss as a function of annealing temperature for the fundamental TE mode. 108

4.1 MRR modulator schematic layout (left) and phase-shifter cross-section (right). Reprinted with permission from [19] © The Optical Society. . . . 123

4.2 Normalized EVOA optical attenuation under forward bias for a range of input wavelengths. Reprinted with permission from [19] © The Optical Society. 125

4.3 Normalized attenuation isocurrent lines as a function of wavelength. Dotted lines represent a linear regression of measured data. Reprinted with permission from [19] © The Optical Society. 126

4.4 Simulated free-carrier absorption in the VOA as a function of carrier concentration. Measured data at fixed driving currents are also plotted. Reprinted with permission from [19] © The Optical Society. 127

4.5 Measured MRR spectrum for biases from -10 to 1 V (left) and extracted resonance shift (right). The dashed lines denote zero bias resonance positions. Reprinted with permission from [19] © The Optical Society. . . . 128

4.6 Measured and simulated reverse-bias resonance shift for a MRR modulator with a 30 nm *p*-*n* junction offset. Dashed black line indicates simulation of a 1.55 µm MRR modulator with 450 nm waveguide width. Reprinted with permission from [19] © The Optical Society. 129

4.7 Measured and simulated reverse-bias resonance shift for varying *p*-*n* junction offset. Dashed line denotes simulated results. Reprinted with permission from [19] © The Optical Society. 130

5.1 a) Optical microscope image of the MRR modulator and b) Cross-section of the MRR modulator across dashed cutline A-A'. 141
5.2 a) Optical microscope image of the DM detector and b) Cross-section of the DM detector across dashed cutline B-B'. 142
5.3 Small-signal setup for RF characterization of the MRR modulator. 143
5.4 Small-signal setup for RF characterization of the DM detector. 144
5.5 Large-signal setup for RF characterization of the DM detector. 145
5.6 Large-signal setup for RF characterization of the on-chip optical link (MRR modulator + DM detector). 145
5.7 Free-carrier absorption in 2 µm wavelength doped waveguide test structures. 146
5.8 a) MRR modulator biased spectra and from 0 to -8 V and b) on-off extinction ratio for biases 0 to -8 V. 147
5.9 Measured and simulated biased resonance shift. 148
5.10 Contour plot of a) hole and b) electron concentrations in simulated device for 0 and -4 V bias. 149
5.11 a) Reverse bias resonance shift as a function of junction offset for various voltages and b) waveguide loss as a function of voltage for various junction offsets. 150
5.12 a) Normalized $H_t(\omega_m)$ for the MRR modulator device for zero resonance detuning varying in bias and b) for a fixed bias of -2 V and various values of blue-side resonance detuning. The dotted line denotes the -3 dB bandwidth. 155
5.13 Calculated -3 dB bandwidth of the MRR modulator device for various reverse bias voltages as a function of resonance detuning. 156
5.14 a) Normalized G_{DC} of the MRR modulator for various reverse biases as a function of detuning and b) associated GBW product. 157
5.15 Small-signal RF measurement of the MRR modulator. 158

5.16 a) DM detector dark current and photocurrent for 1.97 μm wavelength with input power of 0.06 mW after coupling losses and b) DM detector responsivities as a function of reverse bias voltage for both 1.97 and 1.55 μm wavelengths. 159
5.17 a) Small-signal measurement of the DM detector and b) 3 dB electrical bandwidth at various voltages. 160
5.18 Eye-diagrams for DM detector at -15 V bias for a) 5 b) 10, and c) 12.5 Gbps PRBS-31 signals. Vertical (voltage) divisions are 17.5, 16.2, and 16.4 mV/div, respectively, and horizontal (time) division are 20 ps/div for all. 161
5.19 Eye-diagrams for on-chip optical link for a) 5 b) 10, and c) 12.5 Gbps PRBS-31 signals. Vertical (voltage) divisions are 9.2, 8.6, and 8.3 mV/div, respectively, and horizontal (time) division are 20 ps/div for all. 162

6.1 (a) Optical image of a ring resonator modulator depicting TiN (dotted red line). (b) Waveguide cross-section (cutline A-A' in (a)) of the ring resonator device. 172
6.2 (a) Heater I-V characteristics. (b) Resonance shift as a function of heater power. 173
6.3 Implant-induced and annealed resonance shifts and calculated change in effective index achieved as a function of implanted defect dose. Inset (a): spectra for device pre- and post- 3×10^{13} cm^{-2} implantation, plus annealing. Extracted Q-factor and notch-depth for these conditions are 5500, 5200, and 6100, and 16.8, 7.3, and 30.3 dB, respectively. 175
6.4 Four-ring device spectra before and after individual ring-trimming to align to 50 GHz spacing denoted by the vertical grid. Pre-trimming describes the device which has received implantation at a dose of 1×10^{13} cm^{-2}. . . . 178

6.5 Normalized transmission in 750 μm long, 1 μm wide waveguides with varying implant dose. 180

7.1 Contour plots of 100 × 100 mm virtual wafers $z'(x,y)$ for a) w_{core}, b) t_{slab}, and c) t_{Si} for 1550 nm waveguide configuration. 192

7.2 Diagram of waveguide dimension interpolation from random sampling of each virtual wafer. 193

7.3 Example spectra depicting resonant order mixing in a 4-ring system subject to manufacturing variation. Dotted, solid, and dashed lines represent the m+1, m, and m-1 resonance orders. 194

7.4 Three different organizations of a 16-ring system with uniform physical spacing d_s between rings. 198

7.5 Example spectra of a 4-ring WDM system with a target frequency spacing of 50 GHz organized in a 'line' with d_s of 1 mm between rings. Red dashed lines represent grid alignment through thermal tuning while blue dotted lines represent grid alignment through trimming. 201

7.6 Mean and standard deviation of power expended to align a) 1550 nm and b) 2000 nm wavelength resonances to a 50 GHz grid in a 4-ring system using 'line', 'matrix', and 'close packed' organizations varying physical spacing d_s between each ring. 204

7.7 a) Mean and standard deviation of power expended to align resonances to various Δf in a 1550 nm wavelength 4-ring system physically spaced by 250, 500, and 750 μm in a 'line' organization and b) mean and standard deviation of distance between adjacent resonances. The black dashed line denotes the target wavelength spacing of a particular Δf and has a slope of ∼8 pm/GHz. 207

7.8 a) Mean and standard deviation of power expended to align resonances to various Δf in a 2000 nm wavelength 4-ring system physically spaced by 250, 500, and 750 μm in a 'line' organization and b) mean and standard deviation of distance between adjacent resonances. The black dashed line denotes the target wavelength spacing of a particular Δf and has a slope of ∼13.3 pm/GHz. 208

7.9 Distribution of resonant wavelengths chosen for 4-ring stacked resonance ($\Delta f = 0$ GHz) and WDM systems of increasing Δf with $d_s = 250$ μm between rings. Each color of distribution represents system resonances sorted lowest to highest. 210

7.10 Mean and standard deviation of power expended to align 1550 and 2000 nm wavelength resonances to $\Delta f = 12.5$ GHz in an N-ring system with $d_s = 250$ μm using the 'line' organization. 212

7.11 a) Boxplots of power consumption to align to a 50 GHz frequency grid with subsequent trimming for a 1550 nm wavelength 4-ring system with 250 μm spacing. b) Boxplots of grid alignment power saved with each subsequent trimming step. Boxplot edges represent 25th and 75th percentiles while whiskers extend to encompass $\pm 3\sigma$. Red lines represent data medians while plotted markers represent data means. Outliers have been omitted. 213

7.12 a) Boxplots of power consumption to align to a 50 GHz frequency grid with subsequent trimming for a 2000 nm wavelength 4-ring system with 250 μm spacing. b) Boxplots of grid alignment power saved with each subsequent trimming step. Boxplot edges represent 25th and 75th percentiles while whiskers extend to encompass $\pm 3\sigma$. Red lines represent data medians while plotted markers represent data means. Outliers have been omitted. 214

7.13 Fraction of 4-ring 50 GHz WDM systems spaced at various values of d_s which are fully-aligned at the specified amount of resonance trimming for a) 1550 nm and b) 2000 nm wavelength configurations. 215

List of Tables

2.1 Empirical free-carrier effect model coefficients. 39

7.1 Calculated effective index and resonance sensitivities for 1550 and 2000 nm wavelength configurations. 203

List of Acronyms

IP	Internet Protocol
DSN	Data Server Network
EDFA	Erbium Doped Fiber Amplifier
WDM	Wavelength-Division Multiplexing
CWDM	Coarse Wavelength-Division Multiplexing
DWDM	Dense Wavelength-Division Multiplexing
SMF	Single-Mode Fiber
FPM	Four-Photon Mixing
NZDF	Non-Zero Dispersion Fiber
PAM	Pulse Amplitude Modulation
QPSK	Quadrature Phase Shift Keying
QAM	Quadrature Amplitude Modulation
CMOS	Complementary Metal-Oxide-Semiconductor
SOI	Silicon-On-Insulator
BOX	Buried-Oxide
SiO2	Silicon Dioxide
PIC	Photonic Integrated Circuit
PD	Photodiode
DM	Defect-Mediated
MRR	Micro-Ring Resonator
LiNbO3	Lithium Niobate
MZI	Mach-Zehnder Interferometer
RC	Resistance-Capacitance

TDFA	Thulium Doped Fiber Amplifier
HC-PCF	Hollow-Core Photonic Crystal Fiber
MIR	Mid-Infrared
SOS	Silicon-On-Sapphire
GOS	Germanium-On-Silicon
CROW	Coupled-Resonator Optical Waveguide
MPW	Multi-Project Wafer
PDK	Process-Design Kit
EVOA	Electronic Variable Optical Attenuator
DC	Steady-State (Direct Current)
TE	Transverse Electric
TM	Transverse Magnetic
OMA	Optical Modulation Amplitude
TPA	Two-Photon Absorption
ER	Extinction Ratio
IL	Insertion Loss
TP	Transmission Penalty
FSR	Free Spectral Range
FWHM	Full-Width at Half-Maximum
BW	Bandwidth
GBW	Gain-Bandwidth
DUT	Device Under Test
PM	Polarization Maintaining
SEM	Scanning-Electron Microscopy
AFM	Atomic Force Microscopy
FDTD	Finite-Difference Time-Domain
SiEPIC	Silicon Electronic Photonic Integrated Circuits

TCAD	Technology Computer-Aided Design
Gbps	Gigabits Per Second
PRBS	Pseudorandom Binary Sequence
HC-PBGF	Hollow-Core Photonic Band Gap Fiber
MZM	Mach-Zehnder Modulator
RF	Radio Frequency (High-Speed)
GS	Ground-Signal
GSG	Ground-Signal-Ground
EYDFA	Erbium-Ytterbium Doped Fiber Amplifier
TEC	Thermo-Electric Cooler
VNA	Vector Network Analyzer
TIA	Trans-Impedance Amplifier
TiN	Titanium Nitride
PECVD	Plasma-Enhanced Chemical Vapor Deposition
BER	Bit Error Rate

Declaration of Authorship

I, David HAGAN, declare that this thesis titled, "Performance considerations in high-speed TDFA-band silicon photonic micro-ring resonator modulators", and the work presented in it are my own. I confirm that:

The design, execution, and analysis of experiments, and manuscript creation including creation of figures, were performed primarily by myself. Collaboration with co-authors typically included developing experimental methods and gathering data.

- In Chapter 2, a chapter written for this thesis: I gathered the data and performed the necessary analyses described in the chapter.
- In Chapter 3, a paper published in *Journal of Optics*: AK conceived of the research and **DH** designed the experiment and gathered and analyzed the data. **DH** wrote the manuscript with contributions and editing from AK. All devices were designed by **DH**
- In Chapter 4, a paper published in *Optics Express*: AP and **DH** conceived of the research and **DH** designed the experiment, gathered and analyzed the data, and wrote the manuscript with editing from AK. With the exception of the commercial device characterized, all devices were designed by **DH**.
- In Chapter 5, a paper prepared for submission: AK and **DH** conceived of the research and experimental design and data analyses were performed by **DH** with assistance from AP and JC. Gathering of experimental data was primarily done by **DH** with assistance from MY, PW. The manuscript was written by **DH** with editing from AK.

- In Chapter 6, a paper published in *Photonics Technology Letters*: **DH** conceived of the research and gathered data with the help of BT. The data was analyzed and manuscript written by **DH** with editing from AK.

- In Chapter 7, a chapter written for the thesis and future submission: **DH** conceived of the research and developed the simulation protocol.

Chapter 1

Introduction

1.1 Optical telecommunication

Global data traffic increases exponentially each year, primarily consumer-driven through online video streaming and cloud-based services such as cloud storage and cloud computing. It is expected that by 2020, global internet protocol (IP) traffic will enter the so-called 'Zettabyte Era', exceeding 2.2 Zettabytes/year [1]. The efficient (low power) and timely (low latency) handling of such an extraordinary amount of data relies on data server networks (DSNs) and their associated interconnections [2]. Data transmitted from data center to client (referred to as 'North-South' traffic) is typically handled by long-haul optical transmission whereby data is encoded onto and transmitted via optical signals across many kilometers of distance through low loss optical fibers. In these and ultra-long-haul applications, it is often necessary to place repeaters downstream to compensate for inherent signal loss due to absorption and scattering in the fiber. These repeaters often incorporate or take the form of optical amplifiers such as the erbium doped fiber amplifier (EDFA), which amplifies wavelengths near 1.55 μm. This wavelength range also experiences very low loss in silica-based optical fibers, which make it ideal for telecommunications.

To address earlier growing bandwidth demands of the 1990's, researchers turned to wavelength-division multiplexing (WDM) systems whereby multiple wavelengths are separately modulated and combined (multiplexed) for transmission through a single fiber, increasing transmitted bandwidth through parallelism. In Coarse WDM (CWDM), the wavelengths channels are spaced by 20 nm and span across the *O*-band (1260 - 1360 nm), *E*-band (1360 - 1460 nm), *S*-band (1460 - 1530 nm), *C*-band (1530 - 1565 nm), and *L*-band (1565 - 1625 nm). CWDM is often the preferred multiplexing scheme when the transmission distance is sufficiently short ($<$ 100 km) and optical amplifiers are not required, and when large variations in central wavelength in less expensive lasers can be tolerated. In longer-haul transmission systems ($>$ 100 km), amplifiers may be required to compensate for propagation loss through the fiber, thus Dense WDM (DWDM) utilizes the full optical gain band of the EDFA by spacing wavelength channels much closer together. In a DWDM system with 100 GHz frequency spacing, wavelength channels are separated by approximately 0.8 nm, thus more variation tolerant components must be used to reduce channel cross-talk. The EDFA has optical gain regions in both the *C*- and *L*-band which afford more than 100 channels at this channel spacing, more at tighter frequency spacing, all defined by the International Telecommunications Union in G.694.1 [3].

A major hurdle researchers needed to overcome in commercially available single-mode fiber (SMF) was dispersion which causes different wavelengths to travel at different speeds (17 ps/nm-km). In single wavelength transmission, a signal's optical bandwidth is typically determined by the spectral width of the laser source. An amplitude-modulated data stream represents a series of optical pulses which, as they travel through fibers with dispersion, will temporally broaden which can lead to inter-symbol transmission errors after long propagation distances. This effect is exaggerated with increasing data rates as the temporal space between bits becomes smaller, reducing the tolerance for pulse

broadening [4]. The solution came in the form of dispersion-shifted fibers where the dispersion was reduced to near-zero ps/nm-km magnitude which drastically reduced pulse broadening. However, in near-zero dispersion environments, a nonlinear effect found in silica fibers called four-photon mixing (FPM) becomes more pronounced [5]. FPM would cause closely spaced wavelengths, such as those in DWDM systems, to generate new wavelengths and cause power fluctuations in the transmitted signals. To solve this issue, non-zero dispersion fiber (NZDF) was developed, which minimized the effects of dispersion but with a sufficiently large dispersion to quell the effects of FPM. NZDF operating in EDFA-band wavelengths was produced with either positive or negative dispersion which could be chained together in equal lengths to cancel out the effects of any accrued dispersion. With the help of the EDFA and NZDFs, WDM telecommunications drastically improved throughout the years.

Due to the finite optical bandwidth of the EDFA coupled with finite laser linewidth, fundamental limitations in the number of channels accommodated by DWDM systems necessitated further ingenuity in the form of advanced modulation formats such as Pulse Amplitude Modulation (PAM) and Quadrature Phase Shift Keying (QPSK). Optical coherent systems, which use interference of a received signal with a local laser source, have paved the way to high single-wavelength data rates through Quadrature Amplitude Modulation (QAM). Specific advanced modulation techniques are generally geared toward particular transmission lengths, with higher symbol rates often reducing potential reach [6], but a common driver between them is to create low-cost, integrated, high-speed devices for modulation and detection as well as provide a platform for scalability of these techniques to multiple wavelengths.

1.1.1 Silicon photonics

Silicon photonics brings together low-cost, scalable, and mature complementary metal-oxide-semiconductor (CMOS) electronics manufacturing technology with the high bandwidth of optical communications. The silicon-on-insulator (SOI) platform has become the standard for the production of active silicon photonic devices and systems for a wide variety of applications, including telecommunications. Most SOI wafers, created through the Smart Cut^{TM} process [7], result in a thin layer of silicon (typically 220 - 400 nm) which sits on a glass buried-oxide (BOX) layer and underneath a thermally-deposited oxide layer, confining light through the strong total internal refraction from the large refractive index contrast between silicon and silicon-dioxide (SiO_2), both of which are transparent at wavelengths between 1.1 - 2.5 μm [8]. On this platform, many densely packed devices such as modulators and detectors can be designed for use in complex systems with tight routing and monolithically fabricated onto a single reticle repeated multiple times across an SOI wafer. In this way, many identical complex photonic integrated circuits (PICs) can be manufactured at one time, drastically reducing production costs over systems which use equivalent bulk components. Due to the small size of waveguide-based modulators, high modulation speeds in the tens of GHz can be achieved with ease, particularly with depletion-type *p*-*n* junction modulators which operate through the free-carrier effect [9]. While this thickness of silicon is ideal for the propagation and manipulation of light, on-chip electronic drivers and digital-signal processing architectures will be impacted due to many factors including decreased thermal conductivity in the oxide which can degrade carrier mobility and shift transistor threshold voltage [10]. One particular remedy comes in the form of hybrid integration whereby CMOS electronics are separately fabricated from the photonic circuit on optimized nodes and bonded through wire- or flip-chip bonding to a PIC [11]. Another approach involves monolithic processing compromising on an SOI thickness which complements both the photonic and electronic components [12], [13].

Light sources in silicon photonic systems are a heavily-studied area of research. Due to the indirect band gap in silicon, it is not ideal for light emission through electrical or optical pumping. Work has been done to demonstrate the operation of all-silicon Raman lasers [14], but they typically requires high-power pump sources which is not ideal for fully-integrated systems. Similarly, all-silicon lasers based on silicon nanocrystals have exhibited good performance but require high pump powers [15] and are unsuitable for electrical pumping due to the oxide hosting the nanocrystals. Electrically-pumped germanium-based lasers have been demonstrated [16] but suffer from poor efficiency and high threshold currents due to its inherent indirect band gap. Hybrid integration of III-V lasers have shown great promise despite the complexities of semiconductor wafer bonding [17]. Through this approach, as well as external coupling of electrically-pumped III-V lasers to a PIC, a highly integrated manufacturing throughput can be maintained.

Photo-detection in silicon photonics has had great success through CMOS integration of germanium photodiodes (PDs) with large responsivities which begin to roll off beyond 1600 nm, thus covering the majority of the EDFA wavelength band [18]. The germanium PD suffers from inherently high dark current which may render it unsuitable for more sensitive applications. Instead, a defect-mediated (DM) silicon-based detector can be used which has low dark current (tens of nano-amps), albeit with low responsivity at low reverse biases [19]. Operating under high reverse bias will cause avalanche photo-detection through impact-ionization of photo-generated carriers which can lead to drastically higher responsivity with voltage. This *p-i-n* PD structure has even been implemented in a resonant micro-ring resonator (MRR) structure to achieve enhanced sensitivity [20].

In non-centrosymmetric materials, such as Lithium Niobate ($LiNbO_3$), the Pockels effect may be used to electrically introduce a change in the material refractive index for use in phase and amplitude modulation with speeds beyond 300 GHz [21]. Silicon

is a centrosymmetric material and thus does not possess the Pockels effect. Hybrid integration of exotic materials with the effect has had much success [22], but is not a CMOS compatible process. Modulation in silicon PICs traditionally relies on the free-carrier effect [9] in *p*-*n* junction waveguides, whereby a varying voltage across the modulator alters the concentration of free-carriers which causes changes in the amplitude and phase of an optical signal. The free-carrier effect remains a popular technique to achieve high modulation speeds as it is completely CMOS-compatible and requires no post-processing.

Due to the relatively weak free-carrier effect in *p*-*n* junction waveguides, two modulation architectures are typically used. The first is the Mach-Zehnder interferometer (MZI) modulator which splits the input light to propagate through two relatively long (up to mm-length) waveguides. The phase of the propagating light is manipulated through the *p*-*n* junction waveguides either in a single-arm push or dual-arm push-pull configuration, resulting in an out-of-phase interference of the light at the output combiner. By using voltage to control the phase, the interference and thus output amplitude of the light can be controlled resulting in an amplitude modulated signal. The second modulation architecture is the MRR modulator, the operation of which is more complex than the MZI modulator. A small fraction of the incident light couples from the bus waveguide to the MRR cavity and circulates within, adding constructively if 'on-resonance'. As the light builds in intensity, it reaches a point where it is sufficiently strong to destructively interfere almost completely with the light in the bus waveguide, causing the transmission through the bus waveguide to decrease substantially. Through integration of a *p*-*n* junction waveguide modulator within the MRR, amplitude modulation can be achieved through shifting the ring on and off resonance. Under reverse bias operation, adequate amplitude modulation extinction ratios can be achieved for very small energies, <1 fJ/bit [23]. The MRR exhibits extremely narrow spectral linewidths which can be used in wavelength-selective applications such as filtering and WDM systems.

While MZI modulators are typically less fabrication and temperature sensitive due to their large size, their high-speed operation is often limited by the Resistance-Capacitance (RC) time constant due to the large capacitance of the long p-n junction lengths as well as the long electrodes which access them. As well, their long lengths often necessitate travelling-wave electrode designs to phase-match the velocities of the electrical and optical signals [24]. In contrast, MRR modulators are more fabrication and temperature sensitive due to their compact size and resonant behaviour, but experience much less junction capacitance which leads to high electrical bandwidths. In a MRR modulator with relatively low cavity loss, the build-up and decay time of the light inside the cavity on- and off-resonance, respectively, can limit the operating speed of the device, but measures can be taken to counteract this, such as intentionally increasing the loss or over-coupling the ring cavity to the bus waveguide. A related phenomenon known as 'optical peaking' can give rise to enhanced bandwidth in MRR modulators [25]. This effect is crucial in accurately estimating high-speed performance of cavity lifetime-limited MRR modulators and is investigated in this thesis.

1.1.2 TDFA-band silicon photonics

In order to accommodate ever-increasing bandwidth requirements and capitalize on DWDM techniques and more advanced modulation formats, researchers are focused on operating in a longer wavelength spectral window near 2 μm, enabled by the recently developed thulium doped fiber amplifier (TDFA) [26]. The TDFA has a demonstrated optical bandwidth over 100 nm, enabling more transmitted channels in DWDM systems for both short- and long-haul operation. In developing devices and systems for the TDFA-band, designers must be aware of the advantages and disadvantages of operating at longer wavelengths. Similarly, while there is a strong interest in mid-infrared wavelengths, particularly due to the large number of spectral 'fingerprints' of fundamental

chemical vibrational modes ranging from 2-20 μm [27], it is not as well-developed as EDFA-band technology, especially for telecommunications applications.

Transmission of TDFA-band wavelengths over traditional silica fiber experiences higher loss and is thus not suited for long-haul; however, intra-data center applications remain viable. As well, specialty fibers for longer wavelengths, such as chalcogenide and fluoride glass can be used in place of silica fibers to further reduce optical loss [28], although they suffer from higher nonlinearity and fragility. A promising fiber platform for TDFA-band transmission is the hollow-core photonic crystal fibers (HC-PCF) which exhibits low nonlinearity due to the propagating mode residing primarily in air [29], which also results in low latency and dispersion [30]. Scattering loss in HC-PCFs follow a λ^{-3} dependence implying lower propagation loss at longer wavelengths, although these fibers have also been demonstrated at EDFA-band wavelengths [31]. Compared to traditional long-haul fibers, HC-PCF still require further work to reduce propagation loss to an acceptable level (sub dB/km) for long-haul transmission of TDFA-band data, however short-reach transmission of error-free amplified data at a rate of 8 Gbps has been demonstrated [32].

For free-space telecommunications applications, two atmospheric spectral windows which appear from 3-5 μm and 8-12 μm are also significant areas of research, prompting the need for integrated photonic devices in order to access them [33]. For mid-infrared (MIR) wavelengths, novel platforms such as silicon-on-sapphire (SOS) [34] or germanium-on-silicon (GOS) [35] are used to avoid inherent material absorption in silicon dioxide (SiO_2), but for wavelengths within the TDFA optical gain band, the SOI platform is viable as it offers negligible material absorption. The SOI platform offers negligible material absorption at these wavelengths as well as the maturity of CMOS technology.

Research in MIR light sources has similarly gained much traction due to the wealth

of sensing applications. Single-line III-V lasers have been demonstrated in both InGaAs/InP [36] and GaSb [37] material systems, and have been used in injection locking experiments which can be used to narrow laser linewidth for telecommunication applications [38]. The availability of commercial electrically-pumped single-line and Fabry-Pérot laser diodes in this wavelength range indicates that the same externally-coupled or III-V wafer-bonded integration which is common in EDFA-band silicon PICs can be extended to the TDFA-band.

III-V Photo-detectors integrated onto silicon PICs have been demonstrated near TDFA-band wavelengths in InGaAs/InP [39], [40] and GaSb [41] material systems, but fabrication and integration remains costly and complex. Recently, an SOI defect-mediated avalanche photodiode was demonstrated with a responsivity of 0.3 A/W at 30 V reverse bias at a wavelength of 2.02 μm [42]. This detector demonstrated high-speed operation with open eye-diagrams at 28 Gbps. A similar device which relies on surface-state absorption was also demonstrated (at a wavelength of 1.55 μm but has the possibility to work at longer wavelengths) with high internal quantum efficiency and 10 Gbps operation at modest reverse bias voltages [43]. Unlike III-V integration, this photodiode architecture has the benefit of being fully-integrated into the fabrication cycle alongside other silicon PIC components with the addition of a post-fabrication implantation step to introduce lattice defects to form mid-band gap states to allow the silicon to absorb wavelengths it is normally transparent to. The defect-mediated silicon detector is replicated in Chapter 5 and used in the demonstration of the first TDFA-band on-chip high-speed link.

At this point, however, there have been few demonstrations of high-speed modulators at these wavelengths on an SOI platform, and these demonstrations have all been Mach-Zehnder interferometer-based [44], [45], [46]. The work presented in Chapter 3 showcases the first demonstration of a *p-n* junction waveguide MRR modulator operating in DC at

TDFA-band wavelengths. This work is expanded upon in Chapter 5 where we present the first demonstration of a p-n^+ junction waveguide MRR modulator operating at TDFA-band wavelengths with a measured small-signal bandwidth of 12.5 GHz, limited by the external detector. This MRR modulator is also used in conjunction with the defect-mediated silicon detector to show the first demonstration of a high-speed on-chip link with open eye-diagrams up to 12.5 Gbps; a large step toward the realization of a short-reach TDFA-band transceiver for use in DSN applications.

1.1.3 Manufacturing variation

Natural variations arising from the SOI fabrication process and CMOS processing techniques give rise to variations in waveguide dimensions which can severely impact the target operating resonance of MRRs and MRR modulators. Both the SOI and CMOS fabrication processes have progressed significantly to deliver single-digit nanometer variation (σ) in silicon thickness, waveguide width, and etch-depth [47]. As well, academic pursuits in wafer processing can further reduce variation through techniques such as corrective etching [48] and higher-resolution optical lithography [49]. Despite these efforts, manufacturing variation is inevitable and can negatively impact silicon photonic devices without correction. In the case of a MRR whose target resonance has shifted due to waveguide dimension variations, a micro-heater can be used to shift it toward target through the thermo-optic effect in silicon, albeit at the expense of power consumption. Extending this stacked resonance systems, for example in higher-order MRR filters [50] or coupled-resonator optical waveguides (CROWs) [51], local variation even in tightly spaced rings will lead to decreased spectral performance without corrective thermal tuning. Furthermore, the thermal distribution from these tightly spaced microheaters contributes to thermal cross-talk which can be complex to remedy. In WDM

systems where multiple MRRs act as multiplexing filters or wavelength-specific modulators, target wavelengths are either determined by the ITU wavelength grid or laser frequency spacing. These MRRs will tend to be physically spaced further apart (sometimes to accommodate high-speed electrodes which can be larger than the ring itself) to mitigate thermal cross-talk but will inherently accrue larger resonance variation due to the spatial variation across a wafer. The thermo-optic effect is unidirectional (toward longer wavelengths), but other techniques can be employed to permanently "trim" the resonance toward shorter wavelengths. Demonstrated trimming techniques include (but are not limited to) electron-beam compaction [52], UV-annealing of photo-sensitive cladding materials [53], electron-beam bleaching [54], cladding etching [55], and laser annealing of implanted Germanium [56]. In Chapter 6, we demonstrate a defect-enhanced trimming technique using in-situ annealing via integrated micro-heaters. In the case of a resonance that is slightly red-shifted from target, one may apply thermal tuning to move an adjacent resonance one free spectral range away toward the target, or one may trim the resonance toward target and eliminate the need for thermal tuning altogether. In systems with multi-line lasers with a particular frequency spacing, it may be more efficient to thermally tune the laser itself to align as close to the MRR resonances as possible to reduce thermal tuning power consumption of their multiple micro-heaters. Further mitigation of power consumption can be achieved through subsequent resonance trimming. Power saving in stacked resonance / WDM systems through resonance trimming is investigated in EDFA- and TDFA-band MRRs in Chapter 7 through Monte Carlo simulation techniques.

1.1.4 'Fabless' methodology and multi-project wafers

CMOS fabrication of silicon photonic devices requires not only industry-standard technologies such as 193 nm lithography, metal deposition, and etching, but the standardized

process control of a dedicated foundry. In order for research groups, who do not have such in-house capabilities, to operate at the cutting edge of technology, state-of-the-art facilities across the world offer affordable fabrication in the form of multi-project wafer (MPW) design runs. This use of out-of-house fabrication is referred to as 'fabless'. Each MPW run involves a design cycle where the foundry sends a Process-Design Kit (PDK) to participating institutions, dictating a strict set of design guidelines to be adhered to, and the designer prepares a design layout of test devices and / or systems, often based on simulations. Designs of a fixed size are submitted and combined into a reticle which is stamped across a wafer. After fabrication, each customer's design is diced from each reticle for delivery. In this way, customers benefit from state-of-the-art design fabrication at a drastically reduced cost. Such foundries which provide MPW runs include IMEC and AMF (formerly A*STAR IME), both of which have been used in the design of work throughout this thesis. Through CMC Microsystems, a not-for-profit organization which manages Canada's National Design Network®, costs associated with MPW runs are heavily subsidized for participating Canadian universities. Simulation tools, such as RSoft which is used extensively throughout the thesis, are also provided heavily subsidized by CMC.

Although we adopt the fabless approach for much of the work throughout this thesis, certain post-processing techniques are used to extend the functionality of these fabricated chips. Such techniques include ion implantation to introduce lattice defects in the defect-mediated detectors presented in Chapter 5 as well as MRRs for defect-enhanced trimming presented in Chapter 6. Subsequent thermal annealing of silicon photonic chips is performed in the defect-implanted test devices presented in Chapter 3. With the integration of oxide-window etching in recent MPW design runs at AMF, a wealth of post-processing techniques can be applied involving the deposition of exotic materials on top of exposed silicon waveguides for the light to interact with.

1.2 Thesis objectives

The objectives of this thesis are to investigate the design and characterization methodologies of high-speed MRRs for TDFA-band operation as well as investigating the advantages and shortcomings of operating at this wavelength range as compared with the well-established EDFA-band, particularly for high-speed telecommunications applications. WDM and stacked resonance systems in both wavelength ranges are also presented in the context of thermal tuning power consumption reduction through resonance trimming. As a whole, this work aims to make a significant step toward the realization of TDFA-band transceivers for use in future short-haul and long-haul telecommunications infrastructure to accommodate ever-growing data bandwidth requirements.

1.3 Statement of thesis work

The work presented in this thesis focuses on the modeling, design, and characterization of high-speed SOI MRR modulators for optimized use at TDFA-band wavelengths. The thesis also explores resonance trimming through integrated annealing and Monte Carlo simulation of power saving through resonance trimming in multi-ring WDM and stacked resonance systems for both EDFA- and TDFA-band wavelengths.

In Chapter 2, MRR modulator theory is presented and we discuss a theoretical steady-state and small-signal high-speed performance comparison between EDFA- and TDFA-band MRR modulators. In Chapter 3, various loss mechanisms, including waveguide sidewall scattering, bending, substrate leakage, free-carrier, and defect absorption losses are discussed for TDFA-band wavelengths. Chapter 4 discusses characterization of an optically broadband electronic variable optical attenuator (EVOA) and an add-drop configuration MRR modulator optimized for TDFA-band operation with modelling of

free-carrier electro-refraction and electro-absorption in both devices. Chapter 5 presents steady-state and high-speed measurement results of an all-pass configuration MRR modulator optimized for TDFA-band operation, as well as a defect-mediated silicon detector. Both devices are used in conjunction to form an on-chip link, demonstrating simultaneous high-speed modulation and detection at these wavelengths. High-speed measurements were performed in collaboration with Dr. John Cartledge of Queen's University. Chapter 6 shifts focus toward resonance trimming through integrated annealing in EDFA-band MRR modulators designed for WDM applications. This method extends to TDFA-band MRR modulators with integrated heaters thus a comparison of resonance trimming through oxide cladding restructuring at both wavelengths is included as well. Chapter 7 builds upon Chapter 6 presenting a theoretical Monte Carlo simulation of power consumption and power saving through resonance trimming in MRR-based WDM and stacked resonance systems in the presence of manufacturing variation. Chapter 8 concludes the thesis with a summary and discussion of future work.

1.4 Publications

Journal articles by the author which contribute to the work presented in this thesis are as follows:

- **Hagan, D.E.** and Knights, A.P., 2017. "Mechanisms for optical loss in SOI waveguides for mid-infrared wavelengths around 2 µm." *Journal of Optics*, 19(2), dec 2016.

- **Hagan, D.E.**, Nedeljkovic, M., Cao, W., Thomson, D.J., Mashanovich, G.Z. and Knights, A.P., 2019. "Experimental quantification of the free-carrier effect in silicon waveguides at extended wavelengths." *Optics express*, 27(1), pp.166-174, jan 2019.

- **Hagan, D.E.**, Torres-Kulik, B. and Knights, A.P., 2019. “Post-Fabrication Trimming of Silicon Ring Resonators via Integrated Annealing.” *IEEE Photonics Technology Letters*, 31(16), pp.1373-1376, jul 2019.

Conference presentations and proceedings by the author which contribute to the work presented in this thesis are as follows:

- **Hagan, D.E.**, Knights, A.P., and Dow, L. "Mid-infrared SOI micro-ring modulator operating at 2.02 microns." *Silicon Photonics XII.* Vol. 10108. International Society for Optics and Photonics, feb 2017.

- **Hagan, D.E.** and Knights, A.P., 2018, August. “On-Chip 2 μm Wavelength Silicon-on-Insulator Optical Interconnect.” In *2018 IEEE 15th International Conference on Group IV Photonics (GFP)* (pp. 1-2). aug 2018.

1.4.1 Internship statement

During the course of the PhD, the author spent 6 months in a paid internship position at Ranovus Inc. in Ottawa, Ontario as a Photonics Engineer. The associated work involved the study of high-speed modulation in MRR modulators, system-level PIC characterization for DWDM applications, and wafer-scale data processing.

Bibliography

[1] Cisco, “VNI Global Fixed and Mobile Internet Traffic Forecasts.”

[2] Q. Cheng, M. Bahadori, M. Glick, S. Rumley, and K. Bergman, “Recent advances in optical technologies for data centers: a review,” *Optica*, vol. 5, no. 11, p. 1354, nov 2018.

[3] International Telecommunication Union. G.694.1: Spectral grids for WDM applications: DWDM frequency grid. https://www.itu.int/rec/T-REC-G.694.1/.

[4] G. P. Agrawal, "Nonlinear Fiber Optics," in *Nonlinear Science at the Dawn of the 21st Century*. Berlin, Heidelberg: Springer Berlin Heidelberg, 2000, pp. 195–211.

[5] S. J. Garth and C. Pask, "Four-photon mixing and dispersion in single-mode fibers," *Optics Letters*, vol. 11, no. 6, p. 380, jun 1986.

[6] P. J. Winzer, D. T. Neilson, and A. R. Chraplyvy, "Fiber-optic transmission and networking: the previous 20 and the next 20 years [Invited]," *Optics Express*, vol. 26, no. 18, p. 24190, sep 2018.

[7] Smart Cut^{TM} technology - Soitec. https://www.soitec.com/en/products/smart-cut.

[8] R. Soref, "Mid-infrared photonics in silicon and germanium," *Nature Photonics*, vol. 4, no. 8, pp. 495–497, aug 2010.

[9] R. A. Soref and B. R. Bennett, "Electrooptical effects in silicon," *IEEE Journal of Quantum Electronics*, vol. 23, no. 1, pp. 123–129, jan 1987.

[10] N. Bresson, S. Cristoloveanu, C. Mazuré, F. Letertre, and H. Iwai, "Integration of buried insulators with high thermal conductivity in SOI MOSFETs: Thermal properties and short channel effects," *Solid-State Electronics*, vol. 49, no. 9, pp. 1522–1528, sep 2005.

[11] D. Liang, G. Roelkens, R. Baets, and J. Bowers, "Hybrid Integrated Platforms for Silicon Photonics," *Materials*, vol. 3, no. 3, pp. 1782–1802, mar 2010.

[12] J. S. Orcutt, R. J. Ram, and V. Stojanović, "Integration of silicon photonics into electronic processes," in *Silicon Photonics VIII*, J. Kubby and G. T. Reed, Eds., vol. 8629. International Society for Optics and Photonics, mar 2013, p. 86290F.

[13] V. Stojanović *et al.*, "Monolithic silicon-photonic platforms in state-of-the-art CMOS SOI processes [Invited]," *Optics Express*, vol. 26, no. 10, p. 13106, may 2018.

[14] O. Boyraz and B. Jalali, "Demonstration of a silicon Raman laser," *Optics Express*, vol. 12, no. 21, p. 5269, oct 2004.

[15] D.-C. Wang *et al.*, "An all-silicon laser based on silicon nanocrystals with high optical gains," *Science Bulletin*, vol. 63, no. 2, pp. 75–77, jan 2018.

[16] R. E. Camacho-Aguilera, Y. Cai, N. Patel, J. T. Bessette, M. Romagnoli, L. C. Kimerling, and J. Michel, "An electrically pumped germanium laser," *Optics Express*, vol. 20, no. 10, p. 11316, may 2012.

[17] A. W. Fang, H. Park, O. Cohen, R. Jones, M. J. Paniccia, and J. E. Bowers, "Electrically pumped hybrid AlGaInAs-silicon evanescent laser," *Optics Express*, vol. 14, no. 20, p. 9203, oct 2006.

[18] M. Piels and J. E. Bowers, "Photodetectors for silicon photonic integrated circuits," *Photodetectors*, pp. 3–20, jan 2016.

[19] D. F. Logan, P. E. Jessop, and A. P. Knights, "Modeling defect enhanced detection at 1550 nm in integrated silicon waveguide photodetectors," *Journal of Lightwave Technology*, vol. 27, no. 7, pp. 930–937, 2009.

[20] J. K. Doylend, P. E. Jessop, and A. P. Knights, "Silicon photonic resonator-enhanced defect-mediated photodiode for sub-bandgap detection." *Optics express*, vol. 18, no. 1, pp. 14 671–14 678, jul 2010.

[21] J. Macario, P. Yao, S. Shi, A. Zablocki, C. Harrity, R. D. Martin, C. A. Schuetz, and D. W. Prather, "Full spectrum millimeter-wave modulation," *Optics Express*,

vol. 20, no. 21, p. 23623, oct 2012.

[22] S. Abel *et al.*, "Large Pockels effect in micro- and nanostructured barium titanate integrated on silicon," *Nature Materials*, vol. 18, no. 1, pp. 42–47, jan 2019.

[23] E. Timurdogan, C. M. Sorace-Agaskar, J. Sun, E. Shah Hosseini, A. Biberman, and M. R. Watts, "An ultralow power athermal silicon modulator," *Nature Communications*, vol. 5, no. 1, p. 4008, sep 2014.

[24] X. Tu, T.-Y. Liow, J. Song, X. Luo, Q. Fang, M. Yu, and G.-Q. Lo, "50-Gb/s silicon optical modulator with traveling-wave electrodes," *Optics Express*, vol. 21, no. 10, p. 12776, may 2013.

[25] J. Müller, F. Merget, S. S. Azadeh, J. Hauck, S. R. García, B. Shen, and J. Witzens, "Optical Peaking Enhancement in High-Speed Ring Modulators," *Scientific Reports*, vol. 4, no. 1, p. 6310, may 2015.

[26] Z. Li, A. M. Heidt, J. M. O. Daniel, Y. Jung, S. U. Alam, and D. J. Richardson, "Thulium-doped fiber amplifier for optical communications at 2 µm." *Optics express*, vol. 21, no. 8, pp. 9289–97, apr 2013.

[27] W. Green *et al.*, "Mid-Infrared Silicon Photonics," in *Optical Fiber Communication Conference/National Fiber Optic Engineers Conference 2013*. Washington, D.C.: OSA, 2013, p. OTh4I.7.

[28] J. S. Sanghera, L. Shaw, and I. D. Aggarwal, "Applications of chalcogenide glass optical fibers," *Comptes Rendus Chimie*, vol. 5, no. 12, pp. 873–883, dec 2002.

[29] J. K. Lyngsø, B. J. Mangan, C. Jakobsen, and P. J. Roberts, "7-cell core hollow-core photonic crystal fibers with low loss in the spectral region around 2 μm," *Optics Express*, vol. 17, no. 26, p. 23468, dec 2009.

[30] D. Mueller, J. A. West, and K. W. Koch, "Interferometric chromatic dispersion measurement of a photonic bandgap fiber," in *Active and Passive Optical Components for WDM Communications II*, A. K. Dutta, A. A. S. Awwal, N. K. Dutta, and K. Okamoto, Eds., vol. 4870. International Society for Optics and Photonics, jul 2002, p. 395.

[31] Y. Chen *et al.*, "Multi-kilometer Long, Longitudinally Uniform Hollow Core Photonic Bandgap Fibers for Broadband Low Latency Data Transmission," *Journal of Lightwave Technology*, vol. 34, no. 1, jan 2016.

[32] M. N. Petrovich *et al.*, "Demonstration of amplified data transmission at 2 μm in a low-loss wide bandwidth hollow core photonic bandgap fiber," *Optics Express*, vol. 21, no. 23, p. 28559, nov 2013.

[33] M. M. Milošević, P. S. Matavulj, P. Y. Yang, A. Bagolini, and G. Z. Mashanovich, "Rib waveguides for mid-infrared silicon photonics," *Journal of the Optical Society of America B*, vol. 26, no. 9, pp. 1760–1766, sep 2009.

[34] T. Baehr-Jones, A. Spott, R. Ilic, A. Spott, B. Penkov, W. Asher, and M. Hochberg, "Silicon-on-sapphire integrated waveguides for the mid-infrared." *Optics express*, vol. 18, no. 12, pp. 12 127–12 135, jun 2010.

[35] Y.-C. Chang, V. Paeder, L. Hvozdara, J.-M. Hartmann, and H. P. Herzig, "Low-loss germanium strip waveguides on silicon for the mid-infrared." *Optics letters*, vol. 37, no. 14, pp. 2883–5, jul 2012.

[36] R. Phelan, J. O'Carroll, D. Byrne, C. Herbert, J. Somers, and B. Kelly, "$In_{0.75}Ga_{0.25}As$/InP Multiple Quantum-Well Discrete-Mode Laser Diode Emitting at 2 μm," *IEEE Photonics Technology Letters*, vol. 24, no. 8, pp. 652–654, apr 2012.

[37] A. Joullié and P. Christol, "GaSb-based mid-infrared 2-5 μm laser diodes," *Comptes Rendus Physique*, vol. 4, no. 6, pp. 621–637, jul 2003.

[38] N. Kavanagh, D. Goulding, and F. C. Garcia Gunning, "Stable injection locking with slotted Fabry-Perot lasers at 2 μm," *Journal of Physics: Photonics*, vol. 1, no. 1, p. 015005, dec 2018.

[39] R. Wang, S. Sprengel, M. Muneeb, G. Boehm, R. Baets, M.-C. Amann, and G. Roelkens, "2 μm wavelength range InP-based type-II quantum well photodiodes heterogeneously integrated on silicon photonic integrated circuits," *Optics Express*, vol. 23, no. 20, p. 26834, oct 2015.

[40] Z. Wang and A. P. Knights, "Dual-ring-assisted MZI silicon modulator for enhanced intensity modulation," in *2016 IEEE 13th International Conference on Group IV Photonics (GFP)*. IEEE, aug 2016, pp. 88–89.

[41] N. Ye and Nan, "High speed photodiode and 90°optical hybrid for 2 μm optical communication systems," 2016.

[42] J. J. Ackert, D. J. Thomson, L. Shen, A. C. Peacock, P. E. Jessop, G. T. Reed, G. Z. Mashanovich, and A. P. Knights, "High-speed detection at two micrometres with monolithic silicon photodiodes," *Nature Photonics*, vol. 9, no. 6, pp. 393–396, may 2015.

[43] J. J. Ackert, A. S. Karar, J. C. Cartledge, P. E. Jessop, and A. P. Knights, "Monolithic silicon waveguide photodiode utilizing surface-state absorption and operating at 10 Gb/s," *Optics Express*, vol. 22, no. 9, p. 10710, may 2014.

[44] M. A. Van Camp, S. Assefa, D. M. Gill, T. Barwicz, S. M. Shank, P. M. Rice, T. Topuria, and W. M. J. Green, "Demonstration of electrooptic modulation at

2165nm using a silicon Mach-Zehnder interferometer," *Optics Express*, vol. 20, no. 27, pp. 28 009–16, dec 2012.

[45] W. Cao *et al.*, "High-speed silicon modulators for the 2 μm wavelength band," *Optica*, vol. 5, no. 9, p. 1055, sep 2018.

[46] W. Wang *et al.*, "Mid-infrared (MIR) Mach-Zehnder Silicon Modulator at 2 μm Wavelength based on Interleaved PN Junction," in *Conference on Lasers and Electro-Optics*. Washington, D.C.: OSA, may 2018, p. STh1B.1.

[47] Dan-Xia Xu, J. H. Schmid, G. T. Reed, G. Z. Mashanovich, D. J. Thomson, M. Nedeljkovic, Xia Chen, D. Van Thourhout, S. Keyvaninia, and S. K. Selvaraja, "Silicon Photonic Integration Platform—Have We Found the Sweet Spot?" *IEEE Journal of Selected Topics in Quantum Electronics*, vol. 20, no. 4, pp. 189–205, jul 2014.

[48] S. K. Selvaraja, E. Rosseel, L. Fernandez, M. Tabat, W. Bogaerts, J. Hautala, and P. Absil, "SOI thickness uniformity improvement using corrective etching for silicon nano-photonic device," in *8th IEEE International Conference on Group IV Photonics*. IEEE, sep 2011, pp. 71–73.

[49] S. K. Selvaraja, W. Bogaerts, P. Dumon, D. Van Thourhout, and R. Baets, "Subnanometer Linewidth Uniformity in Silicon Nanophotonic Waveguide Devices Using CMOS Fabrication Technology," *IEEE Journal of Selected Topics in Quantum Electronics*, vol. 16, no. 1, pp. 316–324, jan 2010.

[50] H. Jayatilleka, K. Murray, M. Á. Guillén-Torres, M. Caverley, R. Hu, N. A. F. Jaeger, L. Chrostowski, and S. Shekhar, "Wavelength tuning and stabilization of microring-based filters using silicon in-resonator photoconductive heaters," *Optics Express*, vol. 23, no. 19, p. 25084, sep 2015.

[51] H. C. L. Tsui, O. Alsalman, A. Alodhayb, H. Albrithen, D. E. Hagan, A. P. Knights, M. P. Halsall, and I. F. Crowe, "Silicon 'photonic molecules' for sensing applications (Conference Presentation)," in *Silicon Photonics XIV*, G. T. Reed and A. P. Knights, Eds., vol. 10923. SPIE, mar 2019, p. 60.

[52] J. Schrauwen, D. Van Thourhout, and R. Baets, "Trimming of silicon ring resonator by electron beam induced compaction and strain," *Optics Express*, vol. 16, no. 6, p. 3738, mar 2008.

[53] Linjie Zhou, K. Okamoto, and S. Yoo, "Athermalizing and Trimming of Slotted Silicon Microring Resonators With UV-Sensitive PMMA Upper-Cladding," *IEEE Photonics Technology Letters*, vol. 21, no. 17, pp. 1175–1177, sep 2009.

[54] S. Prorok, A. Y. Petrov, M. Eich, J. Luo, and A. K.-Y. Jen, "Trimming of high-Q-factor silicon ring resonators by electron beam bleaching," *Optics Letters*, vol. 37, no. 15, p. 3114, aug 2012.

[55] A. H. Atabaki, A. A. Eftekhar, M. Askari, and A. Adibi, "Accurate post-fabrication trimming of ultra-compact resonators on silicon," *Optics Express*, vol. 21, no. 12, p. 14139, jun 2013.

[56] M. M. Milosevic, X. Chen, W. Cao, A. F. J. Runge, Y. Franz, C. G. Littlejohns, S. Mailis, A. C. Peacock, D. J. Thomson, and G. T. Reed, "Ion Implantation in Silicon for Trimming the Operating Wavelength of Ring Resonators," *IEEE Journal of Selected Topics in Quantum Electronics*, vol. 24, no. 4, pp. 1–7, jul 2018.

Chapter 2

A theoretical performance comparison of EDFA-band and TDFA-band wavelengths in a high-speed micro-ring resonator *p-n* junction modulator structure

Preface

This chapter serves as both an introduction to many concepts on which the thesis is built as well as an application of the concepts in a comprehensive theoretical comparison of performance of high-speed micro-ring resonator (MRR) modulators designed on a silicon-on-insulator (SOI) platform for the erbium doped fiber amplifier (EDFA)-band, centered near 1550 nm wavelength, or the thulium doped fiber amplifier (TDFA)-band, centered near 1970 nm. As discussed in Chapter 1, the TDFA-band is a parallel wavelength window enabled by the optical bandwidth of the TDFA (approximately three

times larger than the EDFA) which hold promise for applications in telecommunications. The seemingly mundane choice of using longer wavelengths in the context of MRR modulator design carries complex performance trade-offs which are extensively explored in this chapter to provide the methods and tools to aid in designing future TDFA-band telecommunication devices and infrastructure.

2.1 Introduction

It is known that the plasma dispersion effect used in *p*-*n* junction modulators increases in strength with longer wavelength approximately as λ^2. This metric alone would imply that silicon photonic modulators can be made more efficient by operating at longer wavelengths. While this seems somewhat obvious for the case for thicker, micron scale waveguide devices, such as the electronic variable optical attenuator (EVOA) studied in Chapter 4, sub-micron scale modulators present a series of performance trade-offs which need to be considered when using different wavelengths. In this chapter, I compare and contrast the theoretical steady-state (DC) and high-speed performance of SOI MRR modulators designed for optimized use near EDFA- and TDFA-band wavelengths of 1550 and 2000 nm, respectively. Section 2.2 describes the basic building block of silicon photonic systems; the waveguide. Here, the single-mode cut-off widths and associated confinement factors are determined for 220 nm thick SOI at 1550 and 2000 nm wavelengths. Section 2.3 introduces the free-carrier effect and its description through the Drude model as well as a recently published empirical model which is used throughout this work in simulation and modelling. Various physical mechanisms of free-carrier generation are discussed with emphasis on intentionally-introduced dopants, such as those used to form a *p*-*n* junction for modulation purposes. Section 2.4 describes the physics of a *p*-*n* junction in context of a *p*-*n* junction modulator waveguide with emphasis on operation in reverse bias. Access resistance and junction capacitance calculations are

introduced as crucial properties in calculating the Resistance-Capacitance (RC)-limited bandwidth for a high-speed modulator. Although the RC-limited bandwidth is purely an electrical property, the consequences of choice of wavelength are discussed. Section 2.5 provides a description of the static and dynamic properties of the MRR modulator which pertain to much of the contents of this thesis. Of particular importance is the dynamic property "optical peaking" which critically affects modulation speed as a function of resonance detuning. Both DC and high-speed performance metrics are explored to theoretically compare and contrast an all-pass MRR modulator designed for 1550 or 2000 nm wavelengths for under-coupled, critically-coupled, and over-coupled conditions, as functions of contact-doping separation and resonance detuning.

Frequently, specific dimensions (i.e. waveguide width) and properties (i.e. self-coupling coefficient) will be chosen when displaying simulated results for 1550 and 2000 nm wavelength results. This is a result of working backward from the optimal dimensions and properties of the theoretically compared MRR modulator at both wavelengths. These design choices are explained further in Section 2.2 and Section 2.5.2 and are clarified here before delving further, although explanations of certain terms and concepts will require further reading. The waveguide widths of 500 and 600 nm are chosen in many analyses as these widths present the largest steady-state change in the effective index of the TE_0 mode for wavelengths of 1550 and 2000 nm, respectively, in a centered *p*-*n* junction waveguide modulator at the selected (equal) doping concentrations of 3×10^{17} cm^{-3}. For some analyses, the contact-doping separation values of 500 and 800 nm are chosen for the wavelengths of 1550 and 2000 nm, respectively, as they yield the largest small-signal gain-bandwidth product at self-coupling coefficient values of 0.977 and 0.975. Large-signal modulation analysis is performed with a 2.5 V peak-to-peak voltage swing, beginning from 0.5 V. This value of 0.5V is chosen near the built-in potential of the *p*-*n* junction, where the depletion width disappears and the device enters forward bias if pushed to higher positive voltages. A bias of 0 V is often used to represent

an “unbiased” modulator, which neglects the built-in potential, thus 0.5 V is chosen to produce a larger modulation effect than offered by 0 V. Small-signal modulation analysis is also performed at this bias.

2.2 Silicon-on-insulator waveguides

2.2.1 Effective index

Waveguides are a basic component in the silicon photonics toolbox, allowing for the confinement and guiding of light. In the most general sense, a waveguide is formed of two dissimilar materials: a central core of refractive index n_1 surrounded by a cladding material of refractive index n_2. Light is confined and guided as long as $n_1 > n_2$. From a ray optics perspective, the light is guided through a process of total internal reflection. The SOI platform makes use of a large refractive index contrast between silicon and silicon dioxide (SiO_2), allowing for the fabrication of micron scale photonic devices linked together into complex, small footprint photonic circuits. Another benefit of this large index contrast is the realization of extremely tight waveguide bends with negligible loss. By bending a waveguide into a ring and coupling light to it from an adjacent waveguide, one forms a MRR, the physics of which will be discussed in detail in this chapter.

Waveguides can support the propagation of light in discrete eigenmodes (or more commonly referred to as “modes”), each with an associated propagation constant, β, given by:

$$\beta = k_o n_{eff} \tag{2.1}$$

where k_o is the wavenumber in vacuum, related to the optical frequency through $k_o = \omega/c$, and n_{eff} is a quantity known as the effective index. In general, a mode is supported by a waveguide if it satisfies the condition $n_{clad} < n_{eff} < n_{core}$, where n_{core} and n_{clad} the refractive index of the core and cladding, respectively. Large SOI waveguides may support high-order transverse electric (TE) and transverse magnetic (TM) modes. In most photonic circuits, it is often desirable to only use the fundamental TE or TM modes in so-called single-mode operation. To achieve this, the waveguide dimensions must be reduced until no higher-order modes are supported. The appropriate width can be found analytically using the effective index method [1] or by simulating the effective index of a waveguide via finite element calculations in software packages such as FEMSIM^{TM} by Synopsys.

To begin, we consider an SOI slab waveguide, the simplest form of waveguide, consisting of a semi-infinite silicon slab sandwiched between two SiO_2 cladding layers, reducing the thickness of the silicon slab to 220 nm results in single-mode operation transverse to the propagation direction. Next, the lateral direction becomes clad with SiO_2 to form a channel waveguide structure. For a wavelength of 1550 nm, reducing the waveguide width to approximately 450 nm will result in single-mode operation. This width is referred to as the single-mode cut-off. A wavelength of 2000 nm, however, has a single-mode cut-off close to 650 nm. These values will be similar for ridge waveguide geometries provided the slab is sufficiently thin. Figure 2.1 and Figure 2.2 show the simulated effective indices of a 220 nm thick strip waveguide with varying width for 1550 and 2000 nm wavelengths, respectively. Also included in each figure are effective index values for a ridge waveguide with 90 nm slab thickness.

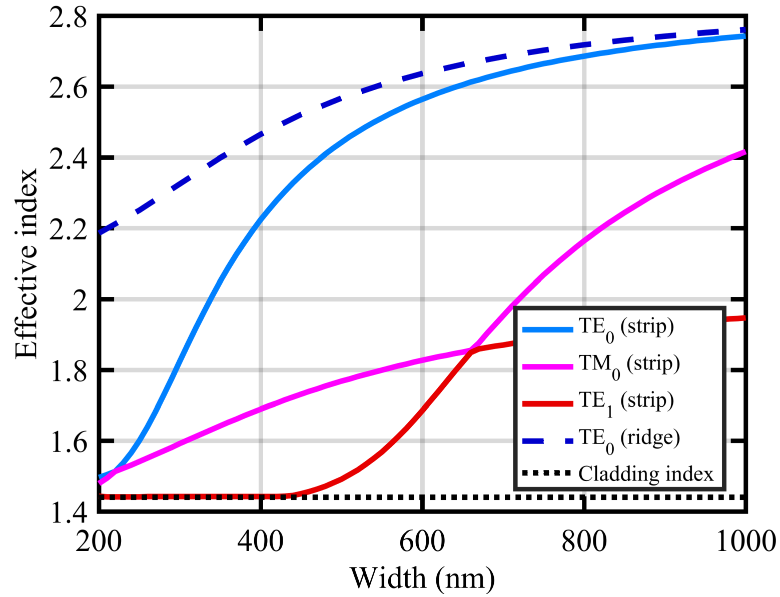

FIGURE 2.1: Simulated effective indices of TE_0, TM_0 and TE_1 modes in SOI strip waveguides varying width at 1550 nm wavelength. TE_0 indices of ridge waveguide with 90 nm slab included as dashed line.

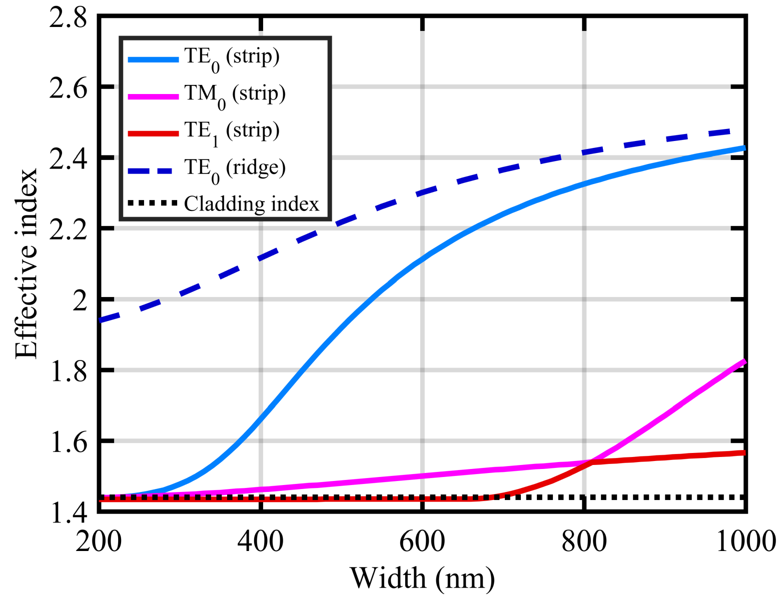

FIGURE 2.2: Simulated effective indices of TE_0, TM_0 and TE_1 modes in SOI strip waveguides varying width at 2000 nm wavelength. TE_0 indices of ridge waveguide with 90 nm slab included as dashed line.

The dotted line in each figure depicts n_{clad}, thus any modes with $n_{eff} < n_{clad}$ are not considered guiding modes. The effective index of 2000 nm light in 220 nm thick silicon waveguides is lower than that of 1550 nm light, owing to the fixed silicon thickness. It is clear that the fundamental TM_0 mode is supported regardless of width, thus polarization handling must be taken into consideration to ensure that only TE_0 polarized light is coupled to the waveguide. Most single-line lasers will output linearly polarized light which simply needs to be rotated to excite the fundamental TE_0 mode in the waveguide; however, broadband sources can emit unpolarized light which first needs to pass through a linear polarizer before being rotated.

2.2.2 Confinement

The effective index of a waveguide mode is a direct reflection of how confined it is in the waveguide core. In silicon photonic modulators, it is crucial to maximize the overlap of the light with the physical phenomenon causing the modulation, which normally occurs inside the waveguide core. Generally, modes with lower effective index are ill-confined and tend to have excess loss, especially around bends, thus it can be advantageous to operate with a waveguide width above the single-mode cut-off to improve the fundamental mode confinement. Additionally, any excited higher-order modes are quickly quelled as long as they are ill-guided. Figure 2.3 shows the confinement factor, Γ (fraction of mode field in the waveguide core vs. total field), for both 1550 and 2000 nm wavelength as a function of waveguide width.

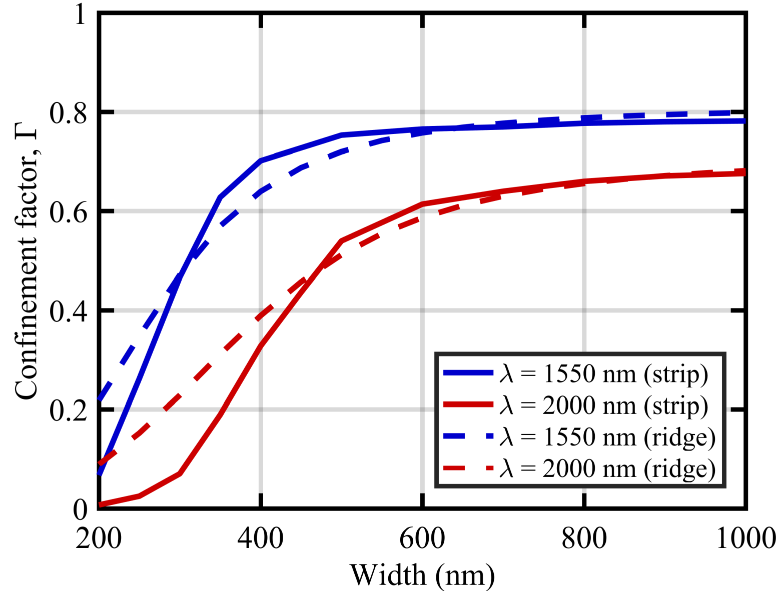

FIGURE 2.3: Confinement factor for TE_0 mode in both strip and ridge waveguide geometries for 1550 and 2000 nm wavelengths.

In both ridge and strip waveguides, Γ is larger at 1550 nm wavelength compared to 2000 nm. Any effects due to a change in the complex refractive index of silicon will be reduced. This is a detrimental consequence for modulation efficiency in *p*-*n* junction devices, but advantageous in the case of thermal fluctuations in the silicon which can negatively affect the stability of long waveguide devices, such as Mach-Zehnder interferometers. It is demonstrated in Section 2.5.1 that MRRs operating at longer wavelengths will actually experience enhanced resonance shift due to thermal effects, as compared to shorter wavelengths. This can cause increased resonance instability but can also lead to more efficient thermal tuning from integrated micro-heaters. Two-photon absorption, a non-linear absorption process discussed in Section 2.3.3.3, can lead to self-heating in waveguides, causing resonance instability in MRRs due to the high intensity of light built-up in the ring cavity. The reduction in Γ can partially mitigate the manifestation of self-heating at the 2000 nm wavelength. To visualize the impact of the latter, we simulate the effective index of the TE_0 modes of both 1550 and 2000

nm wavelengths for various waveguide widths and temperatures. To emulate a change in temperature, the refractive index of the silicon is adjusted from room-temperature to 100°C through the thermo-optic coefficient, dn/dT, which is $1.84{\times}10^{-4}$ K^{-1} at 1550 nm, and $1.78{\times}10^{-4}$ K^{-1} at 2000 nm wavelengths [2]. The change in refractive index with temperature in the SiO_2 cladding is ignored as it is much weaker compared to silicon. The lower thermo-optic coefficient at 2000 nm wavelength shows that in bulk silicon, the refractive index is less sensitive to variations in temperature; however, this effect is compounded in a waveguide where the confinement in the silicon is reduced. Figure 2.4 shows the waveguide thermo-optic coefficient (dn_{eff}/dT) for both 1550 and 2000 nm wavelengths as a function of waveguide width in both strip and ridge geometries.

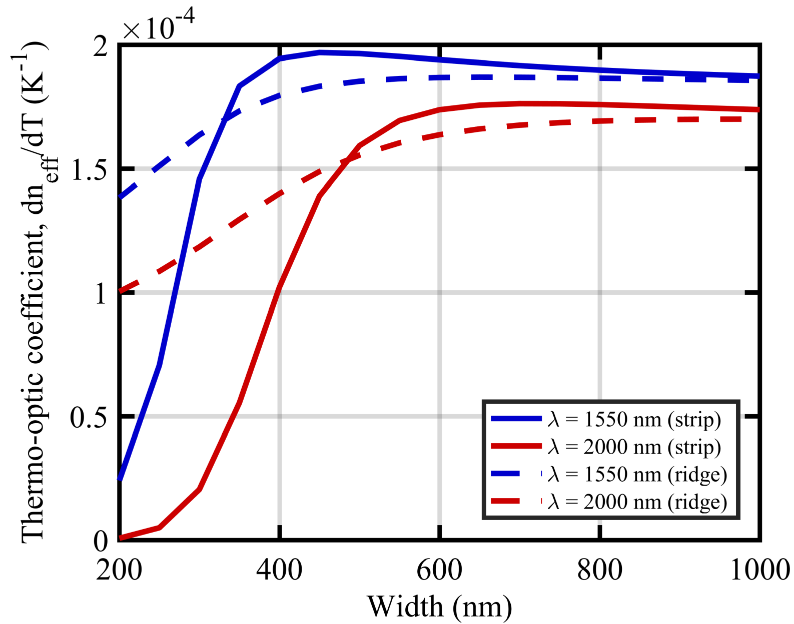

FIGURE 2.4: Thermo-optic coefficient for strip and ridge waveguides varying in width for both 1550 and 2000 nm wavelengths.

The data follows a similar trend as Γ as increasing confinement implies more modal overlap with the silicon where the thermo-optic effect is originating. For a wavelength of 1550 nm at a width of 500 nm, the ridge waveguide geometry has slightly less thermal sensitivity than the strip waveguide, as expected from the slightly reduced confinement

at this width. Similar behaviour is seen at 2000 nm wavelength for a width of 600 nm. Comparing the two wavelengths at these chosen widths, we see the thermal sensitivity reduced by a factor of 1.13 for 2000 nm in a ridge waveguide. This will be important when considering MRR modulator performance.

Figure 2.5 shows the simulated mode profiles of a 500 nm waveguide for 1550 nm wavelength and 600 nm width for 2000 nm wavelength.

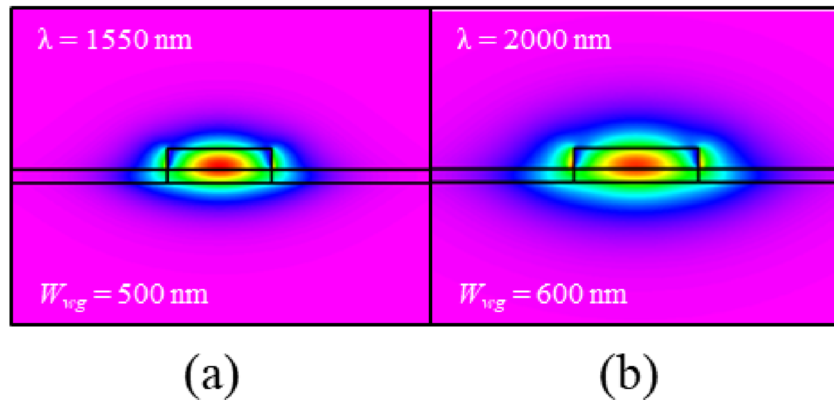

FIGURE 2.5: Mode profiles for 500 and 600 nm wide ridge waveguides for 1550 and 2000 nm wavelengths, respectively.

It is apparent from the mode profiles that a large reduction in confinement stems from the fixed 220 nm thickness chosen. Although thicker SOI is available, 220 nm SOI is standard in many silicon photonic foundries and is thus cost-effective. Additionally, thicker silicon has a negative impact on the modulation speed of modulators as will be discussed in Section 2.4, thus we restrict our devices to a 220 nm SOI platform.

2.2.3 Group index and dispersion

Group index and group velocity are important parameters in waveguide physics which describe its dispersive properties, or, how different wavelengths behave in the same

structure. This is of particular importance, for example, in pulsed laser applications where an ultra-short pulse in time has a large optical bandwidth. As such, the temporal properties of the pulse are strongly dictated by the propagating speeds of its constituent wavelength components. Figure 2.6 shows the group index in 220 nm thick SOI ridge waveguides of various widths across wavelengths.

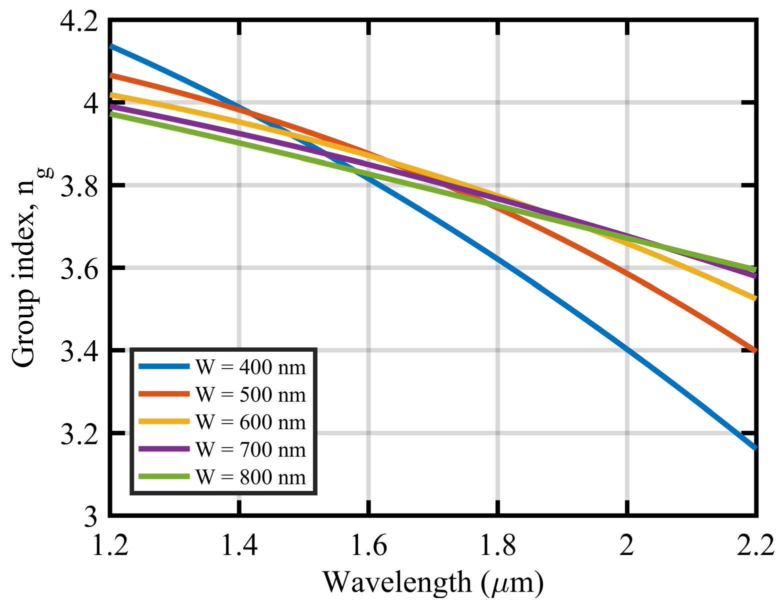

FIGURE 2.6: Fundamental TE_0 mode group indices for 220 nm thick SOI ridge waveguide with 90 nm slab and varying widths.

We see that the group index at 2000 nm is lower than that of 1550 nm across all relevant waveguide widths which will be important when discussing the operation of a MRR. A more general example of the detrimental effects of dispersion is in systems utilizing a single-line laser. The laser output has a finite optical linewidth which causes modulated data to broaden as they travel through a dispersive medium; a detrimental effect which is exaggerated with higher data rates. Material dispersion is a bulk material property,

given by:

$$D_m = -\frac{\lambda}{c}\left(\frac{d^2 n}{d\lambda^2}\right) \tag{2.2}$$

In a waveguide structure, (2.2) can be augmented by replacing n with neff to calculate waveguide dispersion, Dwg. Figure 2.7 shows the material dispersion of silicon and SiO_2 as well as the waveguide dispersion in 220 nm thick SOI ridge waveguides with a 90 nm slab, varying in width.

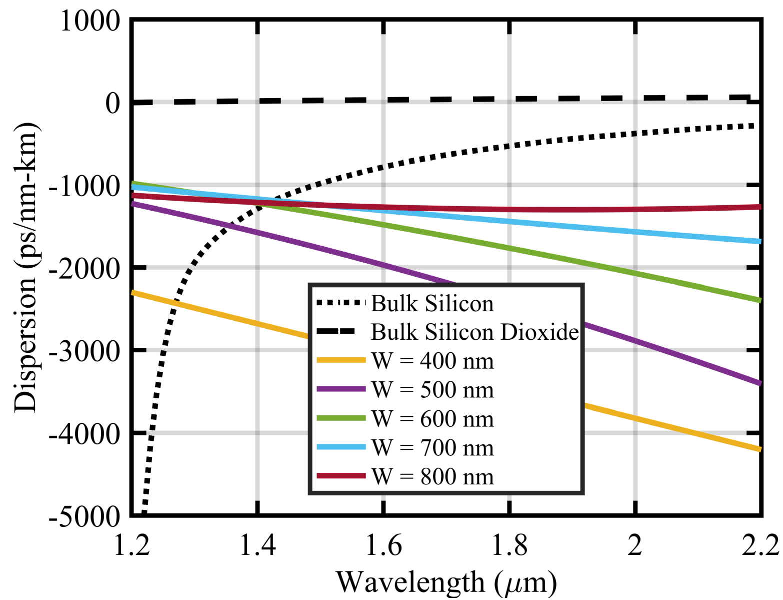

FIGURE 2.7: Material dispersion for bulk silicon and SiO_2, and simulated waveguide dispersion in 220 nm SOI ridge waveguide geometry of varying width.

Figure 2.8 shows the waveguide dispersion at wavelengths of 1550 and 2000 nm as a function of waveguide width.

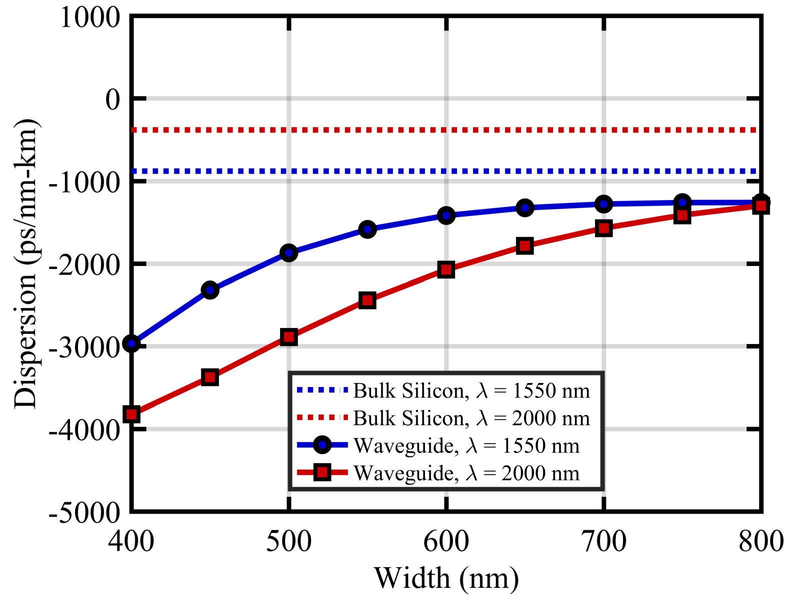

FIGURE 2.8: Bulk and waveguide dispersion as a function of width for wavelengths of 1550 and 2000 nm.

The dispersion of silicon becomes larger as it approaches 1100 nm wavelength near the band gap and flattens out in the opposite direction toward mid-infrared wavelengths. Narrow waveguides offer larger negative dispersion than wider waveguides, and larger negative dispersion still at longer wavelengths. It should be noted that near the single-mode cut-off widths of 500 and 600 nm for wavelengths of 1550 and 2000 nm, respectively, the dispersion is similar but slightly larger at 2000 nm. SiO_2 has remarkably flat, near-zero dispersion. This is one of the reasons long-haul optical fiber is made from glass. Many long-haul fibers have dispersion in the tens of ps/nm-km, and in some designs, zero or negative dispersion. Often, non-zero dispersion is unavoidable, but can be compensated through various optical components such as counter-dispersive fiber of appropriate length, or integrated optics. From Figure 2.7, a 400 nm wide waveguide operating near 1550 nm has a dispersion of approximately -3000 ps/nm-km and a 1 cm length could compensate for 2 m of 15 ps/nm-km positive dispersion fiber. Efforts have been made in waveguide engineering to produce structures with active dispersion

control, such as thermally tuned Bragg gratings [3]. A very relevant example pertains to the use of MRR modulators in dispersion control whereby, in an over-coupled state, can provide negative frequency chirp to a signal for use in dispersion-uncompensated long-haul transmission systems [4]. This phenomenon will be explored further in this chapter.

Transmitting TDFA-band wavelengths short distances, i.e. within intra-data center, can be done with standard core fiber without much propagation loss and distortion from dispersion [5], but long distances presents challenges due to the excess background loss at these wavelengths. Much work has been done on low-nonlinearity hollow-core photonic crystal fibers (HC-PCFs), including demonstrations of short-reach amplified data transmission at 2000 nm [6] and dispersion of tens of ps/nm-km at the central transmission wavelength [7]. Efforts must continue, however, to reduce the propagation loss to acceptable long-haul tolerances.

With the basic understanding of the waveguide properties discussed, more advanced devices built upon the waveguide can be explored, such as the MRR. We will proceed to discuss the free-carrier effect under which most high-speed SOI modulators, including the MRR modulator, operate.

2.3 Free-carrier effect in SOI waveguides

2.3.1 The Drude model

The plasma dispersion effect is a well-studied phenomenon whereby the presence of free-carriers, electrons and holes, causes a change in a crystalline material's complex

refractive index, given as:

$$\tilde{n} = n + ik, \tag{2.3}$$

where n is the real part of the refractive index and k is the imaginary part, often referred to as the extinction coefficient. The physical explanation of the plasma dispersion effect can be described through the Drude model which describes the complex refractive index perturbation as a result of a change in the plasma frequency of the free-carriers. The plasma dispersion relations describe this change in refractive index and absorption as:

$$\Delta n = -\left(\frac{e^2\lambda^2}{8\pi^2 c^2 \varepsilon_0 n}\right)\left[\frac{\Delta N_e}{m^*_{ce}} + \frac{\Delta N_h}{m^*_{ch}}\right], \tag{2.4}$$

$$\Delta \alpha = \left(\frac{e^3\lambda^2}{4\pi^2 c^3 \varepsilon_0 n}\right)\left[\frac{\Delta N_e}{{m^*_{ce}}^2 \mu_e} + \frac{\Delta N_h}{{m^*_{ch}}^2 \mu_h}\right], \tag{2.5}$$

where e is the elemental charge, λ is the wavelength, c is the speed of light in vacuum, ε_0 is the permittivity in vacuum, n is the unperturbed real refractive index of the material, ${m^*}_{ce}$ and ${m^*}_{ch}$ are the conductivity effective masses (the mean effective mass in different crystallographic directions) of electrons and holes and μ_e and μ_h are the electron and hole mobilities in the material, respectively. α is the material absorption coefficient, which is related to the extinction coefficient, k, through:

$$k = \frac{\alpha\lambda}{4\pi} \tag{2.6}$$

The plasma dispersion relations demonstrate that in the presence of free-carriers, the real refractive index will decrease and the absorption coefficient will increase. These two

effects are complementary and cannot be uncoupled. Generally, the change in absorption is the undesirable side-effect of a free-carrier based modulator. It has been shown that by straining silicon, one can enhance the free-carrier effect [8]. Similarly, dispersion-engineered waveguides such as photonic crystal waveguides can enhance the free-carrier effect, as well as nonlinear effects, through slow-light interaction [9].

2.3.2 Empirical models

The plasma dispersion effect was studied in silicon in a momentous paper by Soref and Bennet [10]. In this study, it was found that, contrary to the Drude model, the change in refractive index due to holes is actually stronger than electrons for free-carrier concentrations below approximately 5×10^{19} cm^{-3}. In a more recent study, an empirical model for the plasma dispersion effect was developed which extends into the mid-infrared, including simplified equations for Δn and $\Delta\alpha$ which vary only on the concentration of electrons and holes and parameterized coefficients [11]. The generalized equations are:

$$-\Delta n = p(\lambda)\,\Delta {N_e}^{q(\lambda)} + r(\lambda)\,\Delta {N_h}^{s(\lambda)} \tag{2.7}$$

$$\Delta\alpha = a(\lambda)\,\Delta {N_e}^{b(\lambda)} + c(\lambda)\,\Delta {N_h}^{d(\lambda)} \tag{2.8}$$

where the wavelength dependent coefficients p, q, r, s, a, b, c, and d are summarized in Table 2.1.

Table 2.1: Empirical free-carrier effect model coefficients.

Coefficient	λ = 1550 nm	λ = 2000 nm
$p(\lambda)$ (cm^3)	5.40×10^{-22}	1.91×10^{-21}
$q(\lambda)$	1.011	0.992
$r(\lambda)$ (cm^3)	1.53×10^{-18}	2.28×10^{-18}
$s(\lambda)$	0.838	0.841
$a(\lambda)$ (cm^2)	8.88×10^{-21}	3.22×10^{-20}
$b(\lambda)$	1.167	1.149
$c(\lambda)$ (cm^2)	5.84×10^{-20}	6.21×10^{-20}
$d(\lambda)$	1.109	1.119

Figure 2.9 and Figure 2.10 show the change in refractive index and absorption coefficient, -Δn and $\Delta\alpha$, respectively, calculated using (2.7) and (2.8) for both 1550 and 2000 nm wavelengths.

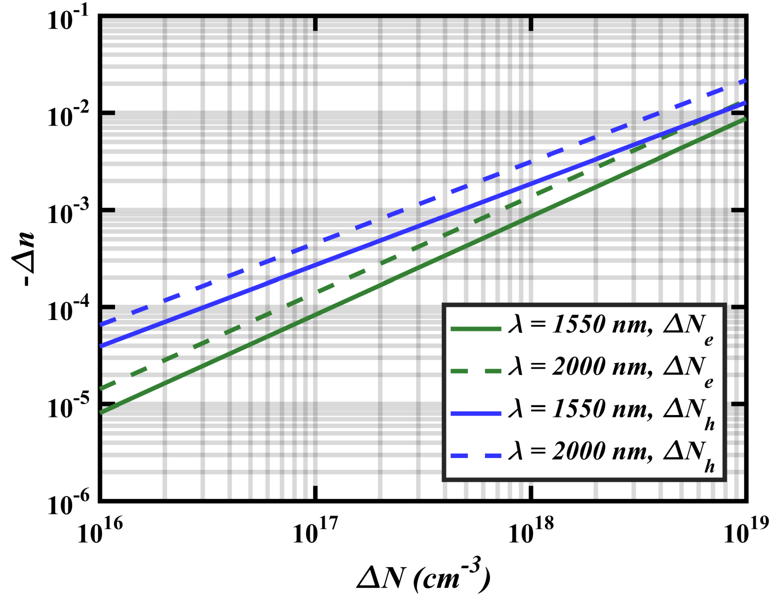

FIGURE 2.9: Change in refractive index, -Δn, as a function of doping concentration for both 1550 and 2000 nm wavelengths. Green lines denote electron-only concentrations while blue denote hole-only concentrations.

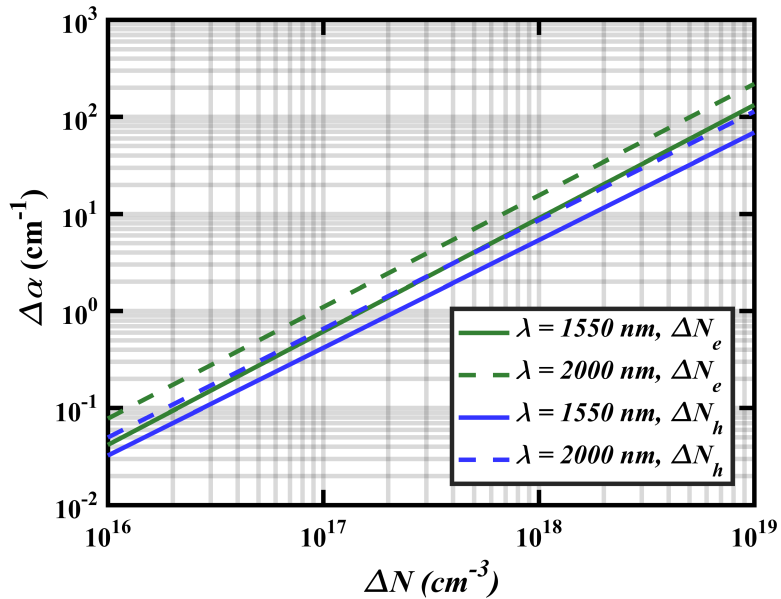

FIGURE 2.10: Change in absorption coefficient, $\Delta\alpha$, as a function of doping concentration for both 1550 and 2000 nm wavelengths. Green lines denote electron-only concentrations while blue denote hole-only concentrations.

From Figure 2.9, we see that the change in refractive index is indeed stronger at a wavelength of 2000 nm for both electrons and holes as compared to 1550 nm. Further, we see that the effect is stronger for holes at both wavelengths as compared with electrons, as predicted by Soref and Bennett [10]. Figure 2.10 shows that the change in absorption coefficient is again stronger at 2000 nm, but the effect due to electrons is stronger than holes this time. Due to this, most phase-shifting modulators, discussed later, which rely on the refractive index change due to free-carriers benefit from p-type centric designs. For example, a p-n^+ junction modulator will employ a junction with a heavily doped n-type region with the junction offset toward the n^+-type region. In this way, the depletion width of the junction which grows under reverse bias will mostly extend into the p-type region, giving a larger change in refractive index. This design, in a MRR architecture, also has the benefit of a large free-carrier absorption due to the highly-doped n-type region which lowers the Quality (Q)-factor of the cavity and associated photon cavity lifetime, ultimately increasing its modulation bandwidth, albeit at the expense of its optical modulation amplitude (OMA) which will be discussed in Section 2.5.3. [12].

2.3.3 Generation of free-carriers

2.3.3.1 Impact-ionization

Processes exist that can create free-carriers in silicon by using external energy to promote carriers across the band gap. By applying an extremely large electric field across a sample of silicon (on the order of MV/cm), intrinsic free-carriers will be accelerated and may collide with bound carriers. Sufficient kinetic energy will lead to impact-ionization causing secondary carriers to become unbound and accelerate under the applied field, thus cascading the process. This is known as an “avalanche breakdown” effect which ultimately multiplies the number of free-carriers present. The ionization coefficient for

electrons is higher than holes thus the avalanche process preferentially creates excess free-electrons. A photonic crystal cavity resonator modulator has been proposed which uses the breakdown effect to achieve absorption modulation at high speeds and relatively low energy [13], but requires very large voltage swings which complicates the driving circuitry.

2.3.3.2 Optical absorption

Optical absorption in silicon uses an incident photon of sufficient energy to promote carriers across the energy band gap and convert them into free-carriers. One could probe a silicon sample with light beyond 1100 nm where it is transparent and pump it intermittently with visible light where it is highly absorbing to create a population of free-carriers to attenuate the probe signal, known as all-optical absorption. The generated free-carriers, however, can lead to enhanced absorption which disrupts the generation of free-carriers in the form of modulation instability [14]. To avoid the accumulation of free-carriers ultra-fast pulses may be used where the repetition rate of the laser is longer than the carrier recombination time. Although, a slew of new challenges arise when dealing with ultra-fast pulses including self-phase modulation [15].

2.3.3.3 Two-photon absorption

Two-photon absorption (TPA) is a nonlinear effect whereby two photons with energy less than the band gap are absorbed through an intermediate "virtual" state allowing an electron into the conduction band. This process becomes more evident at high-intensities such as within a MRR cavity, causing detrimental instabilities such as self-heating [16] and nonlinear loss, both of which can temporarily alter the resonant properties. Self-heating strongly manifests on the red-side near resonance when the intensity build-up

in the ring causes a thermal red-shift, leading to more build-up, and so on. Under steady-state source operation, this can lead to the resonance being displaced to a stable point on the blue-side. Self-heating can be mitigated by operating on the blue-side of the resonance where a red-shift is countered by a decrease in intensity build-up in the ring. TPA becomes a less probable event at longer wavelengths in silicon and rolls-off beyond energies of $2E_g$, or $\lambda \sim 2200$ nm [17]. The TPA coefficients (β_{TPA}) for 1550 and 2000 nm are approximately 0.75 and 0.25 cm/GW, respectively, indicating a three-fold decrease in TPA at 2000 nm [18]. With sufficiently low input powers, modulation on the red-side of a MRR modulator resonance may be permitted without the associated thermal instability which can lead to detrimental power fluctuations and bit errors.

2.3.3.4 Defect-mediated absorption

Optical absorption processes can be enhanced with the use of intentionally-introduced mid-band gap defect states [19] where carriers can be promoted to an intermediate state before being promoted to the conduction or valence band thermally. This can be similar to TPA in that it is a two-step process but the effect requires a single photon and increases linearly with power.

2.3.3.5 Intrinsic free-carriers

In the absence of any of the aforementioned external processes, free-carriers exist in silicon due to finite thermal energy which probabilistically leads to thermal excitation of electrons and holes across the band gap. The intrinsic concentration of free-carriers in silicon can be calculated through a temperature dependent function given by [20]:

$$n_i\left(T\right) = 2\left(\frac{2\pi kT}{h^2}\right)^{3/2}\left(m_n^* m_p^*\right)^{3/4} e^{\left(\frac{-E_g}{2kT}\right)} \tag{2.9}$$

where h is Planck's constant, $m_n{}^*$ and $m_p{}^*$ are the electron and hole effective masses, and E_g is the band gap energy of silicon. In intrinsic silicon, $n_i = p_0 = n_0$ where p_0 and n_0 are the intrinsic p-type and n-type free-carrier concentrations. The exponential portion of (2.9) is the dominant factor, thus scaling the intrinsic carrier concentration exponentially with temperature. Physically, increasing the silicon's temperature imparts more energy to the bound electrons and holes in the valence and conduction bands, respectively, which allow them to stochastically overcome the energy gap and become free-carriers. The intrinsic concentration of free-carriers in silicon is quite low at room temperature, approximately 1.5×10^{10} cm^{-3}. While this value increases exponentially with temperature, temperatures above 1000 K would be required to begin to reach the typical free-carrier concentration changes where most silicon photonic modulators operate.

2.3.3.6 Extrinsic doping

In order to increase the free-carrier concentration n-type or p-type species, typically phosphorus and boron respectively, can be introduced into the silicon. As silicon is a group IV element on the periodic table, the introduction of these species will contribute an extra electron or an extra hole, respectively, once incorporated into the silicon crystal matrix through high-temperature annealing. In modern semiconductor processing, dopants are introduced via ion implantation and subsequent thermal annealing to promote electrical activation. By carefully controlling the ion implantation conditions, such as the species dose, implant energy, and angle of the sample, as well as the annealing conditions, a precise free-carrier distribution can be engineered in silicon. The implantation of ions, being a stochastic process, tends to follow a Gaussian distribution which

can be described in 1-D as:

$$N(x) = \frac{\phi}{\sqrt{2\pi}\Delta R_p} e^{-\frac{1}{2}\left(\frac{x - R_p}{\Delta R_p}\right)} \tag{2.10}$$

where ϕ is the implant dose in ions/cm^2, R_p is the projected implant range governed by inter-atomic collisions between the ion and the host material, and ΔR_p is the so-called straggle, which is the full-width of the distribution at a value of $e^{-1/2}$ of the peak implant concentration. Ion implants will vary in their projected range and straggle depending on the species, implant energy, and material-related nuances (i.e., channelling at specific crystallographic orientations in certain materials), thus a quasi-uniform doping profile can be achieved through multiple implants at with tailored parameters. Consider N separate implants, $N_i(x)$, with parameters ϕ_i, R_{pi}, and ΔR_{pi}, where i = 1, 2, 3, ..., N. The total implant, $N_T(x)$ would simply be:

$$N_T(x) = \sum_{i=1}^{N} N_i(x) \tag{2.11}$$

A more elegant approach to estimating the projected range and straggle of an ion implanted dopant is to use Monte Carlo simulations whereby pre-calculated collision cross-sections are used to stochastically simulate each ion's path through the material lattice. R_{pi}, and ΔR_{pi} can then be extracted from the resultant positions. Large numbers of ions are required for an accurate result thus there is a trade-off between accuracy and computational resources.

Post-implantation, these dopants must be activated through high-temperature annealing whereby the silicon lattice may break intra-silicon bonds in order to incorporate the dopants. Once bonded, the dopant may contribute either the excess electron or hole whether it is n-type or p-type. While this annealing process is normally short (on

the order of seconds or a few minutes), it occurs at temperatures typically exceeding 900 °C, at which the ions are mobile. The high-temperature kinetics of the ions will cause them to diffuse away from the area of high concentration. In this way, multiple implants can be performed and then "smoothed-out" into a more uniform concentration through annealing. One may create a tailored distribution of dopant atoms by performing multiple annealing steps with varying temperatures and durations. By implanting two adjacent regions with *p*- and *n*-type dopants, a *p*-*n* junction is formed. Through successive masked implants at different doses and energies to form the *p*-*n* junction and highly doped p^{++} and n^{++} regions to contact, a *p*-*n* junction waveguide modulator can be created.

2.4 The *p*-*n* junction modulator

Many silicon photonic modulators utilize the free-carrier effect to alter the phase or amplitude of light travelling through the material. By doing so reversibly and quickly, high-speed data signals can be encoded onto light and transmitted. The *p*-*n* junction modulator is an architecture which can operate at high-speed and with very low power consumption.

Another notably similar variation is the *p*-*i*-*n* junction which is used in photodiodes, electronic variable-optical attenuators (EVOAs), and forward bias modulators. The latter two operate under forward bias carrier injection whereby free-carriers flood into the intrinsic region (in equal concentration of electrons and holes) to create a very large phase-shift and absorption. In an EVOA, such as the one characterized in Chapter 4, the micron scale waveguide is large enough that there is little difference between the waveguide confinement factor at 1550 nm and 2000 nm wavelengths, meaning the DC attenuation performance essentially follows the λ^2 scaling presented by the plasma

dispersion effect. The high-speed performance of this device, being of the carrier injection variety, is limited by carrier diffusion and recombination and is thus similar for both wavelengths. Due to this recombination-limited bandwidth, forward bias modulation is not considered here and while higher bandwidths are achievable through various digital signal processing methods including pre-emphasis and de-emphasis, there is additional power consumption in the driving circuitry [21]. To begin, we will examine the operation of a reverse biased p-n junction waveguide modulator.

For this case study, the p-n junction is formed in a ridge waveguide at the center of the waveguide core where the optical mode is most intense. Under equilibrium, a built-in potential develops across a space-charge region, defined as a depletion width, W_d, devoid of free-carriers as a result of the balance between free-carrier drift and diffusion across the junction. This built-in potential is described as:

$$V_0 = \frac{kT}{q} ln \left(\frac{N_A N_D}{n_i^2} \right) \tag{2.12}$$

where k is the Boltzmann constant, T is the temperature, q is the elemental charge, and n_i is the intrinsic carrier concentration in silicon. N_A and N_D are the p- and n-type doping densities, respectively, which for this case study will be assumed equal in concentration of 3×10^{17} cm^{-3}. An equal concentration of electrons and holes will mean that the depletion width which forms does so equally toward both the p- and n-type regions. By applying an external electric field across the junction, W_d will grow or shrink thus altering the concentration of free-carriers which can interact with the optical mode in a controllable manner described as:

$$W_d = \sqrt{\frac{\varepsilon_0 \varepsilon_r (V - V_0)}{q} \left(\frac{N_A + N_D}{N_A N_D} \right)} \tag{2.13}$$

where ε_0 is the permittivity of free space, ε_r is the relative permittivity of silicon, and V is the applied voltage. From (2.13), we see that the W_d grows quadratically with voltages below $V = V_0$, and since V_0 is normally non-zero and positive, reverse bias p-n junction modulators may sometimes operate slightly under forward bias as this is where $\delta W_d/\delta V$ is largest. Since $N_A = N_D$ in this case, W_d will grow equally toward either side of the junction with voltage.

Intrinsically, the p-n junction will have an associated access resistance and junction capacitance. Figure 2.11 shows an equivalent electrical circuit model of a p-n junction waveguide modulator. More extensive models have been constructed which take into account additional elements such as top and bottom oxide capacitance and silicon handle resistance, as well as electrode resistance, pad capacitance, and inductance [22], [23], but for the purpose of the analyses performed, the intrinsic electrical bandwidth estimation will suffice.

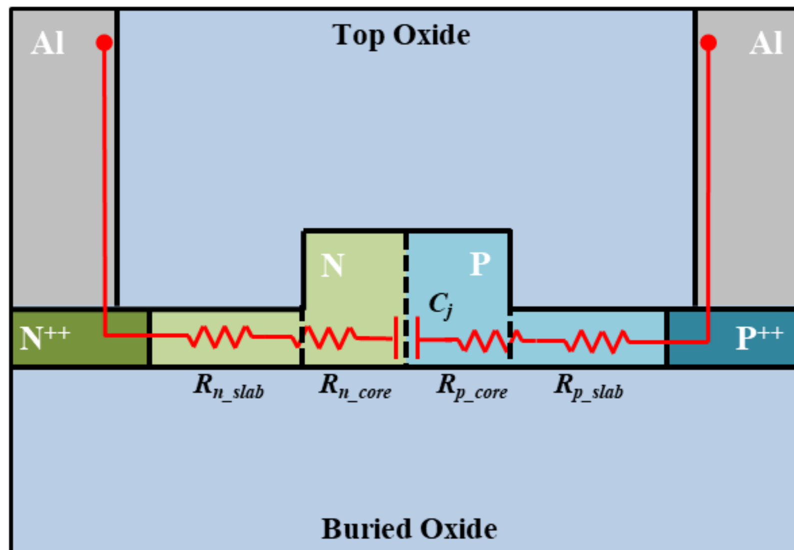

FIGURE 2.11: Equivalent electrical circuit of the p-n junction modulator.

The access resistance is determined by the resistance of the silicon slab and core segments shown in Figure 2.11 connecting the electrical contacts to the *p*-*n* junction:

$$R_j = \frac{(R_{n_slab} + R_{p_slab} + R_{n_core} + R_{p_core})}{L} + R_{load} \tag{2.14}$$

where L is the length of the device and R_{load} is a 50 Ω series load resistance from the measurement system or driver circuitry. Each segment's resistance is calculated as:

$$R = \frac{\rho w}{t} \tag{2.15}$$

where ρ is the silicon resistivity at a particular doping density and species, w is the width of the segment, and t is the silicon thickness of that region. In the case of the waveguide core sections, the $W_d/2$ is subtracted from w on either side. The junction capacitance in a 1-D approximation can be calculated as:

$$C_j = \frac{\varepsilon_0 \varepsilon_r A}{W_d} \tag{2.16}$$

where A is the capacitor area (A=tL). The intrinsic electrical 3 dB bandwidth can be estimated as:

$$f_{RC} = \frac{1}{2\pi R_j C_j} \tag{2.17}$$

From (2.14) and (2.16), we observe that if we ignore R_{load} and increase the device length, the decrease in R_j cancels out the increase in C_j in (2.17). In practice, however, R_{load} cannot be ignored and increasing device length will ultimately reduce the electrical bandwidth. Long devices such as Mach-Zehnder modulators will have very large junction

capacitance. While the access resistance will proportionally decrease with length, in the presence of R_{load}, the bandwidth may ultimately be RC-limited. In these cases, the bandwidth may be improved through electrode design, such as the use of travelling-wave electrodes [24].

By applying a reverse bias to the *p*-*n* junction with W_d growth, the lengths used to calculate R_{n_core} and R_{p_core} shrink by $W_d/2$ each, decreasing R_j, albeit slightly since R_{n_core} and R_{p_core} are generally less than R_{n_slab} and R_{p_slab} in a ridge waveguide structure. From (2.16), we see that an increase in W_d will proportionally decrease C_j thus the electrical bandwidth will increase under reverse bias. At the same time, since W_d grows quadratically with reverse bias, device performance from free-carrier modulation will begin to decrease, presenting a design trade-off between modulation amplitude and bandwidth [12].

To accommodate a larger wavelength with a fixed waveguide and slab height, the waveguide width must be increased which will ultimately increase R_{n_core} and R_{p_core}. The longer wavelength's lateral evanescent field will tend to extend further and thus the highly-doped regions are often placed further away to mitigate parasitic absorption, increasing R_{n_slab} and R_{p_slab} in the process. It is fair to say that R_j will be higher, and f_{RC} reduced in a device re-designed to accommodate longer wavelengths.

It is common to determine the energy consumed by a modulator by energy-per-bit, calculated as:

$$E_{bit} = \frac{1}{4}CV^2 \tag{2.18}$$

where C is the device capacitance and V is the peak-to-peak driving voltage. In

depletion-type p-n junction devices, the energy consumed stems from capacitive charging and discharging [25]. MZI modulators typically have large capacitances due to their lengths; conversely, a MRR modulator driven at the same peak-to-peak voltage will have much lower energy consumption due to the lower capacitance from its reduced footprint. The work contained in this thesis which pertains to wavelengths near 2000 nm was performed on a 220 nm thick SOI platform. Another common thickness to use, especially to accommodate longer wavelengths, is 300 nm. From (2.16), we see that the capacitance is proportional to the silicon thickness, thus we expect that the capacitance, and thus the energy consumed to be approximately 1.36 times larger on a 300 nm platform. Consequently, f_{RC} will also be reduced. We will restrict the following analysis to 220 nm thick silicon.

2.5 Micro-ring resonator modulator modelling

In MRR modulators, f_{RC} can be quite large due to the reduced footprint. Instead, the modulator may be limited in modulation bandwidth by other processes, such as the photon cavity lifetime. To understand the dynamics of the MRR modulator, we first start by describing the static transfer function.

2.5.1 Micro-ring resonator static transfer function

The all-pass MRR, shown in Figure 2.12, features a single bus waveguide coupling light to a ring cavity.

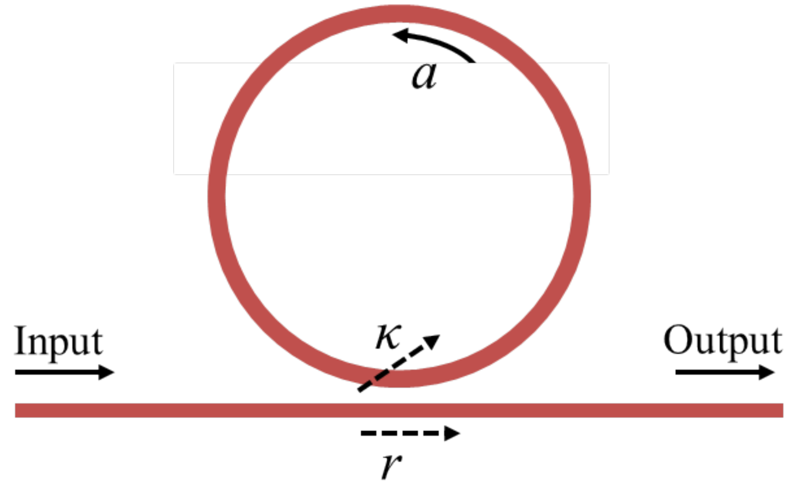

FIGURE 2.12: All-pass ring resonator configuration.

The amount of light coupled is typically a small percentage of the total amount of light, denoted by the power-coupling coefficient, κ^2. Once coupled into the ring, it travels around the cavity length, L, experiencing loss, due to various mechanisms, described by the single-pass amplitude transmission, a, which is related to the power attenuation coefficient as $a^2 = \mathrm{e}^{(\text{-}\alpha L)}$. In a passive ring resonator, the dominant loss mechanism is typically waveguide sidewall scattering, whereas in a p-n junction modulator, it is free-carrier absorption. Under certain circumstances, it may be advantageous to create a ring with a very small radius which, if small enough, can cause bending loss to become the dominant loss mechanism.

Particular wavelengths will resonate within the ring if their round trip phase shift is an integer multiple of 2π, where the light coupled in from the bus waveguide will constructively interfere with the light in the ring. Conversely, the out-coupled light will destructively interfere with the light in the bus waveguide. The wavelength orders which

satisfy this condition can be calculated as [26]:

$$\lambda_{res} = \frac{n_{eff}L}{m}, m = 1, 2, 3... \tag{2.19}$$

where m is the resonance order. On-resonance, the light becomes "trapped" almost entirely in the ring and the through transmission significantly drops. The transmission of an all-pass ring resonator can be described as:

$$T = \frac{a^2 - 2ra\cos(\phi) + r^2}{1 - 2ra\cos(\phi) + (ra)^2} \tag{2.20}$$

where r is the self-coupling coefficient, related to κ through r^2=1- κ^2, and ϕ is the single-pass phase shift, related to the propagation constant β as $\phi = \beta L$. The phase, φ, is given by:

$$\varphi = \pi + \arctan\left(\frac{r\sin\phi}{a - r\cos\phi}\right) + \arctan\left(\frac{ra\sin\phi}{a - ra\cos\phi}\right) \tag{2.21}$$

The basic operation of a MRR modulator involves altering the effective index, n_{eff}, of the waveguide mode, related to β through $\beta = 2\pi n_{eff}/\lambda$, thus altering the round trip phase-shift observed in the resonance spectrum. While using a single-line laser source at a fixed wavelength, a shift in the resonance spectrum can result in a large change in transmission amplitude depending on the laser's position along the transmission curve, referred to as resonance detuning. The optimal resonance detuning (δ) depends on the application of the ring resonator structure. For instance, a ring resonator with an integrated heater may operate as a low-speed switch, turning the signal on (high amplitude) and off (low amplitude) when necessary. The integrated heater operates by changing the optical path length of the ring resonator through the thermo-optic

effect which results in an increase in the effective index of a mode travelling in the ring waveguide. For a mode mostly confined in the silicon core of the waveguide, this can result in a large Δn_{eff} which will red-shift the resonance spectrum with relative ease. We calculate the resonant shift through a modified version of (2.19):

$$\Delta\lambda_{res} = \frac{\Delta n_{eff} L}{m} \tag{2.22}$$

For ridge waveguide geometries in a 15 μm radius ring resonator, the value of m which results in a resonance near 1550 and 2000 nm wavelengths for 500 and 600 nm waveguide widths are 156, and 108, respectively. We can divide both sides of (2.22) by dT then substitute the waveguide thermo-optic coefficient at these respective geometries and wavelengths (dn_{eff}/dT = 1.85×10^{-4} and 1.63×10^{-4} K^{-1}, respectively) to calculate the resonance shift with temperature, which we will call the resonance sensitivity. These values are $d\lambda_{res}/dT$ = 111.9 and 142.8 pm/K, respectively. Despite the reduced waveguide thermo-optic coefficient (seen in Figure 2.4) at 2000 nm wavelength compared with 1550 nm at the dimensions in question, the sensitivity is actually enhanced by a factor of 1.27, regardless of cavity length, L. While this result negatively impacts the thermal stability of MRR devices operating at longer wavelengths, thermal tuning is enhanced. In a different context, the same sized ring resonator requires 78% as much power from an integrated micro-heater to shift its resonance by the same distance, which can result in large power savings in many-ring applications such as wavelength-division multiplexing (WDM) and stacked resonance applications which are examined in Chapter 7.

Returning to the hypothetical thermally-controlled switch, assuming power consumption is not of concern, this switch would operate best with the largest on-off extinction ratio (*ER*) which is the difference in the on and off transmitted power. The largest on-off *ER* occurs precisely between two resonances, or half of the free spectral range (*FSR*), (δ

= $FSR/2$) for the on-state and on-resonance (δ = 0 nm) for the off-state. In practical devices, this often presents design trade-offs, in this case, on-off *ER* versus power consumption, which will vary as a function of detuning. Additional design constraints will factor into the optimal detuning, i.e. on-state signal strength must be greater than -1 dB or off-state must be less than -10 dB.

Design decisions can become quite complex with regards to MRR modulators used in high-speed transceivers. The choice of resonance detuning impacts not only the on-off *ER* and transmitted power levels, but also modulation bandwidth as we will see in Section 2.5.3. Typically, there is a trade-off between modulation amplitude and bandwidth.

In switching and WDM systems, the *FSR* of a MRR, or the distance between adjacent resonant modes, is a crucial parameter. The *FSR* is calculated as:

$$FSR = \frac{\lambda^2}{n_g L} \tag{2.23}$$

Comparing a MRR with fixed length and a waveguide width of 500 and 600 nm for 1550 and 2000 nm wavelengths, respectively, we see a 1.78 factor increase in *FSR*: a 1.66 factor increase from the λ^2 dependence and a 1.07 factor increase from the decrease in n_g from 3.9 to 3.65. This larger *FSR* is advantageous in WDM systems in that more wavelength channels can be incorporated to transmit additional data-streams.

In a MRR modulator, the dimensions are typically sufficiently small that they are not limited by the electrical bandwidth, but the photon cavity lifetime of the ring. This can be rationalized as the time it takes for the light in the ring to sufficiently build or decay in intensity and is a measure of the cavity Q-factor, calculated as the ratio between the

resonant wavelength and the full-width at half-maximum ($FWHM$), calculated as:

$$FWHM = \frac{(1 - ra)\,\lambda_{res}^2}{\pi n_g L \sqrt{ra}} \tag{2.24}$$

where r is the bus waveguide self-coupling coefficient, a is the single-pass amplitude transmission encompassing loss within the ring and losses due to out-coupling to the bus waveguide, λ_{res} is the cavity resonant wavelength, and n_g is the group index. Immediately we can see that, all else constant, an increase in wavelength from 1550 nm to 2000 nm will result in the same 1.78 factor increase in $FWHM$. In the context of WDM systems, the increase in the number of channels due to increase in FSR from operating at 2000 nm is countered by this increase in $FWHM$ which will manifest as an increase in undesirable modulation cross-talk. By substituting (2.24) into the definition of Q-factor, we see it is inversely proportional to λ_{res}, implying a lower Q-factor for longer wavelengths which will improve the optically-limited bandwidth of a MRR modulator. Another useful definition of a ring resonator's Q-factor is expressed as [27]:

$$Q = \frac{\pi \tau c}{\lambda} \tag{2.25}$$

where c is the speed of light in vacuum, and τ is the photon cavity lifetime. This relation directly shows the inverse relationship between Q-factor and wavelength as well as the proportionality between Q-factor and τ. The photon lifetime can be expressed as $\tau^{-1} = \tau_l^{-1} + \tau_e^{-1}$ where τ_l and τ_e are the amplitude decay time constants due to intrinsic loss within the ring and power out-coupling due to the bus waveguide, calculated as [28]:

$$\tau_l = \frac{2}{\nu_g \alpha} \tag{2.26}$$

$$\tau_e = \frac{2L}{\nu_g \kappa^2} \tag{2.27}$$

where ν_g is the group velocity, related to the group index n_g through $\nu_g = c/n_g$, α is the absorption coefficient, L is the cavity length, and κ is the cross-coupling coefficient, related to r through $\kappa^2 = 1 - r^2$. A ring resonator is critically-coupled when $\tau_e = \tau_l$, over-coupled when $\tau_e < \tau_l$, and under-coupled when $\tau_e > \tau_l$. Using τ, the lifetime-limited bandwidth can be estimated as [27]:

$$f_Q = \frac{1}{\pi\tau} \tag{2.28}$$

With a reverse bias voltage, we see from (2.17) that f_{RC} will increase due to the reduction in C_j; however, the same reverse bias will decrease the loss in the ring, α, from the partial depletion of free-carriers, and subsequently increase τ_l, ultimately reducing f_Q. In a heavily over-coupled ring where $\tau_e \ll \tau_l$, a significant change in τ_l will not have a major impact on τ. To ensure τ_e is very small, either a very small cavity length must be achieved (at the expense of modulation efficiency), or κ must be large. Similarly, τ_l can be made very small by increasing loss, by which there are several ways. One may reduce the ring radius to produce sharper bends, adding to loss through coupling the light to lossy radiation modes (again at the expense of modulation efficiency from reduced cavity length), or by adding a drop-port waveguide to couple-off a portion of light in the cavity, this time at the expense of modulation efficiency since the *p*-*n* junction coverage must be reduced to accommodate the waveguide. One may also use a modified p-n^+ junction architecture which can have better modulation efficiency and increased loss from the higher doping in the waveguide [4]. Lastly, one may reduce the distance between the waveguide core edges and the highly-doped contact regions which will increase parasitic loss due to free-carrier absorption as well as marginally decreasing the access resistance

R_j, thus increasing f_{RC}. In this analysis, we will focus on the impact of the last scenario.

By operating at longer wavelengths, α due to free-carrier absorption will increase decreasing τ_l. Additionally, both τ_e and τ_l are inversely proportional to group velocity ν_g which is larger at longer wavelengths, decreasing τ further allowing for higher f_Q. It should be noted that when dealing with MRR modulators affected by both f_{RC} and f_Q, the total modulation bandwidth can be estimated as:

$$\frac{1}{{f_{Total}}^2} = \frac{1}{{f_{RC}}^2} + \frac{1}{{f_Q}^2} \tag{2.29}$$

This estimation of bandwidth, however, does not fully capture the transient time dynamics of MRR modulators. An effect called optical peaking, discussed further in this chapter, can extend the bandwidth of a device beyond the photon lifetime-limited bandwidth.

2.5.2 Micro-ring resonator modulator static response

The static response of a MRR modulator is simulated at DC voltage biases placed across the waveguide p-n junction inside the ring cavity. Effective index simulations were performed for both wavelengths at various contact-doping separations and depletion widths for the associated waveguide widths. The material index profile of the silicon was adjusted according to (2.7) and (2.8) to emulate a homogeneous concentration of 3×10^{17} cm^{-3} electrons and holes in a p-n junction and 1×10^{20} cm^{-3} for the contact-doping regions. The effective index perturbation due to the depletion width in simulation was simply a region of intrinsic silicon which increased uniformly in width centered in the core (the equal doping in both the p- and n-type regions allows for the symmetrical growth of W_d across the junction with bias) yielding curves of n_{eff} and α vs. W_d. To

associate these values with the appropriate applied reverse bias, W_d was calculated for each bias using (2.13) and n_{eff} and α are interpolated from the aforementioned curves. We proceed with waveguide widths of 500 and 600 nm for 1550 and 2000 nm wavelengths, respectively, as these were determined to be the widths which showed the largest change in effective index with voltage while remaining near the single-mode cut-off. Δn_{eff} as a function of voltage relative to the 0.5 V condition is shown in Figure 2.13.

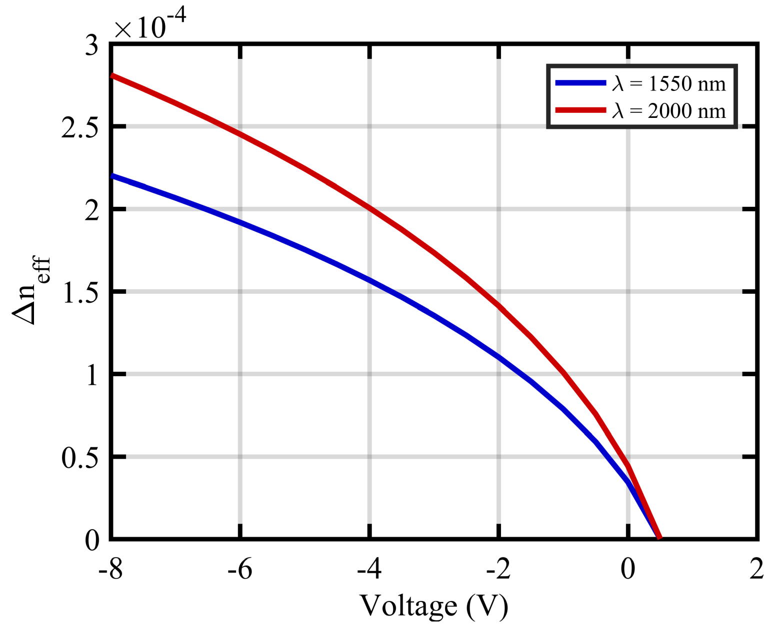

FIGURE 2.13: Change in effective index relative to n_{eff} at 0.5 V bias for 1550 and 2000 nm wavelengths at waveguide widths of 500 and 600 nm, respectively, with theoretical 100% *p*-*n* junction coverage.

The change in effective index in the 2000 nm wavelength MRR modulator is approximately 1.27 times higher than the 1550 nm modulator at each bias. Due to the reduced confinement and larger waveguide width of the 2000 nm wavelength, the overlap of the mode with W_d is reduced. Thus the free-carrier effect, while approximately 1.7 times stronger at 2000 nm wavelength, compared to 1550 nm, is reduced in effective strength due to the nuances of the waveguide. The choice of contact-doping separation affects f_{RC} as discussed previously, but also affects the loss experienced by the mode travelling

in the ring. Reduced separation increases overlap of the mode's exponentially decaying evanescent field outside the waveguide core, thus parasitic absorption can increase dramatically. Figure 2.14 shows $\Delta\alpha$ for 1550 and 2000 nm wavelengths at 500 and 600 nm widths, respectively, as a function of contact-doping separation. Data are plotted for 0.5 and -2 V biases, emulating a 2.5 V peak-to-peak voltage swing.

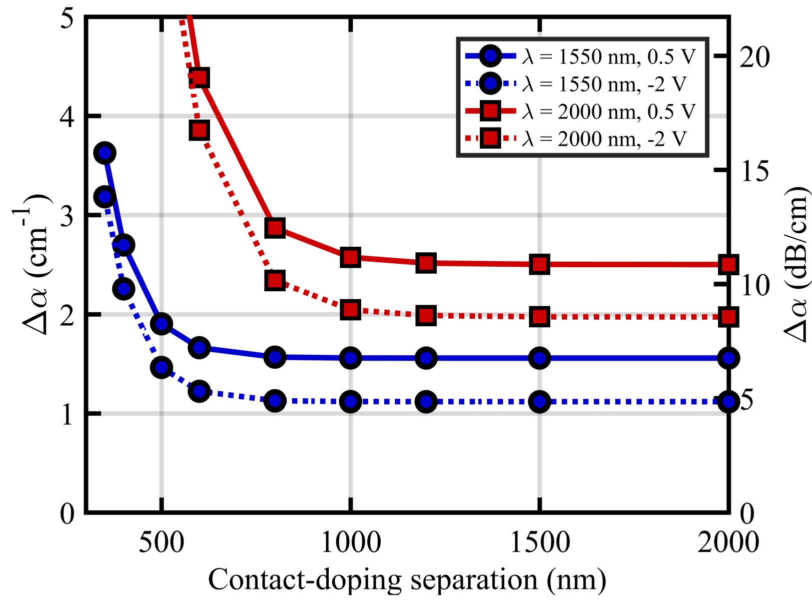

FIGURE 2.14: α for 1550 and 2000 nm wavelengths at 500 and 600 nm waveguide widths, respectively, as a function of contact-doping separation. Solid and dashed lines represent a 2.5 V peak-to-peak swing.

The absorption across all contact-doping separations for 2000 nm wavelength is stronger, as predicted. At large separations where both wavelengths experience negligible parasitic absorption from the contact-doping, α is approximately 1.6 times stronger at 2000 nm. The change in loss, $\Delta\alpha$, between 0.5 and -2 V biases is also slightly stronger. As the separation is reduced, α begins to increase steeply beyond 600 and 1000 nm for 1550 and 2000 nm wavelengths, respectively. While a large value of α will increase f_Q, it does so at the cost of on-off *ER*. From (2.24), we see the *FWHM* becomes larger for small values of a (small a implies large α), which broadens the resonances, requiring a larger resonance

shift to achieve the same on-off ER as a ring with larger values of a. Large on-off ERs are achieved at critical-coupling ($r = a$) where the intensity build-up in the ring is sufficient to completely nullify the transmission at the output of the bus waveguide. Figure 2.15 a) shows the normalized transmission spectra for a MRR modulator critically-coupled at the 0.5 V biased state for both 1550 and 2000 nm configurations and contact-doping separations of 500 and 800 nm, respectively. Figure 2.15 b) shows the on-off extinction ratio of these transmission spectra for increasing voltage swing from 0.5 V increasing in reverse bias.

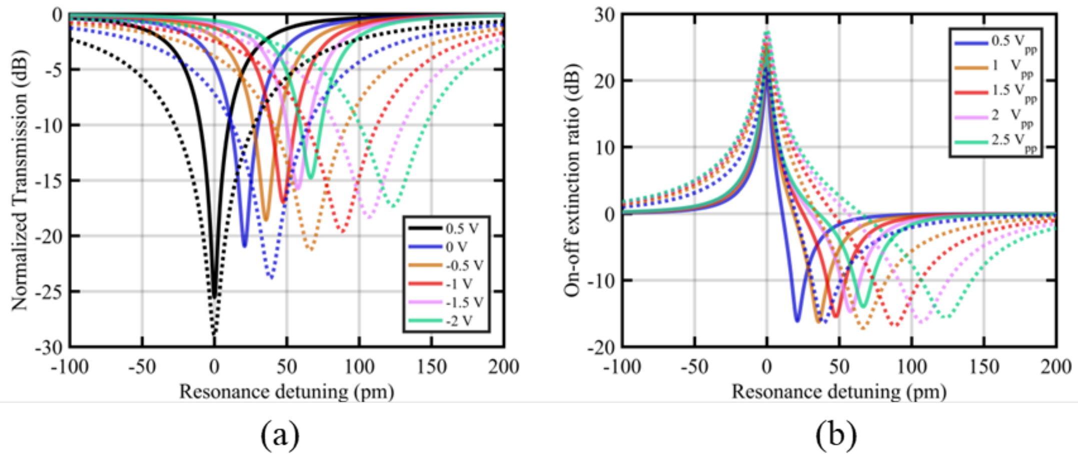

FIGURE 2.15: a) Normalized biased transmission spectra for critically-coupled rings at 1550 (solid lines) and 2000 nm wavelength (dotted lines). b) On-off extinction ratio of transmission spectra for increasing peak-to-peak voltage swings.

We immediately see that the $FWHM$ of the resonances at 2000 nm wavelength are larger than that of 1550 nm and the resonance shift as a function of reverse bias is also greater, both as predicted. Since the MRRs are tuned to critical coupling at the 0.5 V resonance, each subsequent increase in reverse bias produces an over-coupled resonance (due to the dynamic decrease in α as seen in Figure 2.14) with increasingly decreased the notch-depth. Had the resonator been under-coupled, each subsequent resonance would

instead move closer toward critical-coupling producing resonances with increasing notch-depth. The on-off *ER* is more complex as the choice of detuning depends on many other factors. Similar on-off *ER*s at either wavelength are achievable for the same voltage swing at different respective wavelength detunings; however, the wavelength detuning has a critical impact on the high-speed performance as will be explored further in this chapter. The term insertion loss (*IL*), which is a common metric used in determining modulator performance, is simply the normalized transmitted power of the "on" or "high" state at the chosen detuning, representing the optical power cost of operating at that point. Another important metric is known as the transmission penalty (*TP*), given as [27]:

$$TP = -10\log\left(\frac{P_1 - P_0}{2P_{in}}\right) \tag{2.30}$$

where P_1 and P_0 are the transmitted on and off-state power levels, and P_{in} is the input power. *TP* reflects the efficiency with which the input power is used in amplitude modulation. Ideally, the on-state would have zero *IL*, thus $P_1 = P_{in}$, and the off-state would be zero, thus $P_0 = 0$. In the ideal situation, $TP = 3$ dB. *TP* is calculated for the data presented in Figure 2.15 and shown in Figure 2.16.

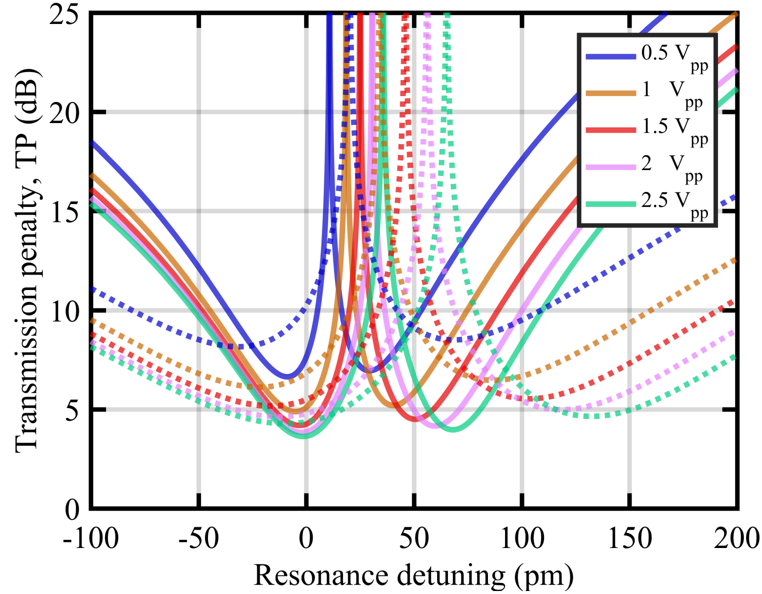

FIGURE 2.16: *TP* for the transmission spectra shown in Figure 2.15 for 1550 nm (solid lines) and 2000 nm (dotted lines) wavelengths.

We see that in general, for larger voltage swings *TP* decreases as a larger contrast between P_0 and P_1 is achieved, as well, the minimum *TP* approaches the resonance position as this is where P_0 is smallest. Most driving circuitry will not be able to supply large voltage swings to the modulator, thus we restrict our analysis to 2.5 V peak-to-peak, which is common in drivers as well as measurement equipment. To set a boundary condition, it is not common to modulate exactly on-resonance, rather to one side or the other. The red-side, or right side, of the resonance is also less favourable due to the detrimental effect of self-heating in which the build-up of light in the cavity leads to an increase in free-carriers from TPA which generate heat that can thermally shift the resonance. Here we reiterate that the TPA coefficient (β_{TPA}) at 2000 nm is approximately 3 times less than at 1550 nm, meaning red-side modulation may be more feasible provided the input power is low enough to avoid TPA. If on the red-side, the voltage swing should be such that it does not “roll over” the resonance notch. There is, however, a specific application of the MRR modulator which involves exactly that. By moving from one side

of the resonance to the other, a phase-shift occurs. With careful design and appropriate wavelength detuning, one may modulate the ring to move the resonance from points of equal transmitted power on either side to produce a π phase-shift for use in such devices as ring-loaded MZI modulators used in binary phase-shift keying (BPSK) [29]. To examine this further, transmission spectra of 1550 and 2000 nm wavelength modulator configurations with several contact-doping separations were calculated using (2.20) with increasing reverse bias (initial bias at 0.5 V to provide the largest resonance shift). As the reverse bias increases, the wavelength detuning is determined where points of equal transmission are found on the red-side of the initial resonance and the blue-side of the increased bias resonance. The induced phase-shift between the two spectra at this detuning is calculated using (2.21). The applied voltage-swing is increased until this phase-shift equals exactly π. To ensure a π phase-shift is achievable, the modulators are operated in the over-coupled condition, which provides a near 2π phase-shift from one side of the resonance to the other. For an arbitrary resonance, the equal transmission and π phase-shift with bias is depicted in Figure 2.17 a) and b), respectively.

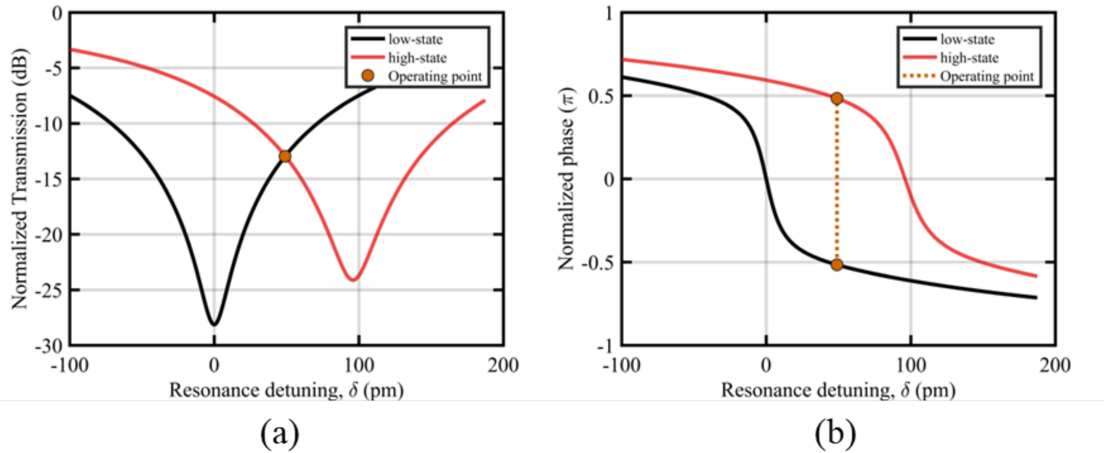

FIGURE 2.17: a) Normalized transmission of MRR modulator spectra for BPSK applications with operating point at equal transmission levels on red- and blue-side of resonance, respectively. b) Associated π phase-shift at operating point.

This process was repeated while sweeping the self-coupling coefficient, r, beginning from just beyond the critical-coupling condition toward the over-coupled direction. The voltage-swing required to achieve a π phase-shift was recorded for each simulation as well as the transmission level of the operating point. Minimum and maximum voltage swings of 1 and 5 V peak-to-peak are considered. For the 1550 nm wavelength modulator configuration, the required voltage-swings for several arbitrarily chosen contact-doping separations are shown as a function of r in Figure 2.18 a) and the associated transmission level in Figure 2.18 b).

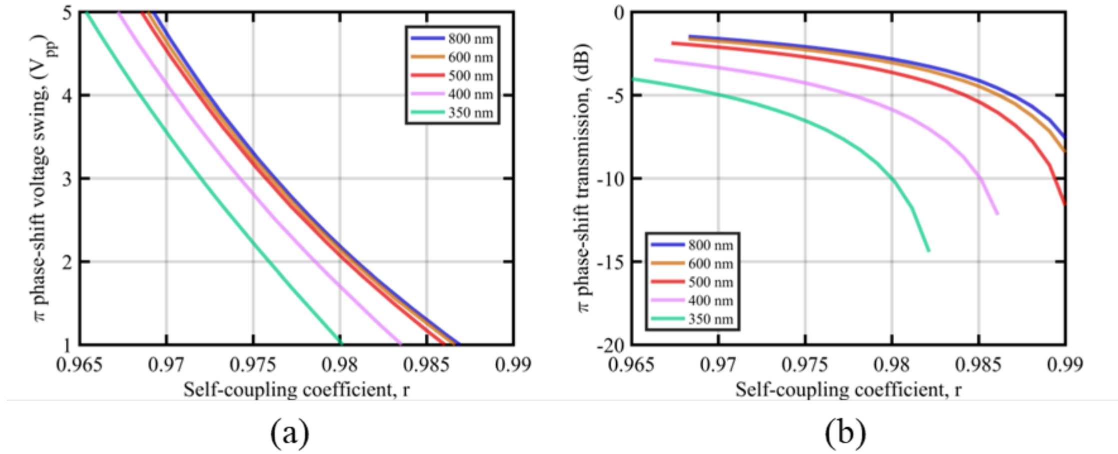

FIGURE 2.18: a) Required voltage swing for a π phase-shift at discrete contact-doping separations as a function of self-coupling coefficient, r, for the 1550 nm wavelength modulator configuration and b) associated transmission at operating point.

The more heavily the modulators are over-coupled, the higher the required voltage-swing becomes due to the shrinking of the phase spectrum, similar to the broadening of the resonances. This is exaggerated with reduced contact-doping separation where parasitic absorption increases drastically. Examining both a) and b), operating points with higher transmission can be achieved but at the expense of larger voltage-swings. This is alleviated toward larger contact-doping separations (lower parasitic loss), but this time at the expense of modulation speed from both f_Q and f_{RC}. The data in b)

is truncated where either a voltage-swing greater than 5 V peak-to-peak is required or if r is larger than a (critical-coupling point). Similar data for the 2000 nm wavelength modulator configuration is seen in Figure 2.19 a) and b).

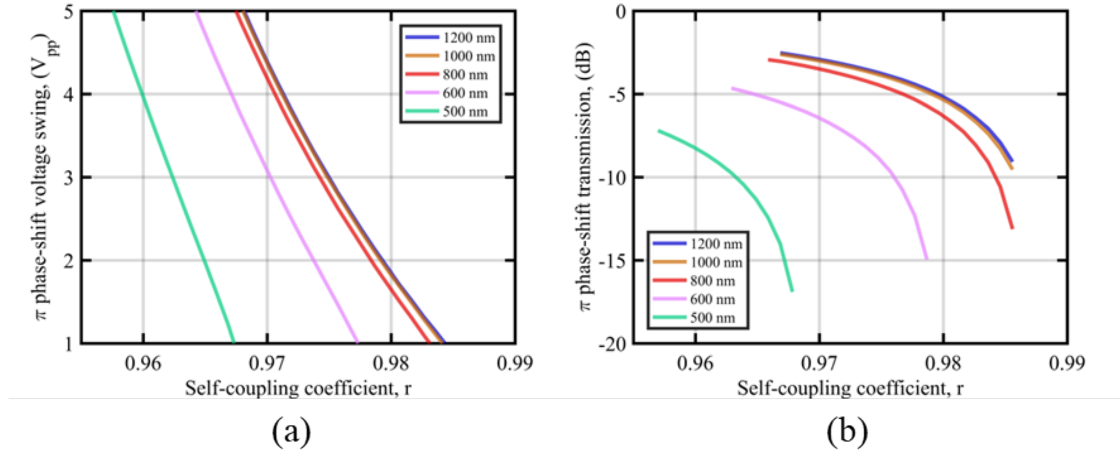

FIGURE 2.19: a) Required voltage swing for a π phase-shift at discrete contact-doping separations as a function of self-coupling coefficient, r, for the 2000 nm wavelength modulator configuration and b) associated transmission at operating point.

Comparing the performance of both wavelength configurations, operating points can achieve higher transmission values in the case of 1550 nm wavelength due to the resonance and phase response broadening at longer wavelengths. Despite this, since BPSK normally operates with modulation including the red-side of resonance, longer wavelengths may be more advantageous depending on input power due to the reduction in detrimental self-heating from TPA.

An important parameter to consider in MRR modulators is modulation chirp, which is inevitable in most cases. It is known that MRR modulators cannot operate chirp-free unless in specific cases such as a coupling-modulated ring where the coupling coefficient is dynamically tuned to have the resonance pass from under- to over-coupled during modulation [30]. For dispersion uncompensated systems, such as a short-reach transmission

with positive dispersion fiber, a MRR modulator can be designed to have negative chirp to counter-act the dispersion to improve signal integrity at the receiver [4]. In the large-signal domain, the on-off α-parameter (not to be confused with the loss coefficient, α) is used to describe the device chirp, given as [31]:

$$\alpha = -2\frac{\Delta\phi}{\Delta I} \tag{2.31}$$

where $\Delta\phi$ and ΔI are the change in the MRR modulator phase and intensity for a particular voltage swing. Here we consider a fixed swing of 2.5 V peak-to-peak, beginning at a 0.5 V bias, again, to produce the largest $\delta n_{eff}/\delta V$. In an over-coupled ring resonator modulator, negative chirp is achieved by modulating on the blue-side of resonance while positive chirp can be achieved on the red-side of modulation. For simplicity, we only consider blue-side modulation here as positive chirp coupled with positive dispersion transmission (typical in most transmission systems) leads to exaggerated pulse broadening and potential inter-symbol interference at the receiver. We simulate the on-off α-parameter for both 1550 and 2000 nm wavelength modulator configurations with contact-doping separations of 500 and 800 nm, respectively, swept across self-coupling coefficients, r, for values just beyond critical-coupling toward over-coupling ($r \leq a$). Figure 2.20 a) shows the on-off α-parameter for the 1550 nm modulator configuration at several arbitrary values of r as a function of resonance detuning while Figure 2.20 b) shows the same data at fixed resonance detunings across r.

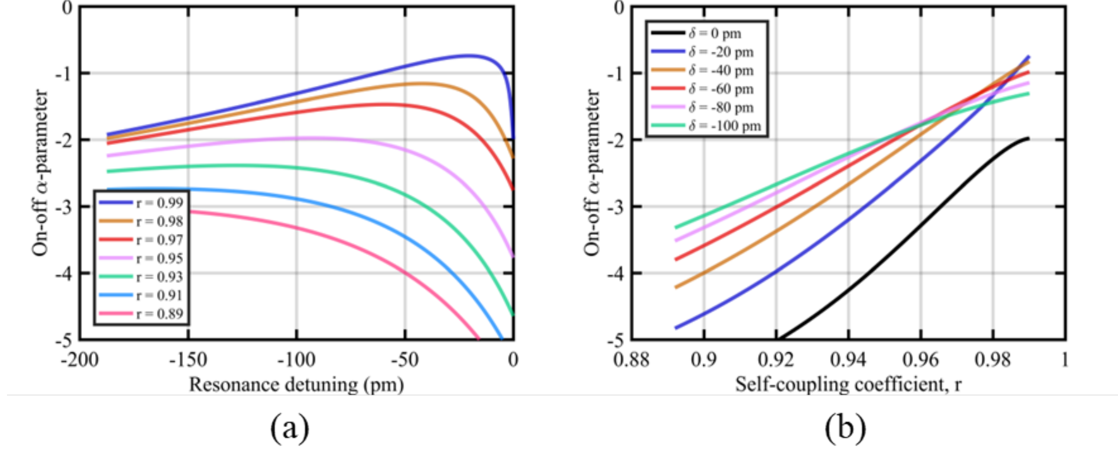

FIGURE 2.20: On-off α-parameter for 1550 nm wavelength modulator configuration a) at fixed values of r calculated across wavelength detunings and b) for fixed detunings across r.

Close to resonance on the blue-side, the on-off α-parameter can become very large as the ring becomes more and more over-coupled, especially if it is near resonance, however this is at the expense of other parameters such as on-off ER and, as we will see shortly, small-signal modulation gain and bandwidth. Similarly, the on-off α-parameter becomes larger with blue-side resonance detuning but with similar trade-offs (although small-signal modulation bandwidth will actually increase). If the design is meant to minimize chirp in an over-coupled ring, a minimum occurs when closest to critical-coupling and detuned slightly away from resonance. With increased self-coupling, we see this minimum become larger and further away from resonance. Figure 2.21 similarly shows the on-off α-parameter for the 2000 nm wavelength modulator configuration.

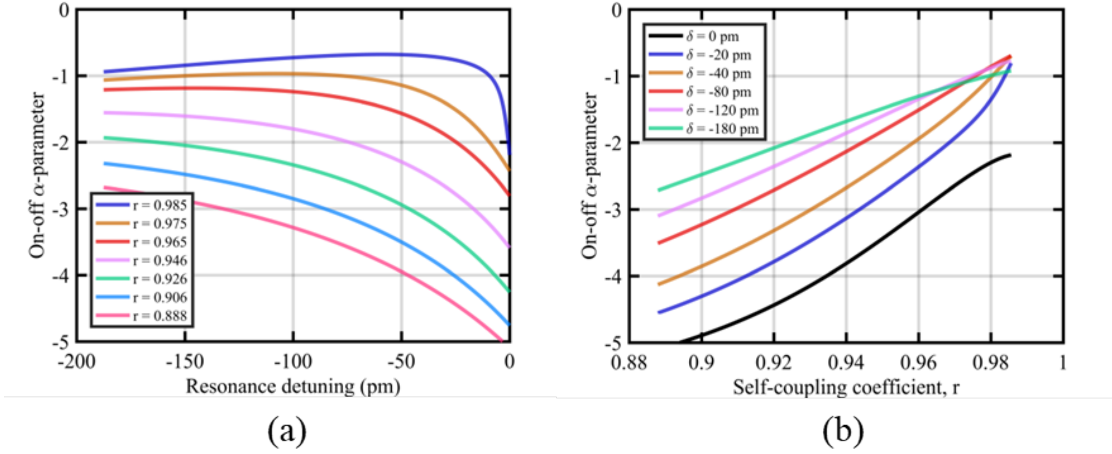

FIGURE 2.21: On-off α-parameter for 2000 nm wavelength modulator configuration a) at fixed values of r calculated across wavelength detunings and b) for fixed detunings across r.

Comparing the on-off α-parameter of 1550 and 2000 nm wavelength modulator configurations, the latter case exhibits lower magnitude values due to the broader resonance and phase response. Comparing two slightly over-coupled rings (first set of data plotted in a) of Figures 2.20 and 2.21), the 2000 nm wavelength configuration maintains a lower value of on-off α-parameter than the 1550 nm case, and for a wider range of wavelength detunings. This offers more flexibility in selecting the appropriate detuning when factoring in other steady-state and high-speed performance metrics. In the case where large positive on-off α-parameter values are desirable (perhaps in applications involving high-power pulse broadening to allow for unsaturated amplification further in the transmission link before subsequent pulse re-compression), the on-off α-parameter exhibits similar behaviour as discussed, though on the red-side of modulation as opposed to blue, where longer wavelengths become more advantageous due to reduced self-heating from TPA.

We now examine a crucial set of high-speed performance metrics commonly used in MRR modulators found through small-signal analysis.

2.5.3 Micro-ring resonator modulator dynamic response

2.5.3.1 Small-signal characteristics

The time-dynamics of a MRR modulator can play a crucial role in enhancing the bandwidth of a device through a phenomenon called optical peaking [32], [33], [34]. When a high-speed signal is applied to the modulator with a rise-time comparable to the photon cavity lifetime of the ring, the device response will have an overshoot on this rising edge. When moving from an on-resonance state to an off-resonance state, the built-up light in the modulator becomes marginally wavelength shifted due to the time-varying change in refractive index from the change in free-carrier concentration in the *p*-*n* junction. As a result of this wavelength shift, the out-coupled light does not immediately interfere with the light in the bus waveguide, producing a large amplitude response. As the refractive index change settles to steady state, the overshoot settles as a damped oscillation with a damping rate related to the photon cavity lifetime and a frequency proportional to the time-varying beating between the slightly detuned ring and bus waveguide wavelengths [35]. In a small-signal RF measurement, optical peaking manifests as a “bump” in the S_{21} response of the device which extends its 3 dB bandwidth into higher frequencies. Resonance detuning, as well as the peak-to-peak driving voltage, affect the prominence of the optical peaking effect as there must be a sufficient intensity build-up near-resonance as well as a sufficient intensity “release” of the built-up light when moving off-resonance. It should be noted that blue- vs. red-side resonance detuning will have asymmetrical peaking in the presence of dynamic waveguide losses from free-carrier modulation [32], meaning one side may be preferable for modulation compared to the other. Red-side modulation is generally avoided due to thermal instability from self-heating caused by detrimental TPA; however, as mentioned previously, MRRs operating at 2000 nm wavelength have a three-fold reduction in β_{TPA} as compared with 1550 nm, thus red-side modulation may be feasible at higher powers, if it is advantageous to do so.

High modulation bandwidth is crucial to achieve in the design of modulators, and in the case of the MRR modulator, wavelength detuning is the determining factor. While increasing detuning increases modulation bandwidth, it does so at the expense of modulation efficiency, often referred to as DC gain (G_{DC}). A popular figure of merit to use in determining the optimal detuning to achieve maximum modulation efficiency and bandwidth is the gain-bandwidth product (GBW). To calculate GBW, we use an elegant and comprehensive model from [27] where the author derives closed-form expressions for the small-signal transfer function which describes the bandwidth and G_{DC} of a MRR modulator taking into account its electrical, electro-optical, and optical parameters. We apply this to an all-pass modulator with varying width and doping separation for both 1550 and 2000 nm wavelengths.

The electrical portion, $H_E(\omega_m)$, of the total transfer function is a simple RC-circuit transfer function using the access resistance and junction capacitance previously discussed:

$$H_E(\omega_m) = \frac{1}{1 + j\omega_m R_j C_j} \tag{2.32}$$

where ω_m is the modulation angular frequency applied from a small sinusoidal electrical signal $V(t) = V_{in}\cos(\omega_m t)$, j is the imaginary number, and R_j and C_j are the access resistance and junction capacitance, respectively. The electro-optical portion, H_{EO}, of the transfer function, which takes into account the change in complex refractive index with voltage across the p-n junction, is described by:

$$H_{EO} = \left(\frac{-\omega_r}{n_g} \frac{\delta n_{eff}}{\delta V}\bigg|_{V_{DC}} + j\frac{\delta(1/\tau)}{\delta V}\bigg|_{V_{DC}} \right) \tag{2.33}$$

where ω_r is the resonance angular frequency, n_g is the group index, and j is again the

imaginary number. $\delta n_{eff}/\delta V$ is the effective index change of the waveguide mode, while $\delta(1/\tau)/\delta V$ is the change in photon cavity decay rate both as a function of applied DC voltage; the latter and former describing the dynamic change in the real and imaginary effective index of the waveguide mode. At waveguide widths of 500 and 600 nm and wavelengths of 1550 and 2000 nm, respectively, the larger DC modulation efficiency and lower group index from operating at 2000 nm increases $\mathrm{Re}(H_{EO})$ by a factor of 1.27 and 1.07, respectively, when operating at low reverse bias voltages, where $\delta n_{eff}/\delta V$ is maximized; however the decrease in ωr reduces $\mathrm{Re}(H_{EO})$ by a factor of 1.29. All factors considered, there is still a marginal improvement in $\mathrm{Re}(H_{EO})$. $\mathrm{Im}(H_{EO})$ also sees an increase by a factor of 1.26 at low reverse bias and increases with reverse bias.

Finally, the optical response, $H_O(\omega_m)$, of the total transfer function is derived using coupled-mode theory [28]. The actual $H_O(\omega_m)$ expression is implicitly derived and encapsulated into the total transfer function, $H_t(\omega_m)$, given as:

$$H_t\left(\omega_m\right) = \frac{2\mu^2 P_{in}(-\frac{\omega_r}{n_g}\frac{\delta n_{eff}}{\delta V})\,|_{V_{DC}}}{\frac{1}{\tau^2}+\Delta\omega^2}\frac{\left(\tan\left(\phi_{HEO}\right)\right)\left(\frac{1}{\tau_l}-\frac{1}{\tau_e}\right)-\Delta\omega}{1+j\omega_m R_{eq}C_{eq}}\times \left[\frac{j\omega_m-\frac{2\frac{\Delta\omega}{\tau_l}+\tan(\phi_{HEO})\left(\Delta\omega^2-\frac{1}{\tau}\left(\frac{1}{\tau_l}-\frac{1}{\tau_e}\right)\right)}{\tan(\phi_{HEO})(\frac{1}{\tau_l}-\frac{1}{\tau_e})-\Delta\omega}}{-\omega_m^2+\frac{2}{\tau}\left(j\omega_m\right)+\Delta\omega^2+\frac{1}{\tau^2}}\right] \tag{2.34}$$

where μ is the mutual ring to bus waveguide coupling coefficient, calculated as $\mu^2{=}2/\tau_e$, P_{in} is the input power (here normalized to 1), $\Delta\omega = \omega_o - \omega_r$ is the frequency detuning where ω_o is the input laser frequency, and ϕ_{HEO} is the phase of H_{EO}. The DC gain,

G_{DC}, can be determined by evaluating $H_t(0)$, which simplifies to:

$$G_{DC} = \frac{2\mu^2 P_{in}\left(\frac{\omega_r}{n_g}\frac{\delta n_{eff}}{\delta V}\mid_{V_{DC}}\right)}{\omega_n^4}\left(2\frac{\Delta\omega}{\tau_l} + \tan\left(\phi_{HEO}\right)\left(\Delta\omega^2 - \frac{1}{\tau}\left(\frac{1}{\tau_l} - \frac{1}{\tau_e}\right)\right)\right) \tag{2.35}$$

where $\omega_n = (\Delta\omega^2 + \tau^{-2})^{1/2}$.

Before $H_t(\omega_m)$ can be calculated, several boundary conditions must be established to reduce the scale of the design parameter space. Regarding the dimensions of the modulator waveguide, only 220 nm thick silicon modulators are considered for this simulation due to its availability in most silicon photonic foundries. Secondly, the slab thickness is fixed at 90 nm as this is a standard etch depth available in most fabrication processes. The waveguide widths of 500 and 600 nm were chosen from mode simulation results showing the largest $\delta n_{eff}/\delta V$ while maintaining near single-mode operation. The separation between the waveguide core edge and the highly doped contact regions is the first variable in these simulations as reduced separation will have an impact on many factors, namely α, which will affect $H_t(\omega_m)$ through τ_l. The self-coupling coefficient, r, is the second variable as for any given α, r can be adjusted to determine the ideal coupling condition to maximize GBW since it is tied to $H_t(\omega_m)$ indirectly by μ. Lastly, the wavelength detuning, δ, is varied as it will affect $H_t(\omega_m)$ through $\Delta\omega$. The ring is assumed to have 100% coverage of the p-n junction across the ring to simplify the calculations. Since the dominant waveguide loss is due to the p-n junction doping, scaling the coverage can be approximated by equivalently scaling α as well as the voltage-dependent properties $\delta(1/\tau)/\delta V$ and $\delta n_{eff}/\delta V$. The ring cavity is a radius of 15 µm, large enough to avoid bending losses at both 1550 and 2000 nm wavelengths. Scattering loss due to sidewall roughness is ignored as the doping loss is dominant. The driving voltage is fixed at V_{pp} = 2.5 V which is a common driving voltage supplied by measurement equipment and

readily available integrated drivers.

$H_t(\omega_m)$ was then calculated as a function of resonance detuning, and from it, device bandwidth is obtained by locating the frequency where $H_t(\omega_m)$ decreases by 3 dB. Figure 2.22 a) and Figure 2.22 b) show the normalized curves of $H_t(\omega_m)$ for a MRR modulator with a 500 and 600 nm wide waveguide at 1550 and 2000 nm wavelength, respectively, for several wavelength detunings. The contact-doping separation is 2000 nm, the device is biased to 0.5 V, and the self-coupling coefficient is tuned to the value which yields the largest gain-bandwidth product (determined later) at a bias of 0.5 V. Both rings are in an over-coupled state.

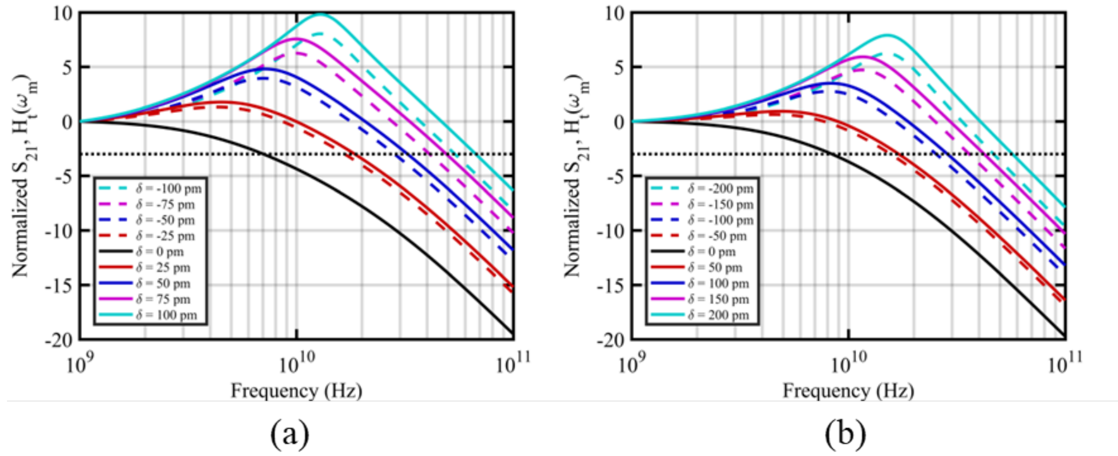

FIGURE 2.22: Normalized $H_t(\omega_m)$ for a) 1550 nm wavelength modulator with a width of 500 nm, doping separation of 500 nm and $r = 0.977$, and b) 2000 nm wavelength modulator with a width of 600 nm, doping separation of 800 nm and $r = 0.975$.

In these configurations, optical peaking begins to occur while detuning away from resonance with either positive or negative detuning and, as previously mentioned, the presence of dynamic waveguide losses gives rise to asymmetry in the optical peaking enhancement for equal positive and negative detunings. Arbitrary detunings were chosen for both modulators to remain within normalized optical power transmissions below -1

dB. It is evident that larger detuning is required in a 2000 nm wavelength modulator to achieve similar bandwidth enhancements as the 1550 nm wavelength modulator due to the larger $FWHM$ when operating at longer wavelengths. The dashed line indicates the 3 dB bandwidths where the normalized $H_t(\omega_m)$ curves drop from their initial value by half. By extracting the 3 dB bandwidth from $H_t(\omega_m)$, we can visualize the detuning trend more clearly. Figure 2.23 a) and Figure 2.23 b) show the 3 dB bandwidths from Figure 2.22 a) and b) as a function of resonance detuning for several reverse bias voltages.

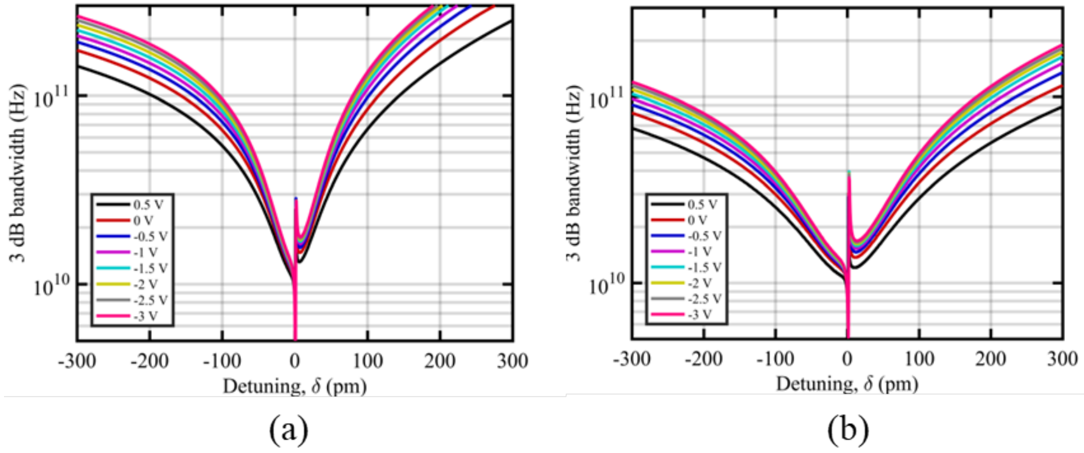

FIGURE 2.23: Extracted 3 dB bandwidth for a) 1550 nm modulator configuration with $r = 0.977$ and b) 2000 nm modulator configuration with $r = 0.975$.

At both wavelengths, increasing reverse bias results in a bandwidth increase. The bandwidth continues to increase for each bias with detuning, but it is known that the modulation efficiency begins to suffer with excessive detuning. Near resonance (zero detuning), the bandwidth appears unstable though G_{DC} will tend to zero near resonance which will produce a GBW product near zero as well, thus it is of no concern. G_{DC}, calculated using (2.35), is shown in Figure 2.24 a) and b) for 1550 and 2000 nm wavelength modulator configurations, respectively, as a function of detuning for several biases.

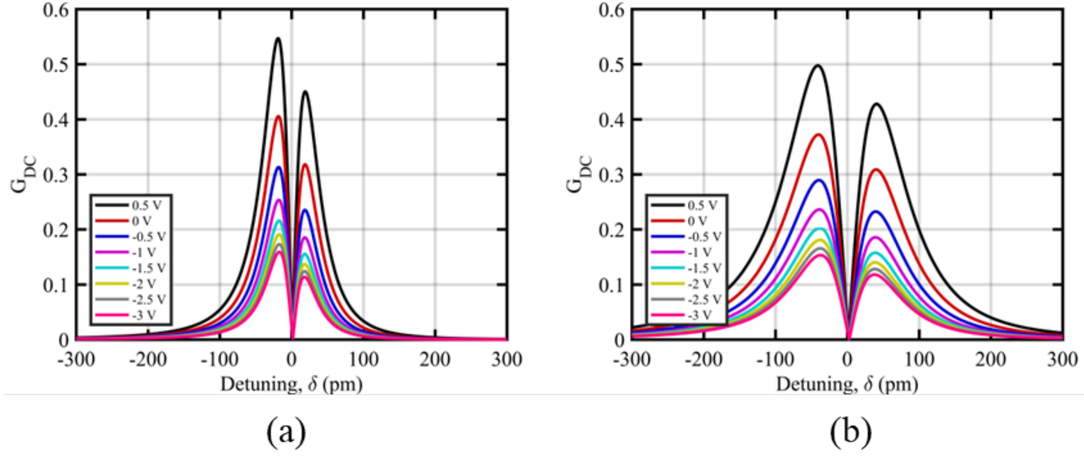

FIGURE 2.24: G_{DC} for a) 1550 nm modulator configuration with $r = 0.977$ and b) 2000 nm modulator configuration with $r = 0.975$.

The modulation efficiency has one maximum on both blue- and red-side detuning and begins to decrease with further detuning. We also see that higher reverse bias voltages result in decreased modulation efficiency, largely due to the decrease in $\delta n_{eff}/\delta V$ as reverse bias increases. Finally, the GBW product is calculated, shown in Figure 2.25 a) and b) for 1550 and 2000 nm wavelength modulator configurations, respectively, as a function of detuning for several biases.

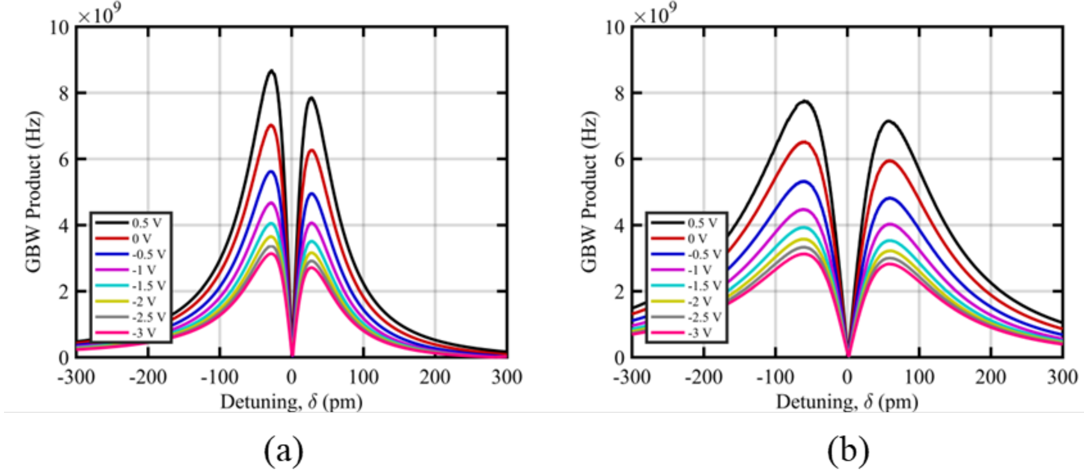

FIGURE 2.25: GBW product for a) 1550 nm modulator configuration with $r = 0.977$ and b) 2000 nm modulator configuration with $r = 0.975$.

The maxima on the blue- and red-side detuning indicate the ideal detuning to maximize the balance modulation efficiency and speed. GBW product on the blue-side of resonance is higher than the red-side in both instances, which appears to occur for all self-coupling coefficient values of $r \leq a$, i.e. over-coupled rings, and some values of r just above a, regardless of doping separation. This same behaviour occurs with the associated values of G_{DC} while the opposite trend was observed in the associated 3 dB bandwidth. The maximum GBW product for the 1550 nm wavelength modulator configuration is higher than that of the 2000 nm configuration, on both the blue- and red-side of resonance, however, the apexes in the latter case are more stable and resilient to variations in detuning which may arise from thermal fluctuations. To explore the parameter space further, detunings which result in the maximum GBW product (GBW_{max}) are determined on both blue- and red-side of resonance sweeping values of the self-coupling coefficient, r, (only one value for each modulator has been presented thus far) to determine GBW_{max} behaviour for different coupling conditions. Figure 2.26 a) and b) show GBW_{max} values on the blue-side of resonance for 1550 and 2000 nm wavelengths calculated at each r for various contact-doping separation values at a bias of 0.5 V.

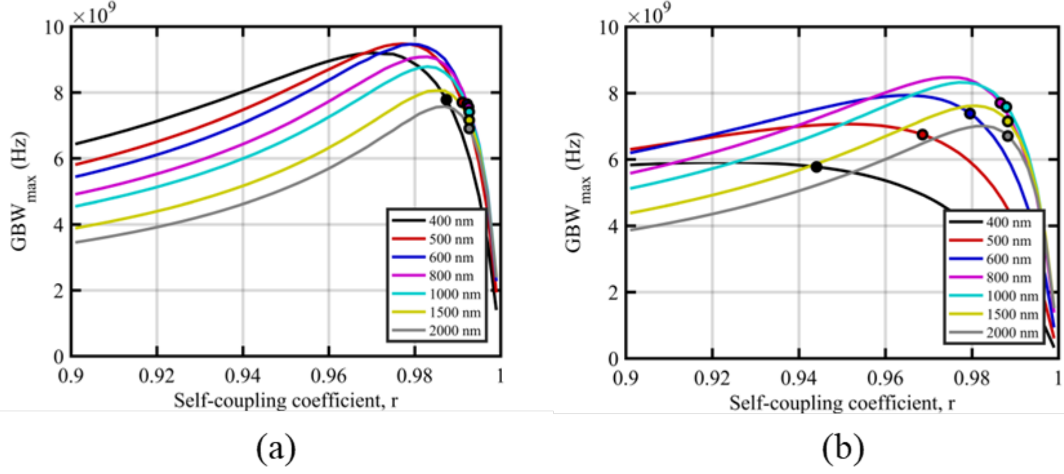

FIGURE 2.26: Blue-side modulation GBW_{max} for 0.5 V bias in a a) 1550 nm wavelength modulator configuration and b) 2000 nm configuration. Markers indicate critical-coupling point.

The largest value of maximum GBW_{max} for the 1550 nm wavelength modulator configuration occurs at a doping separation of 500 nm, while it occurs for the 2000 nm wavelength configuration at a separation of 800 nm, with corresponding values 9.46×10^9 and 8.47×10^9 Hz, respectively. Although lower for the 2000 nm wavelength, it should be noted that there is a higher tolerance for achieving the appropriate self-coupling coefficient to achieve the highest value of GBW_{max} for a given doping separation. The critical-coupling point for each of these curves, depicted by markers, exists toward higher values of r than at the highest GBW_{max}, thus highest GBW_{max} is achieved in the over-coupled condition. Figure 2.27 a) and b) show the maximum GBW_{max} values again, this time on the red-side of resonance.

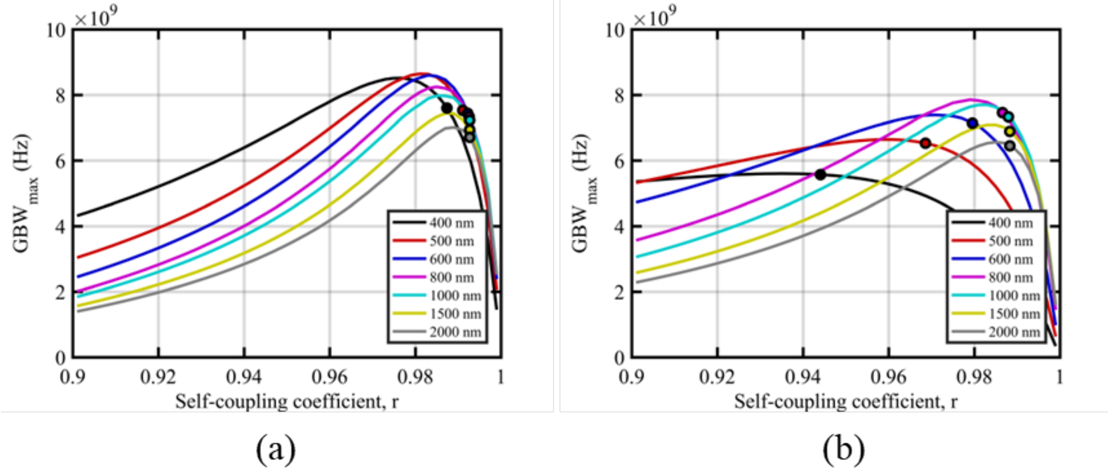

FIGURE 2.27: Red-side modulation GBW_{max} at 0.5 V bias for the a) 1550 nm wavelength modulator configuration and b) 2000 nm wavelength configuration. Markers indicate critical-coupling points.

The highest maximum GBW values are reduced to 8.64×10^9 and 7.86×10^9 Hz for 1550 and 2000 nm wavelength configurations, but occur at the same contact-doping separations as in the case of blue-side modulation. Comparing Figure 2.26 and Figure 2.27, there does not appear to be any immediate benefit to operating on the red-side of resonance from a GBW point of view, but it should be reiterated that the TPA coefficient at 2000 nm wavelength is a factor of 3 lower than 1550 nm making it more feasible to operate on the red-side at sufficiently low powers. By taking the largest values of GBW_{max} from Figure 2.26 and Figure 2.27, we can plot G_{DC} (Figure 2.28) and 3 dB bandwidth (Figure 2.29) as a function of contact-doping separation.

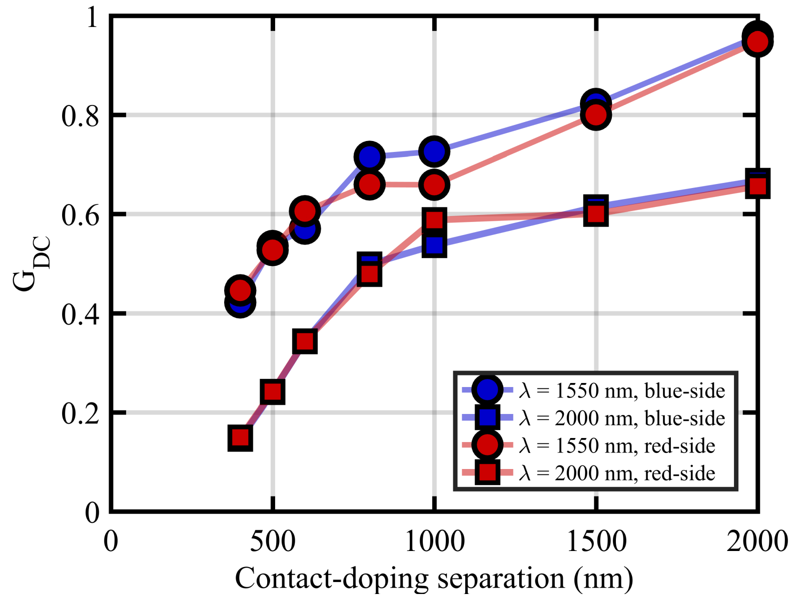

FIGURE 2.28: G_{DC} at highest values of GBW_{max}.

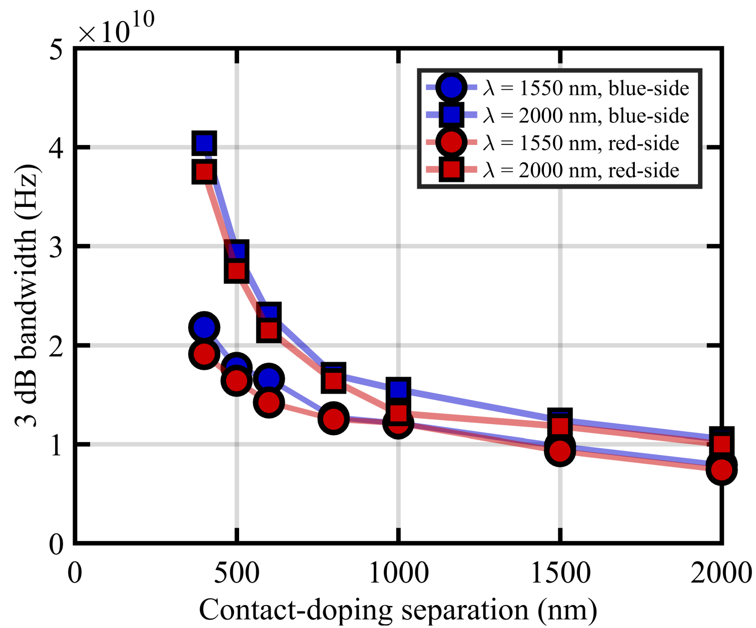

FIGURE 2.29: 3 dB bandwidths at highest values of GBW_{max}.

From these figures we see a few general trends. Firstly, G_{DC} for each doping separation is lower at 2000 nm wavelength for both blue- and red-side modulation, and larger

contact-doping separations have higher values of G_{DC}. This is countered by the higher 3 dB bandwidth of 2000 nm wavelength and the increased 3 dB bandwidth toward smaller contact-doping separations, likely due to the decrease in photon cavity lifetime as parasitic loss increases. If we compare the optimal (highest global values of GBW_{max}) contact-doping separations of 500 and 800 nm for 1550 and 2000 nm wavelengths, respectively, we ultimately see very similar performance in G_{DC}, and 3 dB bandwidth, but with the aforementioned improved detuning stability of operating at longer wavelengths in a MRR modulator structure.

At this point it must be stressed that the GBW product is a figure-of-merit directed toward small-signal analysis. In such a test environment, the applied signals are small enough to elicit an effectively linear response from the device; however, MRR modulators are inherently nonlinear in their transfer function, thus the GBW as a figure-of-merit does not adequately extend to large driving signals [27]. All of the previously discussed performance metrics, both steady-state and dynamic, are important when considering the design and operation of MRR modulators for high-speed applications.

2.6 Conclusion

This chapter presented a comprehensive theoretical examination of high-speed SOI MRR modulator design considerations when optimizing operation for TDFA-band wavelengths as well as a theoretical performance comparison between MRR modulators designed for EDFA- and TDFA-band wavelengths under similar specifications (radius, doping concentrations, silicon thickness, etc.).

Both wavelength regimes are explored for fundamental properties of the waveguide, upon which more complex devices are built. Of the basic waveguide properties, reduced waveguide confinement at longer wavelengths leads to smaller effective and group indices

in both strip and ridge waveguides. Ultimately, this smaller confinement at longer wavelengths reduces mode interaction with the silicon which negatively affects DC modulation performance in *p-n* junction waveguide modulators but also serves to reduce detrimental effects which impact resonance stability in MRR-based devices, such as TPA which can lead to self-heating. Additionally, the TPA coefficient at 2000 nm wavelength is approximately 3 times lower than at 1550 nm, further mitigating the effects of self-heating further and allowing for the possibility of red-side resonance modulation (such as in BPSK-type systems) at sufficiently low powers.

The free-carrier effect is approximately 1.7 times stronger at a wavelength of 2000 nm as compared with 1550 nm. This implies more efficient free-carrier modulation in *p-n* junction waveguide modulators, although at waveguide widths optimized for each wavelength regime and similar doping profiles, $\delta n_{eff}/\delta V$ is only 1.27 times stronger at 2000 nm wavelength due to the reduced waveguide confinement. Electrically, the *p-n* junction in the larger width waveguide at this wavelength presents a reduced f_{RC}, but not significantly.

MRR modulator transfer function metrics were examined and show that operating at longer wavelengths causes an increase in $FWHM$ which necessitates larger blue-side resonance detuning in order to achieve similar on-off ER performance at shorter wavelengths as well as higher IL and TP at these detunings. The phase response is similarly broadened at longer wavelengths, requiring larger voltage-swings to achieve a π phase-shift for use in BPSK systems and resulting in higher IL at the associated equal-transmission operating points as compared to shorter wavelengths.

The higher static and dynamic free-carrier absorption at longer wavelengths results in decreased photon cavity lifetime in the MRR modulator which increases f_Q, although this estimated bandwidth is further complicated by the effect of optical peaking which demonstrates enhanced bandwidths in MRR modulators for non-zero detuning. The

impact of optical peaking is determined through the use of a small-signal modulation model which shows reduced G_{DC} and bandwidth performance as compared with the 1550 nm wavelength MRR configuration, however, there is increased resonance stability of the detuning required to maintain a maximum GBW product in the case of the 2000 nm wavelength configuration; that is to say, perturbations in resonance detuning due to thermal fluctuations will not have as severe a performance impact as it would in the former case.

TDFA-band MRR modulators in the context of this analysis may operate with reduced DC and high-speed performance as compared with EDFA-band MRR modulators, but this reduction is far from prohibitive for telecommunication applications. Furthermore, the reduced TPA coefficient at longer wavelengths mitigates the effects of self-heating during red-side modulation which makes them more attractive for BPSK-type systems.

Bibliography

[1] L. Chrostowski and M. Hochberg, *Silicon Photonics Design.* Cambridge: Cambridge University Press, 2015.

[2] B. J. Frey, D. B. Leviton, and T. J. Madison, “Temperature-dependent refractive index of silicon and germanium,” E. Atad-Ettedgui, J. Antebi, and D. Lemke, Eds., jun 2006, p. 62732J.

[3] C. Klitis, M. Sorel, and M. J. Strain, “Active On-Chip Dispersion Control Using a Tunable Silicon Bragg Grating,” *Micromachines*, vol. 10, no. 9, p. 569, aug 2019.

[4] Z. Wang, Y. Gao, A. S. Kashi, J. C. Cartledge, and A. P. Knights, “Silicon Microring Modulator for Dispersion Uncompensated Transmission Applications,”

Journal of Lightwave Technology, vol. 34, no. 16, pp. 3675–3681, aug 2016.

[5] N. MacSuibhne *et al.*, "Wavelength Division Multiplexing at 2μm," in *European Conference and Exhibition on Optical Communication.* Washington, D.C.: OSA, 2012, p. Th.3.A.3.

[6] M. N. Petrovich *et al.*, "Demonstration of amplified data transmission at 2 μm in a low-loss wide bandwidth hollow core photonic bandgap fiber," *Optics Express*, vol. 21, no. 23, p. 28559, nov 2013.

[7] D. Mueller, J. A. West, and K. W. Koch, "Interferometric chromatic dispersion measurement of a photonic bandgap fiber," in *Active and Passive Optical Components for WDM Communications II*, A. K. Dutta, A. A. S. Awwal, N. K. Dutta, and K. Okamoto, Eds., vol. 4870. International Society for Optics and Photonics, jul 2002, p. 395.

[8] Y. Kim, M. Takenaka, T. Osada, M. Hata, and S. Takagi, "Strain-induced enhancement of plasma dispersion effect and free-carrier absorption in SiGe optical modulators," *Scientific Reports*, vol. 4, no. 1, p. 4683, may 2015.

[9] C. Monat *et al.*, "Slow Light Enhanced Nonlinear Optics in Silicon Photonic Crystal Waveguides," *IEEE Journal of Selected Topics in Quantum Electronics*, vol. 16, no. 1, pp. 344–356, 2010.

[10] R. A. Soref and B. R. Bennett, "Electrooptical effects in silicon," *IEEE Journal of Quantum Electronics*, vol. 23, no. 1, pp. 123–129, jan 1987.

[11] M. Nedeljkovic, R. Soref, and G. Z. Mashanovich, "Free-carrier electrorefraction and electroabsorption modulation predictions for silicon over the 1-14-μm infrared wavelength range," *IEEE Photonics Journal*, vol. 3, no. 6, pp. 1171–1180, dec 2011.

[12] H. Yu, D. Ying, M. Pantouvaki, J. Van Campenhout, P. Absil, Y. Hao, J. Yang, and X. Jiang, "Trade-off between optical modulation amplitude and modulation bandwidth of silicon micro-ring modulators," *Optics Express*, vol. 22, no. 12, p. 15178, jun 2014.

[13] M. Xin, C. E. Png, and A. J. Danner, "Breakdown delay-based depletion mode silicon modulator with photonic hybrid-lattice resonator," *Optics Express*, vol. 19, no. 6, p. 5063, mar 2011.

[14] D. Chaturvedi and A. Kumar, "Impact of Free Carriers on Modulational Instability in Silicon-on-insulator Nanowaveguides," jun 2016.

[15] E. Dulkeith, Y. A. Vlasov, X. Chen, N. C. Panoiu, and R. M. Osgood, Jr., "Self-phase-modulation in submicron silicon-on-insulator photonic wires," *Optics Express*, vol. 14, no. 12, p. 5524, jun 2006.

[16] Z. Wang, D. J. Paez, L. Dow, and A. P. Knights, "Intrinsic resonance stabilization in depletion-type silicon micro-ring modulators," in *2017 IEEE 14th International Conference on Group IV Photonics (GFP)*. IEEE, aug 2017, pp. 35–36.

[17] X. Liu, J. B. Driscoll, J. I. Dadap, R. M. Osgood, S. Assefa, Y. A. Vlasov, and W. M. J. Green, "Self-phase modulation and nonlinear loss in silicon nanophotonic wires near the mid-infrared two-photon absorption edge," *Optics Express*, vol. 19, no. 8, p. 7778, apr 2011.

[18] A. D. Bristow, N. Rotenberg, and H. M. van Driel, "Two-photon absorption and Kerr coefficients of silicon for 850-2200nm," *Applied Physics Letters*, vol. 90, no. 19, p. 191104, may 2007.

[19] P. J. Foster, J. K. Doylend, P. Mascher, A. P. Knights, and P. G. Coleman, "Optical attenuation in defect-engineered silicon rib waveguides," *Journal of*

Applied Physics, vol. 99, no. 7, p. 073101, apr 2006.

[20] B. G. Streetman and S. Banerjee, *Solid state electronic devices.* Prentice Hall., 2016.

[21] M. A. Seyedi, C.-H. J. Chen, M. Fiorentino, and R. G. Beausoleil, "Data rate enhancement of dual silicon ring resonator carrier-injection modulators by PAM-4 encoding," in *2015 International Conference on Photonics in Switching (PS)*. IEEE, sep 2015, pp. 363–365.

[22] M. Shin, Y. Ban, B.-M. Yu, M.-H. Kim, J. Rhim, L. Zimmermann, and W.-Y. Choi, "A Linear Equivalent Circuit Model for Depletion-Type Silicon Microring Modulators," *IEEE Transactions on Electron Devices*, vol. 64, no. 3, pp. 1140–1145, mar 2017.

[23] G. Li, X. Zheng, J. Yao, H. Thacker, I. Shubin, Y. Luo, K. Raj, J. E. Cunningham, and A. V. Krishnamoorthy, "25Gb/s 1V-driving CMOS ring modulator with integrated thermal tuning," *Optics Express*, vol. 19, no. 21, p. 20435, oct 2011.

[24] X. Tu, T.-Y. Liow, J. Song, X. Luo, Q. Fang, M. Yu, and G.-Q. Lo, "50-Gb/s silicon optical modulator with traveling-wave electrodes," *Optics Express*, vol. 21, no. 10, p. 12776, may 2013.

[25] D. A. B. Miller, "Energy consumption in optical modulators for interconnects," *Optics Express*, vol. 20, no. S2, p. A293, mar 2012.

[26] W. Bogaerts, P. De Heyn, T. Van Vaerenbergh, K. De Vos, S. Kumar Selvaraja, T. Claes, P. Dumon, P. Bienstman, D. Van Thourhout, and R. Baets, "Silicon microring resonators," *Laser & Photonics Reviews*, vol. 6, no. 1, pp. 47–73, jan 2012.

[27] S. Karimelahi, "Silicon Ring Modulators for High-speed Optical Interconnects," Ph.D. dissertation, University of Toronto, 2016.

[28] B. Little, S. Chu, H. Haus, J. Foresi, and J.-P. Laine, "Microring resonator channel dropping filters," *Journal of Lightwave Technology*, vol. 15, no. 6, pp. 998–1005, jun 1997.

[29] Z. Wang and A. P. Knights, "Dual-ring-assisted MZI silicon modulator for enhanced intensity modulation," in *2016 IEEE 13th International Conference on Group IV Photonics (GFP)*. IEEE, aug 2016, pp. 88–89.

[30] T. Ye, Y. Zhou, C. Yan, Y. Li, and Y. Su, "Chirp-free optical modulation using a silicon push-pull coupling microring," *Optics Letters*, vol. 34, no. 6, p. 785, mar 2009.

[31] D. Petousi, L. Zimmermann, K. Voigt, and K. Petermann, "Performance Limits of Depletion-Type Silicon Mach-Zehnder Modulators for Telecom Applications," *Journal of Lightwave Technology*, vol. 31, no. 22, pp. 3556–3562, nov 2013.

[32] J. Müller, F. Merget, S. S. Azadeh, J. Hauck, S. R. García, B. Shen, and J. Witzens, "Optical Peaking Enhancement in High-Speed Ring Modulators," *Scientific Reports*, vol. 4, no. 1, p. 6310, may 2015.

[33] Q. Xu, S. Manipatruni, B. Schmidt, J. Shakya, and M. Lipson, "125 Gbit/s carrier-injection-based silicon micro-ring silicon modulators," *Optics Express*, vol. 15, no. 2, p. 430, jan 2007.

[34] X. Xiao, X. Li, H. Xu, Y. Hu, K. Xiong, Z. Li, T. Chu, J. Yu, and Y. Yu, "44-Gb/s Silicon Microring Modulators Based on Zigzag PN Junctions," *IEEE Photonics Technology Letters*, vol. 24, no. 19, pp. 1712–1714, oct 2012.

[35] Q. Xu, B. Schmidt, J. Shakya, and M. Lipson, “Cascaded silicon micro-ring modulators for WDM optical interconnection,” *Optics Express*, vol. 14, no. 20, p. 9431, oct 2006.

Chapter 3

Mechanisms for optical loss in SOI waveguides for mid-infrared wavelengths around 2 μm

Preface

The following chapter presents various optical loss mechanisms which are important to consider in the design of silicon photonic devices and systems. These loss mechanisms are particularly crucial in the design of a micro-ring resonator modulator as its spectral properties depend heavily on balancing the anticipated amount of light coupled into the ring with an accurate estimate of the round-trip loss. While these loss mechanisms are frequently measured and modelled for erbium doped fiber amplifier (EDFA)-band wavelengths centered near 1550 nm, it has been relatively unexplored in thulium doped fiber amplifier (TDFA)-band wavelengths centered near 1970 nm.

Advantages of designing silicon photonic devices and circuits for one wavelength

regime versus the other often hinge on factors as simple as optical loss. For example, Section 3.3.1 demonstrates that waveguides with appropriate geometry for 2000 nm wavelength on a 220 nm silicon-on-insulator (SOI) platform will experience less optical scattering due to waveguide sidewall roughness than 1550 nm wavelength in a waveguide with its appropriate geometry. In long waveguide circuits, such as optical delay lines, this reduction in optical loss may be advantageous in a photonic circuit with a tight power budget. This chapter also demonstrates potential pitfalls when designing for the TDFA-band on an SOI platform, as compared with the EDFA-band. Section 3.3.1 demonstrates that larger buried oxide (BOX) thickness must be used to mitigate loss due to substrate leakage. Similarly, section 3.3.2 shows that in ring resonators, which are discussed throughout the thesis, a larger bend radius is required to mitigate loss from coupling to radiation modes. For several of the loss mechanisms considered, analytic and / or simulated modelling is performed and compared with measured data to validate the predictions and use of these models at extended wavelengths. Section 3.3.3 explores the enhanced optical loss due to free-carriers at longer wavelengths which is a major driving force in modulator design for high-speed TDFA-band telecommunications. The free-carrier loss measurements are used to further validate an empirical model which is used in subsequent chapters and was used in the design and / or modelling of all active TDFA-band devices throughout the thesis. Section 3.3.4 investigates the optical loss due to intentionally introduced defects, which are integral in the operation of the defect-mediated detector used in Chapter 5. A discrepancy between measured and analytically modelled defect-related loss, implying the model requires improvement to adequately predict performance at extended wavelengths.

By investigating the loss properties of fabricated test structures at TDFA-band wavelengths on a globally standard 220 nm SOI platform, we also demonstrate the feasibility of using standard CMOS fabrication techniques to create passive TDFA-band devices

for use in active structures including variable optical attenuators, modulators, and detectors. Despite the non-ideal thickness of 220 nm SOI for longer wavelengths, these measurements adequately show its viability for use at these wavelengths.

David E. Hagan, and Andrew P. Knights

McMaster University, 1280 Main Street West, Hamilton, ON, Canada

This paper was published in the *Journal of Optics* on December 19, 2016.

DOI: 10.1088/2040-8986/19/2/025801

Abstract

We report the measurement of optical loss in submicron silicon-on-insulator waveguides at a wavelength of 2.02 μm for the fundamental TE mode. Devices were fabricated at IMEC and at A*STAR's Institute of Microelectronics (IME) and thus these measurements are applicable to studies which require fabrication using standard foundry technology. Propagation loss for strip and rib waveguides of 3.3 ± 0.5 and 1.9 ± 0.2 dB/cm were measured. Waveguide bending loss in strip and rib waveguides was measured to be 0.36 and 0.68 dB per 90° bend for a radius of 3 μm. Doped waveguide loss in rib waveguides was measured for both *n*-type and *p*-type species at two doping densities for each doping type. Measured results from propagation, bending, and free-carrier loss were found to be in good agreement with analytical or numerical models. Loss due to lattice defects introduced by ion-implantation is found to be underestimated by a previously proposed empirical model. The thermal annealing of the lattice defects is consistent with removal of the silicon divacancy.

3.1 Introduction

The mid-infrared wavelength regime continues to evolve as a topic of interest for silicon photonics research [1], [2], [3], [4]. Applications in this extended wavelength regime include chemical and biological sensing, environmental monitoring, and spectroscopy. Also, with the advent of the thulium-doped fibre amplifier [5] and advances in silicon-on-insulator (SOI) based modulation [6] and detection [7], a spectral window centred around 2 μm has become a promising region for future telecommunication infrastructure. The opening of new wavelength bands is seen as an attractive route to addressing the impact of the capacity crunch anticipated as a result of the exponential increase in demand for bandwidth [8]. Although several device platforms such as silicon-on-sapphire [9] or germanium-on-silicon [10] are preferred for certain mid-infrared wavelength windows, SOI remains optimal for wavelengths up to 2.5 μm and from 3 to 3.6 μm, outside of which the SiO_2 cladding begins to act as an absorber [11].

A wealth of silicon photonic devices, which have been created in SOI for the traditional telecommunication O, C and L wavelength bands, can be translated for operation to the mid-infrared with an appropriate change in waveguide geometry. Further, certain wavelength-dependent properties of SOI waveguides make longer wavelengths desirable; for instance, reduced sidewall scattering [12] and increased free-carrier interaction [13]. High-contrast submicron waveguides such as those fabricated in SOI experience significant interaction between the propagating optical mode and the waveguide sidewalls, often the cause of excess optical loss due to sidewall roughness. This problem is mitigated at longer wavelengths due to the decrease of scattering which is related to wavelength as λ^{-4}. Waveguides doped with impurities exhibit excess absorption and reduced refractive index from free-carrier interactions described by the plasma dispersion relations. These interactions, related to wavelength as λ^2, are enhanced at longer wavelengths leading to stronger electro-absorption and electro-refraction.

In this paper, we report the design and characterization of single-mode SOI waveguides fabricated in standard silicon foundries. These waveguides form the building blocks of SOI devices suitable for communication links in a 2 μm centred window. We examine propagation loss, bending loss and free-carrier absorption. Additionally, we examine the optical absorption induced by the introduction of lattice defects in the SOI waveguide, a mechanism which forms the basis for optical detection at high-speed [7]. Experimental results are compared to analytical models with generally good agreement observed.

3.2 Experimental

3.2.1 Design and fabrication

All waveguides for this work were designed for single mode operation. Devices used to measure undoped and defect-implanted waveguide propagation loss and bending loss were fabricated at IMEC using 200 mm SOI wafers with 220 nm thick silicon on a 2 μm buried oxide (BOX) utilizing 193 nm DUV lithography. The BOX is sufficiently thick to render substrate leakage loss negligible. The silicon waveguide is clad with a 1.25 μm thick oxide. Structures were patterned with photoresist and etched using ICP-RIE technology. Strip waveguides were fabricated through a full etch to the BOX while rib waveguides were fabricated through a partial etch leaving a nominal 50 nm thick silicon slab. The resulting core dimensions for the strip and rib waveguides of 530×220 nm and 560×220 nm, respectively, satisfying the single TE-mode condition for the 2 μm wavelength of interest.

In order to couple light into and out of test structures, shallow-etch focused grating couplers, described previously in reference [14], were placed on either end of each test structure. The pitch and etch depth were 1.1 μm and 150 nm, as required for use at wavelengths centred around 2 μm.

The cut-back method was employed to measure the transmission through multiple structures of varying length allowing the extrapolation of the waveguide propagation loss via linear regression. Longer waveguide lengths required folded geometries including bends (R_{min} = 15 µm) for which losses are assumed to be negligible. This assumption is justified elsewhere in this submission. Multiple chips were measured to reduce random error.

Similar waveguide structures as described above were subjected to high-energy (900 keV) B^+ ion implantation to introduce lattice defects. Samples were implanted using the 1.25 µm thick top oxide as an implant screen. Implantation doses (Q) were varied for each chip such that Q = 1, 3, 6, 10, or 15×10^{12} cm^{-2}. The waveguides implanted with doses of 6 and 15×10^{12} cm^{-2} were subjected to subsequent, sequential thermal annealing at 50 °C intervals for 5 minutes in the range 100 to 400 °C with propagation loss measurements performed after each interval.

S-bend structures with multiple 90 degree bends of varying radii were designed to measure waveguide bend loss. This method uses forty bends to exacerbate the loss and assumes extra propagation distance between S-bends incurs negligible loss. Bend radii (R) were varied such that R = 3, 4, 5, 10, 15, or 30 µm. Multiple chips were measured for each radii to reduce random error.

Devices used to measure doped waveguide propagation loss were fabricated at A*STAR's IME (hereafter simply denoted as IME) on 200 mm SOI wafers with 220 nm thick silicon on a 2 µm BOX using 248 nm DUV lithography. Rib waveguides were fabricated through a partial etch leaving a nominal 90 nm thick silicon slab. In this case, the grating coupler pitch and etch depth were 1 µm and 130 nm. The core dimensions of 600×220 nm satisfy the single TE-mode condition for the 2 µm wavelength of interest.

During the fabrication process, windows were patterned on sections of rib waveguide

devices, with n-type (phosphorus) or p-type (boron) dopants introduced via ion implantation and activated through thermal annealing. Doped waveguide propagation loss was measured via the cut-back method described previously.

3.2.2 Loss measurement

The individual chips were mounted on an XYZ translation stage. Light from a Fabry-Pérot EP2020-FP series laser diode with a central wavelength of 2.02 μm was fibre-coupled in and out of grating structures of the device under test (DUT), using Thorlabs PM2000 polarization maintaining (PM) fibres on angled arms mounted on individual XYZ translation stages with XY micrometers for precision alignment. The laser was powered and thermally stabilized by a Newport 6000 combination laser diode driver and temperature controller. The laser diode was driven with 60 mA of current and thermally stabilized at 20 °C with a corresponding output optical power of approximately 4 mW to which all measurements in dB are normalized. The output optical power was measured using a Thorlabs PDA10D InGaAs detector. The coupling angle was optimized for maximum transmission corresponding to a measured system loss of approximately 26 dB.

3.3 Results and discussion

3.3.1 Waveguide propagation loss

Waveguide transmission is plotted in figure 3.1 (a) for the fundamental TE mode in both strip and rib waveguide geometries for lengths varying from 0.29 to 0.69 cm. The bend radii and number of bends between structures was held constant to ensure extrapolated loss was predominantly due to propagation.

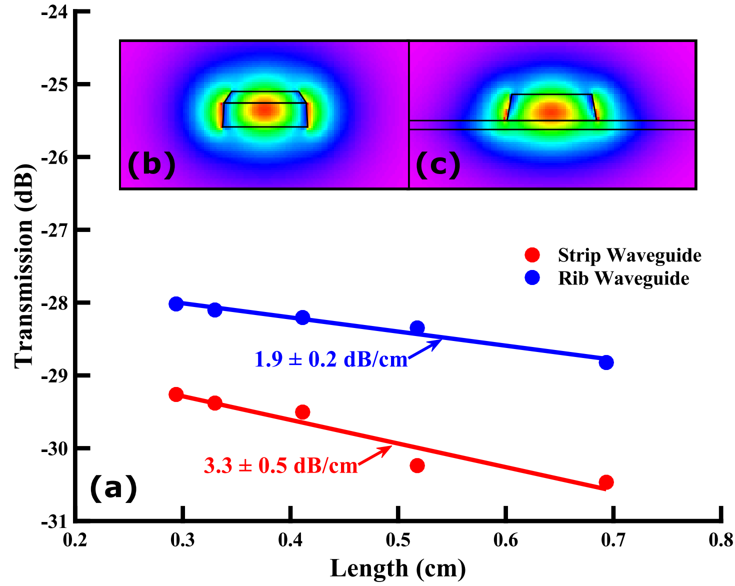

FIGURE 3.1: (a) Transmitted power for various waveguide lengths in passive strip and rib waveguides for the fundamental TE mode. Data were fit using linear regression to extract waveguide propagation loss. Inset: Mode profiles for fabricated strip (b) and rib (c) waveguides.

It is assumed that sidewall roughness is identical for all waveguides and between chips (fabricated on the same wafer). The standard deviation of the measured transmission of three identical devices (on three separate chips) was calculated to examine repeatability. For waveguide lengths (L) of L = 0.29, 0.33, 0.41, 0.52, and 0.69 cm, the standard deviation σ of transmitted power for strip and rib waveguides are σ_{strip} = 0.10, 0.18, 0.16, 0.50, and 0.3 dB and σ_{rib} = 0.12, 0.20, 0.25, 0.16, and 0.31 dB respectively. Linear fitting of the measured transmission data gives propagation loss (α) for strip and rib waveguides of $\alpha_{strip} = 3.3 \pm 0.5$ dB/cm and $\alpha_{rib} = 1.9 \pm 0.2$ dB/cm respectively with the associated uncertainty calculated as the standard error of regression.

The main source of propagation loss in SOI waveguides is due to scattering from sidewall roughness introduced through vertical etching during fabrication. This scattering is dependent on mode confinement determined by waveguide width. Wide waveguides will

confine the fundamental mode such that there is a relatively low electric-field overlap with the sidewall roughness; however, if the waveguide is excessively wide, it will support higher-order modes. The strip waveguide geometry supports single mode propagation for widths up to 680 nm. As the waveguide becomes narrower, the mode becomes less confined increasing electric-field overlap with the sidewalls, up to a maximum value. Beyond this point, the mode exists mostly in the cladding. Sidewall scattering in dielectric slab waveguides was investigated by Marcuse [15] and a simplified analytic model was developed from this by Payne and Lacey [12]. This model has also been applied to 3-D strip [16], [17], [18] and rib [19] SOI waveguides. The sidewall scattering loss α_s in dB per unit length can be calculated from:

$$\alpha_s = 4.34 \frac{\sigma^2}{\sqrt{2} k_o d^4 n_1} g \cdot f, \tag{3.1}$$

where σ^2 is the mean square deviation of sidewall roughness, k_o is the free-space wave vector, d is the waveguide half-width, and n_1 is the refractive index of the waveguide core. The expression g is determined by waveguide geometry and material, while f is additionally determined by the correlation length (L_C) of the sidewall roughness. Both σ and L_C are typically measured through scanning-electron microscopy (SEM), or atomic force microscopy (AFM) of a waveguide with no top-cladding. We apply the Payne-Lacey model in figure 3.2 to examine the fundamental TE mode sidewall scattering loss in a strip waveguide with dimensions 530×220 nm for propagation wavelengths of 2.02 and 1.55 µm (for comparison) at various values of σ and L_C.

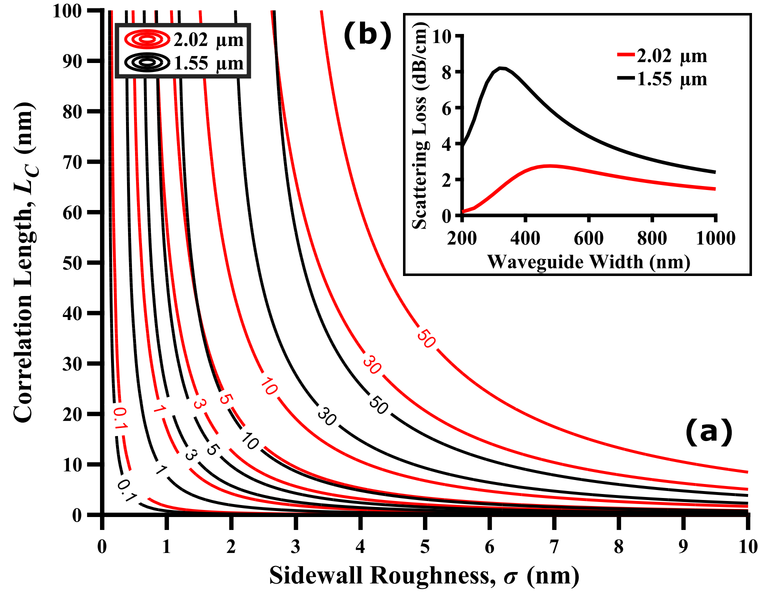

FIGURE 3.2: (a) Waveguide sidewall scattering loss contours (dB/cm) for 2.02 µm (red) and 1.55 µm (black) wavelengths for the fundamental TE mode in a strip waveguide with dimensions 530×220 nm. (b) Scattering loss as a function of waveguide width for $\sigma = 1$ nm and $L_C = 50$ nm.

Previously reported sidewall roughness and correlation length appear to vary with fabrication process [19] as well as measurement technique [20]. For SOI fabrication methods similar to those used here, sidewall roughness is on the order of 1 to 2 nm [18], [19], while sub nanometer roughness can be obtained through smoothing techniques [17]. Similarly, a reasonable value for correlation length is approximately 50 nm [18], [21]. Values of $\sigma = 1$ nm and $L_C = 50$ nm show that the scattering loss at 2.02 µm wavelength is lower across a large range of waveguide widths for a waveguide height of 220 nm. For the fabricated width of 530 nm (used here), the Payne-Lacey model predicts that for $L_C \lesssim 300$ nm, sidewall-scattering loss at 2.02 µm wavelength will always be less than that for 1.55 µm, and for $L_C \lesssim 250$ nm, this holds for all widths. Propagation loss in a rib waveguide (shown in figure 3.1) was measured to be lower than that of a strip waveguide as one might expect. The relative reduction in loss can be attributed to the partially-etched sidewalls and mode confinement in the slab both acting to reduce

the effective mode overlap with the sidewall roughness. As waveguide cross-sectional area decreases, the mode spot size and resulting evanescent coupling to the substrate will both increase [22]. Despite these concerns, finite-element simulations using RSoft's FEMSIM^{TM} suite show that the 2 µm thick BOX used in our devices is sufficiently thick to isolate the waveguides from the substrate at the wavelength of interest. Figure 3.3 shows simulated substrate leakage in strip waveguides for both 1.55 and 2.02 µm wavelengths for BOX thicknesses of 1, 2, and 3 µm.

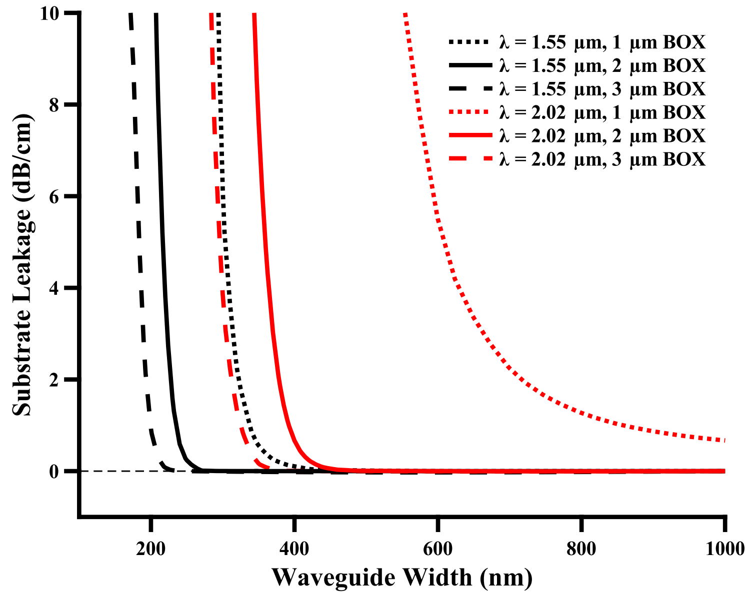

FIGURE 3.3: Substrate leakage in strip waveguides on SOI simulated using RSoft's FEMSIM^{TM} finite-element software with varying BOX thickness at wavelengths of 1.55 and 2.02 µm for the fundamental TE mode.

We note that devices requiring narrow waveguides, such as inverse tapers for edge-coupling [23], may be prohibitively lossy on an SOI substrate without sufficient BOX thickness. This problem is exacerbated at longer wavelengths.

3.3.2 Bending loss

Waveguide bending loss is plotted in figure 3.4 for the fundamental TE mode in both strip and rib waveguide geometries for radii varying from $R = 3$ to 15 μm in S-bend structures described previously in section 2.

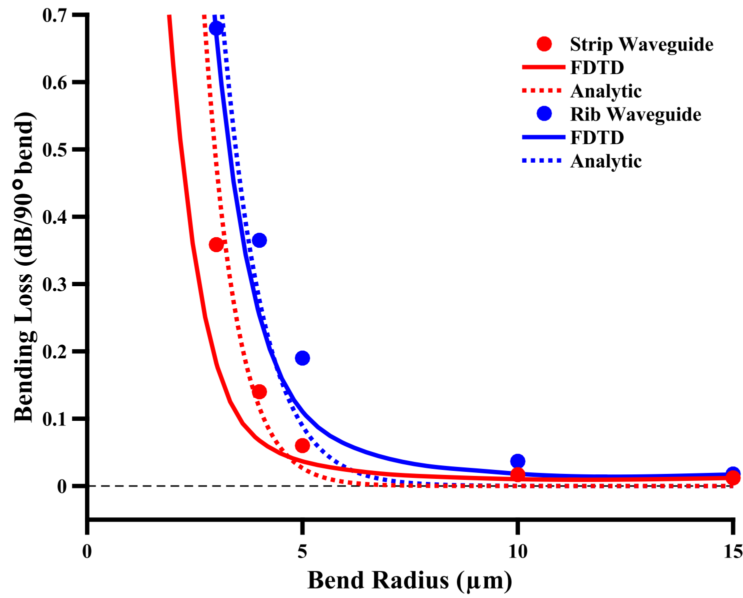

FIGURE 3.4: Waveguide bending loss plot for various 90° bend radii in strip and rib waveguides for the fundamental TE mode. Waveguide dimensions were used to simulate bending loss (solid lines) using RSoft FullWAVE FDTD software. Loss was calculated analytically (dashed lines) using the Marcuse bending loss model.

Loss per 90° bend was normalized to transmission from straight, strip and rib waveguide structures on each chip. For a bend radius of 3 μm, the loss per bend in strip and rib waveguides is 0.36 and 0.68 dB respectively. Bending loss for a bend radius of 30 μm (not plotted) has loss similar to that of 15 μm within measurement error. Measured data agrees well with FDTD simulations (also plotted) which were performed using RSoft FullWAVE. Theoretical models for bending loss in two-dimensional (2-D) slab waveguides [24], [25], can be used to estimate losses in 3-D waveguide geometries

through transforming the latter into the former via the effective index method [26]. These models agree well with experimental data in weakly guiding material systems [27] but suffer in cases with stronger confinement where the effective index method becomes less accurate, as well as cases where the radiated power is substantial as compared to the guided mode power. More accurate approaches for modeling bending loss in high index contrast waveguides have been developed [28], [29], although they are lacking simplified closed form expressions. We apply a widely adapted bent slab waveguide model, developed by Marcuse [24], utilizing the effective index method for both strip and rib waveguides. The bending loss coefficient per unit length can be calculated as:

$$\alpha_B = C_1 e^{-C_2 R}, \tag{3.2}$$

where constants C_1 and C_2 are defined as:

$$C_1 = \frac{{\alpha_x}^2 {k_x}^2 e^{\alpha_x w}}{{k_o}^3 N_{eff3}({N_{eff1}}^2 - {N_{eff2}}^2)(1 + \alpha_x \frac{w}{2})}, \tag{3.3}$$

$$C_2 = \frac{2\alpha_x^3}{3(k_o N_{eff3})^2}, \tag{3.4}$$

and constants α_x and k_x are defined as:

$$\alpha_x = k_o \sqrt{{N_{eff3}}^2 - {N_{eff2}}^2}, \tag{3.5}$$

$$k_x = k_o \sqrt{{N_{eff1}}^2 - {N_{eff3}}^2}. \tag{3.6}$$

N_{eff1},N_{eff2}, and N_{eff3}, are the effective indices of the rib, slab, and slab-rib-slab regions of a waveguide, respectively, and w is the half-width of the waveguide. The measured

data agrees well with the analytic model despite deviation from the weakly guiding approximation and the assumption that the ratio between radiated and guided mode power is small.

Lower losses can be seen in similarly sized waveguides for a wavelength of 1.55 μm [30]; however, our results are not prohibitive for waveguide routing or devices requiring relatively tight bends, such as ring resonators. Bending loss in single-mode waveguides is critically impacted by mode confinement in the waveguide. The further the evanescent-tail of the mode extends into the cladding the more probable for radiation loss to occur as the extended portion of the mode cannot travel with sufficient velocity to maintain constant phase with the mode. For a given waveguide width, longer wavelengths will be less confined and have higher bending loss, although the single-mode cut-off occurs at a larger waveguide width [13], and thus this loss can be reduced by using a wider waveguide. In a bent waveguide, the mode becomes offset laterally toward the outside of the bend leading to mode-mismatch losses at the junction between waveguide straights and bends. This lateral offset and thus loss increases with decreasing radius. Loss can be reduced by adiabatically varying the radius along the bend [31], [32], or laterally offsetting the straight and bent waveguides from each other at each junction [33].

3.3.3 Losses resulting from free-carriers

Waveguide doping loss is plotted in figure 3.5 for the fundamental TE mode in rib waveguide geometries for two n-type and p-type doping densities, typical of those used in the fabrication of active silicon photonic devices, namely 2.8×10^{17} and 3.4×10^{18} cm^{-3} for n-type doping, and 4.8×10^{17} and 1.9×10^{18} cm^{-3} for p-type doping.

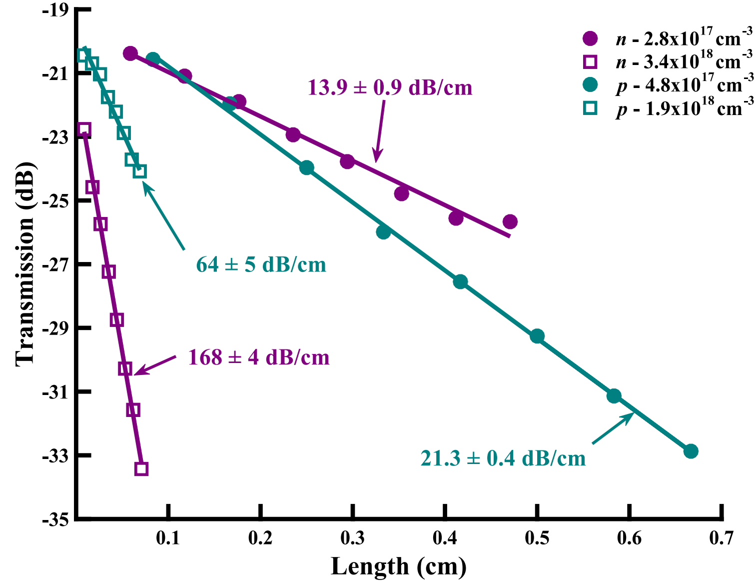

FIGURE 3.5: Waveguide doping loss plot for two levels of n-type and p-type doping levels (indicated on plot) in fabricated rib waveguides for the fundamental TE mode. Propagation loss was extracted through linear regression.

The propagating mode interacts with free-carriers present in doped silicon leading to a change in refractive index and absorption via the plasma dispersion effect [13]. According to the Drude model, the plasma dispersion relations used to describe this change in electro-refraction and electro-absorption are given as:

$$\Delta n = -\left(\frac{e^2\lambda^2}{8\pi^2 c^2 \epsilon_o n}\right)\left[\frac{\Delta N_e}{m^*_{ce}} + \frac{\Delta N_h}{m^*_{ch}}\right], \tag{3.7}$$

$$\Delta \alpha = \left(\frac{e^3\lambda^2}{4\pi^2 c^3 \epsilon_o n}\right)\left[\frac{\Delta N_e}{{m^*_{ce}}^2 \mu_e} + \frac{\Delta N_h}{{m^*_{ch}}^2 \mu_h}\right], \tag{3.8}$$

where e is the charge of an electron, λ is the wavelength, c is the speed of light, ϵ_o is the permittivity of free space, n is the refractive index of undoped silicon, ΔN is the change

in carrier concentration, m^*_{ce} and m^*_{ch} are the conductivity effective masses of electrons and holes, and μ_e and μ_h are the respective carrier mobilities.

A classical study of the plasma dispersion effect by Soref and Bennett in bulk silicon [34] showed that free-carrier modulation can be used for silicon photonic modulators; work that has largely spurred the development of silicon photonics. More recently, empirical solutions were developed for mid-infrared wavelengths [35] which we have adopted here to simulate doping loss in SOI rib waveguides with dimensions of 600×220 nm with a 90 nm slab height. We extract values of Δn and $\Delta\alpha$ using this empirical model for various values of ΔN at both 1.55 and 2.02 µm wavelengths to fix the complex refractive index profile in FEMSIM^{TM} in order to emulate free-carrier interactions in doped silicon. Simulations were performed assuming constant doping concentration (values indicated in figure 3.5) throughout the silicon layer. We note, however, that the doping is introduced using a multiple energy ion implantation process and the concentration of dopant will not in fact be perfectly uniform. Thus, the profiles would be better described as "quasi-uniform" with the concentration calculated from the average of the dopant in the silicon layer. Although this approach will not possess the precision of a 2-D overlap integral of the actual dopant profile and the optical mode, we note that it has been used successfully in the design and modelling of sophisticated silicon modulators [36].

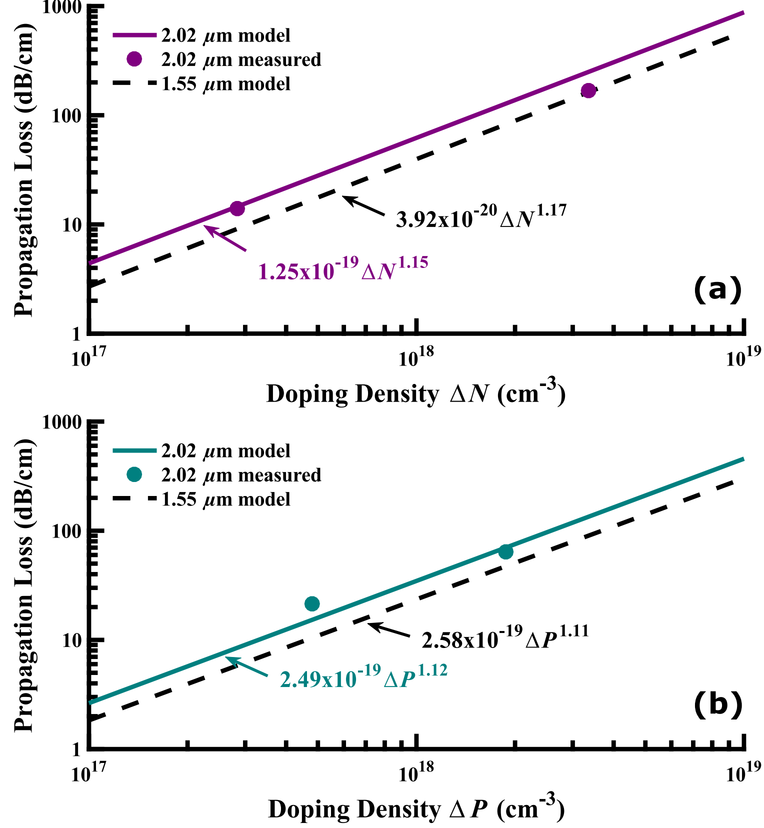

FIGURE 3.6: Propagation loss in *n*-type (a) and *p*-type (b) doped rib waveguides for the fundamental TE mode. Measured data are plotted using calculated doping densities against simulations using the aforementioned empirical model. For comparison, simulations are also plotted for a wavelength of 1.55 µm.

The small sample of measured data agrees well with simulated results in both *n*-type and *p*-type cases. Examining figure 3.6 we see that electro-absorption is stronger at a wavelength of 2.02 µm than 1.55 µm as one may expect from the λ^2 dependence found in the free-carrier absorption relation, summarized in equation (3.8). Similarly, the stronger electro-refraction is expected to increase the efficiency of free-carrier based modulation architectures. At an example *n*-type or *p*-type doping density of 1×10^{18} cm^{-3}, the changes in refractive index and absorption coefficient at 2.02 µm are $\sim$1.7 times stronger than at 1.55 µm meaning active devices in this wavelength regime may

benefit from either a reduction in required doping, or a smaller footprint compared to similar devices at 1.55 μm.

3.3.4 Defect loss

Previous work has shown that high bandwidth waveguide photodetectors operating at wavelengths up to and beyond 2 μm can be fabricated in silicon waveguides using defect engineering [7], [37]. This is of significant interest due the current lack of any other CMOS compatible approach to detection at high-speed at these wavelengths, although the significant work on the GeSn alloy to this end is hereby noted [38]. The optical-to-electrical conversion in reference [7] is mediated by the silicon divacancy, which exhibits strong absorption in the SOI transparency window from 1.1 to 2.5 μm [39]. An empirical expression used to approximate optical absorption in ion-implanted silicon waveguides is adopted here to model defect-induced loss in SOI strip and rib waveguides at the wavelength of 2.02 μm [40]. The model can be summarized in the following expression which provides loss due to the defects α_D in dB/cm:

$$\alpha_D = 4.34 \frac{\Gamma(z)\left(2.79 \times 10^{10} {\phi_A}^{0.63}\right)}{4.69 \times 10^{16}}, \tag{3.9}$$

where $\Gamma(z)$ is the overlap product between the propagating mode and the defect implant profile ϕ_A is the adjusted ion dose, calculated by multiplying implant dose by an adjustment factor equal to the number of divacancies per ion per angstrom at half ion range calculated using the code TRIM [41].The factor 4.69×10^{16} represents divacancy concentration per unit peak absorption coefficient $\Delta N/\Delta\alpha$ interpolated for 2 μm. The aforementioned dose adjustment factor was calculated, for 900 keV B^+ ion implantation, to be 0.09, while $\Gamma(z)$ for strip and rib waveguides was simulated to be 0.40 and 0.47, respectively, using FEMSIM^{TM}.

Defect dominated propagation loss is plotted in figure 3.7 for the fundamental TE mode in both strip and rib waveguide geometries for various implanted B^+ doses. As expected, propagation loss increases with increasing implantation dose. For low doses this propagation loss is reasonably described by the empirical model described by equation (3.9). For doses in excess of 7×10^{12} cm^{-2} the model underestimates the propagation loss. This is a likely consequence of several potential factors including the increasing influence of defect build-up in the oxide cladding or defect evolution from simple point defects to extended defects such as dislocations or voids. The measured propagation loss data for strip and rib waveguides were fitted using linear regression and have the following relation to implant dose (Q): $\alpha_{D(strip)} = 5.39\times10^{-12}Q$ and $\alpha_{D(rib)} = 6.34\times10^{-12}Q$, for the specific implant conditions used here.

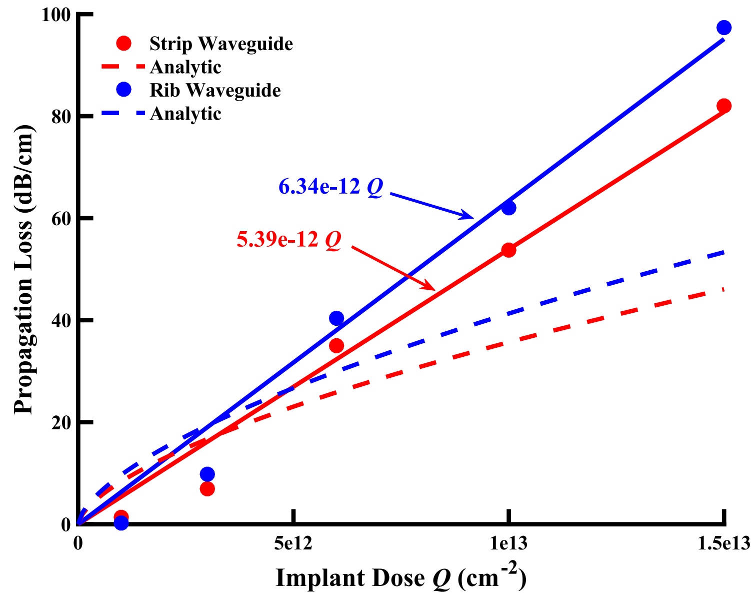

FIGURE 3.7: Waveguide loss in boron-implanted strip and rib waveguide geometries for the fundamental TE mode. Data were fit using linear regression. The boron ion-implantation energy was 900 keV.

Waveguide propagation loss as a function of annealing temperature for two B^+ implanted samples is plotted in figure 3.8. The shape of the annealing curves is consistent

with similar curves associated with the removal of the divacancy following thermal annealing. One may speculate that the implantation induced loss is dominated by the silicon divacancy and thus if more complex defects exist in the sample implanted with a dose of 1.5×10^{13} cm^{-2}, such defects do not dominate the waveguide properties. The reduction in propagation loss with post-implantation annealing provides important data for the determination of the optimal defect concentration for efficient detection which in turn depends upon carrier generation and extraction prior to carrier recombination [42].

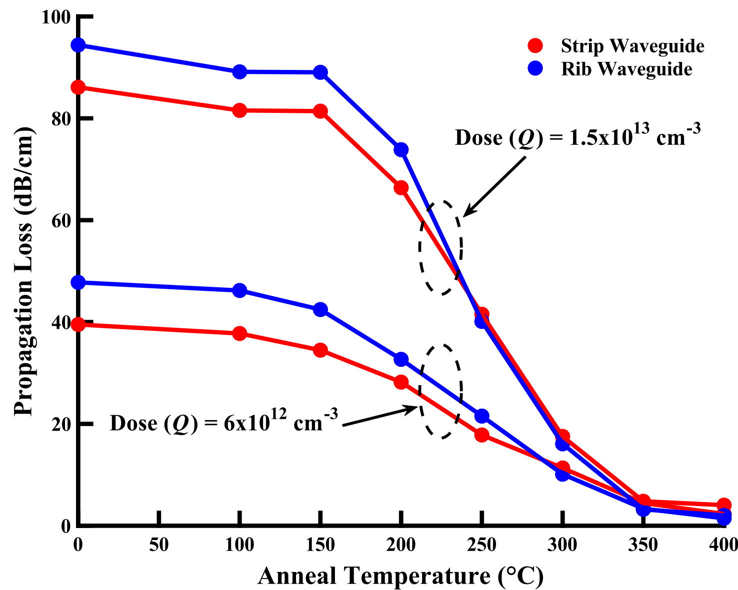

FIGURE 3.8: Defect-implanted strip and rib waveguide loss as a function of annealing temperature for the fundamental TE mode.

3.4 Conclusion and summary

Various loss mechanisms in SOI waveguides have been examined for a wavelength of 2.02 µm. Measured scattering loss due to sidewall roughness was found to be comparable to that of waveguides designed for 1.55 µm. The Payne-Lacey sidewall scattering loss model predicts lower loss at longer wavelengths with appropriate choice of waveguide

width. At the wavelength of interest, sidewall-scattering loss should be less compared to 1.55 μm regardless of width provided $L_C \lesssim 250$ nm. Substrate leakage was simulated with 1, 2, and 3 μm BOX thicknesses for wavelengths of both 2.02 and 1.55 μm. Longer wavelengths experience stronger substrate leakage for a fixed waveguide cross-section due to weaker confinement; however, negligible loss is observed for sufficient BOX thickness and waveguide width. Measured bending loss agrees well with both FDTD simulations and the Marcuse analytical model [24]. Bending loss in curved waveguides is expected to be higher for longer wavelengths for a fixed waveguide cross-section, again, due to weaker confinement; however, wider waveguides may be used to reduce this loss as the single-mode cut-off is extended to greater widths. Measured loss due to free-carrier absorption in doped waveguides agrees well with FEMSIM^{TM} simulations with empirically derived electro-refraction and electro-absorption relations used to fix the real and imaginary refractive index of silicon. The plasma dispersion equations, given in (3.7) and (3.8) predict an increase in electro-refraction and electro-absorption at 2.02 μm as compared to 1.55 μm by a factor of ∼1.7. Loss due to lattice defects from ion implantation is dominated by the silicon divacancy. An empirical model, given in equation (3.9), agrees reasonably well with measured data for implant doses up to 7×10^{12} cm^{-2}; beyond this, the model underestimates the defect induced loss. The results presented in this paper will help form the basis of future designs of modulators and detectors for the 2 μm centred communication window.

Acknowledgments

We would like to acknowledge CMC Microsystems for the provision of products and services that facilitated this research, including Synopsys' Optical Solutions Group, and Mentor Graphics, Corp., for design tools, as well as fabrication services using technology

from IMEC and IME. We gratefully acknowledge the NSERC CREATE Silicon Electronic Photonic Integrated Circuits (SiEPIC) training program and Jack Hendriks at Interface Science Western at Western University.

Bibliography

[1] W. Green *et al.*, "Mid-Infrared Silicon Photonics," in *Optical Fiber Communication Conference/National Fiber Optic Engineers Conference 2013*. Washington, D.C.: OSA, 2013, p. OTh4I.7.

[2] R. Soref, "Mid-infrared photonics in silicon and germanium," *Nature Photonics*, vol. 4, no. 8, pp. 495–497, aug 2010.

[3] M. M. Milošević, P. S. Matavulj, P. Y. Yang, A. Bagolini, and G. Z. Mashanovich, "Rib waveguides for mid-infrared silicon photonics," *Journal of the Optical Society of America B*, vol. 26, no. 9, pp. 1760–1766, sep 2009.

[4] S. Zlatanovic, J. S. Park, S. Moro, J. M. C. Boggio, I. B. Divliansky, N. Alic, S. Mookherjea, and S. Radic, "Mid-infrared wavelength conversion in silicon waveguides using ultracompact telecom-band-derived pump source," *Nature Photonics*, vol. 4, no. 8, pp. 561–564, aug 2010.

[5] Z. Li, A. M. Heidt, N. Simakov, Y. Jung, J. M. O. Daniel, S. U. Alam, and D. J. Richardson, "Diode-pumped wideband thulium-doped fiber amplifiers for optical communications in the 1800 - 2050 nm window." *Optics express*, vol. 21, no. 22, pp. 26 450–5, nov 2013.

[6] M. A. Van Camp, S. Assefa, D. M. Gill, T. Barwicz, S. M. Shank, P. M. Rice, T. Topuria, and W. M. J. Green, "Demonstration of electrooptic modulation at

2165nm using a silicon Mach-Zehnder interferometer," *Optics Express*, vol. 20, no. 27, pp. 28 009–16, dec 2012.

[7] J. J. Ackert, D. J. Thomson, L. Shen, A. C. Peacock, P. E. Jessop, G. T. Reed, G. Z. Mashanovich, and A. P. Knights, "High-speed detection at two micrometres with monolithic silicon photodiodes," *Nature Photonics*, vol. 9, no. 6, pp. 393–396, may 2015.

[8] R. Won, "View from... Communication Networks Beyond the Capacity Crunch: Is it crunch time?" *Nature Photonics*, vol. 9, no. 7, pp. 424–426, jun 2015.

[9] T. Baehr-Jones, A. Spott, R. Ilic, A. Spott, B. Penkov, W. Asher, and M. Hochberg, "Silicon-on-sapphire integrated waveguides for the mid-infrared." *Optics express*, vol. 18, no. 12, pp. 12 127–12 135, jun 2010.

[10] Y.-C. Chang, V. Paeder, L. Hvozdara, J.-M. Hartmann, and H. P. Herzig, "Low-loss germanium strip waveguides on silicon for the mid-infrared." *Optics letters*, vol. 37, no. 14, pp. 2883–5, jul 2012.

[11] R. A. Soref, S. J. Emelett, and W. R. Buchwald, "Silicon waveguided components for the long-wave infrared region," *Journal of Optics A: Pure and Applied Optics*, vol. 8, no. 10, p. 840, 2006.

[12] F. P. Payne and J. P. R. Lacey, "A theoretical analysis of scattering loss from planar optical waveguides," *Optical and Quantum Electronics*, vol. 26, no. 10, pp. 977–986, oct 1994.

[13] G. T. Reed and A. P. Knights, *Silicon Photonics: An Introduction.* West Sussex, England: John Wiley & Sons, Ltd, jan 2004.

[14] Y. Wang, J. Flueckiger, C. Lin, and L. Chrostowski, "Universal grating coupler design," *Photonics North 2013*, p. 89150Y, 2013.

[15] D. Marcuse, "Mode Conversation Caused by Surface Imperfections of a Dielectric Slab Waveguide," *Bell System Technical Journal*, vol. 48, no. 10, pp. 3187–3215, dec 1969.

[16] F. Grillot, L. Vivien, S. Laval, D. Pascal, and E. Cassan, "Size influence on the propagation loss induced by sidewall roughness in ultrasmall SOI waveguides," *IEEE Photonics Technology Letters*, vol. 16, no. 7, pp. 1661–1663, jul 2004.

[17] D. K. Sparacin, S. J. Spector, and L. C. Kimerling, "Silicon waveguide sidewall smoothing by wet chemical oxidation," *Journal of Lightwave Technology*, vol. 23, no. 8, pp. 2455–2461, 2005.

[18] K. K. Lee, D. R. Lim, H.-C. Luan, A. Agarwal, J. Foresi, and L. C. Kimerling, "Effect of size and roughness on light transmission in a Si/SiO_2 waveguide: Experiments and model," *Applied Physics Letters*, vol. 77, no. 11, p. 1617, 2000.

[19] K. P. Yap, A. Delage, J. Lapointe, B. Lamontagne, J. Schmid, P. Waldron, B. Syrett, and S. Janz, "Correlation of Scattering Loss, Sidewall Roughness and Waveguide Width in Silicon-on-Insulator (SOI) Ridge Waveguides," *Journal of Lightwave Technology*, vol. 27, no. 18, pp. 3999–4008, 2009.

[20] G. W. Reynolds and J. W. Taylor, "Correlation of atomic force microscopy sidewall roughness measurements with scanning electron microscopy line-edge roughness measurements on chemically amplified resists exposed by x-ray lithography," p. 2723, 1999.

[21] K. K. Lee, D. R. Lim, L. C. Kimerling, J. Shin, and F. Cerrina, "Fabrication of ultralow-loss Si/SiO_2 waveguides by roughness reduction." *Optics letters*, vol. 26,

no. 23, pp. 1888–1890, dec 2001.

[22] F. Grillot, L. Vivien, S. Laval, and E. Cassan, "Propagation loss in single-mode ultrasmall square silicon-on-insulator optical waveguides," *Journal of Lightwave Technology*, vol. 24, no. 2, pp. 891–895, 2006.

[23] M. Pu, L. Liu, H. Ou, K. Yvind, and J. M. Hvam, "Ultra-low-loss inverted taper coupler for silicon-on-insulator ridge waveguide," *Optics Communications*, vol. 283, no. 19, pp. 3678–3682, 2010.

[24] D. Marcuse, *Light Transmission Optics*, 1972, vol. 87.

[25] E. A. J. Marcatili, "Bends in Optical Dielectric Guides," *Bell System Technical Journal*, vol. 48, no. 7, pp. 2103–2132, 1969.

[26] D. L. Lee, *Electromagnetic principles of integrated optics.* John Wiley & Sons Inc, 1986.

[27] R. Deri, E. Kapon, and L. Schiavone, "Bend losses in GaAs/AlGaAs optical waveguides," *Electronics Letters*, vol. 23, no. 16, p. 845, 1987.

[28] J. Gu, P. Besse, and H. Melchior, "Novel method for analysis of curved optical rib-waveguides," *Electronics Letters*, vol. 25, no. 4, p. 278, 1989.

[29] M. Austin, "GaAs/GaAlAs curved rib waveguides," *IEEE Journal of Quantum Electronics*, vol. 18, no. 4, pp. 795–800, 1982.

[30] Y. Vlasov and S. McNab, "Losses in single-mode silicon-on-insulator strip waveguides and bends." *Optics express*, vol. 12, no. 8, pp. 1622–1631, 2004.

[31] M. Cherchi, S. Ylinen, M. Harjanne, M. Kapulainen, and T. Aalto, "Dramatic size reduction of waveguide bends on a micron-scale silicon photonic platform," *Opt.*

Express, vol. 21, no. 15, pp. 17 814–17 823, jul 2013.

[32] W. Bogaerts and S. K. Selvaraja, "Compact single-mode silicon hybrid rib/strip waveguide with adiabatic bends," *IEEE Photonics Journal*, vol. 3, no. 3, pp. 422–432, jun 2011.

[33] V. Subramaniam, G. N. De Brabander, D. H. Naghski, and J. T. Boyd, "Measurement of mode field profiles and bending and transition losses in curved optical channel waveguides," *Journal of Lightwave Technology*, vol. 15, no. 6, pp. 990–997, jun 1997.

[34] R. A. Soref and B. R. Bennett, "Electrooptical effects in silicon," *IEEE Journal of Quantum Electronics*, vol. 23, no. 1, pp. 123–129, jan 1987.

[35] M. Nedeljkovic, R. Soref, and G. Z. Mashanovich, "Free-carrier electrorefraction and electroabsorption modulation predictions for silicon over the 1-14-μm infrared wavelength range," *IEEE Photonics Journal*, vol. 3, no. 6, pp. 1171–1180, dec 2011.

[36] L. Chrostowski and M. Hochberg, *Silicon Photonics Design*. Cambridge: Cambridge University Press, 2015.

[37] B. Souhan, C. P. Chen, R. R. Grote, J. B. Driscoll, N. Ophir, K. Bergman, and R. M. Osgood, "Error-Free Operation of an All-Silicon Waveguide Photodiode at 1.9 μm," *IEEE Photonics Technology Letters*, vol. 25, no. 21, pp. 2031–2034, 2013.

[38] R. Soref, "Silicon-based silicon-germanium-tin heterostructure photonics." *Philosophical transactions. Series A, Mathematical, physical, and engineering sciences*, vol. 372, no. 2012, p. 20130113, 2014.

[39] H. J. Stein, F. L. Vook, and J. A. Borders, "Direct evidence of divacancy formation in silicon by ion implantation," *Applied Physics Letters*, vol. 14, no. 10, pp. 328–330, 1969.

[40] P. G. Coleman, C. P. Burrows, and A. P. Knights, "Simple expression for vacancy concentrations at half ion range following MeV ion implantation of silicon," *Applied Physics Letters*, vol. 80, no. 6, pp. 947–949, 2002.

[41] J. F. Ziegler and J. P. Biersack, "Treatise on Heavy-Ion Science: Volume 6: Astrophysics, Chemistry, and Condensed Matter," in *Treatise on Heavy-Ion Science.* Boston, MA: Springer US, 1985, vol. 1, pp. 93–129.

[42] D. F. Logan, P. E. Jessop, and A. P. Knights, "Modeling defect enhanced detection at 1550 nm in integrated silicon waveguide photodetectors," *Journal of Lightwave Technology*, vol. 27, no. 7, pp. 930–937, 2009.

Chapter 4

Experimental quantification of the free-carrier effect in silicon waveguides at extended wavelengths

Preface

The following chapter presents two active silicon photonic devices: the electronic variable optical attenuator (EVOA) and the micro-ring resonator (MRR) modulator. Both devices are measured under steady-state (DC) conditions at thulium doped fiber amplifier (TDFA)-band wavelengths centered at 1970 nm to further investigate the free-carrier effect at extended wavelengths and to demonstrate the viability of the 220 nm silicon-on-insulator (SOI) platform for TDFA-band telecommunication applications.

The measured EVOA represents an excellent device to compare the performance of the free-carrier effect across multiple wavelengths to directly demonstrate its enhanced

strength at TDFA-band wavelengths. With its large waveguide cross-section, wavelengths from 1310 to 2020 nm show near-identical cross-sectional mode profiles, allowing for an accurate comparison of the differences in optical absorption through electrically-controlled changes in free-carrier concentrations. In steady-state operation, the concentration of both holes and electrons in the waveguide are approximately homogeneous and equal, allowing for similarly accurate simulation and modelling of the changes in the imaginary refractive index of silicon associated with these losses. Simulations show excellent agreement with the measured results in Section 4.3, further validating the empirical model used throughout the Thesis.

The empirical free-carrier model, further bolstered by the results of the EVOA, was used alongside predictions of optical loss demonstrated in Chapter 3 in the design of the MRR modulator presented in this Chapter. DC results demonstrate the excellent spectral properties and resonance shift performance (in both forward and reverse bias operation) desired in a MRR modulator for telecommunication applications, further supporting the viability of the 220 nm SOI platform's use at TDFA-band wavelengths. Simulation and modelling off free-carrier influence under bias is applied to the MRR modulator using a simple 1-D *p*-*n* junction approximation. Results show good agreement with measured data but prompting the investigation of the more accurate 2-D modelling method demonstrated in Chapter 5. The exemplary DC performance of the MRR modulator served as motivation to measure and model the high-speed performance of re-designed TDFA-band MRR modulators, also presented in Chapter 5.

David E. Hagan,[1] Milos Nedeljkovic,[2] Wei Cao,[2] David J. Thomson,[2] Goran Z. Mashanovich,[2] and Andrew P. Knights[1]

[1]Department of Engineering Physics, McMaster University, 1280 Main Street West, Hamilton, ON, Canada

[2]Optoelectronics Research Centre, University of Southampton, Southampton, SO17 1BJ, United Kingdom

This paper was published in *Optics Express* on January 7, 2019.

DOI: 10.1364/OE.27.000166

Abstract

We examine the electro-optic effect at wavelengths ranging from 1.31 to 2.02 μm for: (1) an Electronic Variable Optical Attenuator (EVOA); and (2) a Micro-Ring Resonator (MRR). For the EVOA, simulations were performed to ascertain the relationship between free-carrier concentration and optical attenuation, and are in agreement with our observation of an increase in attenuation with increasing wavelength. MRRs were fabricated for use around wavelengths of 2 μm to explore the sensitivity of operation to bus-to-ring coupling gap and *p*-*n* junction offset. Trends observed in the experiment are replicated by simulation, calibrated using the observations of the EVOA operation. The previously proposed efficiency increase of operation around 2 μm compared to more traditional wavelengths is demonstrated. Future development of devices for these wavelengths, supported by amplification using thulium doped fiber amplifier (TDFA) technology, is a promising route to aid in the alleviation of increasing demands on communication networks.

4.1 Introduction

Recent expansion of silicon photonics interest into the mid-infrared (MIR) wavelength region has given rise to developments in sensing [1], nonlinear optics [2], and semiconductor lasers [3]. Telecommunication applications have received specific interest as a result of the looming data bandwidth bottleneck [4] with MIR silicon photonics seen to offer a cost-effective method to manufacture integrated components. The C-band, most often used in telecommunication infrastructure, is a wavelength range defined by the amplification spectrum of the erbium doped fiber amplifier (EDFA) and the low-loss transmission spectrum of long-haul optical fibers. However, the finite laser and filter linewidth used in Wavelength Division Multiplexing (WDM) systems places a limit on the spectral efficiency of any wavelength band. An attractive solution is to open a parallel window in the MIR wavelength regime defined by the TDFA gain band [5], the MIR equivalent to the EDFA centered around 2 µm. With the advent of the TDFA and advances in hollow core photonic bandgap fibers [6] along with silicon-on-insulator (SOI) high-speed MIR detectors [7], and modulators [8], many components are in place to develop this multi-band telecommunications infrastructure.

An important device in various photonic systems is the variable optical attenuator (VOA) [9] which allows for precise control over the intensity of light through a system. This is particularly important for devices which can exhibit detrimental nonlinearities at high-power such as the observation of self-heating in micro-ring resonators (MRR) [10], [11]. The silicon-based carrier injection EVOA makes use of the electro-optic effect; the well-studied perturbation of a material's complex refractive index by means of free-carrier interaction [12]. Such free-carriers can be introduced intentionally via p-n structures formed through CMOS-compatible dopant implantation processes and may be used for optical modulation. As the strength of the free-carrier effect is approximately proportional to the square of wavelength, devices based on the free-carrier effect can

be designed for longer wavelengths (compared to the traditional communication bands) with a reduced device footprint and/or lower power consumption.

Devices operating around a wavelength of 2 μm have gained significant attention due to the recent availability of the TDFA, and the promise of TDFA-band communication systems. Of particular interest as a high-speed modulator is the MRR which boasts a large "on-off" extinction ratio and low energy consumption; less than 50 fJ/bit under reverse-bias [13]. In a recently submitted paper [14] we demonstrated modulation using an MRR operating at 2 μm, however, to our knowledge, no systematic study of MRR modulator operation to design parameter variation has yet been performed.

In this paper, we study the electro-optic effect strength in silicon at a 2 μm wavelength in a forward-bias EVOA and demonstrate the steady-state operation of a MRR modulator. Both sets of experimental data are modeled using an empirical expression for the plasma dispersion effect in silicon. The simulations are such that there exists self-consistency.

4.2 Methods and experimental set-up

Active devices in silicon photonics make use of implanted dopants as a means of electrical connection as well as optical phase and amplitude modulation in waveguides (the so-called free-carrier effect) [12], whereby a material with excess electrons or holes experiences a wavelength dependent change in complex refractive index. By changing the concentration of free-carriers in a silicon waveguide, the phase and amplitude of the propagating mode can therefore be modulated. This is the operating principle behind phase modulation devices such as the Mach-Zehnder and MRR modulator, as well as amplitude modulating devices such as the EVOA.

Changes in the real index Δn and the absorption $\Delta\alpha$ in silicon due to free-carriers can be approximated using the Drude model [12] such that:

$$\Delta n = -\left(\frac{e^2\lambda^2}{8\pi^2 c^2 \varepsilon_0 n}\right)\left[\frac{\Delta N_e}{m_{ce}^{*2}} + \frac{\Delta N_h}{m_{ch}^{*2}}\right], \tag{4.1}$$

$$\Delta\alpha = \left(\frac{e^3\lambda^2}{4\pi^2 c^3 \varepsilon_0 n}\right)\left[\frac{\Delta N_e}{m_{ce}^{*2}} + \frac{\Delta N_h}{m_{ch}^{*2}}\right], \tag{4.2}$$

where e is the charge of an electron, λ is the wavelength, c is the speed of light, ε_0 is the permittivity of free space, n is the unperturbed refractive index of silicon, ΔN_e and ΔN_h are the changes in electron and hole concentrations in silicon, m_{ce}^* and m_{ch}^* are the conductivity effective masses of electrons and holes, and μ_e and μ_h are the electron and hole mobilities respectively. The Drude model provides an excellent approximation to plasma dispersion in silicon but has been found to deviate from experimental data [12]. An empirical model has been developed [15] motivated by limitations of the Drude model, especially at extended wavelengths. This model employs a Kramers-Kronig analysis of experimentally measured absorption spectra to estimate free-carrier refraction and absorption for wavelengths from 1.31 to 14 μm in silicon, resulting in simple wavelength-specific equations for Δn and $\Delta\alpha$ which vary only with ΔN_e and ΔN_h. These equations for a wavelength of 2 μm are:

$$\Delta\alpha = 3.22 \times 10^{-20}\Delta N_e^{1.149} + 6.21 \times 10^{-20}\Delta N_h^{1.119}, \tag{4.3}$$

$$-\Delta n = 1.91 \times 10^{-21}\Delta N_e^{0.992} + 2.28 \times 10^{-18}\Delta N_h^{0.841} \tag{4.4}$$

Recently [16] it was used to simulate dopant induced loss in submicron waveguides showing very good agreement with measured results. We apply this empirical model to simulate optical attenuation in a commercial EVOA and modulation using MRRs.

4.2.1 EVOA

To explore free-carrier absorption as a function of wavelength we employed an EVOA operating at wavelengths ranging from 1.31 to 2.02 μm. The device is a relatively large cross-section single-mode silicon waveguide (3 μm wide, 4.2 μm high with a 2.8 μm slab thickness) with an integrated *p*-*i*-*n* diode operating under carrier injection controlled via external bias. The *p* and *n* doping are positioned more than 4 μm from the waveguide edge to prevent measurable parasitic optical absorption when the diode is unbiased. The fabrication details and geometrical description of the device are provided in [17].

The laser sources used for measurements at 1.31, 1.51-1.64, and 2.02 μm were a Luminent MRLDSP04OP laser diode, Agilent 81640A tuneable laser source, and an Eblana Photonics 2020-FP series laser diode, respectively. Similarly the EVOA output light was coupled into an ILX Lightwave FPM-8200 power meter, Agilent 81635A power sensor, and a Thorlabs PDA10D InGaAs detector, respectively. The fiber coupled laser sources were launched into the EVOA via an integrated mode converter that provided efficient coupling at all wavelengths. The EVOA was placed under forward bias using a Keithley 2400 source meter and electrical probes.

4.2.2 MRR

Phase modulation is exploited in devices such as the MRR modulator, the operation of which has been studied extensively [18]. The resonant wavelength of an MRR is given

by:

$$\lambda_{res} = \frac{n_{eff}L}{m}, \quad m = 1, 2, 3, ... \tag{4.5}$$

where n_{eff} is the effective index of the propagating mode and L is the cavity length. Examining Eq. (4.1), it can be seen that under carrier-injection, ΔN_e and ΔN_h increase causing the effective index of the mode to decrease resulting in a blue-shift of the resonant wavelength of the MRR. Under carrier-depletion, the opposite results in a red-shift in the resonant wavelength.

MRR modulators in an add-drop configuration were designed and fabricated via CMC Microsystems through A*STAR IME on a 220 nm SOI platform with a waveguide width of 600 nm, slab height of 90 nm, and a ring radius of 10 μm. A device schematic layout and cross-section can be seen in Fig. 4.1.

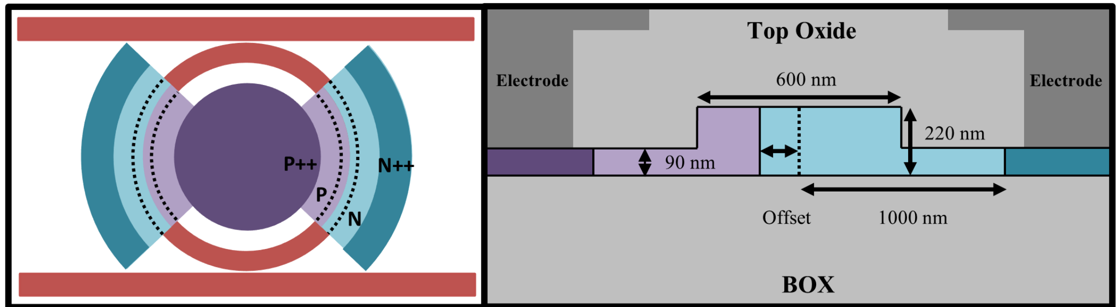

FIGURE 4.1: MRR modulator schematic layout (left) and phase-shifter cross-section (right). Reprinted with permission from [19] © The Optical Society.

The active region covers 64% of the total ring circumference. The inner and outer-ring portion of the waveguide is p-and n-doped, respectively, with doping concentrations of 4.8×10^{17} and 2.8×10^{17} cm^{-3} which were determined previously [16]. The p-n junction offset was varied to optimize resonance shift efficiency.

The MRR was subjected to linearly polarized light from a Sacher Lasertechnik tuneable Littman/Metcalf laser coupled into the bus waveguide via a 180 nm wide inverse nanotaper. The output was coupled via an identical nanotaper into a tapered fiber and then into a Thorlabs PDA10D InGaAs detector. A Keithley 2400 source meter and DC electrical probes were used to electrically bias the MRR.

4.3 Results and discussion

Attenuation measurements via the EVOA were performed for each wavelength as a function of applied forward bias. We estimate the coupling loss to be less than 5 dB per facet for 1550 nm confirming the relatively good optical coupling of the silicon taper used for these devices. The optical output power under zero-bias was used to normalize the biased optical output attenuated by the EVOA shown in Fig. 4.2, such that a relative comparison between wavelengths could be made. We note that with increasing current, the attenuation increases until the injection of free-carriers saturates.

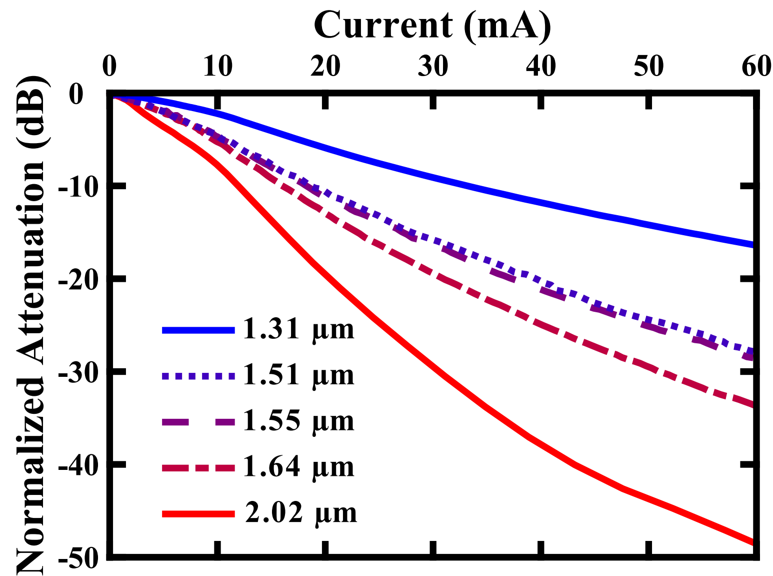

FIGURE 4.2: Normalized EVOA optical attenuation under forward bias for a range of input wavelengths. Reprinted with permission from [19] © The Optical Society.

An increase in attenuation efficiency is seen as the wavelength is varied from 1.31 to 2.02 µm confirming the expected increase in free-carrier absorption at longer wavelengths due to the increasing cross-section for photon/free-carrier interaction. This wavelength dependency is evident in Fig. 4.3 which shows the measured optical attenuation (normalized to the zero bias output for each wavelength) as a function of wavelength plotted for several lines of constant injection current.

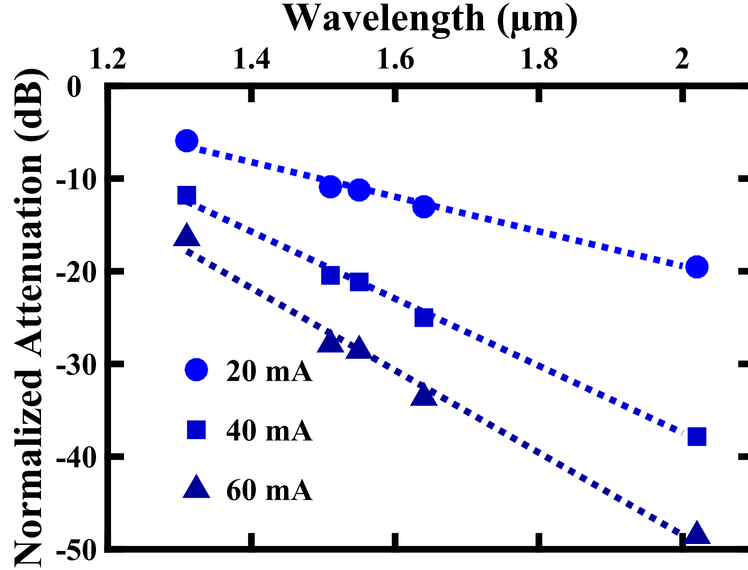

Figure 4.3: Normalized attenuation isocurrent lines as a function of wavelength. Dotted lines represent a linear regression of measured data. Reprinted with permission from [19] © The Optical Society.

The attenuation in dB (relative to the unbiased condition) is essentially linear as a function of wavelength across this wavelength range. From Eq. (4.2), we expect the change in absorption at 2 µm to be approximately 1.7 times greater than at 1.55 µm as predicted by [15].

The cross-sectional dimensions of the device (determined by focused ion beam analysis) were used in a model utilizing finite-element method simulation to generate the mode profile for all wavelengths experimentally measured. The optical confinement coefficient (Γ, defined as the fraction of mode energy density residing in the waveguide core) for all wavelengths was calculated to be almost invariant at $\Gamma = 0.92$ and $\Gamma = 0.91$ for the fundamental TE and TM modes, respectively. The aforementioned empirical model for free-carrier absorption [15] was used to calculate the complex refractive index of the waveguide under forward bias. Under equilibrium conditions, the concentration of electrons and holes is assumed to be equal, although the optical absorption due to holes

is greater than that for electrons. The simulated absorption for 1.31, 1.55, and 2.02 μm is shown in Fig. 4.4.

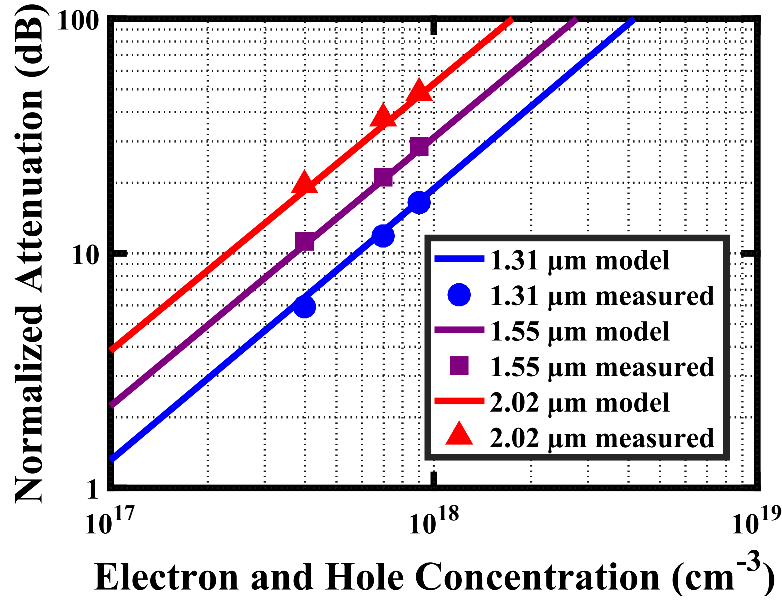

FIGURE 4.4: Simulated free-carrier absorption in the VOA as a function of carrier concentration. Measured data at fixed driving currents are also plotted. Reprinted with permission from [19] © The Optical Society.

The normalized attenuation dependencies were derived by choosing the simulated material absorption coefficient according to [15] for both electrons and holes. The measured attenuation for each driving current is shown in Fig. 4.4 as three vertical sets of solid markers. To estimate the steady-state electron and hole concentrations present in the VOA, these measured data sets are fitted such that they provide the best overall match between the solid lines which result from the modeling described above. The resulting steady-state electron-hole concentration for 20, 40, and 60 mA of driving current are $4{\times}10^{17}$, $7{\times}10^{17}$, and $9{\times}10^{17}$ cm^{-3}, respectively, and appear reasonable for a *p-i-n* silicon diode of this nature [20]. Further, these free-carrier concentrations are consistent with a silicon EVOA with these cross-sectional dimensions and driving currents [9], [21].

For EVOA designs with sub-micron cross-section waveguides, operation at relatively

high-speed is possible [22]. Although not explored further in this work, we note that for wavelengths around 2 µm, attenuation-based modulation may be achieved at lower power or with reduced footprint than at more common communication wavelengths such as those in the *O*, *C* and *L* bands.

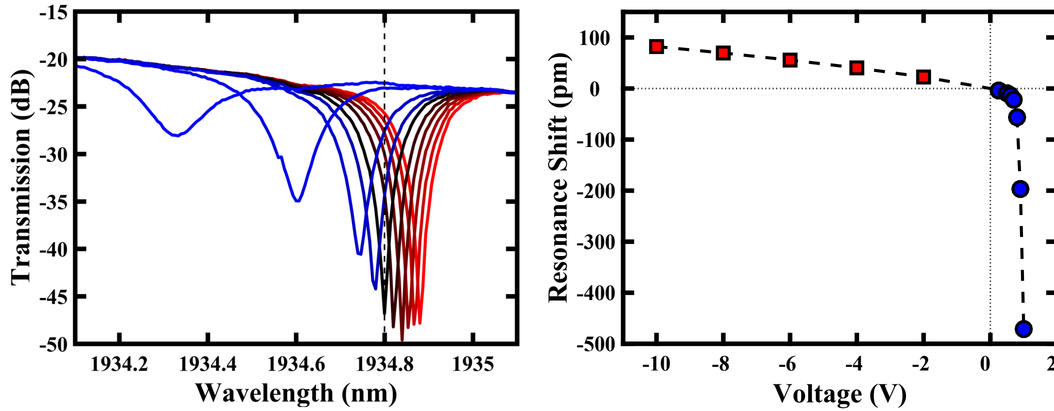

Figure 4.5: Measured MRR spectrum for biases from -10 to 1 V (left) and extracted resonance shift (right). The dashed lines denote zero bias resonance positions. Reprinted with permission from [19] © The Optical Society.

The MRR optical transfer spectrum for biases from -10 to 1 V is shown in Fig. 4.5 (left). The extracted resonance shift (with respect to zero bias) is plotted in Fig. 4.5 (right). The MRR under forward bias of 1 V exhibits a relatively large blue-shift of 471 pm; a result of the large number of injected carriers in this operational regime. This result is consistent with both a substantial decrease in MRR *Q*-factor from 10,000 to 7,500 (calculated as the ratio of resonant wavelength to FWHM), and a decrease in filter notch depth from 24 to 7 dB.

Carrier depletion in a reverse-bias MRR has been studied theoretically in [23]. An approach to simulate the resonance shift in a MRR modulator begins with solving for the MRR waveguide mode analytically using the effective index method described in [24]. Next, a 1-D free-carrier concentration profile is calculated for zero and reverse biases

using simple analytical expressions for an abrupt p-n junction with user-defined dopant concentrations and junction offset [20], which in our case determined concentrations of 2.8×10^{17} and 4.8×10^{17} cm^{-3} for the p- and n-doped regions respectively. The electron and hole distributions are used to calculate the voltage-dependent change in effective index through an overlap integral of the solved mode profile with the free-carrier profile. In predicting the index perturbation caused by the free-carriers, the model for plasma dispersion in [23] is modified using the model described in reference [15]. This is justified by the consistency of simulated and measured results from the EVOA experiment. Finally, the change in effective index for each voltage is used to determine the resonance shift of the MRR analytically from reference [18].

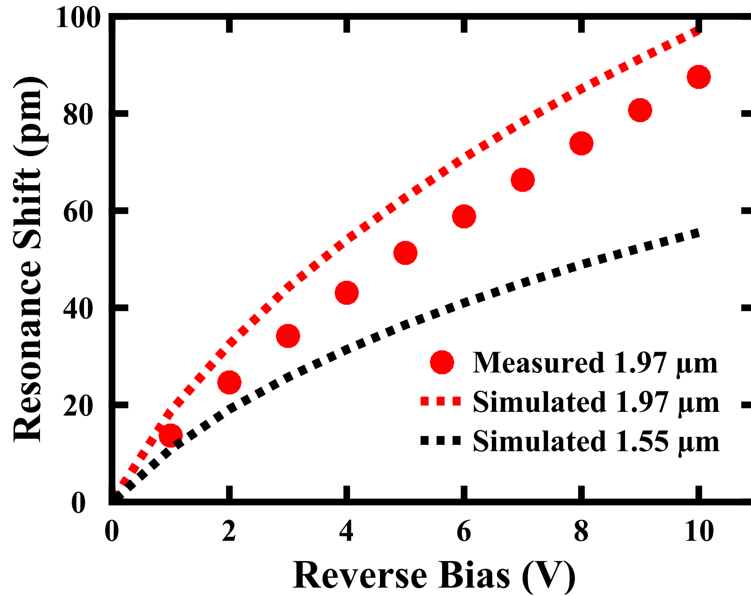

FIGURE 4.6: Measured and simulated reverse-bias resonance shift for a MRR modulator with a 30 nm p-n junction offset. Dashed black line indicates simulation of a 1.55 µm MRR modulator with 450 nm waveguide width. Reprinted with permission from [19] © The Optical Society.

The measured and simulated results for a device with 30 nm p-n junction offset from the waveguide center are shown in Fig. 4.6. The measured resonance shift versus reverse

bias for a wavelength of 1.97 μm is in reasonable agreement with the simulated results, albeit the simulations provide a greater shift. In comparison, simulations of identically doped MRRs operating at 1.97 μm and 1.55 μm wavelengths with waveguide widths of 600 and 450 nm, respectively, show enhanced modulation efficiency in the former due to the stronger free-carrier effect at the longer wavelengths.

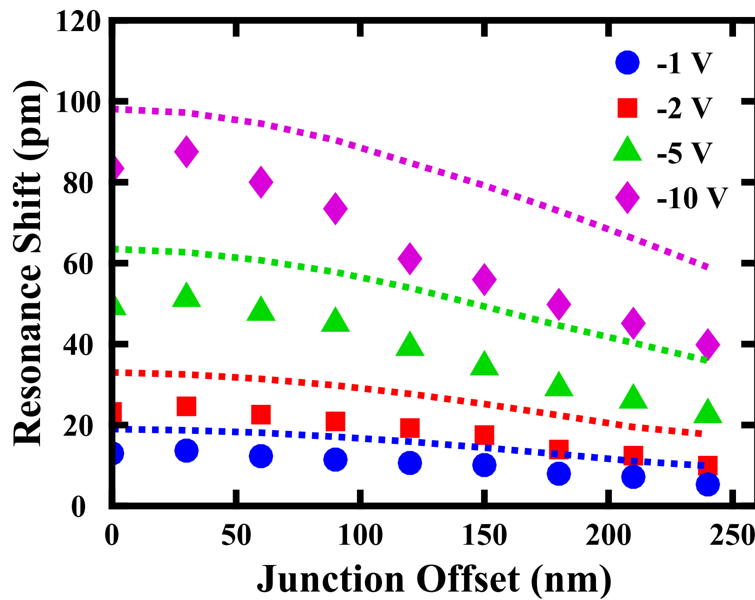

FIGURE 4.7: Measured and simulated reverse-bias resonance shift for varying *p*-*n* junction offset. Dashed line denotes simulated results. Reprinted with permission from [19] © The Optical Society.

Resonance shift measurements were performed for *p*-*n* junction offsets varying from 0 to 240 nm and compared with simulation. These results are shown in Fig. 4.7. Experimentally measured results demonstrate reasonable agreement with simulation (at least in terms of the data trend) and show an optimal junction offset of approximately 30 nm for these doping concentrations. Deviation from measured and simulated results in Fig. 4.6 and Fig. 4.7 may be attributed to several factors but perhaps dominant is the use of a 1-D *p*-*n* junction approximation, coupled with the effective index method [24], for solving the overlap between the propagating mode and the free-carrier profiles.

Additionally, any variation in the waveguide mode in the ring compared to that in a straight waveguide is unaccounted for in the simulation. This effect can shift the modal power distribution in the waveguide and thus the optimal p-n junction offset value [25].

The highly-doped $p{+}{+}$ and $n{+}{+}$ regions in the MRR used to provide low resistance contact to the p-n junction are separated from the waveguide edges by a distance of 1 μm. The separation presents a trade-off between parasitic loss from mode overlap, and increasing electrical bandwidth from reduced device resistance. For high-speed modulation, this separation is a crucial parameter in determining the extinction ratio and electrical bandwidth [26]. The choice in waveguide width and p-n junction doping concentrations also present trade-offs between modulation efficiency and electrical bandwidth. The waveguide width of 600 nm was chosen here such that the waveguide is below the single-mode cut-off point. Although increasing waveguide width and thus confinement can increase reverse-bias modulation efficiency, beyond a critical width the total optical power overlapping the p-n junction depletion width begins to decrease significantly. Similarly, increasing the p-n junction doping concentrations reduces the junction resistance and thus can increase the electrical bandwidth, but at the expense of reduced depletion region growth under reverse-bias. The inclusion of an add-drop bus waveguide is done to reduce the photon lifetime that future high-speed modulation measurements may be limited by. Longer wavelengths exhibit lower intrinsic propagation loss due to scattering in single-mode waveguides, thus for a reverse-bias MRR modulator operating at longer wavelengths, the photon lifetime can be a limiting factor in modulation bandwidth due to the low cavity loss, though this can be partially offset by the increased loss from free-carriers.

High-speed operation of a MRR is contingent on the RC-time constant of the active region as well as the photon lifetime in the ring which is proportional to the Q-factor.

The photon lifetime-limited bandwidth is given by [27]:

$$f_0 = \frac{c}{Q\lambda} = \frac{c\alpha}{\pi n_g}, \tag{4.6}$$

where c is the speed of light, Q is the Q-factor of the resonance, and λ is the wavelength. The equation encompasses the waveguide's group index n_g and loss coefficient α. In comparing all-pass configuration MRRs designed for 1.97 and 1.55 µm described in Fig. 4.6, the former has a lower group index and higher loss due to free-carriers for identical p-n junctions implying a larger photon lifetime-limited bandwidth. The addition of an add-drop waveguide, as done in this work, further increases this bandwidth limit by reducing the Q-factor in a controllable manner. For the data presented, the estimated photon lifetime-limited bandwidth is 15 GHz at 0 V and 20 GHz at 1 V. The electrical RC-limited bandwidth will be examined in future work but is expected to be lower than that of 1550 nm optimized MRR devices due to the increased waveguide width and separation of highly doped $p{+}{+}$ and $n{+}{+}$ regions. Further work will explore the high-speed operation of MRR modulators and in particular the impact of the relative increase of the electro-optic coefficient with increasing wavelength.

4.4 Conclusion

This work details experimental evidence of the impact of increasing wavelength on the operation of silicon photonic devices employing the free-carrier plasma-dispersion effect. Measured results verify enhanced optical attenuation at longer wavelengths using a silicon EVOA. Change in free-carrier absorption is shown to be approximately 1.7 times greater for 2.02 µm compared to 1.55 µm. Optical modulation of TDFA-band wavelengths using a MRR modulator is demonstrated, and the results are simulated using

an analytical model. An increase in modulator efficiency, in terms of resonance shift in simulated optimized structures, is again shown to be approximately 1.7 times greater for 1.96 μm relative to 1.55 μm. These results imply free-carrier based devices with lower operating power and smaller footprint can be used in future TDFA compatible wavelength telecommunication architectures employing silicon photonics. In addition, the results support the empirical free-carrier model of [15], which can be used with confidence in future device design.

Bibliography

[1] R. Soref, "Mid-infrared photonics in silicon and germanium," *Nature Photonics*, vol. 4, no. 8, pp. 495–497, aug 2010.

[2] S. Zlatanovic, J. S. Park, S. Moro, J. M. C. Boggio, I. B. Divliansky, N. Alic, S. Mookherjea, and S. Radic, "Mid-infrared wavelength conversion in silicon waveguides using ultracompact telecom-band-derived pump source," *Nature Photonics*, vol. 4, no. 8, pp. 561–564, aug 2010.

[3] B. Jalali, V. Raghunathan, R. Shori, S. Fathpour, D. Dimitropoulos, and O. Stafsudd, "Prospects for Silicon Mid-IR Raman Lasers," *IEEE Journal of Selected Topics in Quantum Electronics*, vol. 12, no. 6, 2006.

[4] R. Won, "View from... Communication Networks Beyond the Capacity Crunch: Is it crunch time?" *Nature Photonics*, vol. 9, no. 7, pp. 424–426, jun 2015.

[5] Z. Li, A. M. Heidt, N. Simakov, Y. Jung, J. M. O. Daniel, S. U. Alam, and D. J. Richardson, "Diode-pumped wideband thulium-doped fiber amplifiers for optical communications in the 1800 - 2050 nm window." *Optics express*, vol. 21, no. 22, pp. 26 450–5, nov 2013.

[6] Y. Chen *et al.*, "Multi-kilometer Long, Longitudinally Uniform Hollow Core Photonic Bandgap Fibers for Broadband Low Latency Data Transmission," *Journal of Lightwave Technology*, vol. 34, no. 1, jan 2016.

[7] J. J. Ackert, D. J. Thomson, L. Shen, A. C. Peacock, P. E. Jessop, G. T. Reed, G. Z. Mashanovich, and A. P. Knights, "High-speed detection at two micrometres with monolithic silicon photodiodes," *Nature Photonics*, vol. 9, no. 6, pp. 393–396, may 2015.

[8] M. A. Van Camp, S. Assefa, D. M. Gill, T. Barwicz, S. M. Shank, P. M. Rice, T. Topuria, and W. M. J. Green, "Demonstration of electrooptic modulation at 2165nm using a silicon Mach-Zehnder interferometer," *Optics Express*, vol. 20, no. 27, pp. 28 009–16, dec 2012.

[9] D. J. Thomson, L. Shen, J. J. Ackert, E. Huante-Ceron, A. P. Knights, M. Nedeljkovic, A. C. Peacock, and G. Z. Mashanovich, "Optical detection and modulation at 2μm-2.5μm in silicon," *Optics Express*, vol. 22, no. 9, p. 10825, may 2014.

[10] T. Xiaogang, L. Jun, and X. Chenyang, "Thermal nonlinear effect in high Q factor silicon-on-insulator microring resonator," *Optics Communications*, vol. 395, pp. 207–211, jul 2017.

[11] Z. Zhang, G. I. Ng, H. Qiu, W. Wang, X. Guo, M. S. Rouifed, C. Liu, and H. Wang, "Compact microring resonators integrated with grating couplers working at 2 μm wavelength on silicon-on-insulator platform," *Applied Optics*, vol. 56, no. 19, p. 5444, jul 2017.

[12] R. A. Soref and B. R. Bennett, "Electrooptical effects in silicon," *IEEE Journal of Quantum Electronics*, vol. 23, no. 1, pp. 123–129, jan 1987.

[13] P. Dong *et al.*, "Low V_{pp}, ultralow-energy, compact, high-speed silicon electro-optic modulator," *Optics Express*, vol. 17, no. 25, p. 22484, dec 2009.

[14] W. Cao *et al.*, "High-speed silicon modulators for the 2 μm wavelength band," *Optica*, vol. 5, no. 9, p. 1055, sep 2018.

[15] M. Nedeljkovic, R. Soref, and G. Z. Mashanovich, "Free-carrier electrorefraction and electroabsorption modulation predictions for silicon over the 1-14-μm infrared wavelength range," *IEEE Photonics Journal*, vol. 3, no. 6, pp. 1171–1180, dec 2011.

[16] D. E. Hagan and A. P. Knights, "Mechanisms for optical loss in SOI waveguides for mid-infrared wavelengths around 2 μm," *Journal of Optics*, vol. 19, no. 2, p. 025801, feb 2017.

[17] A. Martin, D. Feng, J. Luff, and M. Asghari, "Technical Challenges for Silicon Photonics Transceivers for Data Center Applications," in *Optical Fiber Communication Conference.* Optical Society of America, 2016.

[18] W. Bogaerts, P. De Heyn, T. Van Vaerenbergh, K. De Vos, S. Kumar Selvaraja, T. Claes, P. Dumon, P. Bienstman, D. Van Thourhout, and R. Baets, "Silicon microring resonators," *Laser & Photonics Reviews*, vol. 6, no. 1, pp. 47–73, jan 2012.

[19] D. E. Hagan, M. Nedeljkovic, W. Cao, D. J. Thomson, G. Z. Mashanovich, and A. P. Knights, "Experimental quantification of the free-carrier effect in silicon waveguides at extended wavelengths," *Optics Express*, vol. 27, no. 1, p. 166, jan 2019.

[20] S. M. Sze and K. K. Ng, *Physics of semiconductor devices.* Wiley-Interscience, 2007.

[21] D. W. Zheng, B. T. Smith, and M. Asghari, "Improved efficiency Si-photonic attenuator," *Optics Express*, vol. 16, no. 21, p. 16754, oct 2008.

[22] J. Xia, J. Yu, Q. Yan, and Z. Liu, "High-speed electrooptical VOA integrated in silicon-on-insulator," *Chinese Optics Letters*, vol. 1, no. 4, pp. 217–219, apr 2003.

[23] L. Chrostowski and M. Hochberg, *Silicon Photonics Design.* Cambridge: Cambridge University Press, 2015.

[24] D. L. Lee, *Electromagnetic principles of integrated optics.* John Wiley & Sons Inc, 1986.

[25] A. Brimont, X. Hu, S. Cueff, P. Rojo Romeo, G. Saint Girons, A. Griol, A. Zanzi, P. Sanchis, and R. Orobtchouk, "Low-Loss and Compact Silicon Rib Waveguide Bends," *IEEE Photonics Technology Letters*, vol. 28, no. 3, pp. 299–302, feb 2016.

[26] S. S. Azadeh, F. Merget, S. Romero-García, A. Moscoso-Mártir, N. von den Driesch, J. Müller, S. Mantl, D. Buca, and J. Witzens, "Low V_π Silicon photonics modulators with highly linear epitaxially grown phase shifters," *Optics Express*, vol. 23, no. 18, p. 23526, sep 2015.

[27] G. Li, X. Zheng, J. Yao, H. Thacker, I. Shubin, Y. Luo, K. Raj, J. E. Cunningham, and A. V. Krishnamoorthy, "25Gb/s 1V-driving CMOS ring modulator with integrated thermal tuning," *Optics Express*, vol. 19, no. 21, p. 20435, oct 2011.

Chapter 5

High-speed performance of a TDFA-band micro-ring resonator modulator and demonstration of an optical link

Preface

The following chapter presents steady-state (DC) and high-speed measurements of a micro-ring resonator (MRR) modulator and a defect-mediated (DM) detector operating at thulium doped fiber amplifier (TDFA)-band wavelengths. Design and modelling aspects of the MRR modulator is based on the work presented in Chapter 3 and Chapter 4 while theoretical small-signal analysis presented in Section 5.4.1 is based on the methods explored in Chapter 2. A measured bandwidth of 12.5 GHz, limited by the external detector used during measurement, represents the first demonstration of a fully reverse biased MRR modulator operating at high-speed at this wavelength. Together with the DM detector, they form the first demonstration of a high-speed on-chip link operating

at TDFA-band wavelengths; a step toward the realization of a TDFA-band short-reach optical transceiver.

The work presented in this chapter will be written and submitted as a journal article in the future and is thus presented with a similar article structure as in Chapters 3 and 4. High-speed measurements were performed in collaboration with Dr. John Cartledge at Queen's University.

Abstract

We design and characterize an SOI MRR modulator and DM detector operating at a wavelength near 2 μm for use in the TDFA-band. The measured MRR modulator was critically-coupled with an unbiased notch-depth of 20 dB and Quality (Q)-factor of 4700. The measured resonance shift under reverse bias was 23 pm/V with a calculated $V_\pi L_\pi$ of 2.2 to 2.6 V-cm from -1 to -8 V, respectively. DC simulations performed using the Technology Computer-Aided Design (TCAD) commercial device modelling software Athena^{TM} and Atlas^{TM} by Silvaco, show good agreement with the measured data. The experimental bandwidth is 12.5 GHz, limited by the response of the external detector. Experimentally determined DC parameters were used to estimate the small-signal response using an analytic model which predicts excellent performance in the absence of RC-limiting factors. The DM detector had 1.97 μm wavelength responsivities of 0.042 and 0.14 A/W and bandwidths greater than 16 and 7.5 GHz at -15 and -30 V biases, respectively. Large signal measurements demonstrate open eye-diagrams for the DM detector (measured in isolation) and the on-chip link (modulator + detector) for 5, 10, and 12.5 Gigabits per second (Gbps) pseudorandom binary sequence (PRBS)-31 signals.

5.1 Introduction

Silicon photonics is being employed to address the growing bandwidth requirements of today's network infrastructure [1]. Multi-channel wavelength-division multiplexing (WDM) systems combined with advanced modulation techniques such as PAM-4 provide high data rates but will eventually be limited by the finite number of channels that fit within the telecommunication bands which benefit from optical amplifiers such as the erbium doped fiber amplifier (EDFA) and long-haul optical fibers. The mid-infrared (MIR) wavelength regime has become a promising solution to increase optical bandwidth by using a parallel window defined by the TDFA optical bandwidth, centered at 1.97 μm [2]. Advances in MIR component development such as hollow-core photonic band gap fibers (HC-PBGFs) [3], SOI high-speed detectors [4], and modulators [5] have paved the way to the realization of high-speed MIR transceivers. Recent work has demonstrated high-speed Mach-Zehnder modulators (MZM) operating within this optical bandwidth at 20 Gbps and the first demonstration of a MRR modulator operating at 3 Gbps in a hybrid carrier depletion and injection mode [6]. These results were obtained using an external high-speed detector which, in the case of the MZM, limited the high-speed performance. For the MRR modulator, an integrated driver was used to reduce high-speed (RF) reflection but high-speed performance is likely limited by the carrier recombination lifetime by operating in hybrid forward bias.

In this work, we demonstrate a driverless MRR modulator with an external detector limited 3 dB bandwidth of 12.5 GHz and a DM detector with a maximum 3 dB bandwidth of 16 GHz. Finally, these two devices are used to demonstrate, for the first time, an on-chip MIR optical link operating at 12.5 Gbps. The design of each device will be discussed, followed by DC and RF experimental setup information followed by measured DC and RF results. Performance of the MRR modulator is simulated through an analytical small-signal model which incorporates electrical, electro-optical, and optical parameters

extracted from DC measurements.

5.2 Design

The devices were fabricated at A*STAR IME using a 220 nm SOI platform. The MRR modulator and the DM detector will be discussed individually. The optical link features the MRR modulator followed by the DM detector approximately 2000 μm downstream. The decision to have the link on-chip is simply to avoid excess insertion loss during characterization.

5.2.1 Micro-ring resonator modulator

The design of the MRR modulator is a 15 μm radius all-pass ring resonator configuration with an integrated n^+-p junction diode for optical modulation covering approximately 86% of the ring. The waveguide width of 650 nm and junction offset of 150 nm toward the n^+-type region is optimized for reverse bias modulation of the 1.97 μm fundamental TE_0 mode. The highly-doped n^{++}- and p^{++}-type regions in the 90 nm slab are separated from the waveguide ridge by 1 μm. The MRR modulator also features a TiN heater for thermal resonance tuning (unused in this work) and Ground-Signal-Ground (GSG) electrodes for RF probing. An optical microscope image and cross-section of the MRR modulator is shown in Figure 5.1.

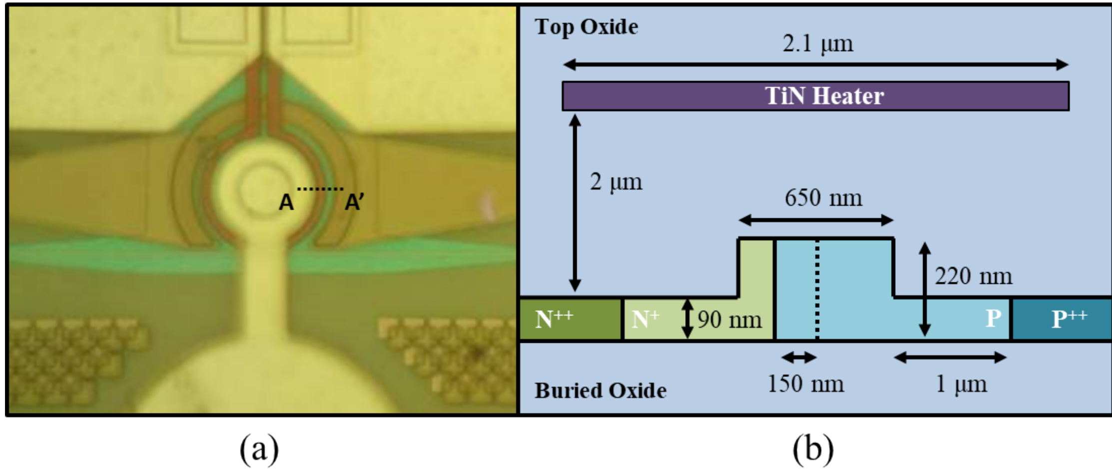

FIGURE 5.1: a) Optical microscope image of the MRR modulator and b) Cross-section of the MRR modulator across dashed cutline A-A'.

5.2.2 Defect-mediated detector

The DM detector comprises an integrated p-i-n diode structure across a 1 µm wide, 750 µm long waveguide with a 90 nm slab. The separation of the highly doped p^{++}- and n^{++}-type regions from the waveguide ridge is 300 nm, large enough to mitigate parasitic free-carrier absorption. A smaller separation, at the expense of increased parasitic absorption, is desirable for improved high-speed performance as it reduces transit time of photo-generated free-carriers. Featured is a 5 µm wide oxide window etch which leaves the silicon waveguide exposed for the introduction of optically-active defects through low energy ion implantation, most notably, the divacancy defect. The large oxide window width implies that defects from implantation may reside in the highly-doped slab region, possibly adversely affecting electrical performance through optically inactive trap sites. The device was implanted with boron at a dose of $1{\times}10^{13}$ cm^{-2} and energy of 70 keV introducing absorption in excess of 475 dB/cm, estimated by comparing transmission through unimplanted and implanted devices. An optical microscope image and cross-section of the DM detector is shown in Figure 5.2.

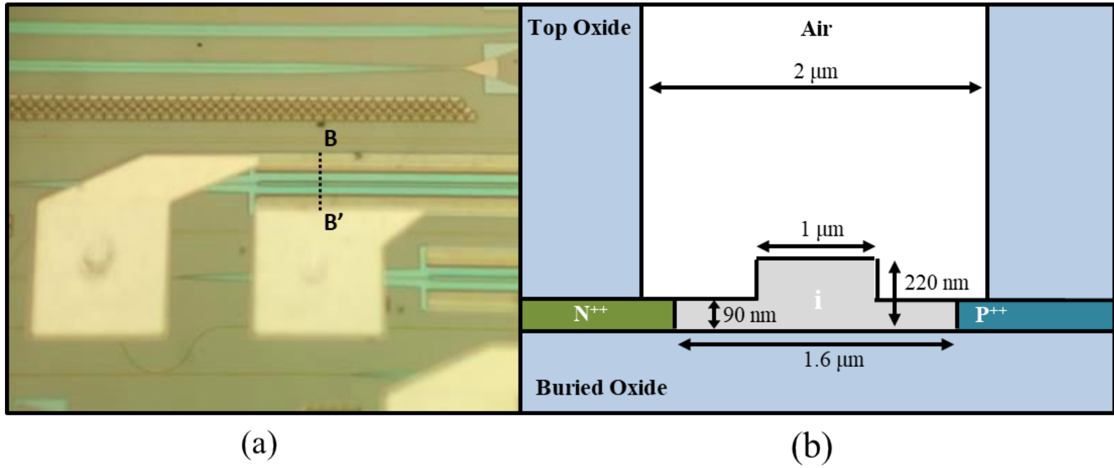

FIGURE 5.2: a) Optical microscope image of the DM detector and b) Cross-section of the DM detector across dashed cutline B-B’.

5.3 Methods and experimental setup

5.3.1 DC characterization setup

DC characterization of the MRR modulator was performed by launching linearly polarized light from a 2 μm wavelength Sacher Lasertechnik tuneable Littman/Metcalf laser source into a custom-built TDFA pumped by an erbium-ytterbium doped fiber amplifier (EYDFA) seeded by a 1.55 μm wavelength Agilent 81640A tuneable laser source. The signal was amplified sufficiently to overcome excess coupling loss while avoiding detrimental nonlinear self-heating effects which would destabilize the resonance or skew the spectral data during measurement. The light was then launched via cleaved fiber into a grating-coupled MRR modulator-only test structure and similarly collecting the light into a Thorlabs PDA10D InGaAs detector. The polarization was adjusted using polarization paddles and the device bias was controlled through electrical probes connected to a Keithley 2400 Source Meter.

The DM detector was characterized by launching linearly polarized light from the same 2 µm laser source via tapered fibers into a nanotaper-coupled DM detector-only test structure and extracting the photocurrent through electrical probes and the Keithley Source Meter.

5.3.2 RF characterization setup

Small-signal RF characterization of the MRR modulator was performed using the setup shown in Figure 5.3. The MRR modulator was thermally stabilized using a thermo-electric cooler (TEC) and reverse biased using GSG RF probes using the Keithley Source Meter and a bias tee. Small-signal S_{21} measurements were performed using an Anritsu 37397C Vector Network Analyzer (VNA) connected to the MRR modulator and an external EOT ET-5000F detector rated for 12.5 GHz operation. This external detector was measured separately using a setup similar to that shown in Figure 5.4.

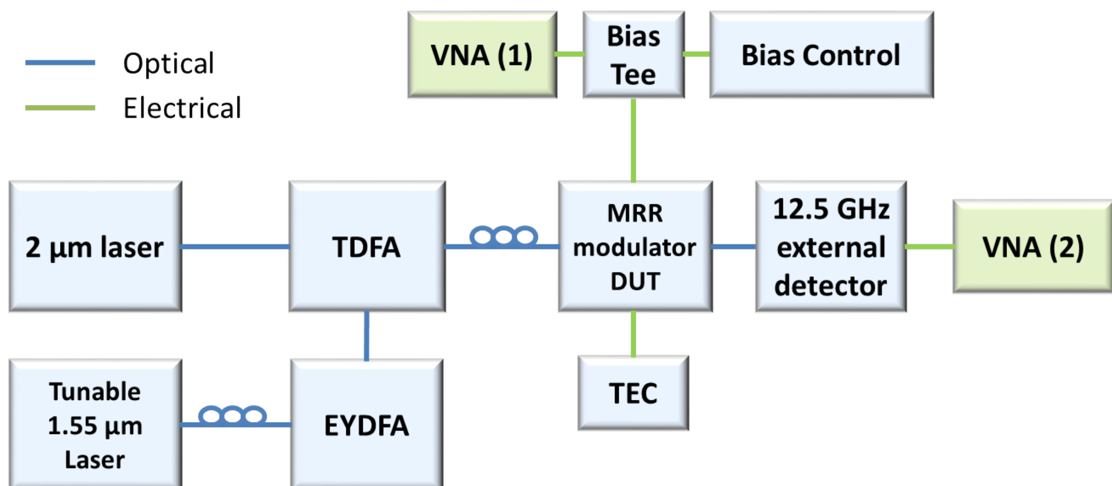

FIGURE 5.3: Small-signal setup for RF characterization of the MRR modulator.

Large-signal RF characterization of the MRR modulator was performed; however, the electrical output from the external ET-5000F detector was insufficient for the oscilloscope

to produce a clean eye-diagram, likely due to the combined large insertion loss of the MRR modulator near-resonance and the non-amplified nature of the external detector.

Small-signal RF characterization of the DM detector was performed using the setup shown in Figure 5.4. The DM detector was reverse biased using Ground-Signal (GS) RF probes using the Keithley Source Meter and a bias tee. Small-signal S_{21} measurements were performed using the VNA connected to an external Anritsu MP9681A E/O Converter, rated for 40 GHz operation, modulating 1.55 µm linearly polarized light from an ANDO AQ4321D single-line laser source amplified using an IPG Photonics EDFA, and the DM detector. 1.55 µm wavelength light was used instead of 2 µm due to the lack of available high-speed equipment designed for this wavelength.

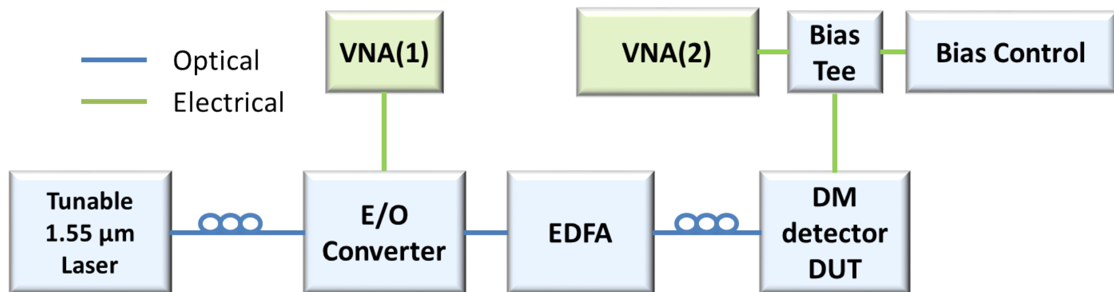

FIGURE 5.4: Small-signal setup for RF characterization of the DM detector.

Large-signal RF characterization of the DM detector was performed using the setup shown in Figure 5.5. It is similar to the small-signal setup but with an Anritsu MP1800A BPG providing a 2.5 V_{pp} PRBS-31 signal to the E/O Converter and an Agilent Infiniium DCA-J 86100C oscilloscope measuring the DM detector output eye-diagram.

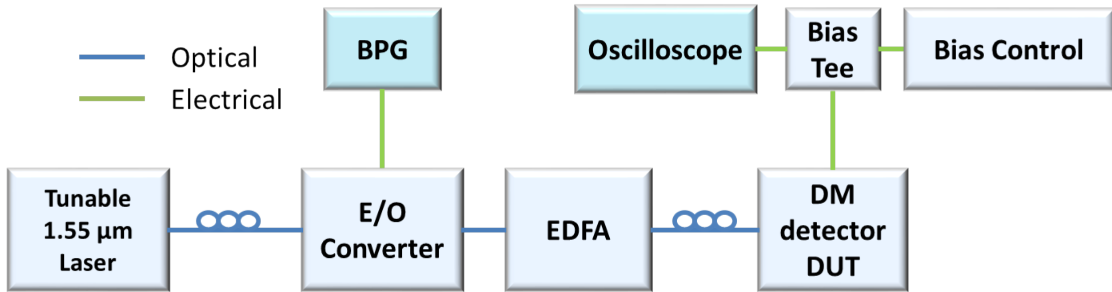

FIGURE 5.5: Large-signal setup for RF characterization of the DM detector.

Finally, large-signal RF characterization of the on-chip optical link (MRR modulator + DM detector) was performed using the setup shown in Figure 5.6. In this, the BPG sends the 2.5 V_{pp} PRBS signal to the MRR modulator through the GSG RF probes and the oscilloscope measures the electrical output from the DM detector through the GS RF probes. Bias control is available for both the MRR modulator and the DM detector.

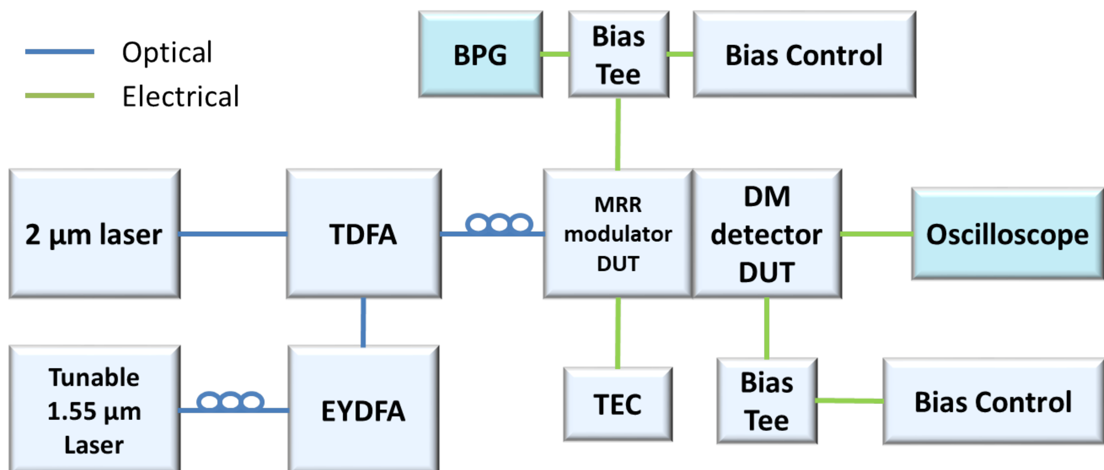

FIGURE 5.6: Large-signal setup for RF characterization of the on-chip optical link (MRR modulator + DM detector).

5.4 Results

5.4.1 Micro-ring resonator modulator

Free-carrier losses from the n-, p-, n^+-, and p^+-type regions used in the modulator were measured using cut-back waveguide test structures with doping throughout as to encompass the entire optical mode. Undoped test structures were also measured to determine background waveguide loss due to scattering. These measurements are shown in Figure 5.7.

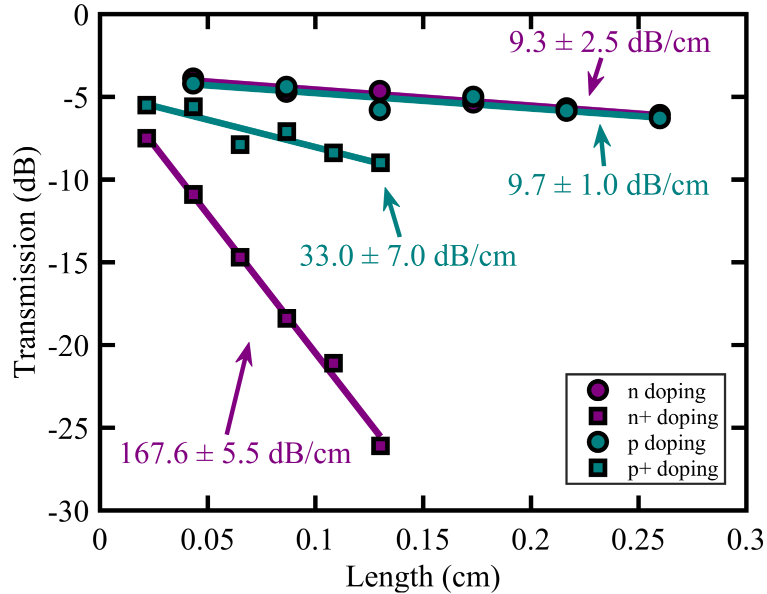

FIGURE 5.7: Free-carrier absorption in 2 μm wavelength doped waveguide test structures.

The background waveguide loss was measured to be 1.17 dB/cm thus the background-subtracted losses due to n-, n^+-, p-, and p^+-type dopants are 8.1, 166.4, 8.5, and 31.8 dB/cm, respectively. The cross-sectional free-carrier concentration profiles of these waveguide test structures were simulated in Silvaco using A⋆STAR IME's proprietary process flow and imported into RSoft's FEMSIM^{TM} suite through a custom MATLAB$^{®}$

interpreter protocol. The protocol converts a 2-D mesh of electron and hole concentration profiles to material imaginary refractive index profiles through the process detailed in [7]. FEMSIM^{TM} was then used to simulate the loss due to free-carrier interaction in the doped waveguide test structures. By fine-tuning the target dose in the simulated structures to match the free-carrier losses of each doping level, we can choose the appropriate dose to simulate the fabrication and characterization of the MRR modulator. The approximate simulated doping concentrations of the critical regions in the waveguide core are 4×10^{17} and 3×10^{18} cm^{-3} for the p- and n^{+}-type regions, respectively.

DC characterization of the MRR modulator was performed by recording the device spectrum for increasing reverse bias voltages. The biased spectra and associated on-off extinction ratio are shown in Figure 5.8.

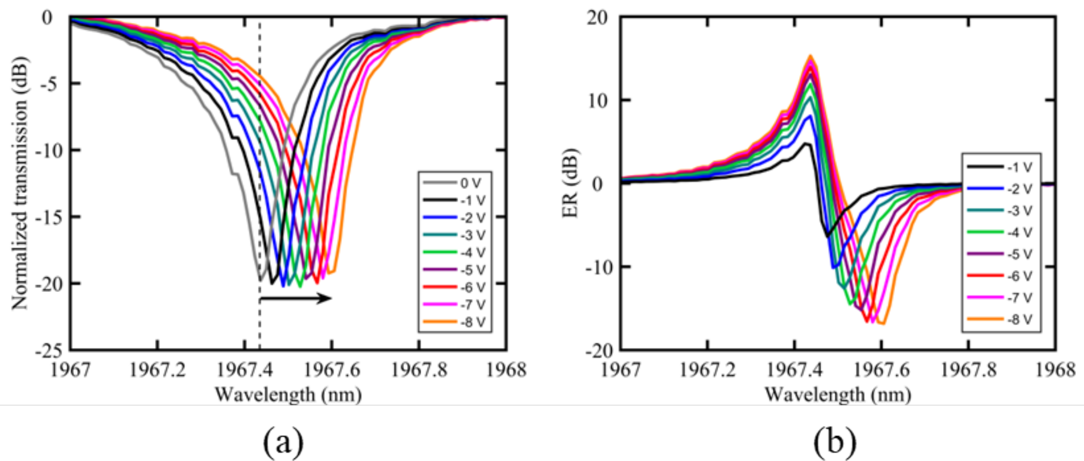

FIGURE 5.8: a) MRR modulator biased spectra and from 0 to -8 V and b) on-off extinction ratio for biases 0 to -8 V.

The measured biased resonance shifts, shown in Figure 5.9, were extracted from these biased spectra. Simulated results agree well with measured results.

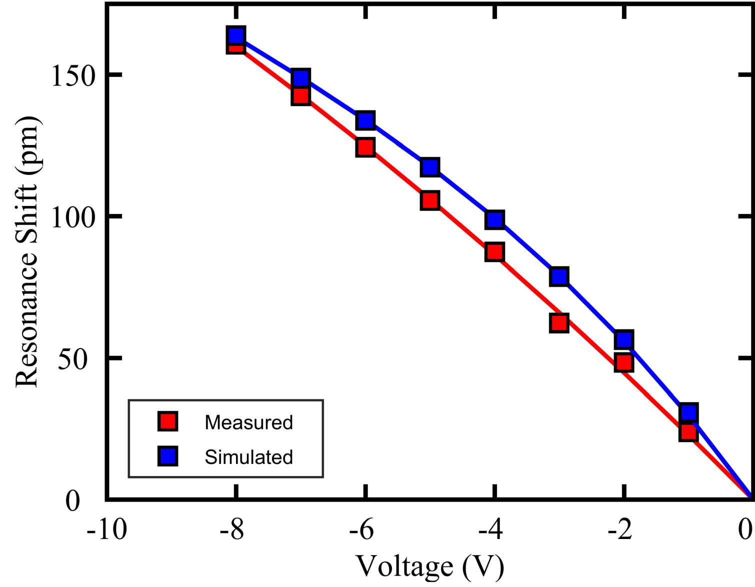

FIGURE 5.9: Measured and simulated biased resonance shift.

At low reverse -bias voltages, the resonance shift is approximately 23 pm/V, while the Q-factors and notch-depths of the ring at 0, and -8 V are 4700, and 5000 and 20.1, and 18.7 dB, respectively. At -1 and -8 V, the modulator has a $V_\pi L_\pi$ of 2.2 to 2.6 V-cm, calculated as:

$$V_\pi L_\pi = \frac{V \times FSR \times \pi R}{\Delta\lambda} \tag{5.1}$$

To simulate the biased resonance shifts, the MRR modulator cross-section was created in Silvaco, once again using A*STAR IME's process parameters but with the amended effective ion implantation doses determined from the measured free-carrier losses prior. The steady-state free-carrier profiles were simulated and used to determine the waveguide mode's effective indices at each bias voltage using FEMSIM^{TM}. The change in effective

index can be equated to a resonance shift through:

$$\Delta\lambda = \frac{2\pi R \Delta n_{eff}}{m} \tag{5.2}$$

where Δn_{eff} is the waveguide effective index change at a given voltage relative to the unbiased device, R is the ring radius of 15 µm, and m is the resonant order nearest 1.97 µm wavelength (in this case, $m = 112$). Contour plots of the hole and electron concentration profiles in the device cross-section at 0 and -4 V is shown in Figure 5.10.

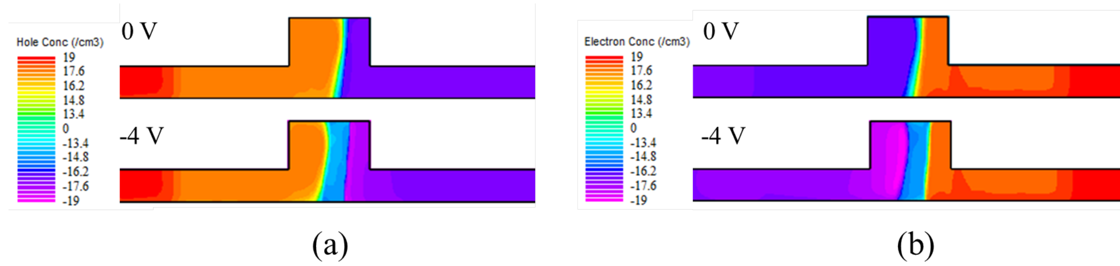

FIGURE 5.10: Contour plot of a) hole and b) electron concentrations in simulated device for 0 and -4 V bias.

Due to the large difference in doping concentration between the p- and n^+-type regions, the depleted region of the junction extends mostly toward the p-type region with increasing reverse bias. This presents a design trade-off between the junction offset and operating bias. To demonstrate this, the biased resonance shift was simulated while varying the junction offset from 0 to 300 nm. The results are shown in Figure 5.11.

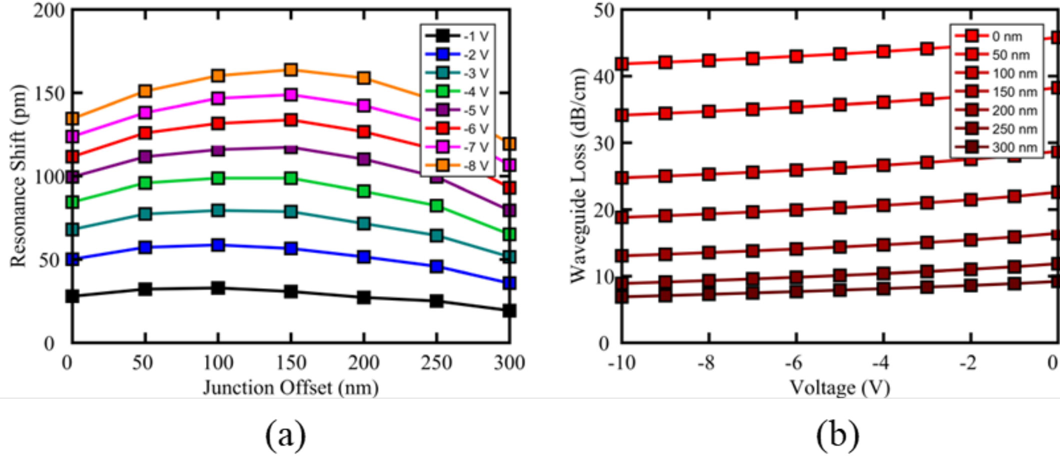

FIGURE 5.11: a) Reverse bias resonance shift as a function of junction offset for various voltages and b) waveguide loss as a function of voltage for various junction offsets.

Figure 5.11 a) shows that for low voltages, the optimal junction offset for efficient modulation begins at approximately 100 nm and quickly approaches 150 nm with increased reverse bias; however, Figure 5.11 b) shows that a lower junction offset quickly increases in loss as the n^+-type region encompasses more of the optical mode. While this can improve the electrical bandwidth of the modulator if it is limited by the photon cavity lifetime, it must be weighed against the accompanying decrease in Q-factor.

We investigate the theoretical bandwidth through modeling of the MRR modulator using the small-signal transfer function described in [8]. This model includes components which describe the electrical characteristics of the n^+-p junction, the electro-optical properties (i.e. dynamic change in photon cavity lifetime), and the purely optical characteristics of the resonator. The model also describes the effect of optical peaking which is a modulation bandwidth increase that occurs when the rise time of the modulation signal is comparable to the photon cavity lifetime of the resonator and appears as a "bump" in a high-speed S_{21} measurement. The sudden change in refractive index causes the light inside the ring to be slightly detuned relative to the light in the bus waveguide

which causes an overshoot of light coupled out of the ring as it does not immediately interfere. This overshoot oscillates with a frequency proportional to the detuning and settles as a damped oscillation with a decay rate related to the photon cavity lifetime [9]. The wavelength detuning from resonance as well as the peak-to-peak driving voltage will have an impact on optical peaking as it requires a sufficient amount of built-up light in the ring to be "released" when the resonance is shifted. To investigate the theoretical bandwidth of the designed MRR modulator, we begin with the electrical transfer function given as:

$$H_E(\omega_m) = \frac{1}{1 + j\omega_m R_j C_j} \tag{5.3}$$

where ω_m is the modulation angular frequency applied from a small sinusoidal electrical signal $V(t) = V_{in}\cos(\omega_m t)$, and R_j and C_j are the access resistance and junction capacitance, respectively. The resistive elements are calculated using the resistivity of doped silicon at the simulated doping concentrations and the dimensions of the waveguide through $R = \rho w/t$, where ρ is the resistivity, w is the region width, and t is the core or slab thickness. R_j can be calculated as:

$$R_j = \frac{(R_{n_slab} + R_{p_slab} + R_{n_core} + R_{p_core})}{L} + R_{load} \tag{5.4}$$

where L is the active length of the device (in this case, 86% of the ring circumference) and R_{load} is a 50 Ω series load resistance from the measurement system. We see that a reduction in the spacing between the waveguide core and the highly-doped contact regions would lead to a decrease in R_j, though this is accompanied by increased parasitic absorption which will decrease the photon cavity lifetime and decrease the on-off extinction ratio. The depletion width W_d, which is calculated using a 1-D approximation [10],

is assumed to extend (from the junction offset of 150 nm toward the n^+-type region) mostly across the p-type region due to the higher doping concentration of the n^+-type region. Thus, the width, w, used to calculate R_{p_core} is approximately equal to half the waveguide width plus the junction offset minus W_d. C_j is calculated through the same 1-D approximation, given as [10]:

$$C_j = \frac{\varepsilon_0 \varepsilon_r A}{W_d} \tag{5.5}$$

where ε_0 is the permittivity of free space, ε_r is the relative permittivity of silicon, and A is the transverse area of the active region, the product of the core thickness and the active device length. Additional capacitances through fringing fields are incorporated but do not significantly impact the total junction capacitance in this case [11]. W_d will vary with reverse bias voltage, thus R_j and C_j will also be affected, thus the estimated RC-limited bandwidth, calculated in isolation as $f_{RC} = 1/(2\pi R_j C_j)$, will be a voltage-dependent quantity. It should be noted here that additional resistance and capacitance due to the electrode design contacting the MRR modulator, RF probes, and the measurement apparatus itself, can have a significant impact on the high-speed performance of the device. Thus we restrict this theoretical calculation only to the calculated R_j and C_j, which at a bias of -2 V, are approximately 200 Ω and 22.3 fF, respectively, which leads to an estimated f_{RC} of 35 GHz. The electro-optical portion, H_{EO}, of the transfer function, which takes into account the change in complex refractive index with voltage across the n^+-p junction, is described by:

$$H_{EO} = \left(\frac{-\omega_r}{n_g} \frac{\delta n_{eff}}{\delta V} \bigg|_{V_{DC}} + j \frac{\delta(1/\tau)}{\delta V} \bigg|_{V_{DC}} \right) \tag{5.6}$$

where ω_r is the resonance angular frequency, n_g is the group index, $\delta n_{eff}/\delta V$ is the

effective index change of the waveguide mode, while $\delta(1/\tau)/\delta V$ is the change in photon cavity decay rate both as a function of applied DC voltage; the latter and former describing the dynamic change in the real and imaginary effective index of the waveguide mode. The values of $\delta n_{eff}/\delta V$ are extracted from the resonance shift data in Figure 5.9 and using (5.2). At a bias of -2 V, $\delta n_{eff}/\delta V$ = -2.52×10^{-5} V^{-1}. To arrive at $\delta(1/\tau)/\delta V$, we calculate the photon cavity lifetime, τ, through:

$$\tau = \frac{Q\lambda_{res}}{\pi c} \tag{5.7}$$

where Q is the Q-factor, λ_{res} is the resonant wavelength, and c is the speed of light. Since there is a measured Q-factor for each bias, we may calculate an associated τ and subsequently, $\delta(1/\tau)/\delta V$ which, for a bias of -2 V is 1.01×10^{9} V^{-1}s^{-1}. The photon lifetime can be expressed as $\tau^{-1} = \tau_l^{-1} + \tau_e^{-1}$ where τ_l and τ_e are the amplitude decay time constants due to intrinsic loss within the ring and power out-coupling due to the bus waveguide, calculated as [8]:

$$\tau_l = \frac{2}{\nu_g \alpha} \tag{5.8}$$

$$\tau_e = \frac{2L}{\nu_g \kappa^2} \tag{5.9}$$

where ν_g is the group velocity, related to the group index n_g through $\nu_g = c/n_g$, α is the absorption coefficient, L is the cavity length, and κ is the cross-coupling coefficient, related to the self-coupling coefficient r through κ^2= 1 - r^2. We point out that the biased spectra in Figure 5.8 a) represent a critically-coupled MRR modulator at approximately -4 V. A ring resonator is critically-coupled when $\tau_e = \tau_l$, thus through (5.7), we use the

critically-coupled biased resonance and Q-factor (approximately 4800) to calculate τ to be 10.1 ps and $\tau_e = \tau_l = 20.2$ ps. τ_e will not change with bias, thus we can now calculate τ_l for the remainder of the biases. We can estimate the optically-limited bandwidth through $f_Q = 1/(\pi\tau)$ which, for a bias of -2 V is 31.5 GHz, slightly lower than the estimated f_{RC}. It is known that when these two bandwidth limitations are involved, their cumulative effect is calculated as:

$$\frac{1}{{f_{Total}}^2} = \frac{1}{{f_{RC}}^2} + \frac{1}{{f_Q}^2} \tag{5.10}$$

which, from the values calculated for a reverse bias of -2 V, yields a reduced f_{Total} of 23.4 GHz, although this estimation does not factor in the effect of optical peaking from resonance detuning. We may now use the final equation to estimate the modulation transfer function:

$$H_t\left(\omega_m\right) = \frac{2\mu^2 P_{in}(-\frac{\omega_r}{n_g}\frac{\delta n_{eff}}{\delta V}) \mid_{V_{DC}}}{\frac{1}{\tau^2} + \Delta\omega^2} \frac{\left(\tan\left(\phi_{HEO}\right)\right)\left(\frac{1}{\tau_l} - \frac{1}{\tau_e}\right) - \Delta\omega}{1 + j\omega_m R_{eq} C_{eq}} \times \left[\frac{j\omega_m - \frac{2\frac{\Delta\omega}{\tau_l} + \tan(\phi_{HEO})\left(\Delta\omega^2 - \frac{1}{\tau}\left(\frac{1}{\tau_l} - \frac{1}{\tau_e}\right)\right)}{\tan(\phi_{HEO})(\frac{1}{\tau_l} - \frac{1}{\tau_e}) - \Delta\omega}}{-\omega_m^2 + \frac{2}{\tau}\left(j\omega_m\right) + \Delta\omega^2 + \frac{1}{\tau^2}} \right] \tag{5.11}$$

where μ is the mutual ring to bus waveguide coupling coefficient, calculated as $\mu^2 = 2/\tau_e$, P_{in} is the input power (here normalized to 1), $\Delta\omega = \omega_o - \omega_r$ is the frequency detuning where ω_o is the input laser frequency, and ϕ_{HEO} is the phase of H_{EO}. $H_t(\omega_m)$ is shown for the MRR modulator in Figure 5.12.

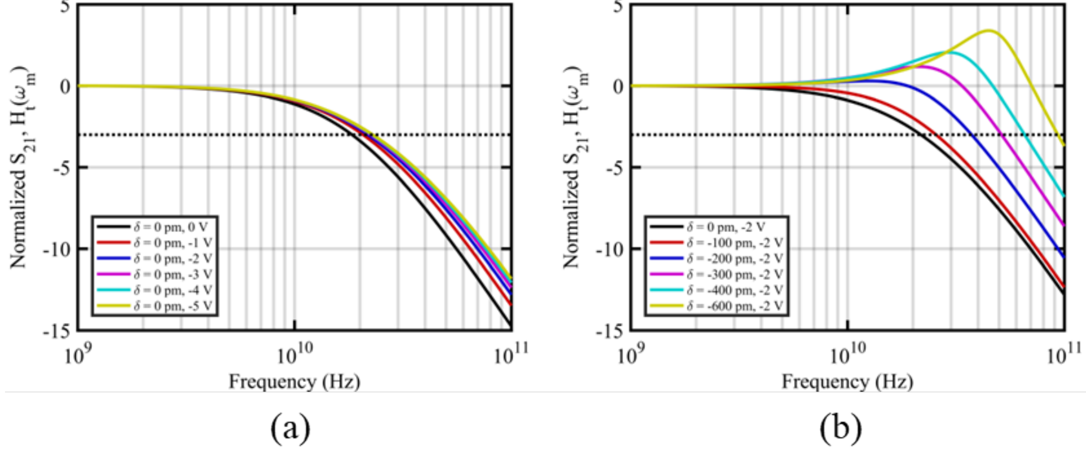

FIGURE 5.12: a) Normalized $H_t(\omega_m)$ for the MRR modulator device for zero resonance detuning varying in bias and b) for a fixed bias of -2 V and various values of blue-side resonance detuning. The dotted line denotes the -3 dB bandwidth.

We notice from Figure 5.12 a) that the 3 dB bandwidth is enhanced under reverse bias mostly due to the reduction in C_j. The depletion of carriers from the waveguide decreases the cavity loss which increases τ, thus the optical bandwidth actually decreases at the same time, but to a lesser extent. From Figure 5.12 b) we see the optical peaking effect begin to emerge for detunings larger than -100 pm leading to enhanced bandwidth. Due to the small Q-factor and the small τ associated with it, optical peaking occurs toward higher frequencies thus in a system with RC-limitations below these frequencies, the peaking effect may not play much of a role in enhancing the bandwidth. It is useful to examine the 3 dB bandwidth as a function of detuning, as shown in Figure 5.13:

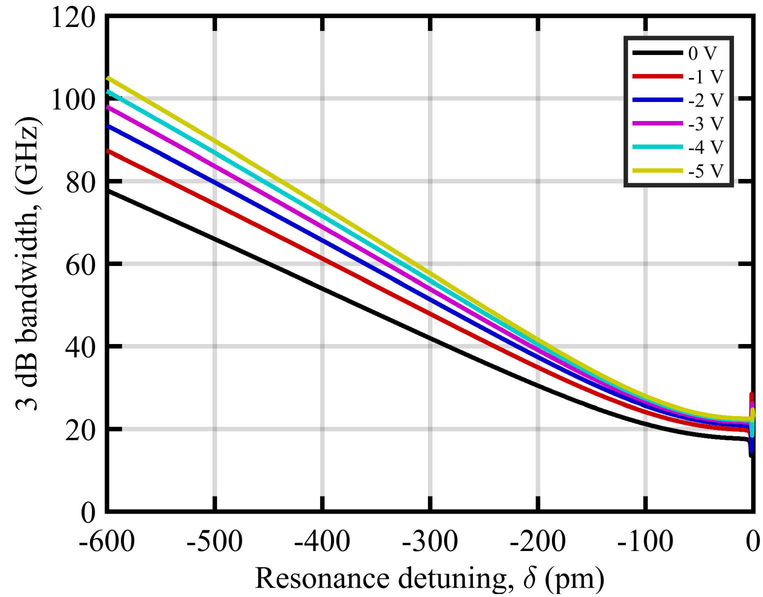

FIGURE 5.13: Calculated -3 dB bandwidth of the MRR modulator device for various reverse bias voltages as a function of resonance detuning.

It is clear that beyond a detuning of approximately -100 pm the 3 dB bandwidth begins to increase, approximately linearly. As compared with the estimated f_{Total}, the bandwidth becomes significantly enhanced by simply detuning the wavelength from resonance. As reverse bias voltage increases, the bandwidth is enhanced approximately quadratically as expected by the quadratic increase in depletion width which influences both $\delta(1/\tau)/\delta V$ and $\delta n_{eff}/\delta V$. Although the bandwidth continues to increase with detuning, this is at the expense of the optical amplitude modulation [12]. The DC gain (G_{DC}), which is evaluated as $H_t(0)$, is a small-signal parameter which describes the modulation efficiency. It is frequently calculated along with an important small-signal figure-of-merit known as the gain-bandwidth (GBW) product used to determine the optimal detuning to maximize bandwidth and G_{DC}. The normalized G_{DC} and GBW product are shown in Figure 5.14 a) and b), respectively.

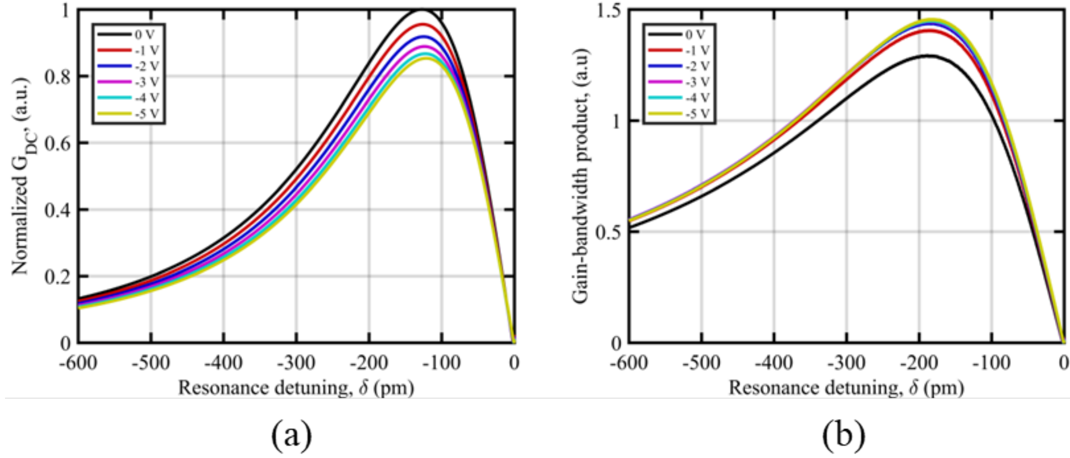

FIGURE 5.14: a) Normalized G_{DC} of the MRR modulator for various reverse biases as a function of detuning and b) associated GBW product.

The maximum G_{DC} for each voltage occurs at a non-zero detuning where, for a small modulation signal, the largest effect may occur. In this case $\delta n_{eff}/\delta V$ is largest at 0 V, therefore the largest G_{DC} is expected and all curves have been normalized as such. With increasing reverse bias, $\delta n_{eff}/\delta V$ begins to decrease quadratically, as does G_{DC}. The GBW product, in this case, reaches a global maximum at a non-zero reverse bias as the decrease in $\delta n_{eff}/\delta V$ is countered by the increase in bandwidth. Due to the increase in bandwidth with detuning, the optimal detuning for the GBW product is pushed further out compared to the optimal detuning for maximum G_{DC}. $H_t(\omega_m)$ is a small-signal calculation and as such does not adequately predict the optimal operating point in the large-signal domain. Nevertheless, it is a good tool to have at one's disposal to estimate the performance of a MRR modulator with many factors involved.

Small-signal RF characterization of the MRR modulator yielded a 3 dB electrical bandwidth of greater than 12.5 GHz, limited by the external ET-5000F detector. Figure 5.15 shows the small-signal response of the MRR modulator biased at -2 V with a resonance detuning of -540 pm, and the ET-5000F external detector.

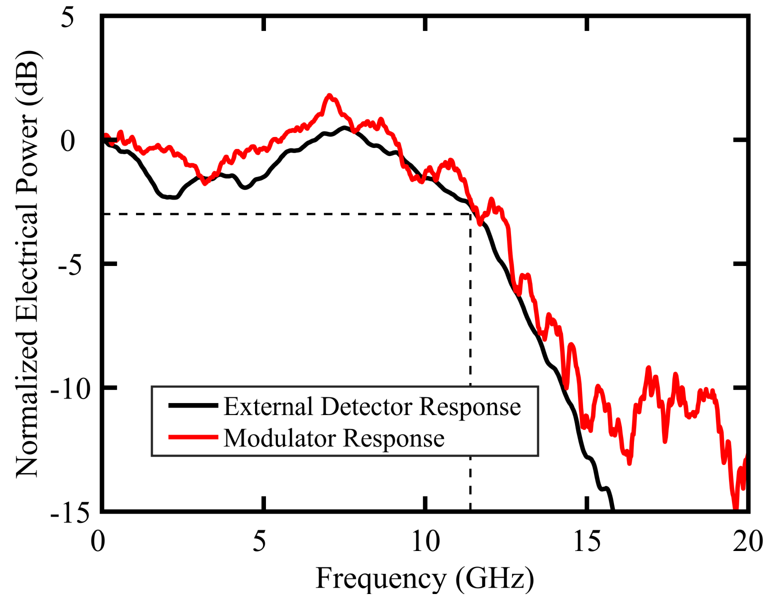

FIGURE 5.15: Small-signal RF measurement of the MRR modulator.

The 540 pm resonance detuning was chosen to maximize the electrical bandwidth but at the expense of modulation amplitude [12]. Although the MRR modulator is limited by the external detector, it is expected to operate at higher speeds as a similar design which operates at 1.55 µm with n^{++}- and p^{++}-type region separations of 2.1 µm and demonstrated with a bandwidth of greater than 17 GHz [13]. From the calculated small-signal results, better performance is predicted in the absence of RC-limiting factors from the electrode design and measurement apparatus.

5.4.2 Defect-mediated detector

DC characterization of the DM detector was performed by measuring the device dark current and photocurrent of edge-coupled test devices under increasing reverse bias for different laser input powers at both 1.97 and 1.55 µm wavelengths. The coupling losses

of the nanotaper for each wavelength were measured to be 2.24 and 0.70 dB, respectively. The results are shown in Figure 5.16.

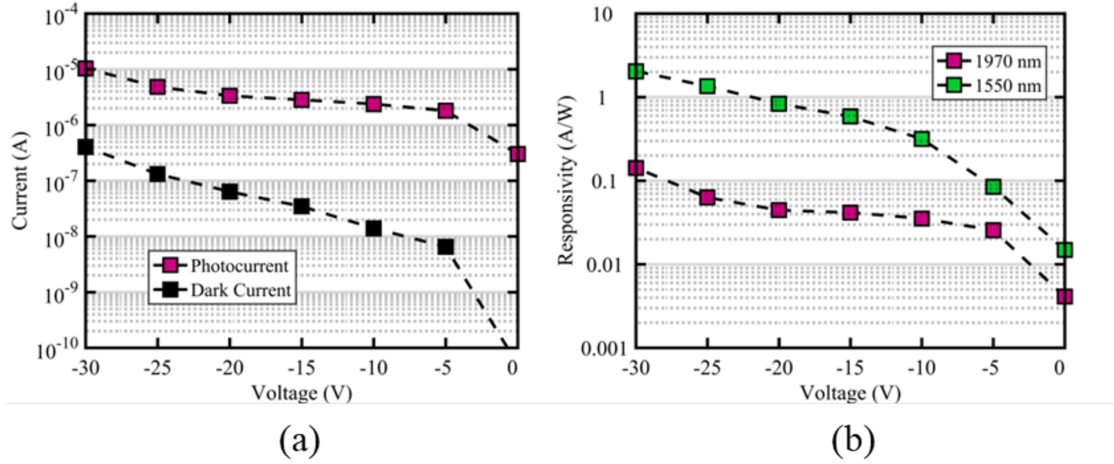

FIGURE 5.16: a) DM detector dark current and photocurrent for 1.97 µm wavelength with input power of 0.06 mW after coupling losses and b) DM detector responsivities as a function of reverse bias voltage for both 1.97 and 1.55 µm wavelengths.

The dark current remains very low despite the intentional introduction of defects even as the device begins to avalanche approaching -30 V. The DM detector responsivity at 1.97 µm wavelength is 0.04 and 0.14 A/W at -15 and -30 V, respectively. At 1.55 µm wavelength, the responsivity is 0.59 and 2.04 A/W at -15 and -30 V, respectively. The data shows improved performance at 1.55 µm over 1.97 µm wavelength as expected due to the mid-band gap nature of the optically-active divacancy defect.

Small-signal RF measurements of the DM detector yielded a 3 dB electrical bandwidth of greater than 16 GHz at a reverse bias of -15 V and a photocurrent of 150 µA, which corresponds to an optical power of 0.25 mW at 1.55 µm wavelength. Greater reverse biases exhibit greater gain from stronger avalanching but lower bandwidth by virtue of the gain-bandwidth trade-off. The small-signal response results are shown in Figure 5.17.

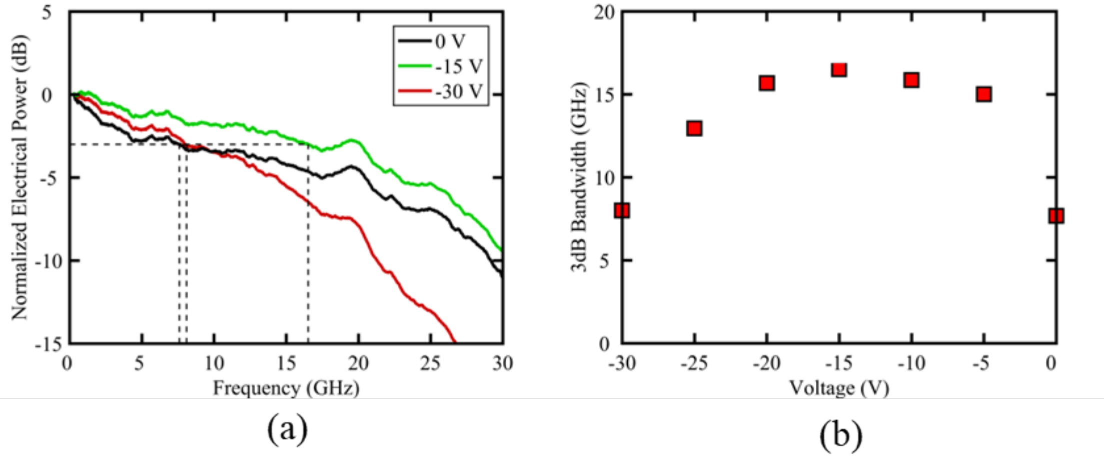

FIGURE 5.17: a) Small-signal measurement of the DM detector and b) 3 dB electrical bandwidth at various voltages.

The bandwidth of the DM detector increases with reverse bias due to the increase in electric field strength across the intrinsic region of the *p*-*i*-*n* diode which reduces carrier transit time. As the device enters the avalanche regime, the bandwidth begins to decrease by virtue of the gain-bandwidth product. The avalanche process in the sudden presence or absence of a signal will have a certain rise/fall time due to the impact ionization kinetics.

Large-signal RF measurements were performed at a bias of -15 V where the highest electrical bandwidth was determined from the small-signal results. The optical power was adjusted to keep the device photocurrent at approximately 1 mA, which corresponds to optical power of 1.7 mW at 1.55 µm wavelength. The BPG supplied a 2.5 V_{pp} PRBS-31 signal at 5, 10, and 12.5 Gbps. The recorded eye-diagrams are shown in Figure 5.18.

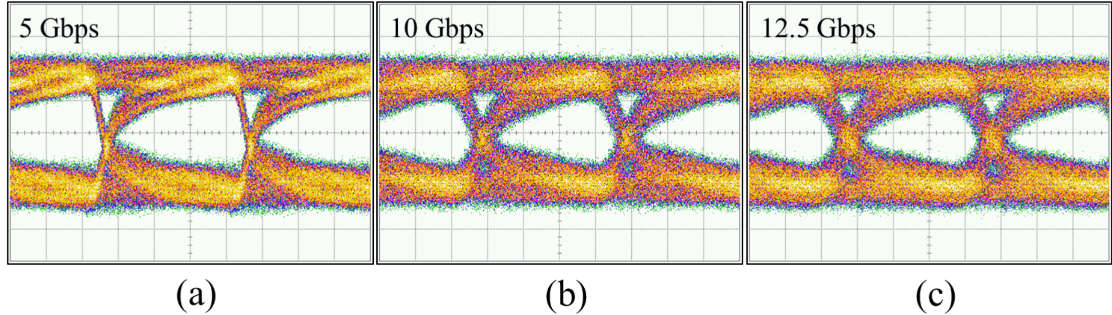

FIGURE 5.18: Eye-diagrams for DM detector at -15 V bias for a) 5 b) 10, and c) 12.5 Gbps PRBS-31 signals. Vertical (voltage) divisions are 17.5, 16.2, and 16.4 mV/div, respectively, and horizontal (time) division are 20 ps/div for all.

Open eye-diagrams are observed at 5, 10, and 12.5 Gbps. Testing at higher data rates was not performed due to equipment restrictions, but open eye-diagrams would be expected at higher data rates as the device dimensions are similar to previous work shown to operate with open eye-diagrams up to 20 Gbps at -15 V for a lower PRBS length of 2^7-1 as opposed to the 2^{31}-1 in this work [4]. Similarly, these results were obtained without the use of a trans-impedance amplifier (TIA) which would significantly improve the eye-diagram quality.

5.4.3 On-chip optical link

Large-signal measurements of the on-chip optical link were performed with the MRR modulator reverse biased at -2 V and a PRBS-31 signal with a V_{pp} of 2.5 V supplied by the BPG. The laser wavelength was blue-side detuned from resonance. The DM detector was held at a larger reverse bias of -30 V and the optical power was adjusted to maintain a photocurrent of 1 mA which corresponds to an optical power of 7.14 mW. The recorded eye-diagrams are shown in Figure 5.19.

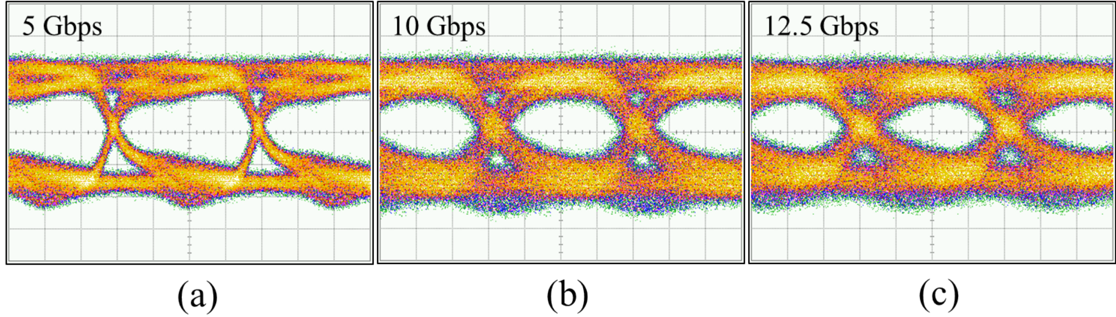

FIGURE 5.19: Eye-diagrams for on-chip optical link for a) 5 b) 10, and c) 12.5 Gbps PRBS-31 signals. Vertical (voltage) divisions are 9.2, 8.6, and 8.3 mV/div, respectively, and horizontal (time) division are 20 ps/div for all.

Open eye-diagrams are observed at 5, 10, and 12.5 Gbps. The larger reverse bias of the detector results in lower electrical bandwidth, as seen in Figure 5.17, which is evident in the eye-diagram quality beyond 5 Gbps. As the DM detector electrical bandwidth at this voltage is the limiting factor, the addition of a TIA would greatly improve the eye-diagram quality for the entire on-chip link. Impedance mismatch between the RF probes connected the 50 Ω terminated measurement equipment and the device leads to large RF reflections which also negatively impacts the eye-diagram. This could be remedied through the design of an integrated 50 Ω doped-silicon resistor in parallel with the MRR modulator [14]. Additionally, 50 Ω RF probes can be used in future measurements. One may estimate the energy consumption per bit of the MRR modulator through [15]:

$$E_{bit} = \frac{1}{4} C {V_{pp}}^2 \tag{5.12}$$

where V_{pp} is the peak-to-peak voltage swing of a large-signal modulation, and C is the total capacitance of the system. If we assume $C = C_j$, a reverse bias of -2 V, and a peak-to-peak voltage swing of 2.5 V, E_{bit} is as low as 35 fJ/bit. This energy consumption

decreases with larger reverse biases and smaller peak-to-peak voltage swings but at the expense of modulation depth.

5.5 Conclusion

We have demonstrated the high-speed operation of a MIR SOI-based MRR modulator operating without an integrated modulation driver at a detector-limited bandwidth of 12.5 GHz. Combined in an optical link with a TIA-less high-speed detector operating with a maximum bandwidth of 16 GHz, open eye-diagrams up to 12.5 Gbps have been demonstrated. Doped waveguide test structures were measured and used to replicate fabrication doping conditions using A*STAR IME's confidential recipes. These fabrication conditions were then applied in the simulation of the MRR modulator using Silvaco in conjunction with RSoft's FEMSIM^{TM}. DC characterization of the MRR modulator shows excellent modulation performance and good agreement with simulated results. The design trade-off between junction offset and modulation performance and waveguide loss was simulated using these conditions to show that the choice of 150 nm junction offset is optimal for maximized performance. Small-signal calculations were performed using a model which incorporates electrical, electro-optical, and optical parameters to estimate high-speed performance of the fabricated device, showing trade-offs in bandwidth and modulation efficiency. RF performance of the MRR modulator was shown to be limited by the external detector but better performance is predicted from the small-signal modelling in the absence of RC-limiting factors in the measurement apparatus. DC measurements of the DM detector showed 1.97 µm wavelength responsivities of 0.04 and 0.14 A/W at -15 and -30 V, respectively. The DM detector exhibited a maximum electrical bandwidth of 16 GHz at -15 V and approximately half of this at -30 V. The on-chip optical link was shown to be limited by the DM detector and is expected to operate at higher speeds in a future design replacing the grating coupler input with a nanotaper

which will significantly improve the signal amplitude reaching the DM detector allowing it to operate at lower biases and thus higher bandwidths. In future, measurements will be performed to explore the gain-bandwidth trade-off of the DM detector.

Bibliography

[1] R. Won, “View from... Communication Networks Beyond the Capacity Crunch: Is it crunch time?” *Nature Photonics*, vol. 9, no. 7, pp. 424–426, jun 2015.

[2] Z. Li, A. M. Heidt, N. Simakov, Y. Jung, J. M. O. Daniel, S. U. Alam, and D. J. Richardson, “Diode-pumped wideband thulium-doped fiber amplifiers for optical communications in the 1800 - 2050 nm window.” *Optics express*, vol. 21, no. 22, pp. 26 450–5, nov 2013.

[3] Y. Chen *et al.*, “Multi-kilometer Long, Longitudinally Uniform Hollow Core Photonic Bandgap Fibers for Broadband Low Latency Data Transmission,” *Journal of Lightwave Technology*, vol. 34, no. 1, jan 2016.

[4] J. J. Ackert, D. J. Thomson, L. Shen, A. C. Peacock, P. E. Jessop, G. T. Reed, G. Z. Mashanovich, and A. P. Knights, “High-speed detection at two micrometres with monolithic silicon photodiodes,” *Nature Photonics*, vol. 9, no. 6, pp. 393–396, may 2015.

[5] M. A. Van Camp, S. Assefa, D. M. Gill, T. Barwicz, S. M. Shank, P. M. Rice, T. Topuria, and W. M. J. Green, “Demonstration of electrooptic modulation at 2165nm using a silicon Mach-Zehnder interferometer,” *Optics Express*, vol. 20, no. 27, pp. 28 009–16, dec 2012.

[6] W. Cao *et al.*, “High-speed silicon modulators for the 2 μm wavelength band,” *Optica*, vol. 5, no. 9, p. 1055, sep 2018.

[7] D. E. Hagan, M. Nedeljkovic, W. Cao, D. J. Thomson, G. Z. Mashanovich, and A. P. Knights, "Experimental quantification of the free-carrier effect in silicon waveguides at extended wavelengths," *Optics Express*, vol. 27, no. 1, p. 166, jan 2019.

[8] S. Karimelahi, "Silicon Ring Modulators for High-speed Optical Interconnects," Ph.D. dissertation, University of Toronto, 2016.

[9] Q. Xu, B. Schmidt, J. Shakya, and M. Lipson, "Cascaded silicon micro-ring modulators for WDM optical interconnection," *Optics Express*, vol. 14, no. 20, p. 9431, oct 2006.

[10] B. G. Streetman and S. Banerjee, *Solid state electronic devices.* Prentice Hall., 2016.

[11] H. Jayatilleka, W. D. Sacher, and J. K. S. Poon, "Analytical Model and Fringing-Field Parasitics of Carrier-Depletion Silicon-on-Insulator Optical Modulation Diodes," *IEEE Photonics Journal*, vol. 5, no. 1, pp. 2 200 211–2 200 211, feb 2013.

[12] H. Yu, D. Ying, M. Pantouvaki, J. Van Campenhout, P. Absil, Y. Hao, J. Yang, and X. Jiang, "Trade-off between optical modulation amplitude and modulation bandwidth of silicon micro-ring modulators," *Optics Express*, vol. 22, no. 12, p. 15178, jun 2014.

[13] Z. Wang, Y. Gao, A. S. Kashi, J. C. Cartledge, and A. P. Knights, "Silicon Microring Modulator for Dispersion Uncompensated Transmission Applications," *Journal of Lightwave Technology*, vol. 34, no. 16, pp. 3675–3681, aug 2016.

[14] H. Yu and W. Bogaerts, "An Equivalent Circuit Model of the Traveling Wave Electrode for Carrier-Depletion-Based Silicon Optical Modulators," *Journal of Lightwave Technology*, vol. 30, no. 11, pp. 1602–1609, jun 2012.

[15] D. A. B. Miller, "Energy consumption in optical modulators for interconnects," *Optics Express*, vol. 20, no. S2, p. A293, mar 2012.

Chapter 6

Post-fabrication trimming of silicon ring resonators via integrated annealing

Preface

The following chapter presents a post-fabrication trimming technique for use in microring resonators (MRRs) and MRR modulators with integrated heaters through the local annealing of lattice defects. Through implantation of increasing doses of ions, introducing more lattice defects, the resonance trimming distance increases. In MRR-based devices, manufacturing variation often leads to deviation of device resonances from target. Trimming techniques are then employed to correct (partially or fully) for this deviation. Many demonstrated techniques are discussed, but it is emphasized that this technique allows for extremely precise resonance shifting with careful control of applied heater bias and duration. This chapter demonstrates alignment of a 4-ring MRR system designed for dense wavelength-division multiplexing (DWDM) applications, with each resonance ultimately spaced by 50 GHz to within ±15 pm of their respective wavelength

targets. Heater power consumption and power saving through partial- and full-alignment of WDM and stacked resonance systems through resonance trimming is explored further in Chapter 7 based on the devices presented here and extended to MRRs designed for thulium doped fiber amplifier (TDFA)-band wavelengths.

While the majority of the work presented in this chapter has been published, the authors now suggest that the resonance shift in unimplanted samples is primarily due to thermally-induced restructuring of the low-quality thermal oxide deposited onto the silicon waveguides causing a change in top cladding refractive index. Section 6.4 is added within the text to include oxide restructuring simulation results in the context of both EDFA- and TDFA-band wavelength MRRs. Similarly, measured results presented here regarding resonance trimming for varying ion implantation doses were performed exclusively at a wavelength of 1550 nm. Section 6.3 is added within the text which includes measured data of absorption through defect-implanted waveguide structures at both 1550 and 2000 nm to elaborate on resonance trimming implications in both wavelength regimes.

David E. Hagan, Benjamin Torres-Kulik, and Andrew P. Knights

McMaster University, 1280 Main Street West, Hamilton, ON, Canada

This paper was published in the *IEEE Photonics Technology Letters* on August 15, 2019.

DOI: 10.1109/LPT.2019.2927323

Abstract

We report post-fabrication trimming of silicon-on-insulator micro-ring resonators via annealing of lattice defects using integrated micro-heaters. Defects are introduced via an inert MeV boron ion implantation at doses ranging from 3×10^{10} to 3×10^{13} cm^{-2}. Ion implantation results in a stable red-shift ranging from 20 to 1200 pm, for the stated dose range. Post-implantation annealing produces a subsequent blue-shift ranging from 380 to 800 pm, dependent on the implantation dose, indicating partial recovery of the silicon lattice through removal of the implantation-induced defects. Evidence is shown also for a resonance blue-shift associated with modification of the micro-ring, even without a prior ion implantation step. With the method described in this work we demonstrate precise trimming of a four-ring filter such that the resonances are separated by 50 GHz, despite the as-fabricated rings having a random resonance separation resulting from fabrication variances.

6.1 Introduction

Increases in data-traffic have necessitated cost-effective means for accommodating bandwidth in optical communications. Silicon photonics has begun to address these needs through low-cost complementary metal-oxide-semiconductor (CMOS)-compatible fabrication of devices utilizing wavelength-division multiplexing (WDM) schemes. A particular device which can address the need for WDM with a low power budget is the silicon Micro-Ring Resonator (MRR) which boasts an ample free spectral range, sharp resonant peaks and a small footprint [1]. The resonant nature of the MRR necessitates stabilization against ambient temperature variations, usually achieved using a closed-loop system containing a micro-heater placed above the ring [2], [3]. Integrated heating

can cause a large resonance shift for a limited power dissipation [4]. For WDM applications, multiple rings can be designed to combine wavelengths from an external source, with resonances for each ring at a fixed spacing (for example, 50, 100, or 200 GHz) [5]. While it is possible to design multiple-ring structures to possess such a spacing, inevitable fabrication variations prevent such realization. Such variations are normally compensated for via individual active thermal tuning. The constant power consumption required to tune such multi-ring systems adds system power dissipation and complexity for feedback and control. In order to mitigate such drawbacks, each ring resonator can be resonance-trimmed by permanently altering the optical cavity length through various methods [6], [7], [8], [9] to bring its resonance closer to the target frequency spacing. One demonstrated method for trimming is to implant the fabricated device with energetic ions which cause the formation of lattice defects in the silicon, and a resultant permanent resonance red-shift [10]. The introduction of lattice defects inevitably increases optical losses, and a reduction of the resonator quality (Q)-factor. Further, it is unreasonable to implant each individual ring with a tailored concentration of defects to control individual degrees of trimming. A more elegant method is to combine implantation with a post-implantation annealing process which can be applied to each individual ring and has the advantage of removing defects to the extent that the Q-factor is impacted minimally. Such a method was recently reported by Milošević *et al* [11], in which defects were introduced during device fabrication, and then removed via a localized UV-laser annealing step. While impressive, these results were obtained via a method which is not post-fabrication in nature, requiring in-process measurements and optical annealing which is subject to variations in the UV-laser performance. In contrast, we demonstrate an in-situ electrically driven trimming process using widely used integrated titanium nitride (TiN) micro-heaters fabricated above the ring resonator to precisely trim its resonance through local annealing of defects, both intentionally introduced after fabrication and intrinsic from fabrication. We apply the technique to a four-ring system to fix the

frequency spacing to 50 GHz. While reports of micro-heating to perform resonance trimming have been made [12], [13], in both cases the integrated heaters were formed through doping of the silicon and required either modification of the optical waveguide or of the cladding material beyond the intended use of the ring resonator. The results reported here leave the device unmodified from its intended application.

6.2 Results

Devices used in this work were fabricated by A*STAR IME on a 220 nm silicon-on-insulator (SOI) platform. They comprised of four ring resonator modulators coupled to a single bus waveguide with radii of 12, 12.005, 12.01 and 12.015 μm, respectively, with the aim to provide a frequency spacing of close to 50 GHz between resonances for WDM applications. The waveguides are designed for single-mode transverse electric (TE) operation with a width of 500 nm and a slab height of 90 nm. Each ring has a 2.1 μm wide TiN heater directly above, with approximately 97% coverage, separated by 2 μm of silicon-dioxide from the silicon. The ring modulator comprises a *p*-*n*+ junction with a central offset of 120 nm and heavily doped contact region separations of 1050 nm from the waveguide center. An example optical image and the waveguide cross-section can be seen in Fig. 6.1. In what follows we treat the ring modulators as passive filters in order to assess the trimming technique described. In a future publication we will quantify fully the impact of the trimming on the modulator performance and show the applicability of the trimming technique to both passive (filters) and active (modulators) devices.

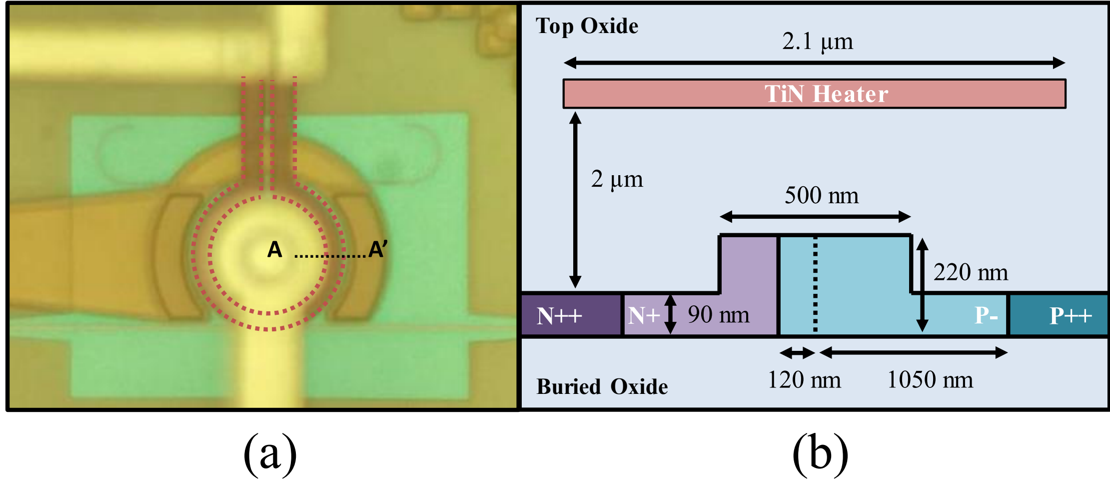

FIGURE 6.1: (a) Optical image of a ring resonator modulator depicting TiN (dotted red line). (b) Waveguide cross-section (cutline A-A' in (a)) of the ring resonator device.

6.2.1 Heater Efficiency

The efficiency of the integrated TiN heater was determined by measuring the device resonance shift in an unimplanted device as a function of heater power. This shift was used to estimate the temperature of the ring resonator under bias. All measurements were performed using a Keysight 8164A Tunable Laser and bias was applied using a Keithley 2400 Source Meter. To determine the effectiveness of the TiN heater for in-situ annealing of lattice defects, it is important to quantify the approximate temperature reached in the silicon with the heater active. The thermo-optic coefficient of silicon is dn/dT = 1.84×10^{-4} K^{-1} [14], valid for variations around room temperature; however, larger temperature increases, such as those expected here, require an improved accuracy by accounting for the change in dn/dT with temperature [15]. Simulations were performed in Synopsys' FEMSIM^{TM} suite in RSoft using the geometry shown in Fig. 6.1. The silicon's refractive index was adjusted in simulations to emulate increasing temperature and mode simulations were performed to extract the change in waveguide effective index

due to the heater, Δn_{env}, across wavelength and temperature. Δn_{env} can be related to a shift in a ring resonance as [1]:

$$\Delta n_{env} = \left(\frac{\Delta\lambda_{res}}{\lambda_{res}}\right) n_g \tag{6.1}$$

where λ_{res} is the resonant wavelength of an unperturbed waveguide, n_g is the group index, and $\Delta\lambda_{res}$ is the resonance shift. We measured the heater I-V characteristics as well as resonance shift $\Delta\lambda_{res}$ in a 12 µm radius ring for a resonance λ_{res} of 1530 nm in an unimplanted device.

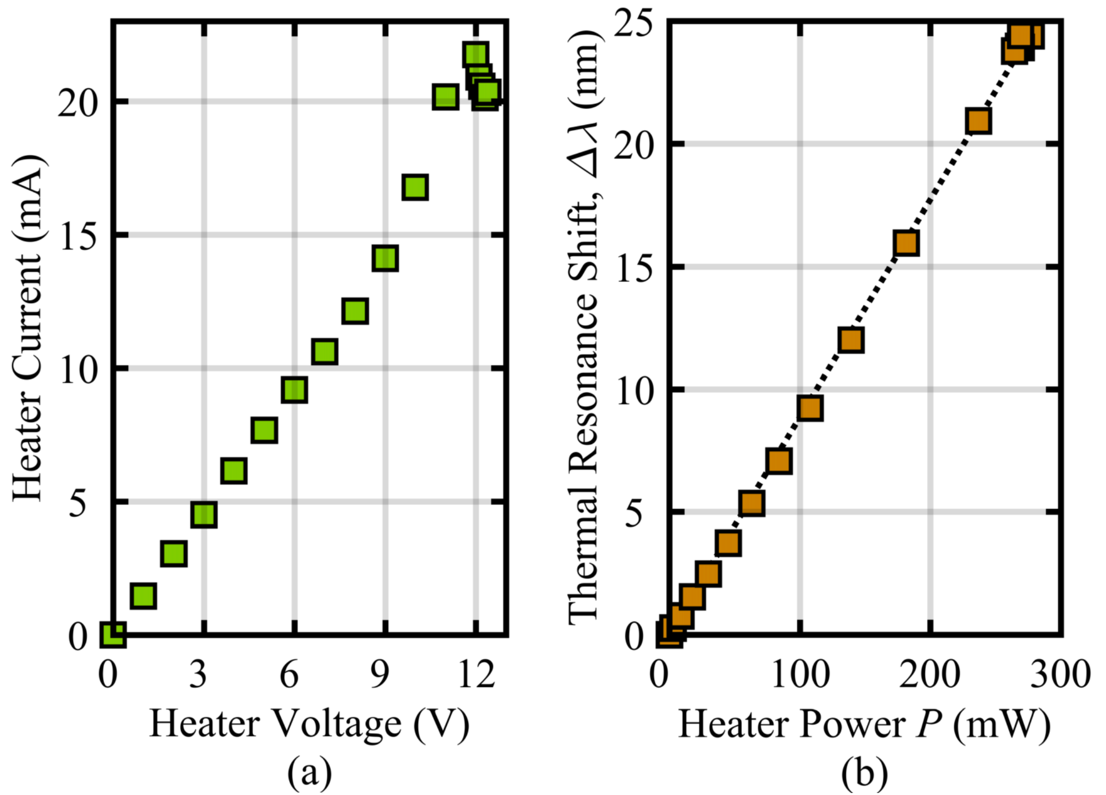

FIGURE 6.2: (a) Heater I-V characteristics. (b) Resonance shift as a function of heater power.

In Fig. 6.2 (a) the heater exhibits linear I-V operation with a slope of 1.54 mA/V

until approximately 10 V, beyond which, the heater current saturates and begins to fail. The suspected failure mechanisms are thermally activated such as burning or melting of the heater or void formation leading to an open-circuit [16]. In Fig. 6.2 (b), we observe linear operation with an efficiency of 8.85×10^{-2} nm/mW. We use (6.1) to calculate each resonance shift's corresponding Δn_{env} from which we can estimate the change in silicon temperature relative to room temperature. From this data we extract a resonance shift of $\Delta\lambda = 9.1\times10^{-2}$ nm/K and a corresponding change in effective index of $\Delta n_{env} = 2.42\times10^{-4}$ K^{-1}.

The maximum absolute waveguide temperature is $T = 293$ °C prior to failure. At this temperature, there is significant annealing of optically active divacancy-type lattice defects [17].

6.2.2 Defect-Induced Resonance Shifts

Multiple chips were subjected to high-energy (3 MeV) boron ion implantation, adequate to penetrate both the TiN heater and the silicon waveguide beneath resulting in the creation of silicon lattice defects. These defects increase the silicon refractive index to produce a red-shift in the device spectrum. This high-energy implantation ensures this trimming process in entirely back-end with no modifications to the process flow of the foundry. To quantify the index change caused by the presence of defects, device spectra from each chip were recorded under thermal stabilization at 25 °C with a thermo-electric cooler (TEC) before being subjected to ion implantation with doses varying from 3×10^{10} to 3×10^{13} cm^{-2}. Post-implantation device spectra were similarly recorded to calculate the defect-induced red-shift as a function of dose, as shown in Fig. 6.3.

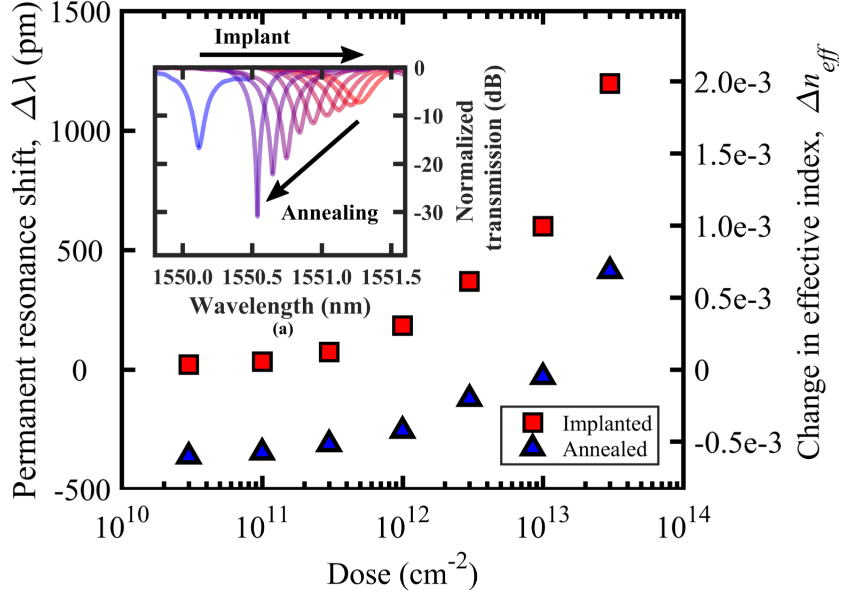

FIGURE 6.3: Implant-induced and annealed resonance shifts and calculated change in effective index achieved as a function of implanted defect dose. Inset (a): spectra for device pre- and post- 3×10^{13} cm^{-2} implantation, plus annealing. Extracted Q-factor and notch-depth for these conditions are 5500, 5200, and 6100, and 16.8, 7.3, and 30.3 dB, respectively.

The change in the waveguide mode's effective index, Δn_{eff} is calculated for each resonance shift as follows [1]:

$$\Delta n_{eff} = \left(\frac{\Delta\lambda_{res}}{L}\right) m, \qquad m = 1, 2, 3... \tag{6.2}$$

where L is the ring cavity length, and m is the order of the resonant mode. The waveguide mode, simulated using FEMSIM in RSoft, yielded an n_{eff} of 2.569 which, with an m of 125, corresponds to a resonant wavelength close to the resonance of interest at 1550 nm. The effect of dispersion is not included in (6.2), although the equation is accurate for small wavelength perturbations such as those measured here. There is a clear trend of increased red-shift with implant dose.

6.2.3 In-Situ Defect Annealing

Annealing a fraction of the defects will produce an appropriate subsequent blue-shift (relative to the implanted devices). Prior to annealing, the spectrum of the four-ring device was recorded. The ring corresponding to the blue-most resonance in the initial spectrum was chosen as the annealing subject. The TiN heater bias was ramped up, held at a bias step for 60 seconds, and then ramped back down followed by a cool-down time of 20 seconds after which a post-annealing spectrum was recorded and the annealing subject's permanent resonance shift calculated. The maximum annealed permanent resonance shift as well as the respective change in effective index as a function of chip implant dose are also shown in Fig. 6.3. The maximum achievable shift for the higher doses indicates only partial recovery likely due to the silicon not reaching temperatures high enough to fully remove the defects introduced. Vacancy-type defects are mobile above room temperature and can migrate to form more complex defects which can survive beyond 500 °C [18]. A surprising result shows that annealed resonance shifts for lower dose implants begin to approach a steady but non-zero blue-shift. This indicates that there are as-fabricated defects present in the devices, possibly surviving defects from the doping to form the p-n+ junction, or defects at the Si-SiO_2 interface, or re-structuring of the cladding oxide. These intrinsic defects are partially or fully removed by the annealing, in turn causing a blue-shift of ∼400 pm. This intrinsic resonance shift was also observed in an unimplanted sample which implies there is an inherent trimming range associated with as-fabricated devices, and such a range does not require the introduction of additional defects. It should be noted, and is evident in the Fig. 6.3 inset, that resonance notch-depth can be precisely controlled also through implantation and annealing, the resulting effect contingent on the coupling condition of the resonator (i.e., over-, under- or critically coupled). The device in Fig. 6.3 inset represents an over-coupled ring resonator prior to implant. A measurable variation in the Q-factor is evident only in devices with the highest implantation dose due to the high waveguide

loss in the modulator. The propagation loss due to the *p-n+* junction is simulated to be in excess of 35 dB/cm while measurable propagation losses in passive ridge waveguide test structures due to ion-implantation (measured following the method of [19]) at the highest three doses of 3×10^{12}, 1×10^{13} and 3×10^{13} cm^{-2} are 10.2, 19.2, and 53.3 dB/cm, respectively. The passive propagation loss for waveguides without defects or doping is approximately 3 dB/cm, likely dominated by sidewall scattering. We note that defect-induced propagation losses for all doses below 3×10^{12} cm^{-2} are comparable with this value, and as such defect implantation has negligible impact on waveguide losses for these lower doses. We note that the annealing of defects (and thus device trimming) requires a heater bias exceeding 200 mW, with the associated waveguide temperature in excess of 200 °C. This is significantly larger than the power applied during normal device operation, and is further consistent with thermal annealing of silicon lattice defects. Specifically, the silicon divacancy has an annealing activation energy of 1.25 eV [20] which suggests that residual defects in the devices trimmed in the manner described here have a 50% removal rate at a temperature of 70 °C over more than 10 years.

Although in this work we do not fully assess the impact on the modulators (treating the devices here as passive filters primarily), we note that the resonance shift at a reverse bias of -4 V compared to zero bias is degraded by 5%, 20% and 30% for devices implanted with defect doses of 1×10^{11}, 3×10^{11}, and 1×10^{12} cm^{-2}, respectively. Similarly, the dark current at this bias in an unimplanted device is approximately 30 nA and increases to 150 nA at the highest implant dose of 3×10^{13} cm^{-2}. This degradation is associated with the reduction in free carrier concentration in the *p-n+* diode, an effect that could be compensated for by an increase in doping during the formation of the junction.

6.2.4 Resonance Trimming

The primary application of the in-situ annealing is to correct for fabrication variances in the ring resonators. We trimmed a four-ring modulator system designed for resonance spacing of 50 GHz, but containing random variations from this spacing due to fabrication variances. The device spectra before and after resonance trimming are seen in Fig. 6.4.

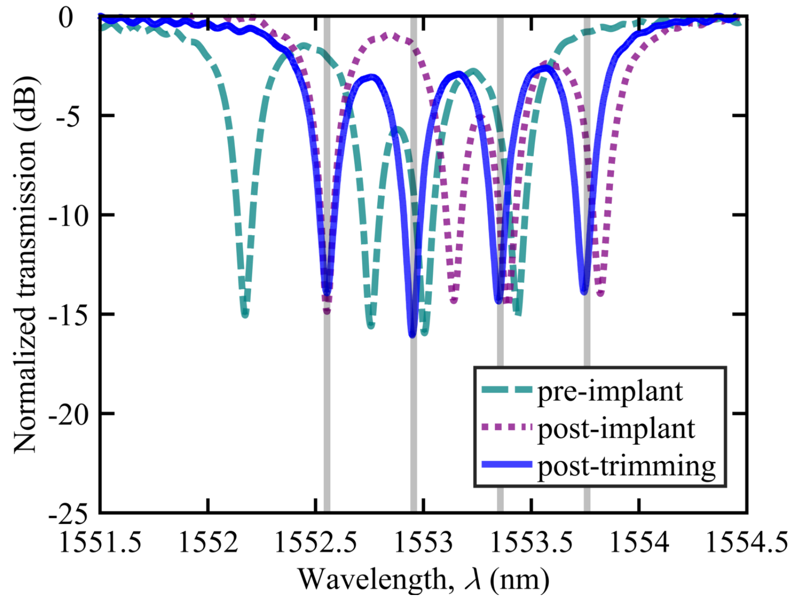

FIGURE 6.4: Four-ring device spectra before and after individual ring-trimming to align to 50 GHz spacing denoted by the vertical grid. Pre-trimming describes the device which has received implantation at a dose of 1×10^{13} cm^{-2}.

After trimming, the resonance spacing from left to right is 49.14, 50.48, and 49.21 GHz with each resonance trimmed to within 15 pm of their target wavelengths. Devices featuring ring resonators are often designed with temperature stabilization in mind and with this approach, the entire device can be thermally tuned and stabilized to a given grid using a single control circuit [21]. This method can be extended to N-ring systems as long as the required shift does not exceed the available range. Another result of the

defect annealing is the precise tuning of optical losses within the ring which can bring an under-coupled ring closer to critical-coupling with a resulting increase in notch-depth.

6.3 Defect absorption at 1550 and 2000 nm wavelength[1]

Defect-enhanced resonance trimming in MRRs can be extended to the longer wavelengths of the TDFA-band so long as defects remain optically-active, despite reduced photon energy, and can be annealed at temperatures achievable with integrated micro-heaters. From Chapter 3 Fig. 3.7 we saw increasing absorption at 2020 nm wavelength due to increasing ion implantation doses indicating the presence of optically-active defects. Similarly, we saw in Fig. 3.8 that these defects anneal appreciably at waveguide temperatures achievable by the MRR micro-heaters presented in this chapter. We compare the defect-related absorption of various ion implantation doses in 750 µm long, 1 µm wide waveguides with exposed silicon through an oxide window etch, similar to the defect-mediated detectors presented in Chapter 5. To characterize the loss, linearly polarized 1550 nm light was launched from a 30 mW JDSU ASE source through polarization paddles and coupled into the waveguide through tapered fiber. The same devices were characterized at 2000 nm by launching linearly polarized light from a 20 mW AdValue Photonics AP-ASE-2000 ASE source through polarization paddles and coupled into each waveguide through tapered fibers. Output power for both wavelengths was measured using a Thorlabs S148C integrating sphere photodiode. The normalized transmission for several implant doses is shown in Fig. 6.5.

[1] This section is not included in the published work.

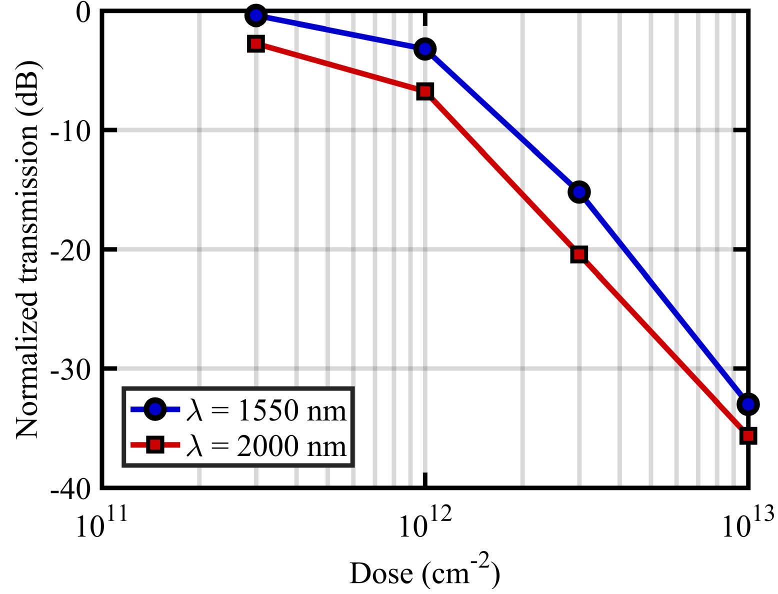

FIGURE 6.5: Normalized transmission in 750 μm long, 1 μm wide waveguides with varying implant dose.

Doses larger than 1×10^{13} cm^{-2} did not yield a measurable signal at either wavelength. For each dose, a larger absorption at 2000 nm wavelength is observed as compared to 1550 nm. Assuming this absorption is due to the divacancy defect, the larger absorption at longer wavelengths would suggest a larger change in refractive index via the Kramers-Kronig relation [22] which implies a stronger trimming effect in waveguides. In a MRR of fixed cavity size L, the lower resonance order m associated with longer wavelengths results in a larger resonance shift through (6.2) compared to shorter wavelengths. These results are encouraging for extending this post-fabrication trimming technique to MRR-based devices in TDFA-band silicon photonic systems.

6.4 Oxide restructuring[2]

It was suggested in the published text that restructuring of the oxide cladding could explain the via in-situ annealing resonance shift observed in unimplanted samples. To investigate this, RSoft FEMSIM^{TM} simulations were performed for the waveguide cross-section in Fig. 6.1 while varying the top cladding refractive index with an index perturbation, γ. The slope of simulated waveguide n_{eff} with γ is then determined through linear interpolation. For a wavelength of 1550 nm and a waveguide width of 500 nm, this slope is $\delta n_{eff}/\delta\gamma = 0.111$. Similar simulations were performed at 2000 nm wavelength (with the assumption of equal γ across wavelengths) for waveguide widths of 600 and 650 nm with resulting $\delta n_{eff}/\delta\gamma = 0.172$ and 0.157, respectively. Due to the extension of the waveguide mode's evanescent field into the top cladding at longer wavelengths, there is enhanced interaction between the light and the refractive index perturbation, resulting in a larger effect. This effect can be further strengthened by removing the bottom cladding layer, pushing the mode profile further into the cladding.

To achieve the ~400 pm resonance trimming measured in an unimplanted device at a wavelength of 1550 nm, we use (6.2) to calculate a required δn_{eff} of -6.6×10^{-4}, necessitating a γ of -5.95×10^{-3} from the simulated results. The same resonance shift at a wavelength of 2000 nm for a ring cavity of L = 12 μm, waveguide width of 600 nm, n_{eff} of 2.301, and resonant order m = 87, δn_{eff} = -4.6×10^{-4}, necessitating a γ of -2.68×10^{-3}. Similarly for a width of 650 nm, n_{eff} of 2.335, and m = 88, δn_{eff} = -4.7×10^{-4}, necessitating a γ of -2.99×10^{-3}. Due to the smaller resonant order in a ring cavity of fixed L for longer wavelengths, as well as the extension of the mode's evanescent field further into the top cladding, less oxide restructuring is required to achieve a similar resonance shift.

[2] This section is not included in the published work.

Restructuring of oxide structure resulting in density reduction has been simulated for deposited oxide films with annealing temperatures at and below 1300 K, demonstrating a density decrease of ~0.15 g/cm^{-3} at T = 1300 K, corresponding to a reduction in oxide refractive index of γ ~0.03 [23]. Assuming a linear relationship between density and γ, a decrease in oxide density of ~0.03 is required to achieve $\Delta\lambda$ = -400 pm in the case of 1550 nm wavelength, approximately 20% of what is achievable at T = 1300 K. According to the simulated data presented in [23], this can conservatively occur at temperatures somewhere between 700 and 1200 K. While the silicon waveguides presented in this work do not quite reach this temperature, it is noted that the oxide qualities likely differ and that the integrated micro-heater here is located within the cladding oxide itself and can therefore achieve higher local temperatures. By using masked oxide etching to laterally isolate the heater and / or reducing the vertical distance between the heater and the waveguide, it is possible that larger temperatures and larger permanent resonance shifts can be achieved.

6.5 Conclusion

Resonance trimming in ring resonator devices is advantageous to reduce the requirements for thermal-tuning and to reduce overall power dissipation. In foundry-fabricated devices, both as-fabricated and intentionally introduced defects can be dynamically and precisely annealed in-situ using micro-heaters. We determine the heater performance via the measured resonance shifts with the heater power and translate them to the silicon waveguide temperature. We demonstrate resonance red-shifting up to 1.2 nm via ion implantation and subsequent blue-shift resonance-trimming up to approximately 800 pm via in-situ annealing. We also demonstrate the practical application whereby a multi-ring modulator system is trimmed to a fixed wavelength spacing of 50 GHz. Future designs may feature oxide etches for better heat distribution to the silicon and masked

regions to allow for a more targeted ion implantation which affects only the optically active waveguide core. This trimming technique is entirely post-fabrication and based upon electrically controlled, localized heating.

Acknowledgment

The authors would like to acknowledge CMC Microsystems for the provision of products and services that facilitated this research, as well as fabrication services using technology from A*STAR IME. We would like to also acknowledge Jack Hendrix at Interface Science Western at Western University.

Bibliography

[1] W. Bogaerts, P. De Heyn, T. Van Vaerenbergh, K. De Vos, S. Kumar Selvaraja, T. Claes, P. Dumon, P. Bienstman, D. Van Thourhout, and R. Baets, “Silicon microring resonators,” *Laser & Photonics Reviews*, vol. 6, no. 1, pp. 47–73, jan 2012.

[2] K. Padmaraju, D. F. Logan, X. Zhu, J. J. Ackert, A. P. Knights, and K. Bergman, “Integrated thermal stabilization of a microring modulator,” *Optics Express*, vol. 21, no. 12, p. 14342, jun 2013.

[3] Z. Wang, D. J. Paez, L. Dow, and A. P. Knights, “Intrinsic resonance stabilization in depletion-type silicon micro-ring modulators,” in *2017 IEEE 14th International Conference on Group IV Photonics (GFP).* IEEE, aug 2017, pp. 35–36.

[4] P. Dong *et al.*, “Low V_{pp}, ultralow-energy, compact, high-speed silicon electro-optic modulator,” *Optics Express*, vol. 17, no. 25, p. 22484, dec 2009.

[5] A. V. Krishnamoorthy, J. F. Buckwalter, J. Li, and X. Zheng, "Scaling Trends for Picojoule-per-Bit WDM Photonic Interconnects in CMOS SOI and FinFET Processes," *Journal of Lightwave Technology, Vol. 34, Issue 11, pp. 2730-2742*, vol. 34, no. 11, pp. 2730–2742, jun 2016.

[6] J. Schrauwen, D. Van Thourhout, and R. Baets, "Trimming of silicon ring resonator by electron beam induced compaction and strain," *Optics Express*, vol. 16, no. 6, p. 3738, mar 2008.

[7] Linjie Zhou, K. Okamoto, and S. Yoo, "Athermalizing and Trimming of Slotted Silicon Microring Resonators With UV-Sensitive PMMA Upper-Cladding," *IEEE Photonics Technology Letters*, vol. 21, no. 17, pp. 1175–1177, sep 2009.

[8] S. Prorok, A. Y. Petrov, M. Eich, J. Luo, and A. K.-Y. Jen, "Trimming of high-Q-factor silicon ring resonators by electron beam bleaching," *Optics Letters*, vol. 37, no. 15, p. 3114, aug 2012.

[9] A. H. Atabaki, A. A. Eftekhar, M. Askari, and A. Adibi, "Accurate post-fabrication trimming of ultra-compact resonators on silicon," *Optics Express*, vol. 21, no. 12, p. 14139, jun 2013.

[10] J. J. Ackert, J. K. Doylend, D. F. Logan, P. E. Jessop, R. Vafaei, L. Chrostowski, and A. P. Knights, "Defect-mediated resonance shift of silicon-on-insulator racetrack resonators," *Optics Express*, vol. 19, no. 13, p. 11969, jun 2011.

[11] M. M. Milosevic, X. Chen, W. Cao, A. F. J. Runge, Y. Franz, C. G. Littlejohns, S. Mailis, A. C. Peacock, D. J. Thomson, and G. T. Reed, "Ion Implantation in Silicon for Trimming the Operating Wavelength of Ring Resonators," *IEEE Journal of Selected Topics in Quantum Electronics*, vol. 24, no. 4, pp. 1–7, jul 2018.

[12] S. Spector, J. M. Knecht, and P. W. Juodawlkis, "Localized in situ cladding annealing for post-fabrication trimming of silicon photonic integrated circuits," *Optics Express*, vol. 24, no. 6, p. 5996, mar 2016.

[13] A. P. Knights, Z. Wang, D. Paez, and L. Dow, "Electrical trimming of the resonance of a silicon micro-ring resonator," in *2017 IEEE 14th International Conference on Group IV Photonics (GFP)*. IEEE, aug 2017, pp. 29–30.

[14] G. T. Reed and A. P. Knights, *Silicon Photonics: An Introduction.* West Sussex, England: John Wiley & Sons, Ltd, jan 2004.

[15] H. H. Li, "Refractive index of silicon and germanium and its wavelength and temperature derivatives," *Journal of Physical and Chemical Reference Data*, vol. 9, no. 3, pp. 561–658, jul 1980.

[16] Y. L. Cheng, B. J. Wei, F. H. Shih, and Y. L. Wang, "Stability and Reliability of Ti/TiN as a Thin Film Resistor," *ECS Journal of Solid State Science and Technology*, vol. 2, no. 1, pp. 12–15, 2013.

[17] D. E. Hagan and A. P. Knights, "Mechanisms for optical loss in SOI waveguides for mid-infrared wavelengths around 2 μm," *Journal of Optics*, vol. 19, no. 2, p. 025801, feb 2017.

[18] J. Srour, C. Marshall, and P. Marshall, "Review of displacement damage effects in silicon devices," *IEEE Transactions on Nuclear Science*, vol. 50, no. 3, pp. 653–670, jun 2003.

[19] P. J. Foster, J. K. Doylend, P. Mascher, A. P. Knights, and P. G. Coleman, "Optical attenuation in defect-engineered silicon rib waveguides," *Journal of Applied Physics*, vol. 99, no. 7, p. 073101, apr 2006.

[20] L. J. Cheng, J. C. Corelli, J. W. Corbett, and G. D. Watkins, “1.8-, 3.3-, and 3.9-μ Bands in Irradiated Silicon: Correlations with the Divacancy,” *Physical Review*, vol. 152, no. 2, pp. 761–774, dec 1966.

[21] W. A. Zortman, D. C. Trotter, and M. R. Watts, “Silicon photonics manufacturing,” *Optics Express*, vol. 18, no. 23, p. 23598, nov 2010.

[22] M. Nedeljkovic, R. Soref, and G. Z. Mashanovich, “Free-carrier electrorefraction and electroabsorption modulation predictions for silicon over the 1-14-μm infrared wavelength range,” *IEEE Photonics Journal*, vol. 3, no. 6, pp. 1171–1180, dec 2011.

[23] F. Grigoriev, E. Katkova, A. Sulimov, V. Sulimov, and A. Tikhonravov, “Annealing of deposited SiO_2 thin films: full-atomistic simulation results,” *Optical Materials Express*, vol. 6, no. 12, p. 3960, dec 2016.

© 2019 IEEE. Reprinted, with permission, from David E. Hagan, Benjamin Torres-Kulik, and Andrew P. Knights, “Post-Fabrication Trimming of Silicon Ring Resonators via Integrated Annealing”, *IEEE Photonics Technology Letters*, Aug/2019

Chapter 7

A Monte Carlo simulation of resonance trimming in wavelength-division multiplexing and stacked resonance photonic circuits

7.1 Introduction

Silicon photonic systems are fabricated under the strict tolerances of complementary metal-oxide-semiconductor (CMOS) manufacturing; however, natural variations in processing lead to variations in device dimensions which can alter desired properties. In systems involving multiple devices, variation in individual device properties can adversely affect the performance of the system as a whole, particularly in wavelength-sensitive devices such as micro-ring resonators. Due to the small footprint of ring resonators, the resonant wavelengths defined by the cavity waveguide can be easily perturbed by small

changes in waveguide dimensions, particularly in submicron waveguides such as those considered here. Systems which involve multiple ring resonators include, but are not limited to, higher-order filters [1], photonic molecules [2], [3], delay lines [4], biological sensor arrays [5], and photonic crossbar and switching networks [6], and wavelength division multiplexing schemes [7]. In many of these systems, micro-heaters can be fabricated above each ring resonator to separately tune their spectral response through the thermo-optic effect [8]. This is commonplace in active silicon photonic systems to counteract deviations from design due to processing variations, particularly, to shift the resonant wavelengths of a ring resonator.

In the absence of thermal tuning, ring resonances can be altered through resonance trimming as discussed in Chapter 6. Other resonance trimming techniques which exist include, but are not limited to, defect annealing [9], plasma-enhanced chemical vapor deposition (PECVD) oxide annealing [10], photo-induced trimming of various cladding materials [11], [12], [13], dopant diffusion [14], electron beam induced compaction [15], ion implantation [16], and laser ablation [17]. Different techniques yield varying magnitudes and direction of resonance shifts as well as associated impact on other operating metrics of the trimmed device (e.g. excess loss due to ion implantation damage could decrease the ring resonator quality-factor) and what state the device must be in to accommodate the trimming technique (i.e. no top cladding for post-fabrication deposition of a cladding material specifically designed for trimming), thus appropriate techniques must be applied in the context of the devices and / or systems being designed. Systems which use thermal tuning to align ring resonator resonances to a specific wavelength (referred to here as 'stacked resonance systems') or to a specific frequency spaced grid (referred to here as 'WDM systems') dissipate a constant amount of thermal power to keep the system aligned. Through the use of resonance trimming techniques, the resonances can be pushed or pulled closer to alignment which will reduce significantly power dissipation.

To quantify manufacturing variation, the Virtual Wafer Method (VWM) may be used [18] whereby measured wafer variation parameters (for example the mean and standard deviation in silicon thickness and its associated correlation length, L_C, across a wafer) can be used to generate a 'virtual wafer' which describes the correlated silicon thickness variation across the wafer. By sampling positions across this virtual wafer, this thickness variation can be ascribed to devices which are spatially separated, introducing resonant wavelength variation in ring resonators. By repeated sampling of this virtual wafer through Monte Carlo simulation, statistical trends can emerge to help designers anticipate the large-scale effects of processing variation on these systems [19].

Most Monte Carlo techniques have been applied to examine the impact of processing variation on ring resonator resonant wavelength at wavelengths in or near the erbium doped fiber amplifier (EDFA) telecommunications band, centered at 1550 nm [20]. We apply similar Monte Carlo techniques to examine ring resonator systems designed for EDFA and systems designed for thulium doped fiber amplifier (TDFA) wavelength bands, the latter of which is centered at 1970 nm [21].

7.2 Method

A Monte Carlo approach is applied to generate several tens of thousands of multi-ring resonator systems (each referred to as a system or generation, interchangeably) subject to correlated variation in three critical waveguide dimensions: width, thickness, and slab height, all of which perturb the target TE_0 resonance wavelengths. These systems are designed as stacked resonance or WDM systems, varying in frequency spacing, Δf, physical separation between rings, and number of rings in the system.

To compensate for this deviation from target wavelengths, thermal tuning may be applied from a micro-heater integrated with each ring resonator. Thermal tuning results

in a resonant wavelength red-shift for a particular device, the efficiency of which is here quoted in pm/mW. The total amount of power to align each device's resonance to the associated target wavelength is captured for each generated system and used throughout this chapter to examine statistical trends which would normally be elusive without the significant sample size afforded by simulating through a Monte Carlo approach.

For each generated system, the simulation applies sequential trimming steps where the resonances are blue-shifted by fixed amounts toward the target wavelengths. Blue-shift resonance trimming is focused on in this analysis but similar results could be expected for red-shift resonance trimming. Partial resonance trimming pulls the resonances toward alignment such that the required thermal tuning decreases with each step. The total amount of power to align each system's resonances to their associated target wavelengths is captured for each generation prior to- and after each sequential resonance trimming step. From here, the savings in power consumption as a function of resonance trimming are calculated.

Both 1550 and 2000 nm wavelengths and their appropriate waveguide dimensions are considered here to determine how these statistical trends might differ for EDFA- and TDFA-band systems. As discussed in Chapter 2, 500 nm wide ridge waveguides with 90 nm slab thickness are commonplace for a wavelength of 1550 nm as this is near the single-mode cut-off. For 2000 nm wavelength, we use a width of 650 nm over the previously explored 600 nm as the confinement is marginally higher and subsequently has less variation in effective index with deviations in width, represented as the slope of the curves in Chapter 2 Figure 2.2. In the case where the systems utilize the ring resonators as modulators, high modulation efficiency is maintained at this width.

7.2.1 Virtual wafer model

The Monte Carlo algorithm uses the VWM to create individual device variation [18], a virtual wafer which represents a spatial map of correlated variation of a particular parameter. Three virtual wafers are created to represent three critical waveguide dimensions considered: waveguide core width (w_{core}), slab thickness (t_{slab}), and silicon thickness (t_{Si}). First, an uncorrelated 2-D Gaussian variation distribution $z(x,y)$, with mean μ and standard deviation σ, is assumed for each device dimension and inverse-sampled across a wafer size, in this case, 100 $\times$ 100 mm. $z(x,y)$ is then convolved with a Gaussian filter $g(x,y)$ defined as:

$$g(x,y) = \frac{1}{\sqrt{\pi}\frac{L_C}{2}} e^{-\left(\frac{x^2}{\frac{L_C{}^2}{2}} + \frac{y^2}{\frac{L_C{}^2}{2}}\right)} \tag{7.1}$$

where L_C is the correlation length of each variation. For this, we have chosen L_C = 4.5 mm, similarly used in [18]. The correlated wafer variation $z'(x,y)$, or virtual wafer, describing each waveguide dimension is then described by:

$$z'(x,y) = \mathcal{F}^{-1}\left(\mathcal{F}\left(z\left(x,y\right)\right) * \mathcal{F}\left(g\left(x,y\right)\right)\right) \tag{7.2}$$

where $\mathcal{F}$ and $\mathcal{F}^{-1}$ denote the Fourier transform and inverse Fourier transform, respectively. For the case of waveguides designed for 1550 nm wavelength (referred to as 'the 1550 nm wavelength configuration' throughout the text), the mean of the uncorrelated variation distributions, $z(x,y)$, are μ_{core} = 500 nm, μ_{slab} = 90 nm, and μ_{Si} = 220 nm, respectively. In the case of devices designed for 2000 nm wavelength (referred to as 'the 2000 nm wavelength configuration' throughout the text), μ_{core} = 650 nm while μ_{slab} and μ_{Si} remain the same. The variation standard deviation of $z(x,y)$ for each dimension are

assumed to be $\sigma_{core} = 2.6$ nm, $\sigma_{slab} = 3.3$ nm, and $\sigma_{Si} = 2$ nm [22]. These three virtual wafers, $z'(x,y)$, are randomly sampled independently in each Monte Carlo generation to ensure adequate diversity of sample dimensions. Examples of these three generated wafers are shown in Figure 7.1:

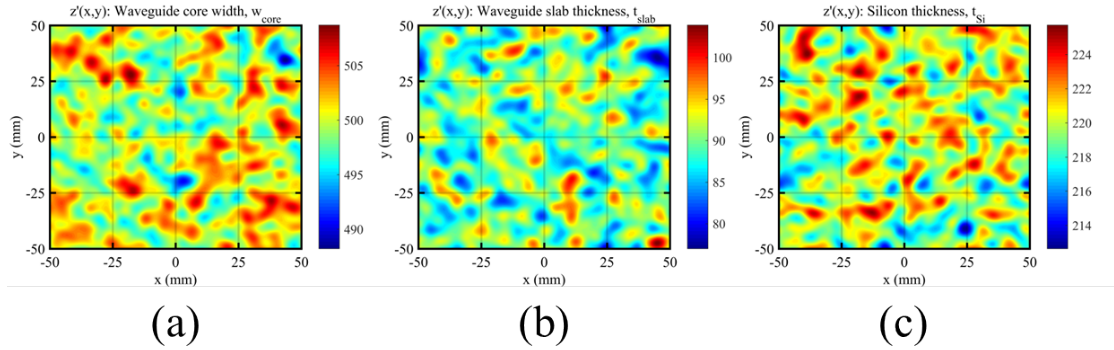

FIGURE 7.1: Contour plots of 100 × 100 mm virtual wafers $z'(x,y)$ for a) w_{core}, b) t_{slab}, and c) t_{Si} for 1550 nm waveguide configuration.

7.2.2 Monte Carlo algorithm

For each Monte Carlo simulation, the number of ring resonators in a system, N, and a uniform physical spacing between them, d_s, is specified. Each generation, w_{core}, t_{slab}, and t_{Si} are determined for each ring resonator by first randomly selecting an initial position (x_o, y_o) on each wafer (representing the first ring resonator) and evaluating the virtual wafer values through interpolation. For an N-ring system, the evaluated values are determined as follows:

$$[p_1, p_2, ..., p_N] = [z'(x_o, y_o), z'(x_o + d_s, y_o), ..., z'(x_o + (N-1)\,d_s, y_o)] \tag{7.3}$$

where p_1, p_2, ..., p_N are the sampled parameters (i.e. w_{core}, t_{slab}, or t_{Si}) for ring resonators 1, 2, ..., and N, respectively. This process is demonstrated for a 4-ring system in Figure 7.2.

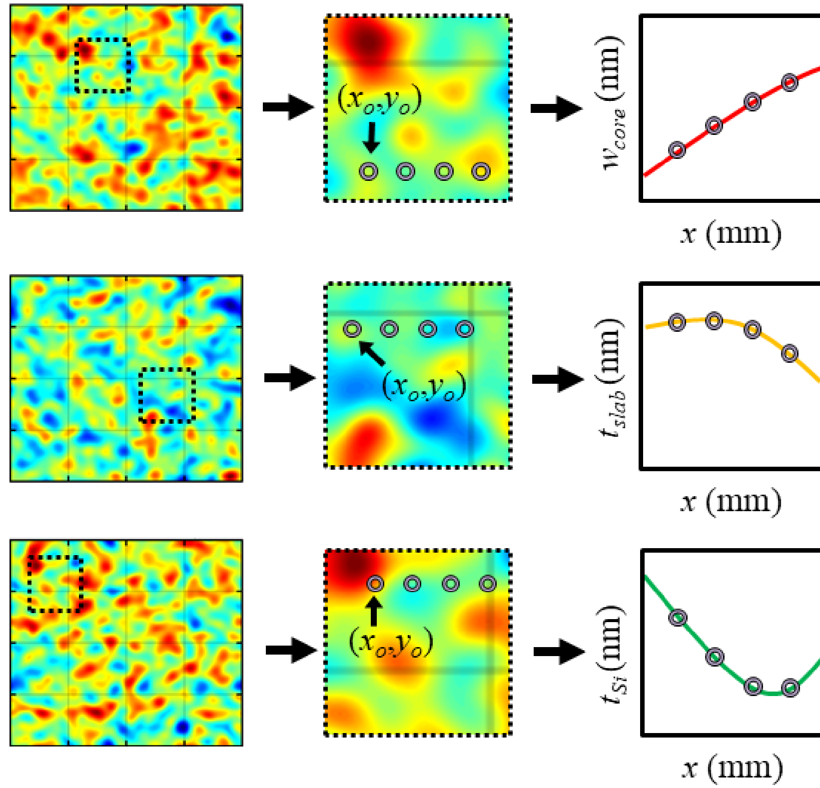

FIGURE 7.2: Diagram of waveguide dimension interpolation from random sampling of each virtual wafer.

With all three dimensions, the waveguide effective index, n_{eff}, is determined for each ring through interpolation of a 3-D matrix of values simulated using RSoft's FEMSIM^{TM} mode solver. Each ring resonator's n_{eff} is then used to calculate its resonant wavelengths, through:

$$\lambda_{res} = \frac{n_{eff} 2\pi R}{m} \tag{7.4}$$

where m is the resonance order and the cavity length has been explicitly stated as the ring circumference, $L = 2\pi R$. This equation is identical to (2.19) in Chapter 2. Resonances corresponding to resonant orders m-1, m, and m+1 are calculated, as opposed to just m, for several reasons. Firstly, as processing variation between rings increases from, for example, increased d_s, the distribution of the system's resonant wavelengths for a particular resonant order will broaden which can generate resonances further away from the target Δf. However, as a resonance gets pushed further away from the target grid due to variation in Δn_{eff}, a neighbouring resonance order moves closer to that same grid. For example, if a particular resonance of order m is severely red-shifted with respect to the other resonances, a second resonance belonging to the m+1 order, which has a shorter wavelength according to (7.4), will be similarly red-shifted. This will be referred to as 'resonant order mixing'. Figure 7.3 shows example spectra depicting this scenario.

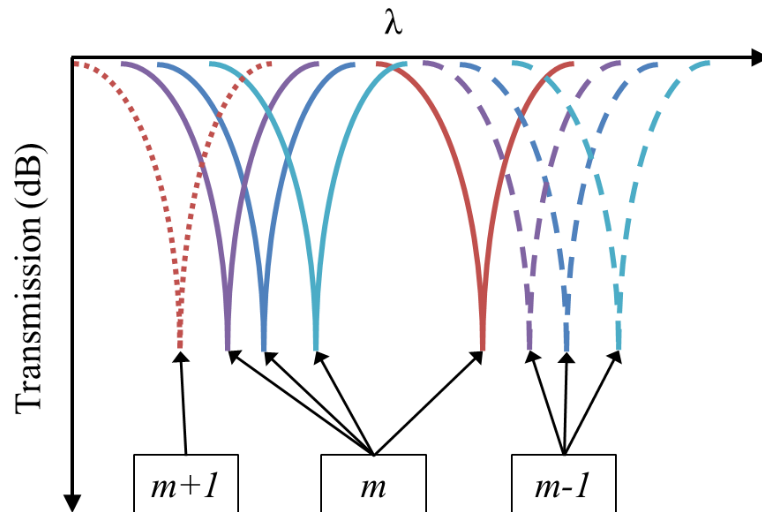

FIGURE 7.3: Example spectra depicting resonant order mixing in a 4-ring system subject to manufacturing variation. Dotted, solid, and dashed lines represent the m+1, m, and m-1 resonance orders.

Secondly, due to the inverse relation between wavelength and frequency, the wavelength

spacing between adjacent dissimilar resonances at lower resonance orders (longer wavelength) will be enlarged. In a stacked resonance system (which is simply a special case of WDM system where Δf is zero), all radii are equal in order to target the same wavelength. According to (7.4), the relative distance between two resonances of order m can be calculated as:

$$\Delta\lambda_m = |\lambda_1 - \lambda_2| = \frac{2\pi R}{m} |n_{eff1} - n_{eff2}| \tag{7.5}$$

The growth or shrinkage of spacing between resonances between different orders is then:

$$\Delta(\Delta\lambda) = \Delta\lambda_{m1} - \Delta\lambda_{m2} = 2\pi R |n_{eff1} - n_{eff2}| \left[\frac{1}{m_1} - \frac{1}{m_2}\right] \tag{7.6}$$

where m_1 and m_2 are the two resonant orders being considered. As an example, if $R = 12$ µm, $n_{eff1} = 2.56$, and $n_{eff2} = 2.563$, then $\Delta\lambda_{125} = 1.809$ nm and $\Delta\lambda_{126} = 1.795$ nm, thus $\Delta(\Delta\lambda)$ grows (shrinks) by 14.36 pm moving down (up) one resonant order. In a stacked resonance system, where $\Delta\lambda_m$ should be minimized between all adjacent resonances (ideally $\Delta\lambda_m = 0$), the highest resonant order (shortest wavelength) range is ideal to align with minimal thermal tuning and resonance trimming since moving to a lower order (longer wavelength) will cause the resonances to move further apart. This effect is more complex in a WDM system where the ring resonator radii must change according to the target Δf. The first ring resonator radius is chosen and each subsequent ring's radius is calculated using (7.4) to achieve the desired Δf between adjacent resonances. We can derive a more succinct expression for the radius of the next ring based on the radius of the previous is:

$$R_{i+1} = \left(\frac{2\pi n_{eff}}{mc}\Delta f + \frac{1}{R_i}\right)^{-1} \tag{7.7}$$

where m is the target resonance order, c is the speed of light, Δf is the desired frequency spacing, and R_i and R_{i+1} are the initial and subsequent ring radii, respectively. Larger Δf necessitate larger sequential ring radii. We now amend (7.5) and (7.6) to include the effect of the differing ring radii:

$$\Delta\lambda_m = |\lambda_1 - \lambda_2| = \frac{2\pi}{m} |R_1 n_{eff1} - R_2 n_{eff2}| \tag{7.8}$$

The growth or shrinkage of spacing between resonances between different orders is then:

$$\Delta(\Delta\lambda) = \Delta\lambda_{m1} - \Delta\lambda_{m2} = 2\pi |R_1 n_{eff1} - R_2 n_{eff2}| \left[\frac{1}{m_1} - \frac{1}{m_2}\right] \tag{7.9}$$

By moving to a lower resonance order, the relative spacing between resonances increases, as in the case with the stacked resonance system, but it is further compounded by the different ring radii. From (7.4), larger variation in λ_{res}, from variation in n_{eff}, will occur in larger radius rings and will be exaggerated in lower resonance orders. This being said, the ideal solution does not universally gravitate toward a higher or lower resonant order as it does in the stacked resonance system because the goal is not to minimize $\Delta\lambda_m$; it is to minimize each resonance's distance to the desired wavelength spacing which also grows and shrinks with resonant order. The ideal resonant order is complex to predict as the scaling of $\Delta\lambda_m$ moving across resonant orders may result in the system being closer or further alignment. There is a tendency for the system to prefer either extreme (lowest or highest resonant order tested) in the absence of resonant order mixing, thus only m-1, m, and m+1 are considered in an effort to maintain central wavelengths near 1550 and 2000 nm for EDFA and TDFA considerations, respectively.

A sufficiently small radius of 12 μm was chosen for investigation with the assumption

that the processing variation affects the dimensions of the ring resonator waveguide uniformly throughout the circumference. This assumption becomes less valid with larger rings. For larger structures, such as Mach-Zehnder interferometers, a different approach must be used to account for local variations along the waveguide length.

For the 12 μm radius, the calculated free spectral ranges of 8.17 nm for 1550 nm wavelength and 14.53 nm for 2000 nm wavelength are sufficiently large to support many-ring (many-channel) systems with commonly used Δf [23]. Due to the larger FSR at longer wavelengths, resonant order mixing may only be encouraged in many-ring systems or with larger values of d_s to enhance the variation in n_{eff} between rings.

The heater efficiency in a 1550 nm wavelength ring can be translated directly to that of a 2000 nm ring. To do so, we begin with the heater efficiency of the ridge waveguide micro-ring resonator modulators measured in Chapter 6 which have waveguide dimensions matching the 1550 nm wavelength configuration used here. This heater efficiency of $d\lambda/dP$ = 88.5 pm/mW, along with the simulated effective index for this geometry of n_{eff} = 2.56 and corresponding resonant order of m = 125, can be used to extract a change in effective index of $dn_{eff}/dP = 1.47\times10^{-4}$ mW^{-1} through (7.4). Using the simulated ridge waveguide thermo-optic coefficient of $dn_{eff}/dT = 1.85\times10^{-4}$ K^{-1} at 1550 nm wavelength from Chapter 2 Figure 2.4, we calculated an associated change in waveguide temperature with applied heater power of dT/dP = 0.79 K/mW. Next, we work backward through this process using the ridge waveguide thermo-optic coefficient at 2000 nm wavelength for a ridge waveguide of 650 nm width, which is approximately $dn_{eff}/dT = 1.66\times10^{-4}$ K^{-1}, to calculate a dn_{eff}/dP of 1.31×10^{-4} mW^{-1}. Finally, using the effective index of 2.33 and an associated mode order of 88, we arrive at a heater efficiency of $d\lambda/dP$ = 112.6 pm/mW, which is approximately 1.27 times larger than the 1550 nm configuration as predicted in Chapter 2. An assumption used by the Monte Carlo algorithm is that both heater efficiencies remain fixed, which is valid for the

sufficiently small variations in n_{eff} invoked through the VWM.

Since the variation across the ring resonators will tend to grow with the physical spacing between them, the physical arrangement, or 'organization' of the ring resonators can have a significant impact and is thus considered as well. The devices may be organized in a 'line', 'matrix', or 'close packed' structure, depicted in Figure 7.4:

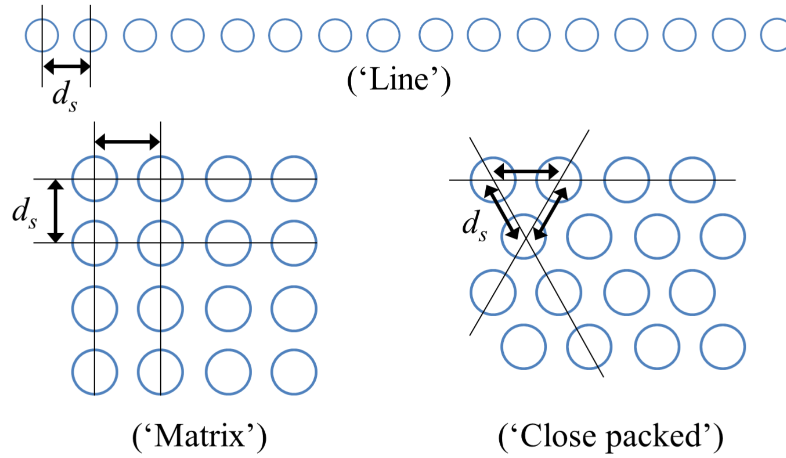

FIGURE 7.4: Three different organizations of a 16-ring system with uniform physical spacing d_s between rings.

Maintaining a fixed distance between devices, the 'line' organization is expected to incur the most variation as it spans a total length of $L_T = N \times d_s$. The 'matrix' organization spans the x and y directions as $L_T = N^{1/2} \times d_s$, which can significantly reduce the variation incurred. The 'close packed' organization is similar to a 'matrix', but d_s is maintained between three adjacent rings in an equilateral triangle, thus minimizing the distance between all nearest neighbours. The span in one direction would simply be $L_T = N^{1/2} \times d_s$, as in the case of the 'matrix' organization, but the other direction is reduced to $L_T = N^{1/2} \times (d_s/2) \times \tan(\pi/3)$. While this organization may not offer much advantage over a 'matrix' for few-ring systems, many-ring systems spanning large areas may see a reduction in overall resonance variation.

Once the resonances of a system have been established for resonant orders of m-1, m, and m+1, the simulation script sorts the resonant wavelengths from lowest to highest and iterates through them in clusters of N-resonances (for an N-ring system), adding the next higher resonance and removing the lowest resonance each time. Each cluster is evaluated by calculating the amount of thermal tuning required to align the system to the target Δf, simply calculated as the sum of the resonances' deviations from their target wavelengths multiplied by the heater efficiency. The amount of resonance trimming (distance) required to align the system is also calculated. The frequency grid aligned through thermal tuning and the grid aligned through resonance trimming represent the same frequency spacing but red-/blue-shifted relative to the resonances, respectively. The cluster with the lowest thermal tuning and resonance trimming required for alignment is chosen to be used for further analysis. This process is necessary to account for resonant order mixing and the subtle differences in resonance wavelength spacing at higher and lower resonant orders.

In each generation, one particular resonance will not require thermal tuning due to the calculation of the frequency grid. Hypothetically, if each resonance required non-zero amounts of thermal tuning to align to a grid, shifting the grid itself left (while maintaining the desired frequency spacing) toward the nearest resonance would ultimately align that particular resonance to the grid while decreasing the other remaining distances. In other words, the grid is established in a way which minimizes the amount of tuning required by finding the optimal resonance to use as an 'anchor' for the grid. Similarly, one resonance will be the 'anchor' of the frequency grid achieved through resonance trimming and will not require resonance trimming. Full alignment to this grid implies that no thermal tuning is required to align the resonances; they have been permanently aligned.

With the ideal cluster of resonances selected, the thermal tuning required is stored as

the total power required for alignment with no resonance trimming. Subsequently, fixed amounts of resonance trimming are applied to the system, moving each resonance back by a set wavelength distance each step (if a resonance reaches its alignment position, no further resonance trimming is applied to it) and the total thermal power required to align to the grid is re-calculated. Note that the same resonance which does not require thermal tuning will require trimming and vice-versa due to the opposite directions in which the resonances move toward each grid, therefore the grid achieved through thermal tuning blue-shifts as the 'anchor' resonance is trimmed, resulting in the reduction in the total power required for alignment. When the two grids coincide, no thermal tuning is required as they have been aligned through trimming. Figure 7.5 shows example transmission spectra (with arbitrary $FWHM$ and notch-depth) of a 4-ring WDM system with a target Δf of 50 GHz generated using the VWM. The red dotted lines represent grid alignment through thermal tuning while the blue dashed lines represent grid alignment through trimming. The 'line' organization and d_s of 1 mm are used to exaggerate the effect of processing variation.

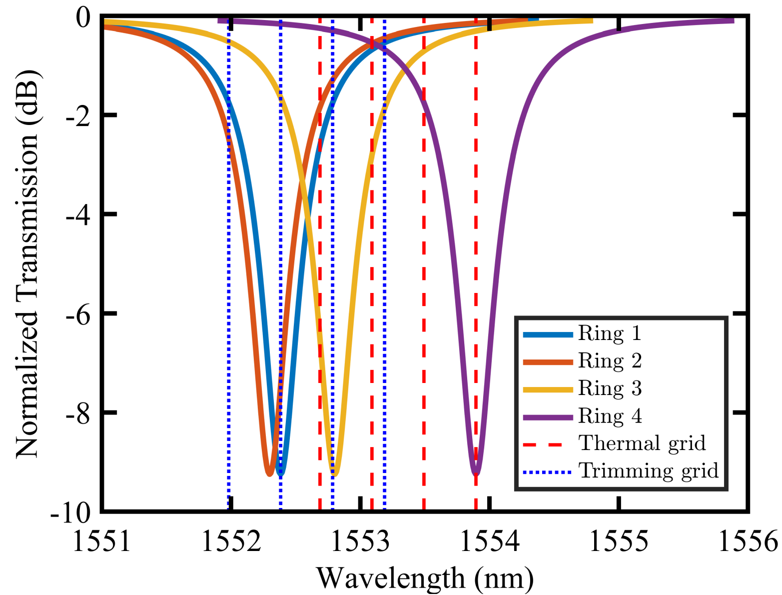

FIGURE 7.5: Example spectra of a 4-ring WDM system with a target frequency spacing of 50 GHz organized in a 'line' with d_s of 1 mm between rings. Red dashed lines represent grid alignment through thermal tuning while blue dotted lines represent grid alignment through trimming.

In the example spectra we see that the order of resonances does not necessarily correspond to the order of the ring resonators. The resonance from ring 4 is the 'anchor' resonance of the thermally-aligned grid, requiring no thermal tuning, while the resonance from ring 1 is the 'anchor' resonance of the trimming grid, requiring no trimming.

Through these Monte Carlo simulations, thermal tuning and trimming data collected for each system are statistically represented through the distribution of values across all generated systems. From here, general trends emerge which can be extended to predict large-scale performance of fabricated devices, and ultimately to a very large arrangement of devices such as is experienced in a data-centre.

7.3 Results and discussion

We begin with a sensitivity analysis of both wavelengths to predict the impact of variation on the devices. Trends in the thermal tuning power consumption for systems across several parameter spaces, in the absence of trimming, are investigated followed by an examination of the power savings through resonance trimming.

7.3.1 Waveguide sensitivity analysis

The variation in waveguide dimensions through random sampling of the virtual wafers is the primary source of deviation from the target resonance of each ring. It is important to determine how each varied parameter affects the target resonant wavelength through sensitivity analysis, particularly at both 1550 and 2000 nm wavelengths considered. To calculate the sensitivity, we assume the aforementioned waveguide dimensions for each wavelength configuration. To determine n_{eff} sensitivity to variations in a particular parameter, a 1-D array of simulated effective indices is collected along the associated parameter's axis in the 3-D effective index matrix, for fixed values of the non-varied dimensions. To determine the local slope (sensitivity), the 1-D array of effective indices is first fit with a third-order polynomial. The derivative of this polynomial is calculated and evaluated at the ideal parameter's value (i.e. 220 nm for t_{Si}). Despite the nonlinear shape of the fitted curve, this slope is a reasonable estimate for small variations. Each extracted sensitivity, $\delta n_{eff}/\delta p$, (where p is the parameter being varied) is converted to a resonant wavelength sensitivity, $\delta\lambda_{res}/\delta p$, through (7.4). Finally, the resonant wavelength shift per standard deviation of variation (σ_{core}, σ_{slab}, and σ_{Si}) is determined. Table 7.1 shows the calculated results for both 1550 and 2000 nm wavelength cases.

Table 7.1: Calculated effective index and resonance sensitivities for 1550 and 2000 nm wavelength configurations.

Parameter		λ = 1550 nm	λ = 2000 nm
w_{core}	$\delta n_{eff}/\delta w_{core}$	8.43×10^{-4} nm^{-1}	6.41×10^{-4} nm^{-1}
	$\delta \lambda_{res}/\delta w_{core}$	0.51 nm/nm	0.55 nm/nm
	$\delta \lambda_{res}(\sigma_{core})$	1.32 nm	1.43 nm
t_{slab}	$\delta n_{eff}/\delta t_{slab}$	1.80×10^{-3} nm^{-1}	1.80×10^{-3} nm^{-1}
	$\delta \lambda_{res}/\delta t_{slab}$	1.08 nm/nm	1.54 nm/nm
	$\delta \lambda_{res}(\sigma_{slab})$	3.61 nm	5.13 nm
t_{Si}	$\delta n_{eff}/\delta t_{Si}$	2.80×10^{-3} nm^{-1}	3.15×10^{-3} nm^{-1}
	$\delta \lambda_{res}/\delta t_{Si}$	1.68 nm/nm	2.70 nm/nm
	$\delta \lambda_{res}(\sigma_{Si})$	3.36 nm	5.40 nm

We see that the effective index sensitivity to silicon thickness is 1.13 times higher in the case of the 2000 nm wavelength as expected due to the less-than-ideal thickness of 220 nm for this wavelength. The resonant wavelength sensitivity becomes 1.6 times larger due to the smaller resonant order, m, corresponding to the 2000 nm wavelength with this cavity size. The effective index sensitivity due to waveguide core width variation is actually 1.31 times lower at 2000 nm wavelength, but the resonant wavelength sensitivity becomes 1.08 times larger again due to the smaller resonant order. Finally, the effective index sensitivity to slab thickness is approximately even at both wavelengths, but the resonant wavelength sensitivity becomes 1.42 times larger. Examining the magnitude of the sensitivities, variation in silicon thickness yields the largest resonance variation, followed by slab thickness, and waveguide core width. The expected variation in any given process is contingent on the process parameters itself, however. For the chosen values of σ_{core}, σ_{slab}, and σ_{Si}, we see that variation in slab thickness presents the largest resonance

variation for the 1550 nm wavelength case while the variation in silicon thickness yields the largest resonance variation in the 2000 nm wavelength case.

7.3.2 Alignment power consumption

The 4-ring WDM system aligned to $\Delta f = 50$ GHz is simulated for both 1550 and 2000 nm wavelength configurations using all three ring organizations and varying d_s. The total power per resonance required to align each generated system through thermal tuning is used to calculate the mean (μ_P) and standard deviation (σ_P) across all 10,000 generated systems. The collected results are shown in Figure 7.6 a) and b) for 1550 and 2000 nm wavelength configurations, respectively.

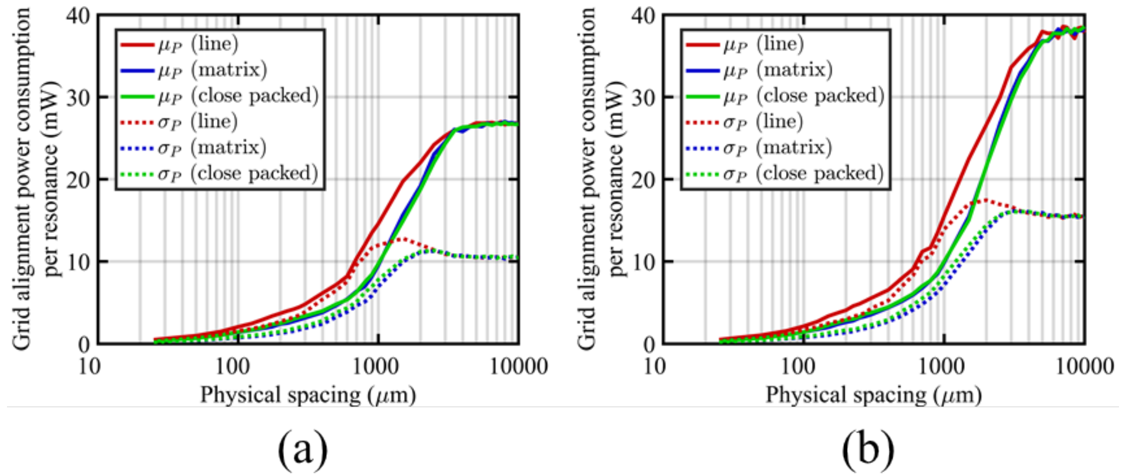

FIGURE 7.6: Mean and standard deviation of power expended to align a) 1550 nm and b) 2000 nm wavelength resonances to a 50 GHz grid in a 4-ring system using 'line', 'matrix', and 'close packed' organizations varying physical spacing d_s between each ring.

Examining Figure 7.6 a), μ_P for all three ring organizations increase with physical spacing as the sampled waveguide dimensions experience more variation until near the correlation length of $L_C = 4.5$ mm where μ_P begins to level off. Similarly, σ_P begins to

level off around this value as well. This makes sense as the same maximum variation will typically be found across and beyond this length. Comparing the three organizations, μ_P is highest for the 'line' across all d_s with a similarly high σ_P. Both 'matrix' and 'close packed' organizations have similar μ_P and σ_P across all d_s due to the fact that few rings are used in this system, but show reduced alignment power consumption as compared to the 'line' organization due to the reduction in device span in both the x- and y-direction as discussed previously. All three organizations converge in μ_P and σ_P near L_C, demonstrating that beyond this ring separation, each organization is equally favourable, although d_s of this magnitude is unrealistic in actual system fabrications. σ_P appears to follow its associated μ_P curve until a certain value of d_s where variation between the ring resonators is sufficiently high for resonant order mixing to occur which places an upper limit on σ_P. Both 1550 and 2000 nm wavelength ring resonator configurations show similar behaviour in the scenario presented, although μ_P and σ_P are universally higher at the longer wavelength, despite the higher heater efficiency. The main reason for this discrepancy is the choice of a fixed Δf for both wavelength cases; at 1550 nm, the wavelength distance between two resonances 50 GHz apart is approximately 400 pm, whereas at 2000 nm, this same frequency spacing results in a distance of 667 pm, approximately 1.67 times larger. For the 'line' organization, a small d_s of 250 µm requires a $\mu_P = 4.21$ mW in the 1550 nm WDM system and $\mu_P = 4.86$ mW in the 2000 nm WDM system, only 1.15 times larger; however, at a separation beyond L_C, for example, 10,000 µm, $\mu_P = 26.7$ mW and 37.8 mW, respectively, which is 1.41 times larger. From this we can deduce that the disparity between the two wavelength WDM systems becomes larger with larger spacing, but is mitigated somewhat by the larger heater efficiency of the 2000 nm wavelength configuration.

WDM and stacked resonance systems will typically have each ring resonator as close as possible to mitigate the effects of processing variation but far enough to avoid thermal crosstalk from the integrated heaters which can affect the resonances in adjacent ring

resonators. We continue investigating systems with d_s = 250 μm as a reasonable distance satisfying this trade-off, particularly with micro-ring resonator modulators where the electrodes typically cover more than 60 × 60 μm each despite having a small ring resonator radius.

The choice of Δf does not immediately suggest a predictable trend for a fixed N-ring system with fixed d_s; however, the different ring radii required in a WDM system to achieve a target Δf is accompanied by an increase in resonance variation which will increase with Δf. It was stated previously that for a given resonant wavelength, an increase in resonant order, m, can be countered by increasing the radius to achieve the same resonant wavelength (i.e. for a $n_{eff} = 2.56$ and $m = 125$, a radius of 12 μm yields a resonant wavelength of 1544.16 nm. For the same n_{eff} and $m = 126$, the same resonant wavelength is achieved at a radius of 12.096 μm). However, when the mode order remains fixed, which is typically the case with few-ring systems with small d_s (thus not incurring enough variation to encourage resonant order mixing) an identical variation Δn_{eff} in two ring resonators will cause a larger resonance variation in a larger ring by virtue of (7.4). Figure 7.7 a) shows μ_P and σ_P for a 1550 nm wavelength 4-ring WDM system with d_s of 250, 500, and 750 μm in a 'line' organization while Figure 7.7 b) shows the mean and standard deviation distance between adjacent resonances, $\mu_{\Delta\lambda}$ and $\sigma_{\Delta\lambda}$, respectively.

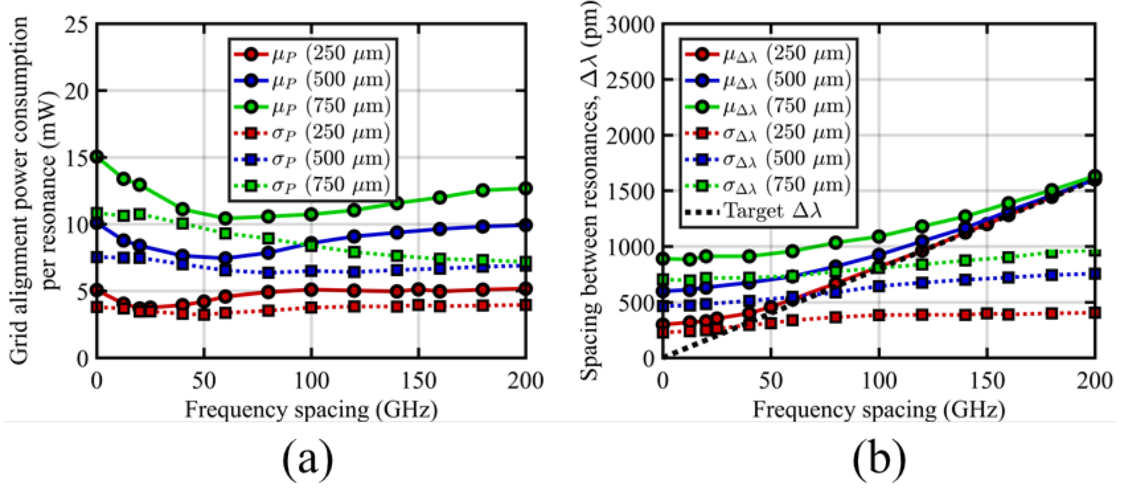

FIGURE 7.7: a) Mean and standard deviation of power expended to align resonances to various Δf in a 1550 nm wavelength 4-ring system physically spaced by 250, 500, and 750 µm in a 'line' organization and b) mean and standard deviation of distance between adjacent resonances. The black dashed line denotes the target wavelength spacing of a particular Δf and has a slope of ~8 pm/GHz.

We again see that larger d_s lead to increased μ_P and σ_P as in Figure 7.6. The aforementioned increase in resonance variation in WDM systems as ring radii sequentially increases leads us to expect an increase in μ_P with larger Δf. However, μ_P at $\Delta f =$ 0 GHz is similarly high as at $\Delta f = 200$ GHz, and furthermore, μ_P begins to decrease above $\Delta f = 0$ GHz reaching a minimum before increasing again. To understand this nuance, we can examine the distribution of spacing between adjacent resonances presented in Figure 7.7 b). At each Δf, there exists a distribution of spacing between adjacent resonances, each with a non-zero mean, $\mu_{\Delta\lambda}$, and standard deviation, $\sigma_{\Delta\lambda}$. In the case of $\Delta f = 0$ GHz, this distribution is represented as a half-Normal distribution with a peak density at 0 pm, but a non-zero $\mu_{\Delta\lambda}$ and $\sigma_{\Delta\lambda}$. As Δf increases, this half-Normal distribution transforms into a Normal distribution with $\mu_{\Delta\lambda}$ converging to the target adjacent resonance spacing $\Delta\lambda$ and increasing in $\sigma_{\Delta\lambda}$. At the two extremes, the half-Normal distribution near $\Delta f = 0$ GHz does not favour the target spacing $\Delta\lambda$ due to its

non-zero $\mu_{\Delta\lambda}$ and the Normal distributions at high Δf have increased $\sigma_{\Delta\lambda}$, both leading to higher thermal tuning requirements. Somewhere between these two extremes exists an intermediate resonance distribution (between half-Normal and Normal) which both favours the target spacing at a given Δf and has a sufficiently low $\sigma_{\Delta\lambda}$ ultimately reducing thermal tuning requirements shown by the minimum in each μ_P curve in Figure 7.7 a). For larger values of d_s, the increased variation leads to increased $\sigma_{\Delta\lambda}$ which further pushes this minimum in μ_P to larger Δf. Figure 7.8 shows similar results for a 2000 nm wavelength configuration:

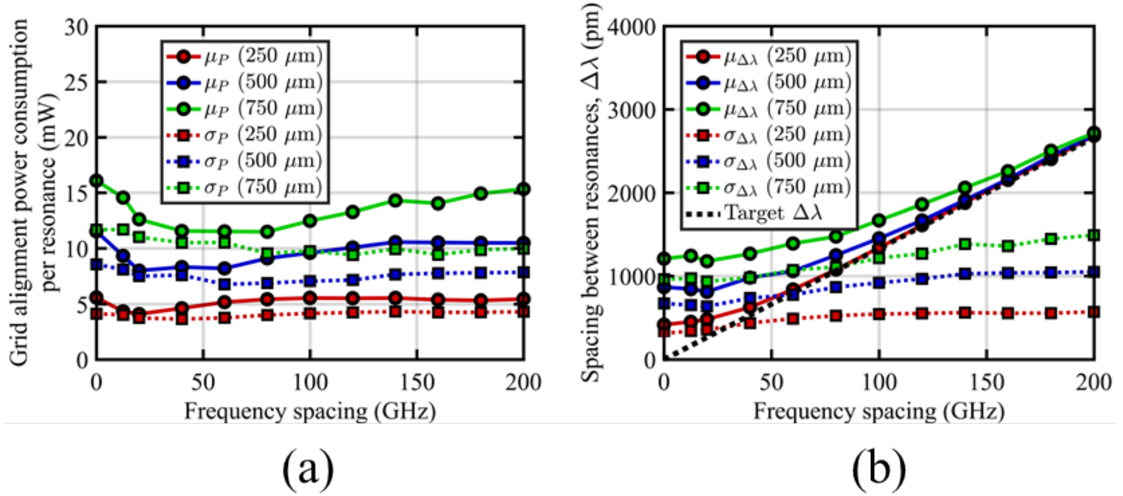

FIGURE 7.8: a) Mean and standard deviation of power expended to align resonances to various Δf in a 2000 nm wavelength 4-ring system physically spaced by 250, 500, and 750 µm in a 'line' organization and b) mean and standard deviation of distance between adjacent resonances. The black dashed line denotes the target wavelength spacing of a particular Δf and has a slope of ∼13.3 pm/GHz.

Overall, the 2000 nm wavelength configuration shows larger μ_P and σ_P as compared to the 1550 nm wavelength, particularly at larger d_s. At $d_s = 250$ µm, however, the results appear fairly similar which suggests that tightly packed stacked systems could see similar resonance variation at both wavelengths.

Another subtle consequence of varying Δf is the Monte Carlo algorithm's selection

of the resonant order, m, which has minimal thermal tuning and resonance trimming required. Due to the inverse nature of frequency and wavelength, a WDM system with ring radii calculated through (7.7) to achieve a particular Δf will manifest as a marginally larger resonance separation in the lower resonant orders, as previously discussed through (7.6). In other words, the wavelength separation between two resonances at a resonant order of m+1 (shorter wavelength) will be smaller than that of m-1 (longer wavelengths). As Δf becomes larger, so too does the disparity in resonance separation between resonant orders due to the larger ring radii required. A generated resonance cluster at order m with resonances spaced closer together or further apart than desired may see a reduction in thermal tuning required for alignment by moving to the m+1 or m-1 resonant order, respectively. Consider $\Delta f = 0$ GHz (stacked resonance), where the ring radii are identical and the ideal separation between resonances is zero: all resonances generated with variation will be spaced further apart than desired, thus all solutions will originate from the m+1 resonant order where these resonances are moved marginally closer together. As Δf increases, so too does the variation in distance between resonances due to the dissimilar ring radii, and generated resonance clusters which are spaced closer together than intended become more prevalent, leaning toward m-1 order which may offer a reduction in thermal tuning. To visualize this, the accumulated distributions of resonances for the 4-ring WDM system in Figure 7.7 with $d_s = 250$ µm are shown for several increasing values of Δf in Figure 7.9. As it is a 4-ring system, four distributions are shown in each subplot to represent the sorted resonances from lowest to highest.

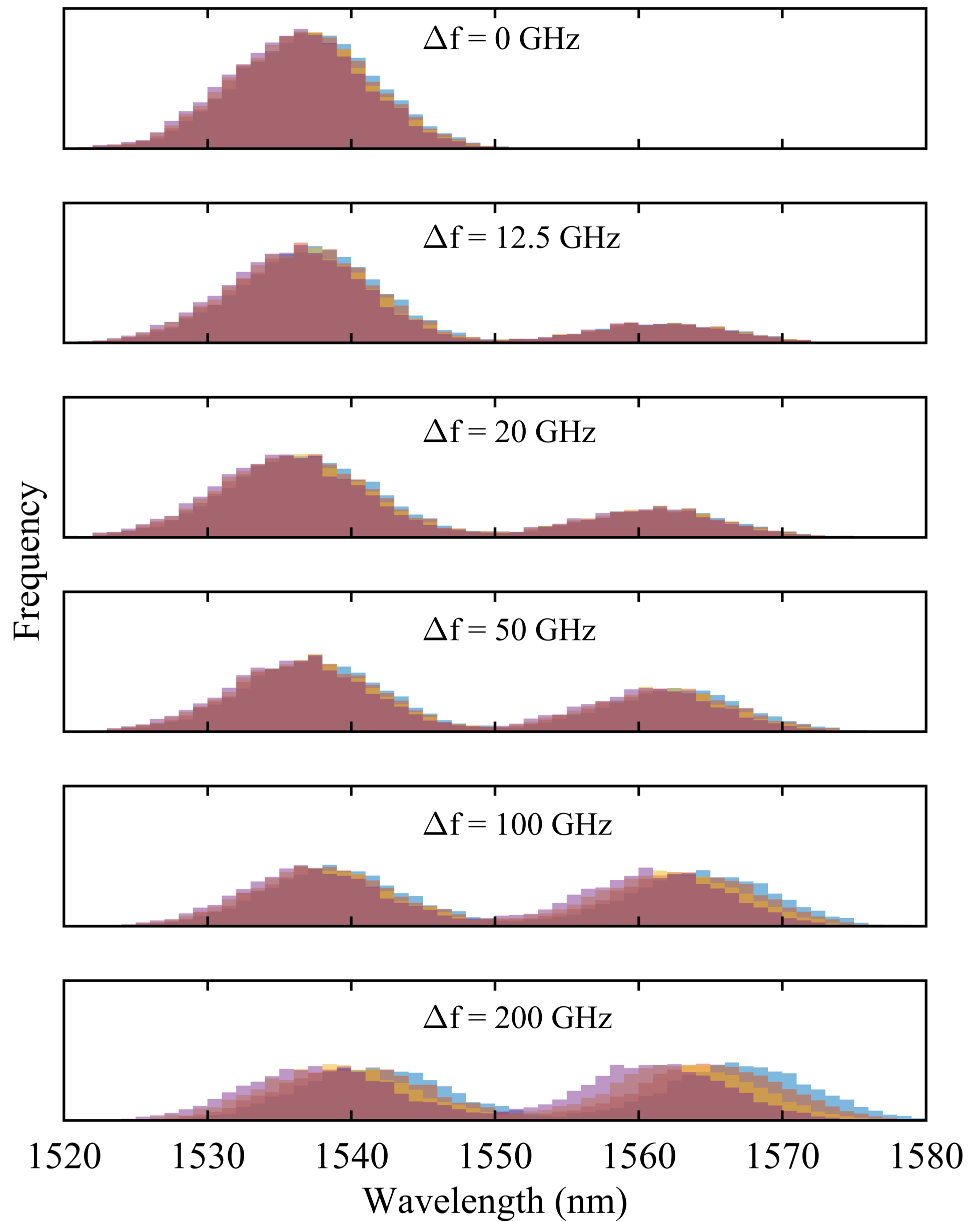

FIGURE 7.9: Distribution of resonant wavelengths chosen for 4-ring stacked resonance (Δf = 0 GHz) and WDM systems of increasing Δf with d_s = 250 μm between rings. Each color of distribution represents system resonances sorted lowest to highest.

Beginning with $\Delta f = 0$ GHz (a stacked resonance system) where the ring radii are equal, the distribution of resonances is centered near 1536 nm, which corresponds to the m+1 wavelength order. As Δf increases, the distribution becomes more bimodal indicating that more suitable solutions begin to appear at the m-1 wavelength order. Since three resonant orders are tested for suitability, we expect three peaks in the distribution. However, if a solution at m is more suitable than m+1 (i.e. less thermal tuning or trimming required), an even more suitable solution will exist at m-1. This is also the case when a solution at m is more suitable than m-1, an even more suitable solution exists at m+1. Had more resonant orders been tested (i.e. $m \pm$ 2, 3, 4, ..., etc.), the distribution would simply remain bimodal with each mode centered at the extreme orders. At a certain Δf, the frequency of both distribution modes becomes approximately even, indicating suitable solutions are equally likely to be found in either resonant order. Beyond this point, the distributions for each resonance begin to diverge from each other due to the larger variation experienced by the larger radii rings required to achieve larger Δf. This will cause μ_P to increase until the variation is strong enough to cause resonant order mixing to occur effectively placing an upper limit on the effect of variation similar to what was seen in Figure 7.6 for $d_s > L_C$.

Finally, it is important to investigate how μ_P and σ_P are affected by the number of rings used in a WDM system. Many-ring systems will span a large area with sufficiently large d_s and thus variation will typically grow with the number of rings. The calculated *FSR* of 8.17 nm for the 1550 nm wavelength configuration can fit approximately 82 resonances at $\Delta f = 12.5$ GHz. Similarly, the calculated *FSR* of 14.53 nm for the 2000 nm wavelength configuration can fit approximately 87 resonances. Figure 7.10 shows the grid alignment power consumption per resonance as a function of number rings for $\Delta f = 12.5$ GHz and $d_s = 250$ µm.

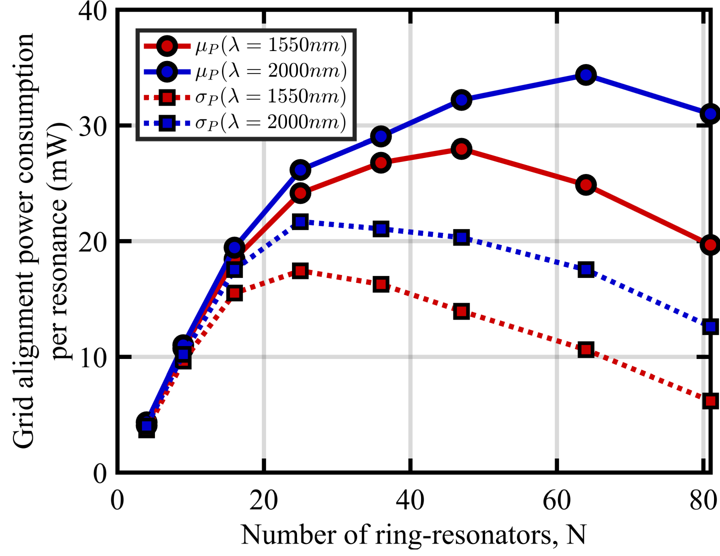

FIGURE 7.10: Mean and standard deviation of power expended to align 1550 and 2000 nm wavelength resonances to $\Delta f = 12.5$ GHz in an N-ring system with $d_s = 250$ µm using the 'line' organization.

We see that μ_P and σ_P for few-ring systems are very similar at both wavelengths but quickly become higher for the 2000 nm wavelength configuration in many-ring systems. Since d_s and Δf remain constant for both wavelengths, the main difference in μ_P and σ_P stem from the increased n_{eff} sensitivity to variation at 2000 nm wavelength as well as the larger resonance variation when using larger ring resonator radii due to the smaller resonant order of longer wavelengths in the same ring resonator cavity length. σ_P in both wavelength configurations seem to behave similarly and reach a maximum with a 25-ring system. With $d_s = 250$, a 25-ring system spans a total length of $L_T = 6.25$ mm, which is just above L_C, beyond which the wafer variation reaches a maximum. Beyond this length, a point is reached in an N-ring system where the variation between ring resonators (exaggerated by their increasingly dissimilar radii required for $\Delta f = 12.5$ GHz) is sufficient to cause resonant order mixing, however due to the smaller *FSR* of the 1550 nm wavelength configuration, this point is reached in a fewer-ring system than in the 2000 nm wavelength case.

7.3.3 Power saving through resonance trimming

We now turn our attention toward resonance trimming as a means of reducing the thermal tuning required to align a given system and, in cases of systems with little variation (small d_s, few rings, tightly packed, etc.), fully-aligning systems permanently via trimming such that no thermal tuning is required. We will focus on the 4-ring system with rings physically spaced by $d_s = 250$ µm aligned to a $\Delta f = 50$ GHz grid. Figure 7.11 a) shows boxplots of total power required for grid alignment with subsequent trimming across all generations. Figure 7.11 b) shows the power saved through subsequent trimming steps relative to each system's untrimmed state.

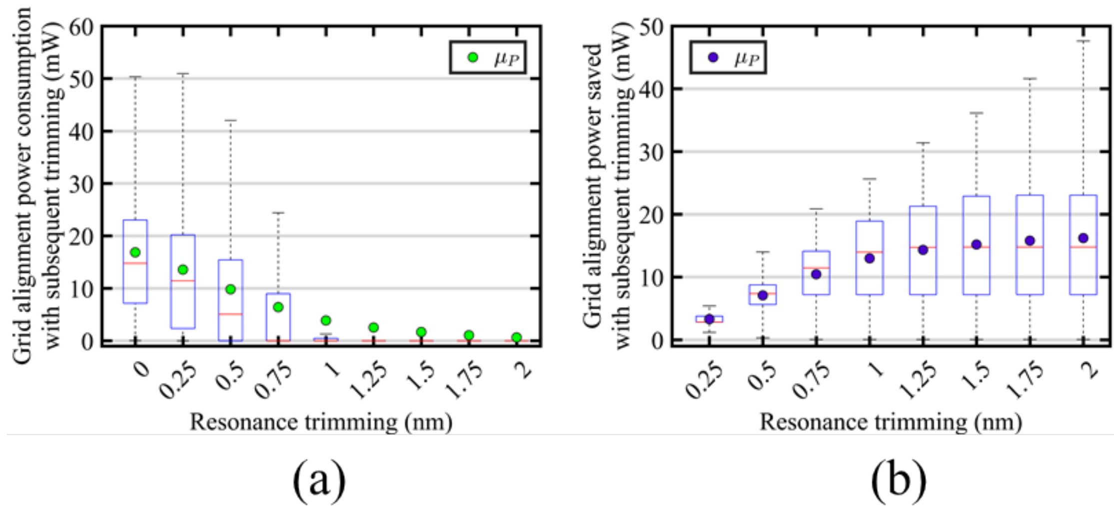

FIGURE 7.11: a) Boxplots of power consumption to align to a 50 GHz frequency grid with subsequent trimming for a 1550 nm wavelength 4-ring system with 250 µm spacing. b) Boxplots of grid alignment power saved with each subsequent trimming step. Boxplot edges represent 25th and 75th percentiles while whiskers extend to encompass ± 3σ. Red lines represent data medians while plotted markers represent data means. Outliers have been omitted.

We see that each trimming step reduces the grid alignment power until most of the generated systems have been fully-aligned and require no thermal tuning. The mean

power consumption μ_P decreases almost linearly approximately until almost all systems have been fully-aligned, beyond which there are diminishing returns as the outlying systems (not plotted) are trimmed due to their extraordinary conditions. This is also why μ_P does not reach zero with the median. μ_P does not necessarily coincide with the data median which implies a skewed distribution, but μ_P is adequate to describe the overall behaviour while including the influence of outlying data points. Similar data for the 2000 nm wavelength configuration are shown in Figure 7.12 a) and b).

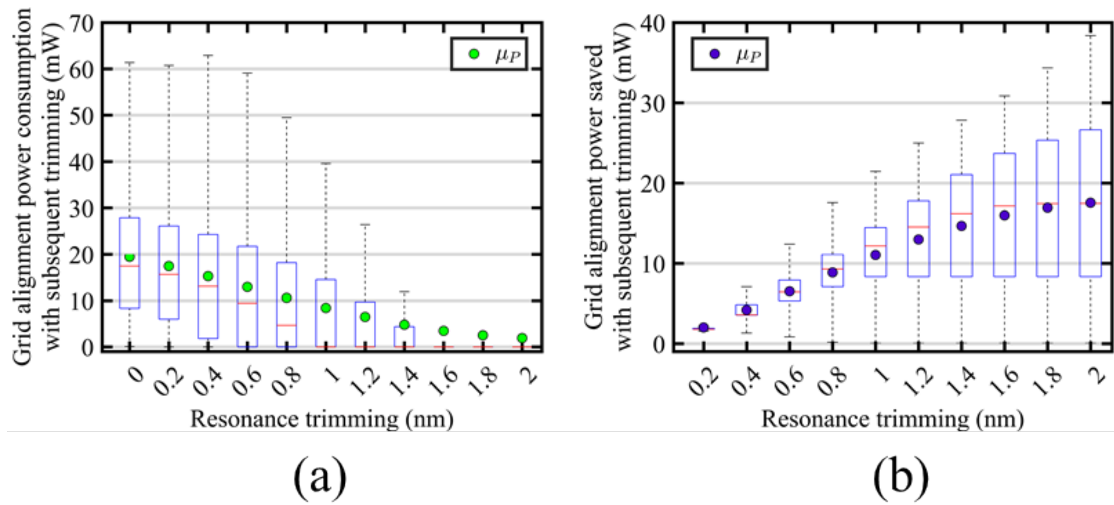

FIGURE 7.12: a) Boxplots of power consumption to align to a 50 GHz frequency grid with subsequent trimming for a 2000 nm wavelength 4-ring system with 250 µm spacing. b) Boxplots of grid alignment power saved with each subsequent trimming step. Boxplot edges represent 25th and 75th percentiles while whiskers extend to encompass $\pm$ 3σ. Red lines represent data medians while plotted markers represent data means. Outliers have been omitted.

Due to the larger resonance variation at the 2000 nm wavelength, μ_P is larger and the whiskers representing $\pm$ 3σ extend further. As well, more trimming is required to fully align the majority of the systems. If each WDM or stacked resonance system created is meant to be fully-aligned through trimming, it is important to know which factors can

impact the amount of trimming required and how to anticipate what fraction of manufactured systems can be fully-aligned. d_s has a major impact on the trimming required thus we examine the 4-ring WDM system with $\Delta f = 50$ GHz in a 'line' organization for both 1550 and 2000 nm wavelength configurations. For each trimming step, a check is performed to see if a system has been fully-aligned. Figure 7.13 a) and b) show the yield, or fraction of fully-aligned systems with various values of d_s for 1550 and 2000 nm wavelength configurations, respectively.

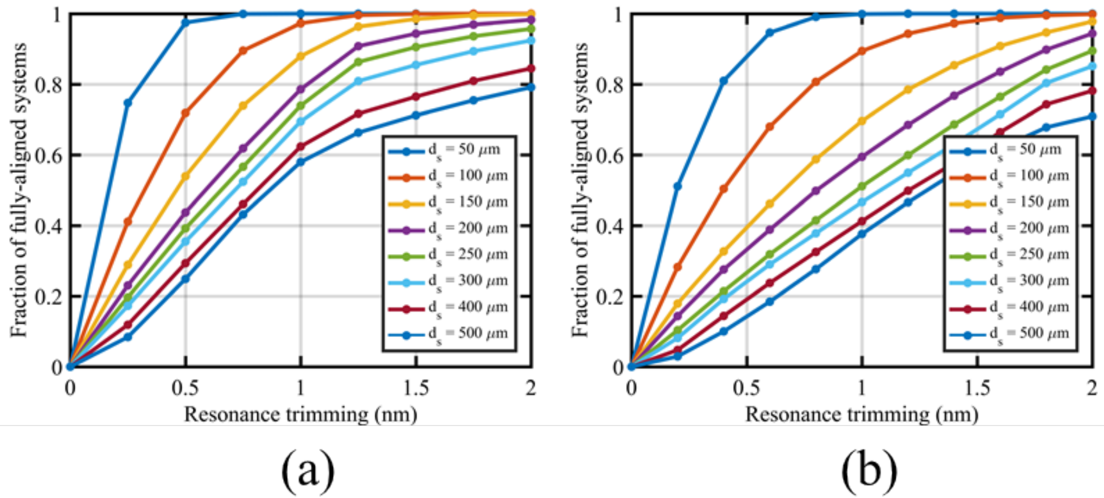

FIGURE 7.13: Fraction of 4-ring 50 GHz WDM systems spaced at various values of d_s which are fully-aligned at the specified amount of resonance trimming for a) 1550 nm and b) 2000 nm wavelength configurations.

For $d_s = 50$ μm, nearly all generated systems can be aligned with just 1 nm of available resonance trimming in both wavelength configurations. As d_s increases up to 500 μm, approximately 60% and 40% of systems at 1550 and 2000 nm wavelengths, respectively, can be fully-aligned. While most systems involve some buffer space between devices to reduce thermal cross-talk from integrated heaters for thermal tuning, this buffer is not required if the goal is to fully-align the system through resonance trimming, thus designers should strive for as small d_s as possible.

7.4 Conclusion

A Monte Carlo simulation was performed for 10,000 N-ring resonator systems designed for stacked resonance or WDM applications at both 1550 and 2000 nm wavelengths to examine trends in thermal tuning power consumption to align the systems to their respective frequency grids, as well as reduction in power consumption through subsequent resonance trimming. Spatial variation between device waveguide dimensions is introduced through the VWM and randomly sampling across independent virtual wafers describing variation in w_{core}, t_{slab}, and t_{Si} with standard deviations of σ_{core} = 2.6 nm, σ_{slab} = 3.3 nm, and σ_{Si} = 2 nm, and a correlation length of L_C = 4.5 mm. Sensitivity analysis is conducted to ascertain n_{eff} sensitivities for both wavelengths in waveguide with dimensions of t_{slab} = 90 nm, and t_{Si} = 220 nm, for both wavelengths, and w_{core} = 500 nm for 1550 nm wavelength and 650 nm for 2000 nm wavelength. Results show for 1550 nm wavelength, the largest effective index sensitivity is $\delta n_{eff}/\delta t_{Si} = 2.81\times10^{-3}$ nm^{-1}, which translates to a resonant wavelength shift of $\delta\lambda/\delta t_{Si}$ = 1.68 nm/nm. Per standard deviation of variation, t_{slab} yields the highest resonant wavelength variation of $\delta\lambda(\sigma_{slab})$ = 3.61 nm. For the 2000 nm wavelength, the largest effective index sensitivity is $\delta n_{eff}/\delta t_{Si} = 3.15\times10^{-3}$ nm^{-1} which translates to a resonant wavelength shift of $\delta\lambda/\delta t_{Si}$ = 2.70 nm/nm. Per standard deviation of variation, t_{Si} yields the highest resonant wavelength variation of $\delta\lambda(\sigma_{Si})$ = 5.40 nm.

The distributions of thermal tuning power required to align a 4-ring system to a Δf = 50 GHz frequency grid varying d_s for three different spatial organizations were examined and show that μ_P increases with d_s until $d_s \approx L_C$ where it remains constant. 'Close packed' ring organization can reduce required thermal tuning substantially in many-ring systems. For few-ring systems, the 'matrix' organization shows only marginally reduced performance compared to the 'close packed' organization. Placing ring resonators in a 'line' organization typically yields the highest variation and thus the highest thermal

tuning required to align to a frequency grid.

For 4-ring systems with fixed d_s in a 'line' organization, stacked resonance systems exhibit half-Normal distributions of resonance spacings, implying a non-zero mean spacing, while systems with larger Δf are Normally distributed with mean resonance spacing close to the desired spacing but with higher standard deviations due to the increasing difference between ring radii required to achieve the Δf spacing. Between these extremes exists a range of Δf with a skewed distribution of resonance spacings with adequate mean resonance spacing and small standard deviation so as to reduce the average thermal tuning required. This range of Δf extend to higher values with larger d_s. Given the choice between resonant orders of m-1, m, and m+1, the Monte Carlo algorithm will find resonance clusters corresponding to the minimum thermal tuning required in the m+1 order (smaller wavelengths) for stacked resonance systems (Δf = 0 GHz). As Δf becomes larger, more resonance clusters are chosen from the m-1 order until the cluster with the minimum thermal tuning required can be found with equal probability in the m+1 and m-1 orders. In any case, these two orders are preferred to the central m order.

In systems with a fixed d_s of 250 μm and Δf of 12.5 GHz in a 'line' organization, varying number of rings, σ_P for both wavelengths appears to reach a maximum for a 25-ring system where $L_T = N \times d_s > L_C$ and μ_P reaches a maximum where the variation (exaggerated by the different ring radii required to achieve Δf = 12.5 GHz) becomes sufficiently large for resonant order mixing to occur. This point occurs at a smaller N for the 1550 nm wavelength due to the smaller FSR of 8.17 nm as compared to the 2000 nm wavelength FSR of 14.53.

Resonance trimming shows drastic reduction in required thermal tuning requirements of a 4-ring system with a d_s of 250 μm and Δf of 50 GHz in a 'line' organization, and complete alignment of most systems with 2 nm of resonance trimming performed, for both 1550 and 2000 nm wavelength configurations. For tightly packed ring resonator

systems (d_s < 50 μm), more than 90% of all systems can be fully-aligned through 0.5 nm of resonance trimming performed. As this separation increases to d_s = 500 μm, approximately 60% of 1550 nm wavelength systems and 40% of 2000 nm wavelength systems can be fully-aligned with 1 nm of resonance trimming performed. More trimming is required for the 2000 nm wavelength systems due to the increased resonance sensitivity with variation as well as the naturally larger wavelength spacing for a given Δf.

This Monte Carlo approach to estimating thermal tuning power consumption across many devices with various parameters representing common design choices is useful for predicting performance of silicon photonic ring resonator systems in large-scale fabrication. WDM systems can see a reduction in thermal tuning requirements from resonance trimming and stacked resonance systems with small physical spacing between ring resonators, such as coupled resonator optical waveguides (CROWs) and higher-order filters, may be fully-aligned with sufficient resonance trimming, eliminating the need for thermal tuning of individual devices.

Bibliography

[1] F. Xia, M. Rooks, L. Sekaric, and Y. Vlasov, “Ultra-compact high order ring resonator filters using submicron silicon photonic wires for on-chip optical interconnects,” *Optics Express*, vol. 15, no. 19, p. 11934, sep 2007.

[2] H. C. L. Tsui, O. Alsalman, A. Alodhayb, H. Albrithen, D. E. Hagan, A. P. Knights, M. P. Halsall, and I. F. Crowe, “Silicon ’photonic molecules’ for sensing applications (Conference Presentation),” in *Silicon Photonics XIV*, G. T. Reed and A. P. Knights, Eds., vol. 10923. SPIE, mar 2019, p. 60.

[3] L. A. M. Barea, F. Vallini, G. F. M. de Rezende, and N. C. Frateschi, “Spectral Engineering With CMOS Compatible SOI Photonic Molecules,” *IEEE Photonics*

Journal, vol. 5, no. 6, pp. 2 202 717–2 202 717, dec 2013.

[4] A. Melloni, A. Canciamilla, C. Ferrari, F. Morichetti, L. O'Faolain, T. Krauss, R. De La Rue, A. Samarelli, and M. Sorel, "Tunable Delay Lines in Silicon Photonics: Coupled Resonators and Photonic Crystals, a Comparison," *IEEE Photonics Journal*, vol. 2, no. 2, pp. 181–194, apr 2010.

[5] K. De Vos, J. Girones, T. Claes, Y. De Koninck, S. Popelka, E. Schacht, R. Baets, and P. Bienstman, "Multiplexed Antibody Detection With an Array of Silicon-on-Insulator Microring Resonators," *IEEE Photonics Journal*, vol. 1, no. 4, pp. 225–235, oct 2009.

[6] B. A. Small, B. G. Lee, K. Bergman, Q. Xu, and M. Lipson, "Multiple-wavelength integrated photonic networks based on microring resonator devices," *Journal of Optical Networking*, vol. 6, no. 2, p. 112, feb 2007.

[7] Q. Xu, B. Schmidt, J. Shakya, and M. Lipson, "Cascaded silicon micro-ring modulators for WDM optical interconnection," *Optics Express*, vol. 14, no. 20, p. 9431, oct 2006.

[8] C. Qiu, J. Shu, Z. Li, X. Zhang, and Q. Xu, "Wavelength tracking with thermally controlled silicon resonators," *Optics Express*, vol. 19, no. 6, p. 5143, mar 2011.

[9] D. E. Hagan, B. Torres-Kulik, and A. P. Knights, "Post-Fabrication Trimming of Silicon Ring Resonators via Integrated Annealing," *IEEE Photonics Technology Letters*, vol. 31, no. 16, pp. 1373–1376, aug 2019.

[10] S. Spector, J. M. Knecht, and P. W. Juodawlkis, "Localized in situ cladding annealing for post-fabrication trimming of silicon photonic integrated circuits," *Optics Express*, vol. 24, no. 6, p. 5996, mar 2016.

[11] A. Canciamilla, F. Morichetti, S. Grillanda, P. Velha, M. Sorel, V. Singh, A. Agarwal, L. C. Kimerling, and A. Melloni, "Photo-induced trimming of chalcogenide-assisted silicon waveguides," *Optics Express*, vol. 20, no. 14, p. 15807, jul 2012.

[12] S. Grillanda, V. Raghunathan, V. Singh, F. Morichetti, J. Michel, L. Kimerling, A. Melloni, and A. Agarwal, "Post-fabrication trimming of athermal silicon waveguides," *Optics Letters*, vol. 38, no. 24, p. 5450, dec 2013.

[13] D. K. Sparacin, C.-y. Hong, L. C. Kimerling, J. Michel, J. P. Lock, and K. K. Gleason, "Trimming of microring resonators by photo-oxidation of a plasma-polymerized organosilane cladding material," *Optics Letters*, vol. 30, no. 17, p. 2251, sep 2005.

[14] A. P. Knights, Z. Wang, D. Paez, and L. Dow, "Electrical trimming of the resonance of a silicon micro-ring resonator," in *2017 IEEE 14th International Conference on Group IV Photonics (GFP)*. IEEE, aug 2017, pp. 29–30.

[15] J. Schrauwen, D. Van Thourhout, and R. Baets, "Trimming of silicon ring resonator by electron beam induced compaction and strain," *Optics Express*, vol. 16, no. 6, p. 3738, mar 2008.

[16] M. M. Milosevic, X. Chen, W. Cao, A. F. J. Runge, Y. Franz, C. G. Littlejohns, S. Mailis, A. C. Peacock, D. J. Thomson, and G. T. Reed, "Ion Implantation in Silicon for Trimming the Operating Wavelength of Ring Resonators," *IEEE Journal of Selected Topics in Quantum Electronics*, vol. 24, no. 4, pp. 1–7, jul 2018.

[17] D. Bachman, Z. Chen, R. Fedosejevs, Y. Y. Tsui, and V. Van, "Permanent fine tuning of silicon microring devices by femtosecond laser surface amorphization and ablation," *Optics Express*, vol. 21, no. 9, p. 11048, may 2013.

[18] Z. Lu, J. Jhoja, J. Klein, X. Wang, A. Liu, J. Flueckiger, J. Pond, and L. Chrostowski, "Performance prediction for silicon photonics integrated circuits with layout-dependent correlated manufacturing variability," *Optics Express*, vol. 25, no. 9, p. 9712, may 2017.

[19] W. A. Zortman, D. C. Trotter, and M. R. Watts, "Silicon photonics manufacturing," *Optics Express*, vol. 18, no. 23, p. 23598, nov 2010.

[20] L. Chrostowski, X. Wang, J. Flueckiger, Y. Wu, Y. Wang, and S. T. Fard, "Impact of Fabrication Non-Uniformity on Chip-Scale Silicon Photonic Integrated Circuits," in *Optical Fiber Communication Conference*. Washington, D.C.: OSA, mar 2014, p. Th2A.37.

[21] Z. Li, A. M. Heidt, J. M. O. Daniel, Y. Jung, S. U. Alam, and D. J. Richardson, "Thulium-doped fiber amplifier for optical communications at 2 µm." *Optics express*, vol. 21, no. 8, pp. 9289–97, apr 2013.

[22] Dan-Xia Xu, J. H. Schmid, G. T. Reed, G. Z. Mashanovich, D. J. Thomson, M. Nedeljkovic, Xia Chen, D. Van Thourhout, S. Keyvaninia, and S. K. Selvaraja, "Silicon Photonic Integration Platform—Have We Found the Sweet Spot?" *IEEE Journal of Selected Topics in Quantum Electronics*, vol. 20, no. 4, pp. 189–205, jul 2014.

[23] X. Zheng *et al.*, "A tunable 1x4 silicon CMOS photonic wavelength multiplexer/demultiplexer for dense optical interconnects," *Optics Express*, vol. 18, no. 5, p. 5151, mar 2010.

Chapter 8

Conclusion

8.1 Summary

The work presented in this thesis presents a study of micro-ring resonator (MRR) modulators optimized for use in the thulium doped fiber amplifier (TDFA) wavelength band centered around 2 μm. The context of much of the work is geared toward wavelength-division multiplexing (WDM) applications in telecommunications infrastructure, in particular, dense WDM (DWDM). A central theme of this thesis involves design and performance comparisons with MRR modulators designed for use in the erbium doped fiber amplifier (EDFA) wavelength band centered around 1.55 μm.

A theoretical performance comparison is presented between MRR modulators designed for TDFA- and EDFA-band wavelengths in Chapter 1. This chapter also serves as a general background chapter, presenting the majority of the background knowledge on which much of the thesis is built. Beginning with the basic building block of silicon photonics, the waveguide, parameters such as mode confinement, effective and group indices, waveguide thermo-optic coefficient, and dispersion are discussed for both wavelength regions on a 220 nm silicon-on-insulator (SOI) platform. The free-carrier effect, a major driving force for extended-wavelength modulation, is discussed. Despite the ~ 1.7

times stronger effect in bulk silicon, the reduced waveguide confinement at TDFA-band wavelengths (due to the fixed silicon thickness) reduces the effective free-carrier effect strength, although it remains stronger than at EDFA-band wavelengths. Static MRR theory and *p-n* junction waveguide modulator physics are presented which suggest that a larger resonance shift can be achieved at longer wavelengths, but at the expense of larger spectral Full-Width at Half-Maximum (*FWHM*), insertion loss (*IL*), and transmission penalty (*TP*). The higher *FWHM* and lower *IL* also translate to lower transmission operating points required for equal-transmission π phase-shifts for Binary Phase Shift Keying (BPSK) applications. Finally, a closed-form model is used to explore the small-signal dynamic operation of MRR modulators at both wavelength bands. Ultimately, slightly reduced performance is seen in TDFA-band MRR modulators, although it is not prohibitively low so as to render these devices inviable for future telecommunication infrastructure. As well, the small-signal performance does not fully describe large-signal performance used in actual devices.

A study of various optical loss mechanisms for SOI waveguides at TDFA-band wavelengths are presented in Chapter 3 with supporting measured results from associated test structures. Waveguide propagation loss due to sidewall scattering is measured through waveguide cut-back measurements and simulated at both EDFA- and TDFA-band wavelengths using the Payne-Lacey model, which demonstrates reduced scattering loss at longer wavelengths as estimated by the λ^{-4} dependence of Rayleigh scattering. Simulated substrate leakage shows that wider waveguide widths and a thicker buried oxide (BOX) layer are required at longer wavelengths to mitigate the extra loss incurred due to the reduced waveguide confinement explored in Chapter 2. This also implies larger coupling losses in inverse-taper/nanotaper structures. Measured bending loss results agree well with both 3-D Finite-Difference Time-Domain (FDTD) simulations and analytic modelling using the Marcuse model. Free-carrier absorption is measured in doped waveguide test structures. Measured results agree relatively well with simulations using

an empirical model used throughout the thesis. Finally, optical loss due to defect-related absorption is measured in ion implanted devices at various doses. Results do not agree with the analytic model used, which indicates a re-work of the model may be necessary in the future. Two samples were annealed with transmission measurements taken in-between. The transmission versus annealing temperature curves exhibit behaviour which strongly supports the presence of optically-active divacancy defects (crucial in the operation of the defect-mediated silicon detector used in Chapter 5) which fully anneal below 400 °C. The results and modelling presented in this chapter were used to improve designs of waveguides, MRRs, and MRR modulators presented in Chapter 4 and Chapter 5.

Chapter 4 presents a study of the free-carrier effect in an electronic variable optical attenuator (EVOA) and MRR modulator device. The EVOA was measured at discrete wavelengths of 1.31, 1.51, 1.55, 1.64, and 2.02 μm. Due to its large waveguide cross-section, all wavelengths have near-equal confinement in the waveguide and thus similar overlap between the optical mode and the injected free-carriers. Under carrier-injection, equal and homogeneous concentrations of electrons and holes are present in the waveguide. Through simulation using the empirical model for free-carrier absorption at each measured wavelength, electron and hole concentrations were determined for discrete forward bias voltages, showing excellent agreement with the model. Steady-state (DC) operation of a TDFA-band MRR modulator is demonstrated with measured results agreeing relatively well with reverse bias simulations based on a 1-D free-carrier profile calculated analytically. The results presented in this chapter demonstrated the validity of the empirical free-carrier effect model used as well as showcasing the device which demonstrated the first steady-state MRR modulator operating in the TDFA-band.

The demonstration of a high-speed MRR modulator, defect-mediated (DM) detector, and on-chip link (modulator + detector) is presented in Chapter 5. The high loss in

the grating couplers used for the modulator and on-chip link measurements are compensated for using a custom-built TDFA provided by Southampton University. A p-n^+ junction MRR modulator is designed and characterized in DC demonstrating a resonance shift of approximately 23 pm/V with a $V_\pi L_\pi$ of 2.2 to 2.6 V-cm at -1 and -8 V, respectively, and notch depth exceeding 18.7 dB. DC results are simulated using 2-D free-carrier profiles simulated in Athena™ and Atlas™ in Silvaco and translated (using a custom MATLAB® interpreter script) to a 2-D complex refractive index profile for optical simulation in RSoft's FEMSIM™. Measured results show excellent agreement with simulations indicating that this technique yields much higher accuracy than the previously demonstrated techniques in Chapter 3 and Chapter 4. High-speed (RF) characterization is performed using small-signal S_{21} measurements which yielded a bandwidth of 12.5 GHz, limited by the external detector used. At this time, this is the highest bandwidth demonstrated for a TDFA-band MRR modulator. DC characterization of the DM detector showed TDFA-band wavelength responsivities of 0.04 and 0.14 A/W at -15 and -30V, respectively. Small-signal S_{21} measurements yielded a maximum bandwidth of 16 GHz at -15 V and approximately half of this at -30 V. Large-signal measurements demonstrated open eye-diagrams up to 12.5 Gbps using a 2.5 V_{pp} Pseudo Random Binary Sequence (PRBS) length of 2^{31}-1. Finally, an on-chip link (modulator + detector) is demonstrated for the first time at TDFA-band wavelengths, demonstrating open eye-diagrams up to 12.5 Gbps for a similar 2.5 V_{pp} PRBS-31 signal. This is a major step toward the realization of an optical transceiver operating in this wavelength regime.

Chapter 6 presents a post-fabrication resonance trimming technique for use in MRR filters and modulators with integrated micro-heaters through the local annealing of defects. Measurements are performed at EDFA-band wavelengths for devices implanted with high energy ions which cause the formation of optically-active divacancy defects, similar to those explored in Chapter 3. These defects cause a resonance red-shift relative to an unimplanted device. Through the application of a high bias of the integrated

micro-heaters above the MRR device, local annealing of these divacancy defects causes a subsequent resonance blue-shift. A red-shift of up to 1.2 nm is demonstrated with a subsequent blue-shift through local annealing of 800 pm. This technique can be precisely controlled as demonstrated by the alignment of a 4-ring WDM system (comprised of four MRR modulators with natural frequency spacing subject to manufacturing variation) to a 50 GHz frequency grid with each resonance within 15 pm of target. Post-publication measurements are performed to demonstrate larger defect absorption at TDFA-band wavelengths which implies a larger resonance shift may be possible using this technique. Unimplanted devices demonstrated a blue-shift of $\sim$400 pm through local annealing, which implies a defect mechanism is present prior to post-fabrication ion implantation. The author suggests this mechanism is restructuring of the low-quality top-cladding oxide which is theoretically achievable at the temperatures which the micro-heater is reaching. Post-publication simulations demonstrate enhanced resonance trimming due to oxide restructuring at TDFA-band wavelengths due to the extension of the mode's evanescent field into the top-cladding as compared to EDFA-band wavelengths.

Finally, Chapter 7 builds on application of resonance trimming, presented in Chapter 6, through Monte Carlo simulations of MRR devices in WDM and stacked-resonance systems subject to spatially-correlated manufacturing variation in waveguide width, slab height, and silicon thickness. Through the generation of many systems, statistical trends emerge which may help designers anticipate large-scale system performance. Of particular importance is the thermal power dissipated by the integrated heaters traditionally used to correct for resonance variations and align the systems to their target wavelength. This fixed power dissipation can be reduced through strategic resonance trimming. In comparing systems designed for TDFA- and EDFA-band wavelengths, the former exhibits larger resonance sensitivities than the latter for waveguide width, slab thickness, and silicon height due to the reduced confinement in the 220 nm SOI platform. Larger alignment powers and resonance trimming distances are required at longer wavelengths

due to the naturally larger wavelength spacing for a fixed frequency spacing caused by the inverse relation between wavelength and frequency. For both wavelengths, organizing the MRR devices into a 'matrix' or 'close-packed' structure acts to reduce the total variation experienced, thus reducing the average alignment power and trimming required. Resonant order mixing can occur in sparsely placed systems or processes with large variation, placing an upper limit on the average thermal tuning power / trimming distance required. For systems with densely spaced devices, such as higher-order filters or coupled resonator optical waveguides (CROWs), trimming techniques can drastically reduce or even eliminate the need for thermal tuning through permanent alignment. Although the parameters presented represent a specific scenario with fixed variation values for waveguide width, slab height, and silicon thickness, this methodology can be customized for any process and MRR design and extended to incorporate more variation parameters and predict other performance metrics.

The work presented in this thesis suggests that telecommunications architectures which incorporates modulators and detectors designed for TDFA-band wavelengths may operate under different constraints than EDFA-band systems, but are nonetheless viable to transmit high-speed data and adopt advanced modulation techniques, both currently employed and researched. The additional data bandwidth afforded by the TDFA optical bandwidth for DWDM applications should be considered to aid in alleviating anticipated future bandwidth limitations.

8.2 Suggested future work

Suggested extensions of work presented in this thesis are discussed. Following the demonstration of a high-speed MRR modulator presented here, work should continue to improve device performance to further demonstrate its viability. To push the device higher

in terms of performance, collaborations should be fostered to improve aspects which are outside of the group's expertise, such as electrode design. Furthermore, advanced modulation formats may be easily demonstrated through collaborations with dedicated silicon photonics groups. Internally, device performance can be improved through careful simulation, particularly through Silvaco where electrical bandwidth can be estimated through device capacitance and resistance.

Along with improving individual device performance, system-level design which makes use of the available modulation speed should be a major focus. A DWDM system should be demonstrated with the novelty of utilizing the device trimming technique presented in Chapter 6 to fully-align the system if possible. Creating a segmented ring for PAM-4 modulation demonstration may also prove to be a significant next step. In either case, multiplexing the signals into a single short-reach transmission, or long-haul transmission with a TDFA for improved signal integrity, and using high-speed DM-detectors on the receiving chip can demonstrate a full transceiver with currently available components. Bit error rate (BER) testing should also be performed to give more concrete large-signal performance results of the MRR modulator.

Defects introduced through ion implantation present a large parameter space which should be explored further. A comprehensive exploration should be performed of not only absorption at different implant doses, energies, and annealing temperatures, but of defect composition as well if possible. One measurement which should be investigated is the lifetime of the various defects existing in an implanted sample.

The oxide etch used to expose silicon waveguides to form DM-detectors is a powerful tool only recently added for designers to use. By using strategic oxide etches, devices can be thermally isolated to mitigate thermal crosstalk (a particular hindrance in closely spaced devices). Conversely, an oxide etch around the heater region itself may reduce

thermal leakage and increase tuning performance as well as the temperatures demonstrated for in-situ defect annealing and oxide restructuring. If temperatures beyond 800 °C can be achieved in the silicon, the door opens to on-chip processing techniques such as in-situ oxidation and dopant diffusion, both of which have applications in resonance trimming and device performance tuning.

A comprehensive experiment should be performed involving the deposition of varying oxide qualities onto bare silicon photonic chips with MRRs followed by subsequent annealing steps to investigate trimming through the oxide restructuring posited in Chapter 6. Both EDFA- and TDFA-band wavelengths should be tested. To extend this, active MRR devices with oxide etches above the resonant cavity can and should be used as the basis for these relatively low-temperature material depositions. By using a MRR, very small changes in the cladding refractive index can be detected. As well, the integration of a micro-heater near the oxide etch (designed not explicitly to tune the ring, but to anneal the material) can be used to influence the deposited material, producing a permanent resonance shift for trimming purposes. Since there are design restrictions when using foundry-fabricated devices, in-house processing and oxide etching techniques should be investigated more intently, with particular emphasis on targeted mask-writing tools.

The Monte Carlo simulation approach demonstrated in Chapter 7 can be further developed and refined in collaboration with either CMC Microsystems or directly with a participating foundry and to examine the impact on silicon photonic systems which suffer from manufacturing variation. Provided the parameter space is sufficiently small, other effects not discussed (i.e. variations in doping concentration, waveguide sidewall angle, small footprint device grating pitch, etc.) can be incorporated.